



Technische Universität München  
Fakultät für Chemie  
Lehrstuhl für Technische Chemie I

# Perfluorosulfonic acid-based membrane electrode assemblies in PEM water electrolysis

Impact of PFSA ionic interactions on catalyst decomposition and  
membrane resistance

Kim-Marie Vetter

Vollständiger Abdruck der von der Fakultät für Chemie der Technischen  
Universität München zur Erlangung des akademischen Grades einer

**Doktorin der Naturwissenschaften (Dr. rer. nat.)**

genehmigten Dissertation.

Vorsitzender: Prof. Dr. Klaus Köhler

Prüfende der Dissertation:

1. Prof. Dr.-Ing. Kai-Olaf Martin Hinrichsen
2. Hon.-Prof. Dr. Maximilian Fleischer

Die Dissertation wurde am 27.09.2021 bei der Technischen Universität München  
eingereicht und durch die Fakultät für Chemie am 09.11.2021 angenommen.







*Für Dich, Papa*

*Du hast mir Flügel verliehen und mich geliebt. Du wirst mich nie allein lassen.  
Ab dort, wo nur noch eine Spur im Sand zu sehen ist, trage ich Dich.  
In meinem Herzen.*



Mein besonderer Dank gilt meinem Doktorvater

Prof. Dr.-Ing. Kai-Olaf Hinrichsen

für die freundliche Aufnahme in sein Fachgebiet der Technischen Chemie, die Integration in seinen Lehrstuhl, die Schaffung einer ausgesprochen positiven Arbeitsatmosphäre, seine Verbindlichkeit, sowie das entgegengebrachte Vertrauen bei der Umsetzung all meiner Projekte. Weiterhin danke ich ihm für seine Offenheit gegenüber neuen Forschungsfragen und -gebieten sowie für seine professionellen Ratschläge, die ich bereits seit meiner Masterarbeit als richtungsweisend für meinen Werdegang empfunden habe.

Ein weiterer, besonderer Dank gebührt meinem Betreuer

Dr. Günter Schmid

für die Aufnahme und Einführung in das firmeninterne Forschungsumfeld, seine Unterstützung bei der Themenfindung sowie seine Hilfe bei der Umsetzung eines Projekts von der Idee bis hin zur Publikation mit allen damit verbundenen organisatorischen und finanziellen Implikationen. Weiterhin danke ich ihm für die Eröffnung neuer Sichtweisen, seine exzellenten fachlichen Ratschläge und die Akzeptanz meiner Entscheidungen in der finalen Phase meiner Dissertation.





# Danksagung

Ich betrachte das vorliegende Dokument als Frucht einer Etappe meines Lebens, die mir für immer im Gedächtnis bleiben wird. Unsicherheit, Zweifel und Ängste wichen wachsender Zuversicht, Demut und bleibender Dankbarkeit. Ich bin dankbar und möchte diesem Gefühl ansatzweise durch die Nennung meiner wichtigsten Wegbegleiter:innen Ausdruck verleihen.

Zuvorderst spreche ich meinen Dank meinen exzellenten Korrekturleser:innen **Anika Spiesberger, Laura Kuhlmann, Nemanja Martić, Olaf Conrad** und **Thomas Reichbauer** aus. Durch eure Rückmeldung und Verbindlichkeit konnte ich der vorliegenden Arbeit ihre Form und den letzten Feinschliff verleihen.

Mein aufrichtiger Dank gilt meinem professionellen Umfeld zunächst bei der Siemens AG, später bei Siemens Energy. Besonders hervorzuheben ist hierbei mein Praktikant und Masterand **Jamie Härtl**, sowie meine zweifache Praktikantin **Camila Mauro**. Ich danke euch für euer Vertrauen, eure Zuverlässigkeit und die gigantisch gute Arbeit, die ihr geleistet habt! **Thomas Reichbauer, Nemanja Martić, David Reinisch** und **Christoph Vogl** gaben mir ein Gefühl der Zugehörigkeit und nicht zu selten eines der Andersartigkeit, zwei Extrema, welche die Komplexität menschlicher Interaktionen in 35/409 nur oberflächlich anzudeuten vermögen. Vielen Dank, dass wir zu einem echten Team zusammengewachsen sind, in dem jede:r den Freiraum erhält, der grade nötig ist. Danke, **Jane Leung** für unsere enge Bindung trotz der Distanz, Deine Freundschaft und all die Worte, die Du wie kaum ein:e andere:r zu wählen vermagst. Besonders hervorheben möchte ich außerdem **Anna Maltenberger**. Danke Anni für Dein strahlendes Lächeln und eine Weisheit, die ich nie vergessen werde. Mein aufrichtiger Dank gilt überdies **Prof. Max Fleischer** für sein Mentorat und die zuverlässige Unterstützung in der finalen Phase meiner Promotion. Ebenso danke ich der gesamten Abteilung (hie sie nun PXS, COS oder DEV) in Erlangen und in München inklusive aller personellen Wechsel, die ich begleiten durfte, für Unterstützung, Einblicke und zahlreiche neudeutsche Learnings. Über die Abteilung hinaus gebührt mein Dank außerdem diversen Nachbarabteilungen, die mich in den verschiedensten Fragestellungen unterstützt haben.

Kein einzelner Part dieser Arbeit wäre möglich gewesen ohne die Unterstützung seitens der Technischen Universität München. Begonnen bei dem **Lehrstuhl für Technische Chemie I** und seinen aktuellen sowie ehemaligen Mitgliedern, die mich ungeachtet meines Status als „Externe“ herzlich in ihre Reihen aufgenommen haben.

Unsere Diskussionen bereicherten mich und meine wissenschaftliche Arbeit ungemain! Ebenso bin ich dem **Fakultätsgraduierenzentrum Chemie** (FGCh), insbesondere **Dr. Markus Drees** zu aufrichtigem Dank verpflichtet für zügigste Antworten, unermüdliche Erklärungen und unbeschwerte Leichtigkeit. Ich habe mich durch Kontakte, den Zugang zu verschiedensten Analysemethoden und ein breites Seminarangebot sowohl fachlich als auch überfachlich unterstützt und gefördert gefühlt. Mein Werdegang hat seine Wurzeln in Hargesheim, einem kleinen Dorf in Rheinland-Pfalz. Danke **Jutta Ewen** für die Hinführung zur Chemie erst in der Mittel-, dann in der Oberstufe und die Möglichkeit zu einer Facharbeit über bunte Glasperlen. Wie schön doch die Chemie sein kann!

Meine tiefste Verbundenheit möchte ich meinen Freund:innen ausdrücken. **Anna Köhlmeier**, ich danke Dir für eine Freundschaft, die ihresgleichen sucht. Nicht nur in Sachen Doktorarbeit sondern in jedem erdenklichen Bereich meines Lebens kann ich mich an Dich wenden. **Anika Spiesberger**, Du lebst Treue und Zuverlässigkeit aber auch Kommunikationsfähigkeit und Verbindlichkeit wie keine Zweite. Wenn ich den Werdegang unserer Freundschaft extrapoliere, blicke ich der Zukunft mit meinem breitesten Lächeln entgegen! Ich danke meiner gesamten Base für Diversity, Charaktere, Crashes, Ratschläge und präzise Fragen, die wehtun. Danke **Nicole Kühn** für Tee, Kekse und einen unangenehmen Rat im richtigen Moment. Danke **Madlena Sutor** für Positivität und Psychologie und beides vereint in Madis Buch. Danke **Laura Kuhlmann** für tiefste Gespräch und der Anregung zu Reflexionen beyond compare. Danke **Tina Lindner** für Deinen Glauben an mich und so viel Vorbild auf Augenhöhe. Außerdem danke ich dem **22. Jahrgang** der Bayerischen EliteAkademie sowie dem gesamten Team des LadyFitnessClubs in Forchheim und insbesondere **Mandy Mazur** für ihren Beitrag zu physischer Stärke und mentaler Balance.

Von tiefstem Herzen danke ich meinem Partner **Olaf Conrad** für das wunderbare Geschenk seiner Liebe. Meine schwesterlichste Verbundenheit gilt meinen Geschwistern **Sukie** und **Bent** sowie meiner gesamten Familie und insbesondere meiner **Mutter**. Mama, Du bist der wichtigste Mensch in meinem Leben und ich danke dir für Deine Akzeptanz, Dein Vorbild, die größte Menschlichkeit, Deine vertrauensvolle Freundschaft und mütterliche Liebe. Dank Dir und dank euch allen konnte diese Arbeit entstehen.

## Abstract

The world is currently facing two important challenges: global warming and an increasing energy demand of its growing population. On the way towards green and sustainable energy carriers, the interest in electrochemical applications powered by green electricity has seen tremendous growth. In this context, hydrogen is widely seen as the number one sustainable energy carrier that has the potential to shape the future energy landscape.

Scaling up green technologies, such as proton exchange membrane (PEM) electrolysis, is important to make them broadly available in society and thus replace traditional energy carriers, such as coal and oil. However, there are still many challenges to overcome with some of them addressed in this thesis: First, catalyst materials used in PEM electrolysis are scarce. State-of-the-art anode catalyst iridium is among the rarest materials in the world and needs to be replaced by affordable, earth-abundant alternatives. Second, the functionalized polymers linking both electrochemical half-cells and their behavior upon treatment with ion containing solutions are not fully understood yet.

This thesis deals with the water electrolyzer's core, the membrane electrode assembly (MEA) and covers three parts: The anode side catalyst, the membrane itself and its implications for the cathode side, where using electrolytes that contain alkali metal cations is very common in further electrochemical applications, such as CO<sub>2</sub> electroreduction. In the first part, the cobalt polyoxometalate (POM) anion [Co<sub>9</sub>(H<sub>2</sub>O)<sub>6</sub>(OH)<sub>3</sub>(HPO<sub>4</sub>)<sub>2</sub>(PW<sub>9</sub>O<sub>34</sub>)<sub>3</sub>]<sup>16-</sup> is investigated as an iridium alternative for oxygen evolution reaction (OER). The as-synthesized material was investigated employing various characterization techniques (Brunauer-Emmett-Teller surface analysis, scanning electron microscopy, thermogravimetric analysis and X-ray diffractometry), followed by an integration into a scalable MEA based on perfluorosulfonic acid (PFSA) polymer (Nafion<sup>®</sup>). The obtained results showed that acid lability prevents its usage in PEM water electrolysis, since POM clusters decomposition releases soluble products, such as Co<sup>2+</sup>.

Continuing *via* the PFSA polymer itself, the second part investigates cation-sulfonate interactions as a lever to tune the polymers viscoelastic properties. For example, it was found that Li<sup>+</sup> introduction into the polymer matrix enhances polymer stability during processing. During operation, Li<sup>+</sup> cations are quantitatively driven out of

the membrane, a process called potential-driven substitution (PDS) thus identifying cation-proton exchange as an important tool for membrane modification.

The third part of the dissertation elaborates on PFSA-cation interactions during operation. PEM water electrolysis is used as a model system, where a PEM water electrolyzer was fed with high molar electrolytes. PFSA resistance and cell potential contributions are identified and quantified providing a knowledge applicable for electrochemical reduction of CO<sub>2</sub>. Bearing in mind scale-up and its implications for society, the focus of all three studies is on scalability and industrial applicability.

## Zusammenfassung

Die Welt sieht sich zur Zeit mit zwei wichtigen Herausforderungen konfrontiert: Die globale Klimaerwärmung und ein steigender Energiebedarf ihrer wachsenden Bevölkerung. Auf dem Weg zu grünen, nachhaltigen Energieträgern wächst das Interesse an elektrochemischen Anwendungen, die durch grüne Elektrizität angetrieben werden, enorm. In diesem Kontext wird Wasserstoff weithin als Nummer Eins der erneuerbaren Energieträger betrachtet und birgt das Potenzial, die künftige Energielandschaft der Welt mitzuprägen.

Die Skalierung grüner Technologien, wie etwa Protonentauschermembran (*engl.* proton exchange membrane, PEM)-Elektrolyse, ist wichtig, um sie der Gesellschaft in breitem Umfang zur Verfügung zu stellen und so traditionelle Energieträger, wie Kohle und Öl, zu verdrängen. Bei diesem Unterfangen gilt es noch wichtige Herausforderungen zu bewältigen, von denen einige in dieser Thesis behandelt werden: Erstens sind die Katalysatormaterialien, die in der PEM-Elektrolyse zum Einsatz kommen, Seltenerdmetalle. Der modernste Katalysator, Iridium, rangiert unter den seltensten Materialien der Welt und muss durch erschwingliche, reichlich vorhandene Alternativen ersetzt werden. Zweitens sind die funktionalisierten Polymere, welche die zwei elektrochemischen Halbzellen verbinden, und ihr Verhalten im Kontakt mit ionenhaltigen Lösungen noch nicht vollständig verstanden.

Diese Thesis beschäftigt sich mit dem Herzen des Wasserelektrolyseurs, der Membran-Elektroden-Anordnung (MEA), und besteht aus drei Teilen: Der erste beschäftigt sich mit dem Anodenkatalysator, der zweite mit der Membran selbst und der dritte mit den Auswirkungen der Membran auf die Kathodenseite, auf der es für weitere elektrochemische Anwendungen, wie etwa die CO<sub>2</sub>-Elektroreduktion, üblich ist, alkalimetallionenhaltige Elektrolyte einzusetzen. Im ersten Teil wird das Cobaltpolyoxometallat (POM)-Anion [Co<sub>9</sub>(H<sub>2</sub>O)<sub>6</sub>(OH)<sub>3</sub>(HPO<sub>4</sub>)<sub>2</sub>(PW<sub>9</sub>O<sub>34</sub>)<sub>3</sub>]<sup>16-</sup> hinsichtlich seiner Eignung als Iridiumersatz für die Sauerstoffentwicklungsreaktion (*engl.* oxygen evolution reaction, OER) untersucht. Das Material wird verschiedensten Charakterisierungstechniken unterzogen (Brunauer-Emmett-Teller-Oberflächenanalyse, Rasterelektronenmikroskopie, Thermogravimetrie, Röntgendiffraktometrie) und anschließend in eine skalierbare MEA integriert, die auf Perfluorosulfonsäure (*engl.* perfluorosulfonic acid, PFSA)-Polymer (Nafion<sup>®</sup>) basiert. Es wurde erkannt, dass seine Säurelabilität die Verwendung des POMs in der PEM-Wasserelektrolyse verhindert, da bei der Zersetzung lösliche Spezies, wie etwa Co<sup>2+</sup>, entstehen.

Der zweite Part widmet sich dem PFSA-Polymer selbst und seinen Interaktionen mit Fremdkationen, die als Hebel zur Modifikation der viskoelastischen Polymereigenschaften genutzt werden können. Es wurde gezeigt, dass die Einführung von  $\text{Li}^+$  in die Polymermatrix die Polymerstabilität während der Verarbeitung erhöht. Im Betrieb werden  $\text{Li}^+$ -Kationen quantitativ aus der Membran getrieben, ein Prozess, der potenzialgetriebene Substitution (*engl.* potential-driven substitution, PDS) genannt wird. Der Kationen-Proton-Austausch wurde folglich als wichtiges Werkzeug für Membranmodifikationen identifiziert.

Der dritte Teil der Dissertation beschäftigt sich mit PFSA-Kationen-Wechselwirkungen während des Betriebs. PEM-Wasserelektrolyse wird hier als Modellsystem verwendet, in dem der PEM-Wasserelektrolyseur mit hochmolaren Elektrolyten gespeist wird. Der PFSA-Widerstand sowie Beiträge zum Zellpotential werden identifiziert und quantifiziert und liefern Wissen, das direkt auf die  $\text{CO}_2$ -Elektroreduktion übertragbar ist. In allen Teilen der Arbeit liegt der Fokus auf Skalierbarkeit und industrieller Anwendbarkeit, um die Bereitstellung in der Gesellschaft zu ermöglichen.

# Table of Contents

|  |            |
|--|------------|
| <b>Abstract</b>  | <b>I</b>   |
| <b>Zusammenfassung</b>   | <b>III</b> |
| <b>1. Introduction and motivation</b>  | <b>1</b>   |
| 1.1. PEM water electrolysis – spotlight on green hydrogen production in the context of historic developments . . . . . | 1          |
| 1.2. Challenges in scaling electrolysis . . . . .  | 3          |
| 1.3. Electrocatalysts for oxygen evolution reaction and their role in green hydrogen production . . . . .              | 5          |
| 1.3.1. Oxygen evolution reaction and its implications at industrially relevant current densities . . . . .             | 5          |
| 1.3.2. Iridium scarcity – catalyst alternatives towards profitable energy solutions . . . . .                          | 7          |
| 1.3.3. Polyoxometalates and their catalytic potential in oxidation reactions . . . . .                                 | 10         |
| 1.3.4. POM catalytic properties and methodology to assess catalyst suitability . . . . .                               | 11         |
| 1.4. PFSA-based Proton exchange membranes and their application in PEM water electrolysis . . . . .                    | 14         |
| 1.4.1. PFSA applications – established functional polymer in electrolysis and beyond . . . . .                         | 14         |
| 1.4.2. Perfluorosulfonic acid – a robust polymer with the ability to selectively transport cations . . . . .           | 15         |
| 1.4.3. Sulfonate-metal cation interactions as a key lever for PFSA property modification during processing . . . . .   | 17         |
| 1.4.4. Li-sulfonate interactions – a pathway for morphological membrane modification . . . . .                         | 20         |
| 1.4.5. Potassium-based electrolytes and their impact on electrolysis applications . . . . .                            | 21         |

|  |            |
|--|------------|
| 1.4.6. Proton-metal cation exchange – methods to assess its potential for optimizing industrial electrolysis . . . . .   | 22         |
| 1.5. Scope of this thesis . . . . .  | 26         |
| <b>2. Results and discussion</b>   | <b>27</b>  |
| 2.1. Stability evaluation of earth-abundant metal-based polyoxometalate electrocatalysts for oxygen evolution reaction towards industrial PEM electrolysis at high current densities . . . . . | 27         |
| 2.1.1. Publication summary . . . . .   | 27         |
| 2.1.2. Introduction . . . . .  | 29         |
| 2.1.3. Experimental . . . . .  | 31         |
| 2.1.4. Results and discussion . . . . .  | 36         |
| 2.1.5. Conclusion . . . . .  | 54         |
| 2.2. Morphological tuning of membrane processing by temporal proton-metal cation substitution in perfluorosulfonic acid membranes . . . . .  | 57         |
| 2.2.1. Publication summary . . . . .   | 57         |
| 2.2.2. Introduction . . . . .  | 59         |
| 2.2.3. Experimental . . . . .  | 61         |
| 2.2.4. Results and discussion . . . . .  | 66         |
| 2.2.5. Conclusion . . . . .  | 89         |
| 2.3. K <sup>+</sup> transport in perfluorosulfonic acid membranes and its influence on membrane resistance in CO <sub>2</sub> electrolysis . . . . .   | 91         |
| 2.3.1. Publication summary . . . . .   | 91         |
| 2.3.2. Introduction . . . . .  | 93         |
| 2.3.3. Experimental . . . . .  | 97         |
| 2.3.4. Results and discussion . . . . .  | 101        |
| 2.3.5. Conclusion . . . . .  | 126        |
| <b>3. Summary and outlook</b>  | <b>128</b> |



---

|  |            |
|--|------------|
| <b>4. References</b>   | <b>132</b> |
| <b>5. List of Figures</b>  | <b>147</b> |
| <b>6. List of Tables</b>   | <b>154</b> |
| <b>7. Reprint permissions</b>  | <b>156</b> |
| 7.1. Wiley articles . . . . .  | 156        |
| 7.2. Elsevier article . . . . .  | 167        |
| <b>8. Bibliographical data for complete publications</b>   | <b>168</b> |
| 8.1. Stability evaluation of earth-abundant metal-based polyoxometalate electrocatalysts for oxygen evolution reaction towards industrial PEM electrolysis at high current densities . . . . . | 168        |
| 8.2. Morphological tuning of membrane processing by temporal proton-metal cation substitution in perfluorosulfonic acid membranes . . . . .  | 169        |
| 8.3. K <sup>+</sup> Transport in perfluorosulfonic acid membranes and its influence on membrane resistance in CO <sub>2</sub> electrolysis . . . . .   | 170        |
| <b>9. List of publications and conference contributions</b>  | <b>171</b> |
| 9.1. Journal articles . . . . .  | 171        |
| 9.2. Conference contributions . . . . .  | 172        |
| 9.3. Patents and invention disclosures . . . . .   | 172        |
| <b>A. Supporting information of publications</b>   | <b>175</b> |



## 1. Introduction and motivation

Green hydrogen as a part of a sustainable energy strategy requires high commitments both, in research and society, as well as for policy makers.<sup>[1]</sup> Green hydrogen can be produced *via* proton-exchange-membrane (PEM), alkaline, high-temperature and emerging anion exchange membrane (AEM) electrolysis. Alkaline as the most traditional technique among these uses iron- and nickel-based catalyst materials in alkaline environment. PEM and AEM electrolysis are defined by the use of a specialized ion exchange membrane, selectively permeable for either cations (PEM) or anions (AEM). High-temperature electrolysis is performed in a solid-oxide electrolyzer cell at 500 - 850 °C and thus also called steam-electrolysis. In this dissertation, the focus is on PEM electrolysis due to its highly dynamic operation and high efficiency. In this context, the search for suitable catalyst materials as well as processing special polymer membranes are among the most important challenges of the global energy transition today and will be addressed within this thesis.

### 1.1. PEM water electrolysis – spotlight on green hydrogen production in the context of historic developments

In the context of the global energy transition and an increasing worldwide energy demand, hydrogen plays an important role as a green energy carrier when produced in a sustainable fashion. Proton-exchange or polymer electrolyte membrane (PEM) electrolysis has been attracting increasing attention over the last few decades due to its ability to produce pure, high-quality hydrogen.

A requirement for the production of green hydrogen *via* electrolysis is electricity generated from renewable energy sources. Therefore, well-established energy supply chains, such as photovoltaics, wind turbines and hydrothermal resources, need to be complemented by biomass and further high-potential energy generation channels.<sup>[2,3]</sup> The electrolysis step itself, splitting water (H<sub>2</sub>O) into hydrogen (H<sub>2</sub>) and oxygen (O<sub>2</sub>) can then be accomplished either by alkaline, PEM or high-temperature water electrolysis.<sup>[4]</sup> After storage and transportation, hydrogen can then be reused to produce electricity and heat (e.g. in fuel cell drives), as substitutes for diesel and kerosene and as a raw material for industrial purposes, such as special chemical or plastic production.<sup>[1]</sup>

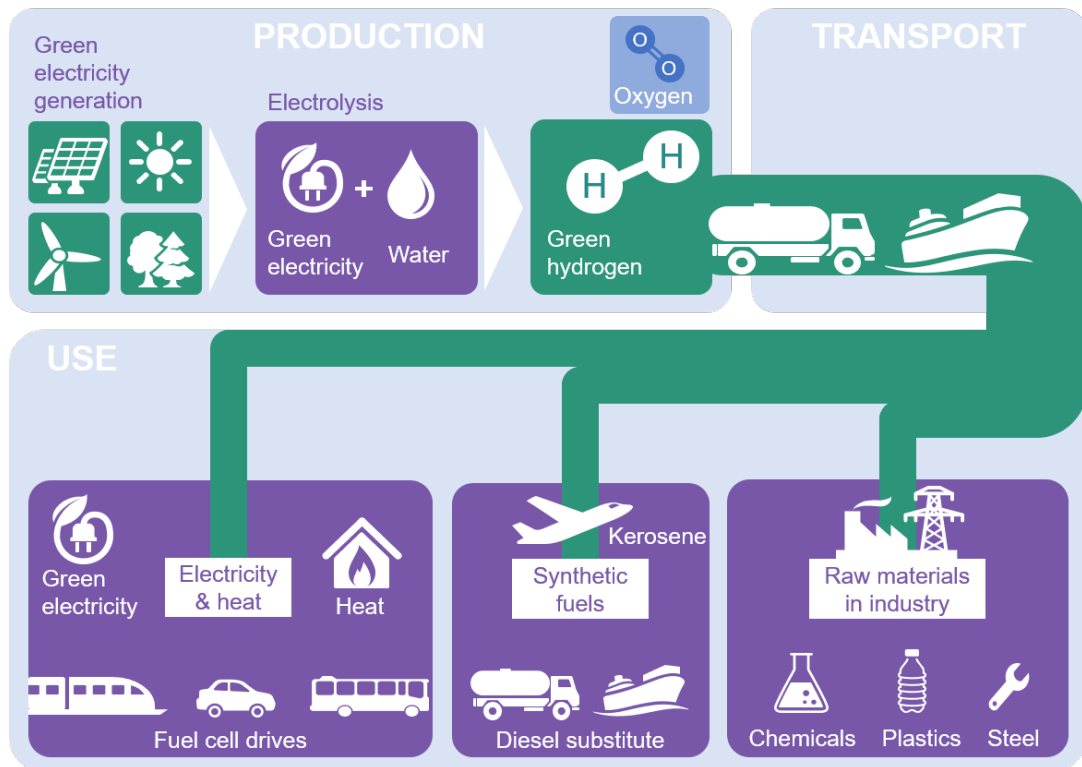
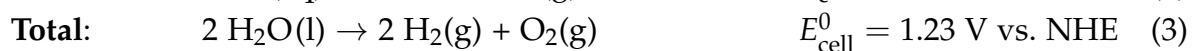
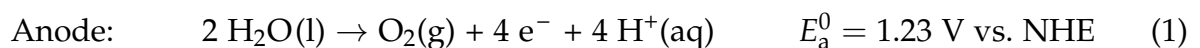


**Figure 1:** Production of green hydrogen and its role in the energy supply chain in Germany 2021.<sup>[1]</sup>

Electrochemical water splitting into  $H_2$  and  $O_2$  is composed of two half-cell reactions in PEM electrolysis: the cathodic hydrogen evolution reaction (HER, reduction) and the anodic oxygen evolution reaction (OER, oxidation).<sup>[5]</sup> This way, electricity is converted into chemical energy and stored in the form of the hydrogen single H-H bond (435 kJ/mol).<sup>[6]</sup>



PEM electrolysis is one part of general membrane electrolysis techniques for water splitting, being the most intensively developed electrochemical units employing a membrane. This development is driven by the need for highly flexible and efficient technology for storage and subsequent energy recovery when needed.<sup>[7]</sup>

PEM electrolysis was first introduced in the 1960s by General Electric with initial performances yielding 1.88 V at 1.0 A/cm<sup>2</sup> to make up for alkaline electrolysis shortcomings.<sup>[8]</sup> High efficiency and current densities (up to 0.6 - 2.5 A/cm<sup>2</sup>), dynamic operation and high gas purity caused a sudden interest and are the key drivers for their development from the 1970s until present.

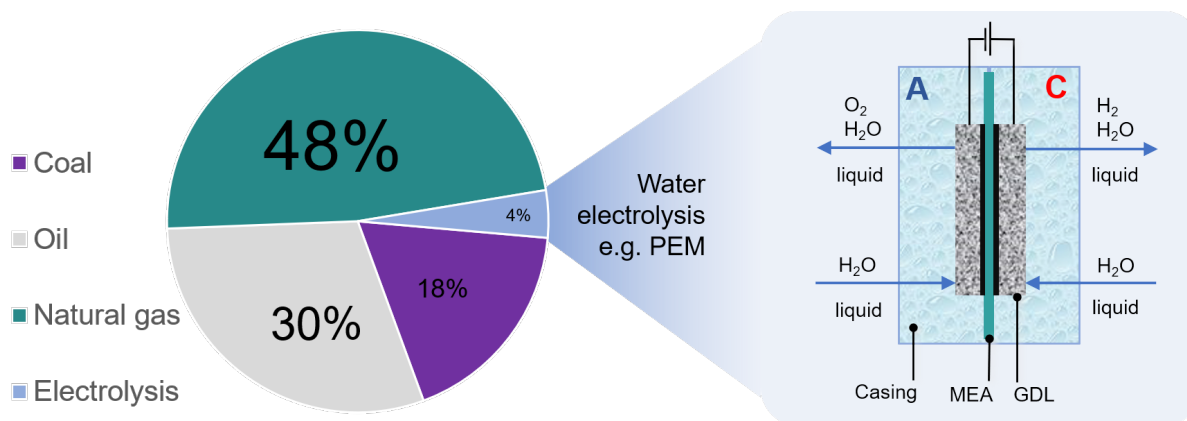


**Figure 2:** Worldwide total industrial hydrogen production by source,<sup>[9]</sup> pointing out the small share of electrolysis applications.

Still today, electrolysis applications only contribute to the total hydrogen production per year by 4%.<sup>[9]</sup> This is alarming given the fact that alternative production paths, especially *via* steam reforming of natural gas (48%) is an allothermal, thus energy-consuming, process releasing carbon dioxide (CO<sub>2</sub>) as a greenhouse gas. Such methods produce so-called grey hydrogen, which can be developed to blue hydrogen, when the CO<sub>2</sub> is captured. The reason why the focus is still on traditional techniques despite extensive funding programs not only in Germany but internationally, is low profitability:<sup>[10]</sup> New technologies must be profitable to guarantee their broad integration and availability in society.

## 1.2. Challenges in scaling electrolysis

„Scaling-up“ implies providing technologies for sustainable energy conversion and storage beyond the megawatt (MW) scale. This aim can only be achieved by substantial development in technical and chemical infrastructure. Once the infrastructure is created and the energy system relies more heavily on renewable sources, an excess of 250–300 TWh solar and wind power could be converted to hydrogen by 2050.<sup>[11]</sup> To be consistent, water electrolysis must uncompromisingly be coupled to sustainable energy sources<sup>[12]</sup> to proceed towards an effective hydrogen economy. At the

same time scaling-up still requires for many advancements that need to proceed in parallel both, in PEM and alkaline electrolysis. Scale-up cannot be seen as a single-step accomplishment but the sum of many steps towards individualized application. Within this scope, new technologies must fulfill the requirements of producibility, profitability and industrial automation to achieve large-scale availability and broad application in the energy sector.

Within this framework, sustainable energy must be distributed over a large geographical area, thus favoring decentralized approaches starting at 20 000 t fuel production per year.<sup>[13]</sup> Within the next years, a certain „economy of scale“ will come into play, where flexible adaption of the technical details and the degree of scaling can lead to tailored solutions and enable a worldwide sustainable energy strategy, e.g. starting in Germany with new plant installations of 5 GW total performance until 2030.<sup>[14]</sup>

Adaption to local needs requires versatility and dynamic operation.<sup>[15]</sup> Systems with an ability to tolerate the intermittent nature of electricity supply coming from renewable sources as well as partial and overloads while short ramp up and shut down times are highly desirable. Therefore, in PEM electrolysis, the membrane-electrode assembly (MEA), which is the core of the electrolyzer, needs to be mechanically, chemically, thermally and oxidatively stable to bear different conditions arising from flexible operation modes.<sup>[16]</sup> Overall, the systems energy efficiency is a prerequisite for profitability including energy recycling and low thermal losses. The awareness for the need of scaling-up is reflected in a €1.4 B funding from 2016 - 2026 in Germany. The budget is for example intended for projects towards serial production (H<sub>2</sub>Giga), offshore (H<sub>2</sub>Mare) and H<sub>2</sub> transportation (TransHyDE).<sup>[14]</sup>

This funding will be used to improve the *status quo* of important technical achievements such as long-term operation (> 20 000 h)<sup>[5]</sup>, long system lifetimes (> 10–20 years<sup>[17]</sup>) and high current densities (2.0 A/cm<sup>2</sup><sup>[5]</sup>). This involves handling large H<sub>2</sub> (and O<sub>2</sub>) volumes, pumping speed adaption and gas compression. Further points to consider are first, advanced coating techniques for catalyst layer production. Second, anti-corrosive casing and electrical contact (ideally material-efficient and easily installable) must be taken into account.<sup>[18]</sup> Regarding the catalyst, it is desirable to aim for a high density of active centers on a molecular level enabling high throughputs and low catalyst loadings and thus potentially reducing the amount of noble metal catalysts such as platinum (Pt) and iridium (Ir).<sup>[19]</sup> Their use is mainly neces-

sitated by their exceptional stability during water splitting involving harsh acidic, oxidative and corrosive conditions at the anode side of the cell.

### 1.3. Electrocatalysts for oxygen evolution reaction and their role in green hydrogen production

#### 1.3.1. Oxygen evolution reaction and its implications at industrially relevant current densities

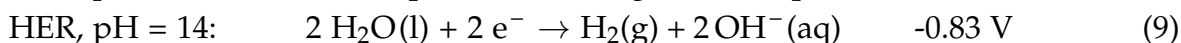
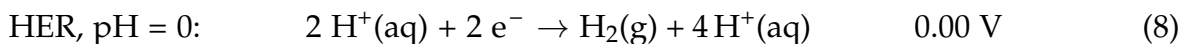
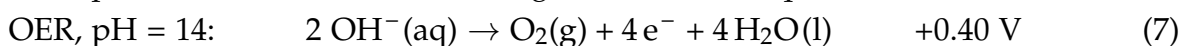
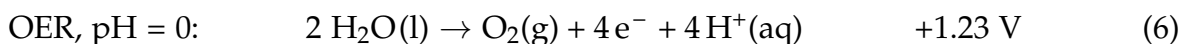
During the OER as shown in equation (1), molecular oxygen is produced from water (in acidic and neutral environments) or from hydroxyl ( $\text{OH}^-$ ) ions involving a series of proton-electron coupled processes.<sup>[20]</sup> An external driving force needs to be applied to overcome the thermodynamic limit of  $\Delta G = 1.23$  V (for PEM electrolysis and OER from water), which is performed in real applications by an applied potential causing harsh acidic and oxidative conditions at the anode side of the cell. This implies instability of any element, alloy or species with an electrochemical oxidation potential above 1.23 V. Since proton formation is involved in OER, the overall process is highly pH-dependent. Even if protons are transported over the proton-conducting perfluorosulfonic acid (PFSA) membrane to get reduced to  $\text{H}_2$  at the cathode side, the local pH at the OER catalyst site is very low and differs significantly from the bulk pH.<sup>[21]</sup> For PEM water electrolysis, where ultrapure water is commonly used instead of an electrolyte-containing liquid medium, a difference  $\Delta\text{pH} > 7$  at high current densities can be expected.

The low local pH (around 0) affects the electrode potential of all electrochemical potentials, explained by the *Nernst* equation. The electrode potential  $E$  is calculated from the standard potential  $E^0$ , the universal gas constant  $R = 8.31447$  J/(mol K), the absolute Temperature  $T$ , the number of transferred electrons  $z_e$ , the Faradaic constant  $F = 96485.34$  C/mol and the activity of each redox partner  $a$  (4). At room temperature ( $T = 298.15$  K = 25 °C) with the concentration element for  $\text{H}^+$   $a = 1$  and under conversion of the natural to the decadic logarithm, one obtains the potential difference caused per pH step being 0.059 V (5).<sup>[22]</sup>

$$E = E^0 + \frac{RT}{z_e F} \ln\left(\frac{a_{\text{ox}}}{a_{\text{red}}}\right) \quad (4)$$

$$\Delta E = -0.059 \text{ V}(pH_1 - pH_2) \quad (5)$$

To understand the scope of this phenomenon, a hypothetical look at HER and OER at different pH-values allows to determine, which reaction is thermodynamically favored under acidic or basic conditions:



It becomes visible that high pH favors OER while low pH favors HER. Analogous shifts in potential affect any conceivable competing reaction, for example corrosion processes of metal casings all being oxidation reactions. This provides first insights why noble metals are preferably used as OER catalysts in PEM water electrolysis.

These contemplations lead to an additional factor that needs to be considered when searching for corrosion-resistant materials. Their ability to withstand oxidative and acidic conditions is summarized in their general stability, which is crucial for long-term operations.<sup>[23]</sup>

In addition to the thermodynamically required minimum potential, there are additional contributions (called overpotentials) to be considered during OER, especially the catalyst overpotential (sometimes also referred to as onset potential). It is considered the most important factor for evaluation of catalyst performance in OER but difficult to observe as a distinct value. For this reason, the value at 10 mA/cm<sup>2</sup> is commonly used as a reference point for such measurements.<sup>[24]</sup> Materials with overpotentials in the range of 300 - 400 mV are considered excellent catalysts and there are only few examples with overpotentials lower than this (e.g. Ir, Ru). Another evaluation criterion is a low *Tafel* slope, which is based on the *Tafel* equation that gives



the relation between overpotential and current density. Combined with high current densities, it provides insights into the reaction kinetics and mechanism.

Based on the described criteria, the next step is to build a bridge between the low-current density range to industrially relevant regimes. Although commonly applied in literature, a more accurate value than  $\Delta G$  for comparison under real conditions is  $\Delta H = 1.48$  V for OER.<sup>[25]</sup> It comprehensively considers realistic influences such as latent heat.<sup>[26]</sup>  $\Delta G$  is only valid in a non-adiabatic system at constant pressure and temperature, which is true for a turnover of 0. The system is in equilibrium with its surroundings. Under industrially relevant conditions at high current densities, this is not valid, since latent heat needs to be taken into account. The difference between  $\Delta G$  and  $\Delta H$  equals  $T\Delta S$ .

### 1.3.2. Iridium scarcity – catalyst alternatives towards profitable energy solutions

Taking scale-up and harsh, oxidative conditions into account, OER catalysts facilitating the anodic reaction must be efficient, abundant and economical while at the same time showing good stability during processing and under operating conditions at high current densities ( $> 1$  A/cm<sup>2</sup>). Although metal oxides are *per se* not thermodynamically stable under acidic conditions due to water formation and the release of solvation energy as a driving force, their decomposition can be kinetically hindered. This holds true for the state-of-the-art OER catalyst, iridium, combining both, exceptional activity and stability.

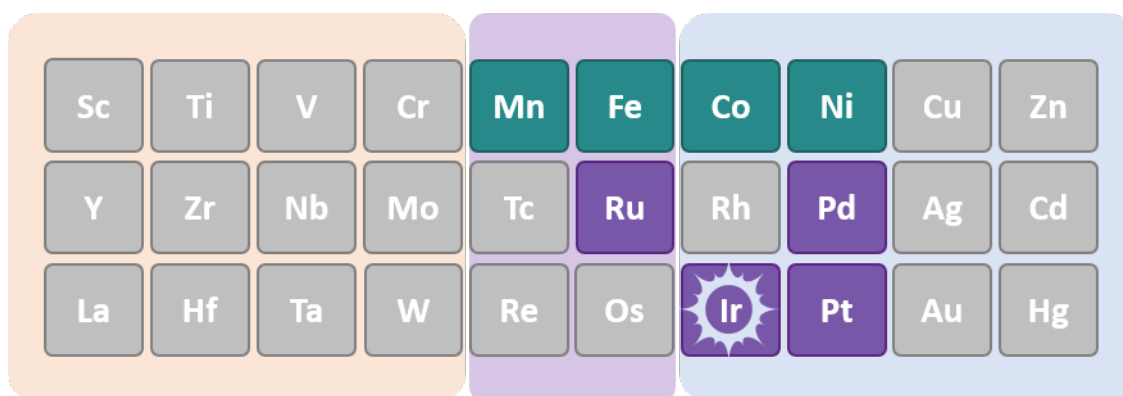


**Figure 3:** Overview of transition metals as OER catalyst materials clustering in noble (violet) vs. earth-abundant (turquoise) metals and the so-called oxo-wall depicted as a violet background.<sup>[27]</sup>

For finding stable catalyst alternatives, knowledge about the reaction mechanism is crucial to adapt catalyst properties to the mechanistic key steps and create an envi-

ronment that energetically enables proceeding along the desired reaction coordinate. For OER, the mechanism is still heavily disputed. But it is known, that part of the evolved oxygen originates from the  $\text{IrO}_2$  lattice itself.<sup>[28]</sup> An interesting explanation approach is based on the so-called oxo-wall, a thought line in the periodic table of the elements (PSE) right of group 8 (Fe, Ru, Os). It subdivides the PSE in two parts: Elements on the right are not able to bear two- or threefold bound oxo-ligands in a tetragonal environment.<sup>[27]</sup> This is relevant for  $\text{IrO}_2$  with its tetragonal crystal structure: oxy-species with a loose coordination (instable iridyl compounds) might be volatile and dynamic and thus facilitate rapid turnover in OER.

Noble metal catalysts, especially platinum (Pt), palladium (Pd), iridium (Ir) and ruthenium (Ru) all exhibit high OER activity with a general trend being  $\text{Pt} < \text{Pd} < \text{Ir} < \text{Ru}$ .<sup>[29–31]</sup> Since Ir (or  $\text{IrO}_2$ , respectively) is even more stable under relevant OER conditions, it outperforms Ru in an overall property comparison<sup>[32]</sup> and makes its way into many PEM application systems.

Pi *et al.* found that nanostructuring Ir increases its OER activity compared to commonly used nanoparticles (NPs) towards onset potentials of 1.45 V in acidic and 1.43 V in basic aqueous environments and *Tafel* slopes of 40.8 mV/dec and 32.7 mV/dec, respectively.<sup>[32]</sup>

Mixture of both active materials, Ir and Ru, were investigated by Andichon *et al.* who found an activity close to  $\text{RuO}_2$  for the co-precipitate  $\text{Ru}_{0.9}\text{Ir}_{0.1}\text{O}_2$  with a significantly enhanced stability.

At the same time, iridium scarcity is a bottleneck given the ambitious scale-up plans and the low production (7.0–7.5 t/y) at 1.0–2.5 g/kW needed at present. This enables no more than 30–75 GW growth potential within the next decade.<sup>[33]</sup> While there are many attempts to reduce the overall Ir loading on the membrane and thus enhance catalyst efficiency,<sup>[34]</sup> e.g. in the form of super thin Ir nanolayers,<sup>[35]</sup> Ir scarcity and price motivate intense research towards noble metal-free, earth-abundant alternatives.

Earth-abundant transition metals are especially attractive as Ir alternative since they can switch between different oxidation states, among which  $\text{Me}^{2+}$ ,  $\text{Me}^{3+}$  and  $\text{Me}^{4+}$  are the most relevant for OER.<sup>[36–38]</sup> Key criteria beyond oxidation state are morphology (and a large active surface area), composition, 3d electron number, binding energy of surface oxygens and the enthalpy between lower and higher oxide transitions. A broad variety of studies is targeting a single catalyst material or group, each, but there are also several review and overview articles providing different sys-

tematic approaches.<sup>[5,9,24,39]</sup> Tahir *et al.* present the 2017 *status quo* by differentiating noble from earth-abundant metals and further deep-diving into different anions, supports and structures.<sup>[24]</sup>

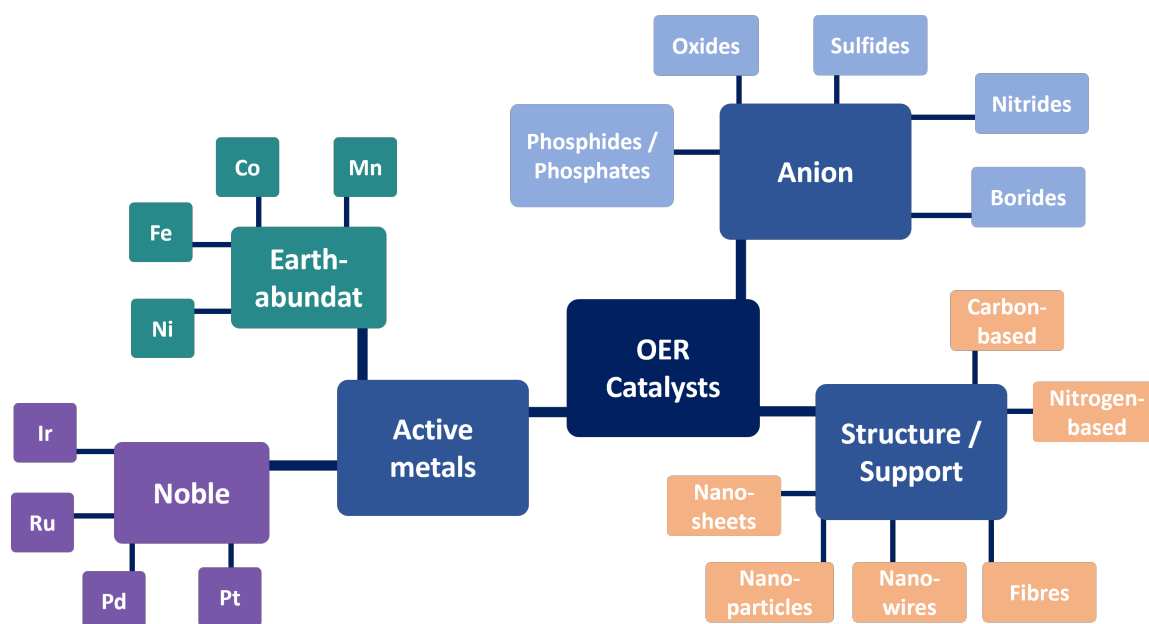


**Figure 4:** Structural approach to gain a systematic overview of OER catalyst materials as presented by Tahir *et al.*<sup>[24]</sup>

As elaborated earlier, an important suitability criterion is acid stability, which was assessed by McCrory and co-workers.<sup>[40]</sup> The authors compared 26 existing OER catalysts under identical conditions (1 M H<sub>2</sub>SO<sub>4</sub>, 2 h operation time, 10 mA/cm<sup>2</sup>) but could not identify a single stable and active candidate to replace Ir (or Ru).

In fact, every metal including noble metal catalysts that are said to be stable are prone to oxidation and corrosion: Ru, Au, Ir, Rh, Pt and Pd all display both transient dissolution during oxide formation at the beginning of the electrochemical process and steady-state dissolution during the OER.<sup>[41]</sup> If oxide dissolution takes place or not, is determined by its dissolution kinetics: They may vary by orders of magnitude for different metals, rendering the dissolution quick or slow, the latter one desired for OER catalyst materials. Water formation is the driving force for dissolution in many cases but Wang *et al.* identified 68 acid-stable candidates using computational high-throughput screenings.<sup>[42]</sup> They found that especially antimony (Sb), tungsten (W) and germanium (Ge)-based compounds may render known active metals (Mn, Co, Fe, Ni) acid stable when present as binary oxides (e.g. CoSbO<sub>4</sub>). A group of

tungstate-based cobalt compounds, cobalt polyoxometalates (POMs), will thus be an important part of this thesis, combining high OER activity with acid stability.

### 1.3.3. Polyoxometalates and their catalytic potential in oxidation reactions

Polyoxometalate (POM) materials combine high catalytic activity in oxidation reactions with the potential of sufficient stability to withstand the above-mentioned anodic conditions.<sup>[43]</sup> The POM framework, including heteropolytungstates, consists of formal  $d^0$  W(VI) atoms bound to oxo ( $O^{2-}$ ) ligands rendering them oxidatively resistant, thus particularly attractive as oxidation catalysts.<sup>[44]</sup> Large anionic oxide clusters equip POM materials with molecular as well as oxide fragment properties.<sup>[45]</sup> Additionally, some Keggin-type anionic POM clusters are able to conduct protons,<sup>[46]</sup> which makes them even more attractive as catalysts integrated in a cation-exchange membrane-based MEA.

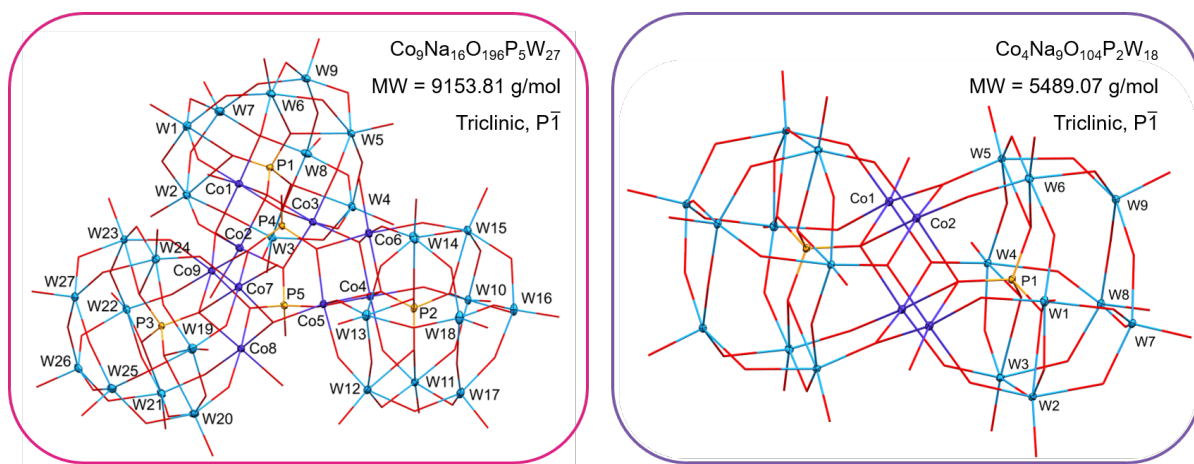


**Figure 5:** Single crystal structures of POM anionic clusters obtained as sodium salts ( $Na^+$  omitted for clarity). The anionic clusters were investigated as OER catalysts in their insoluble form (as barium salt).<sup>[47]</sup>

As the first of its kind, POM anion  $[Co_4(H_2O)_2(PW_9O_{34})_2]^{10-}$  ( $[Co_4]^{10-}$ ) was found to be a homogeneous carbon-free OER catalyst from earth-abundant materials.<sup>[43]</sup> At  $pH = 8$ , it was discovered to be one of the fastest OER catalysts up to date (2017) reaching high initial turnover frequencies ( $> 5 s^{-1}$ ).<sup>[48]</sup> This compares to present Ir values and its soluble complexes (TOFs up to  $0.5 s^{-1}$ )<sup>[49]</sup> but lacks of long-term evaluation and industrial processability.

A heterogenous, industrially relevant alternative was presented in 2013 by Soriano-Lopez *et al.* who precipitated the larger  $[Co_9(H_2O)_6(OH)_3(HPO_4)_2(PW_9O_{34})_3]^{16-}$

([Co<sub>9</sub>]<sup>16-</sup>) with Ba<sup>2+</sup> or Cs<sup>+</sup> to modify amorphous carbon-based electrodes.<sup>[50]</sup> [Co<sub>9</sub>]<sup>16-</sup> is obtained as a side product during [Co<sub>4</sub>]<sup>10-</sup> synthesis exhibiting a similar composition of structural moieties.<sup>[51]</sup> From an industrial point of view, Soriano-Lopez *et al.* reported short-term stability at low current densities (8 h at 0.5 mA/cm<sup>2</sup>).

Blasco-Ahicart *et al.* embedded [Co<sub>9</sub>]<sup>16-</sup> (as a barium salt) into a carbon paste with organic binder and demonstrated that it was able to outperform IrO<sub>2</sub> under acidic conditions (1 M H<sub>2</sub>SO<sub>4</sub>) at low current densities (up to 15 mA/cm<sup>2</sup>). Constant performance was shown for approx. 24 h on an electrode surface of 0.07 cm<sup>2</sup> with subsequent catalyst recovery as proven by XRD.<sup>[52]</sup>

As elaborated earlier for binary oxides, there are also POM-related studies where a change in the tungstate framework is used to achieve enhanced stability and even improved catalytic activity.

Martin-Sabi *et al.* reported redox tuning of [Co<sub>4</sub>]<sup>10-</sup> by exchanging W by Mo in the tungstate framework leading to a lowered OER overpotential by 188 mV (achieving 517 vs. 705 mV for the undoped parent compound).<sup>[53]</sup> In the case of isobutane oxidation towards methacrylic acid, antimony doping leads to enhanced selectivity as well as catalytic activity.<sup>[54]</sup>

From the presented studies, one can deduce that POMs hold a great potential as a substitute of iridium, however, reliable testing data under industrially relevant conditions is still missing in order to draw any further conclusions. For this reason, this dissertation will focus on synthesizing and implementing POMs in a scalable setup (e.g. MEA) in order to test them under real conditions needed to achieve high current densities (> 250 mA/cm<sup>2</sup>) and long-term stability (> 1000 h).

#### 1.3.4. POM catalytic properties and methodology to assess catalyst suitability

Given the issue of Ir scarcity, literature has come up with many promising catalyst candidates with several of them being investigated towards their activity and electrochemical overpotential in OER. Due to higher costs coming with each scaling step, many catalysts remain on a very basic level. The key question answered in this first part of the thesis is, if a very promising POM OER catalyst candidate can be integrated into a scalable MEA setup. This builds the bridge between academia and industry, which is important to translate scientific knowledge into applications for society.

Building on fundamental R&D activities presented above, only few electrocatalysts fulfill the requirements for further investigations towards industrial application and relevant durability ( $> 1 \text{ A/cm}^2$ ,  $> 20\,000 \text{ h}$ ).<sup>[55]</sup> Methods used in this first part of the thesis comprise adaption of the synthesis procedure, a thorough characterization of the material properties, processing and final investigation in the PEM electrolyzer.

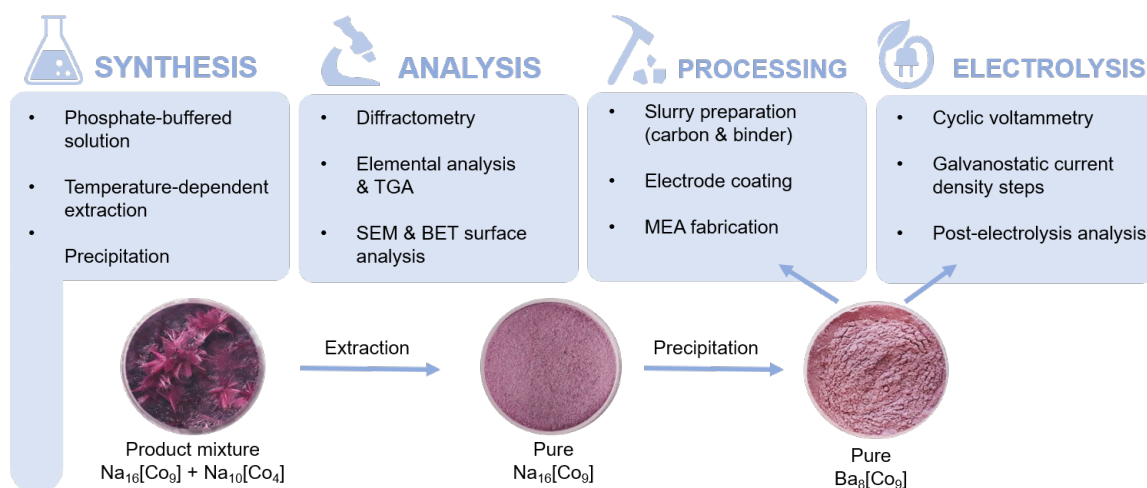


**Figure 6:** Overview of methods used in the first part of this thesis.

The literature-known synthesis by Weakley was modified by Finke *et al.* and Galan-Mascarós *et al.*<sup>[51,56,57]</sup> It comprises a two-step synthesis approach including cluster assembly and precipitation with an extraction step to separate  $[\text{Co}_9]^{16-}$  from the less water-soluble  $[\text{Co}_4]^{10-}$ .<sup>[58]</sup>

Analysis of the catalyst material was performed *via* single crystal and powder X-ray diffractometry (XRD) as well as inductively coupled plasma optical emission spectroscopy (ICP-OES) for elemental analysis (EA) to determine catalyst composition and confirm the existence of its Keggin-structure.<sup>[59]</sup> and thermogravimetric analysis (TGA) to quantify crystal water content. Visual analysis was performed using light as well as scanning electron microscopy (SEM) and the catalyst specific surface area was determined by Brunauer-Emmett-Teller (BET) method.

In addition to TGA, a thermal treatment of the catalyst combined with frequent interruptions for XRD analyses yielded information about its decomposition temperature, since POMs and heteropoly acids (POM protonated form), decompose upon thermal treatment.<sup>[60]</sup> Acid stability was assessed by UV-Vis spectroscopy making use of shifted absorption wavelengths upon acidic decomposition (originating from free  $\text{Co}^{2+}$ ).<sup>[61,62]</sup>

MEA preparation was performed with a three-step approach preparing the catalyst-slurry in methanol first.<sup>[63]</sup> This was then coated onto a support and heat transferred in a standard decal-transfer procedure.<sup>[64]</sup> A more detailed description is provided in the results part for each chapter of this dissertation.

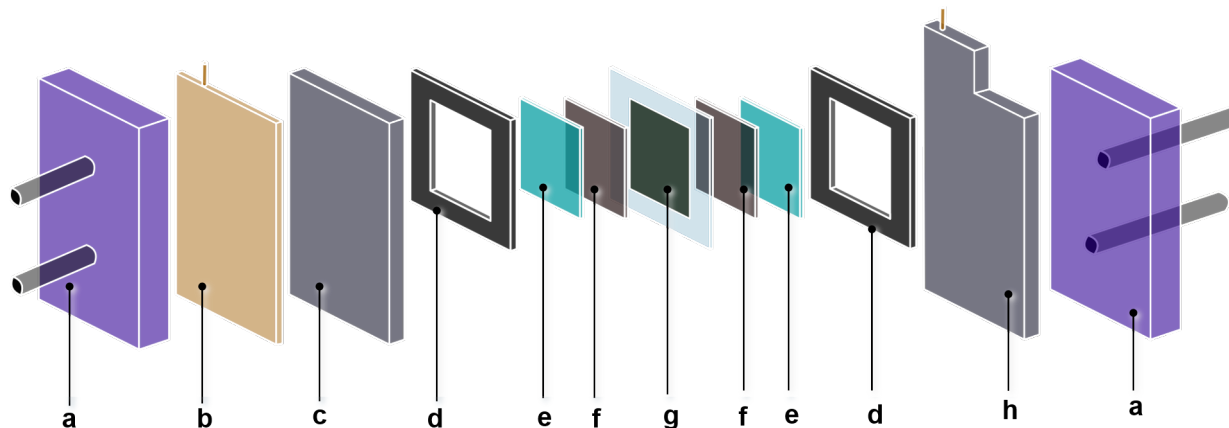


**Figure 7:** Scribner installation for water electrolysis. The cathode side is shown on the left, the anode side is shown on the right. The setup is composed of two end plates (a), a current collector (b), a graphite (c) and a titanium (h) flow field, EPDM sealings (d), titanium grids with different mesh widths (e, f) and the MEA in the middle (g).<sup>[65]</sup>

Regarding electrochemical procedures, freshly made MEAs were assembled into a commercially available Scribner cell setup and subjected to various analysis procedures: Complementing literature, which often focuses on linear sweep (LSV) rather than on cyclic voltammetry (CV),<sup>[52]</sup> the latter was performed in this thesis to yield information about reversibility and reproducibility of electrochemical processes. Galvanostatic current density steps were employed to track POM decomposition *in situ* and post-electrolysis MEA analyses (e.g. *via* XRD) finalized the presented study.

## 1.4. PFSA-based Proton exchange membranes and their application in PEM water electrolysis

After considering acid-mediated POM decomposition when integrated in a PFSA-based MEA and subjected to PEM water electrolysis conditions, the following chapters focus on PFSA membrane properties and their role in PEM water electrolysis.

### 1.4.1. PFSA applications – established functional polymer in electrolysis and beyond

The first perfluorosulfonic acid polymer was developed in the 1960s by Walter Grot as a Teflon modification for Chemours (today: DuPont).<sup>[16]</sup> It was following a series of exchange resin creations in the 40s, which opened a whole new era of functionalized ionic polymers.<sup>[66]</sup> Today, PFSA and its derivatives made their way in numerous applications fields due to their acidity, stability and their special ability to selectively transport cations (especially protons) and water.

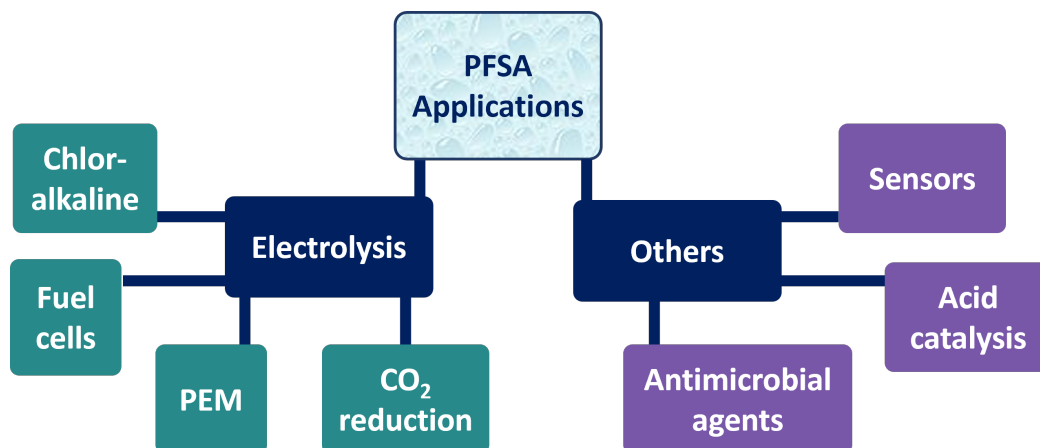


Figure 8: Overview of PFSA application fields.

PFSA usage is not only pronounced in electrolysis applications but also beyond, for example in superacid catalysis. Nafion-H resins have been employed to perform a 1,2-hydride shift to convert an epoxide into an aldehyde and introduce protection moieties such as O-trialkylsilyl groups to protect alcohols.<sup>[67]</sup>

In electrolysis, PFSA is used in the chloralkali process as a membrane cell to provide an environmentally and less harmful alternative to the diaphragm cells which employ asbestos as a raw material and the mercury cell using Hg-Na amalgam to



separate sodium from the cell.<sup>[66]</sup> In this application case,  $\text{Na}^+$  is transported instead of protons to accomplish charge balance over the cell.

It is furthermore used in carbon dioxide ( $\text{CO}_2$ ) reduction reaction ( $\text{CO}_2\text{RR}$ ) applications providing a green and sustainable opportunity of carbon capture and storage (CCS) as well as  $\text{CO}_2$  revalorization by producing feedstock chemicals, such as carbon monoxide ( $\text{CO}$ ).<sup>[13,68]</sup> It can either be used as a membrane with an Ir coating at the anode side or it is employed as a binder material in the catalyst paste to guarantee layer stability and functionalization. Here, PFSA is often combined with high-molar ( $> 0.5 \text{ M}$ ) electrolyte solutions and cation transport is employed to close ionic balance across the cell. Further electrochemical applications comprise fuel cell and PEM technology with the latter one being the focus of this thesis.

#### 1.4.2. Perfluorosulfonic acid – a robust polymer with the ability to selectively transport cations

The PFSA selective cation transfer ability originates from its molecular polymeric structure. As can be seen from Figure 9, the polymer consists of polytetrafluoroethylene (PTFE,  $-\text{CF}_2-$ ) backbone, which bears polyfluoroether side chains tethered by a hydrophilic sulfonic acid moiety ( $-\text{SO}_3\text{H}$ ). In its protonated form, the sulfonate anions ( $-\text{SO}_3^-$ ) are saturated by protons. The proton-sulfonate bond is very loose, resulting in a high acidity of the ionomer solution and respective membranes in aqueous environments ( $\text{pK}_a \approx -6$ ).<sup>[69]</sup> The combination of both, hydrophobic backbone with crystalline as well as amorphous areas and hydrophilic side chains results in a particular channel-like structure that enables proton transport. Early models describe approx.  $40 \text{ \AA}$  channel thickness for the main transport channels, interconnected by smaller wires (approx.  $10 \text{ \AA}$ ).<sup>[70]</sup> However, under real electrolysis conditions, the whole polymer matrix can be assumed to be highly dynamic and flexible.<sup>[71]</sup>

As an important parameter for PFSA membranes, the acid capacity is expressed by the so called equivalent weight ( $\text{EW} = 1100 \text{ g/mol}$  for Nafion N117), defining the amount of polymer (in g) per mole of sulfonic acid groups. This translates in the acid capacity of a membrane piece, which is experimentally determined by acid-base titration.<sup>[74]</sup>

Once in contact with water, PFSA dissociates quantitatively.<sup>[75]</sup> It is known that already the first water molecule induces dissociation of the sulfonic acid groups form-

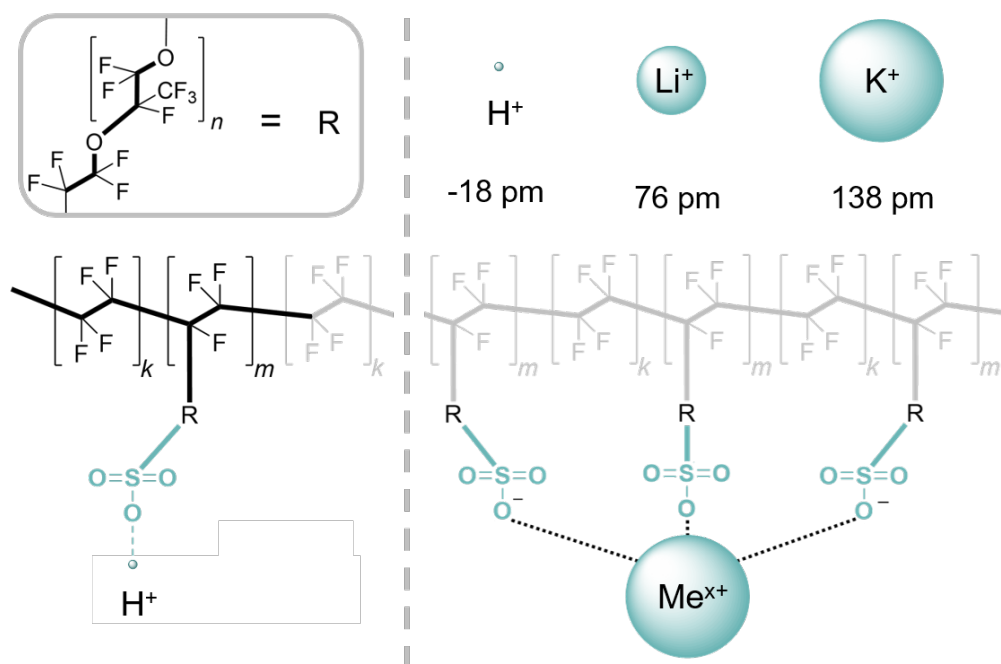


**Figure 9:** PFSA molecular structure and potential bonding of a trivalent metal cation. Ionic radii are given for  $\text{H}^+$ ,  $\text{Li}^+$  and  $\text{K}^+$ . The depiction is true to scale and the proton is illustrated with an assumed radius of 10 pm, since the theoretical, effective radius is negative.<sup>[72,73]</sup>

ing a sulfonate ( $-\text{SO}_3^-$ ) and a hydronium ion ( $\text{H}_3\text{O}^+$ ). Undissociated  $\text{SO}_2\text{OH}$  cannot be proven.<sup>[76]</sup> At ambient conditions (45% relative humidity [RH]), approx. three  $\text{H}_2\text{O}$  molecules surround one sulfonic acid group, which equals 5 wt.-%.<sup>[77]</sup> In the presence of an excess amount of water, one sulfonate tether bears approx. 15 water molecules, which enables proton mobility and polymer chain movement.<sup>[77]</sup> During operation, the water behavior within the membrane is bulk-like. This means that even though it is gas-impermeable, dissolved gases can cross the membrane, which causes the effect of gas-crossover between the anode and the cathode side in PEM water electrolysis, potentially leading to big safety concerns.<sup>[71]</sup> Gas diffusivity becomes even more pronounced in high-pressure applications, since elevated pressure facilitates gas solubility in water.

During transport, protons behave in a *Grotthuß*-like fashion: instead of physical displacement, bonds can just be switched, which is the reason for quick and highly dynamic transport properties.<sup>[78]</sup> Along with proton transport, also water is able to pass the membrane in the form of a hydration shell, even though PFSA is also water permeable without the presence of a potential gradient across the electrolysis cell.<sup>[79]</sup>

### 1.4.3. Sulfonate-metal cation interactions as a key lever for PFSA property modification during processing

Just as protons possess a certain affinity to sulfonic acid groups (inversely expressed as acidity), also metal cations and further cationic species exhibit sulfonate affinities. As opposed to hydrogen bonds for protons (approx. 20 kJ/mol for  $\text{H}_3\text{O}^+ - \text{O}$ ), ionic interactions are stronger (approx. 170–1500 kJ/mol) due to local complex formation with  $-\text{SO}_3^-$ .<sup>[80]</sup> The energy required to facilitate transport of these ions across a PFSA membrane can thus be assumed to exceed proton transport significantly. Yoder *et al.* found that PFSA possesses a twelve times higher proton conductivity compared to metal cations, such as  $\text{Na}^+$ ,  $\text{Ca}^{2+}$  and  $\text{Fe}^{3+}$ .<sup>[81]</sup>

In most electrolysis and fuel cell applications, PFSA membranes are used in their protonated form. Cation conductivity with an optimum at 55–65 °C as well as water uptake are crucial parameters to be considered when applying the MEAs in a real cell setup.<sup>[82]</sup> But when coming to PFSA processing for MEA preparation, further properties need to be considered: Upon thermal treatment, PFSA tends to depolymerize and form toxic tetrafluoroethene ( $\text{C}_2\text{F}_4$ ) at around 280 °C.<sup>[83]</sup> The polymeric side chains are prone to losing the sulfonate groups during thermal decomposition, beginning above 300 °C, when the polymer is in its protonated form. This is of importance during MEA production, which is performed *via* decal transfer, meaning the heat- and pressure-mediated transfer of a supported catalyst layer onto the membrane. It is known that the incorporation of  $\text{K}^+$  prevents the C-S-cleavage and thus renders the polymeric structure more stable.<sup>[63]</sup>

This is also expressed in an increased glass transition temperature ( $T_g$ ), which is based on chain movement: The temperature required for initiating a throughout, global mobilization of the polymer is called  $\alpha$ -relaxation and has been associated with the glass transition temperature ( $T_g$ ) in scientific literature.<sup>[84,85]</sup> Additional local, low-temperature movements are called  $\beta$ -relaxations (movement of the polymeric PTFE-backbone above 25 °C) or  $\gamma$ -relaxation (local movement of  $-\text{CF}_2$ -fragments at approx. -10 °C).<sup>[86]</sup> These phenomena are functionally related to the polymer morphology and its ionic structure, which will be considered in chapter 1.4.4.

Iwai *et al.* reported that also  $\text{Na}^+$  incorporation increases polymer stability while especially multivalent ions (e.g.  $\text{Al}^{3+}$  or  $\text{Fe}^{3+}$ ) decrease its stability by different mechanisms. Iron cations react in a *Fenton*-like way forming hydrogen peroxide, which subsequently initiates C-F-cleavage. HF and fluoride ( $\text{F}^-$ ) can thus be found in the

process water, leading to heavy corrosion and potential health issues. Further, non-iron *Fenton*-like agents are  $\text{Al}^{3+}$ ,  $\text{Cr}^{3+}$  and  $\text{Cu}^{2+}$ .<sup>[87]</sup> A long-term contamination study (829 h) at  $0.5 \text{ A/cm}^2$  even demonstrated *Fenton* activity in very small concentrations (1 ppm  $\text{Fe}_2(\text{SO}_4)_3$ ).<sup>[88]</sup> Aluminum cations are known to attack the side chain ether bond due to its Lewis acidity and catalyzes side chain cleavage. Bas *et al.* introduced a measure for judging metal cations towards their effect in PFSA-based applications, the Lewis acid strength (LAS). They found that the thermal stability of the side chain is improved for cation contaminants with LAS values lower than 0.3, which is lower than the corresponding critical Lewis base strength of the sulfonate groups. Cations with  $\text{LAS} > 0.3$  enhance the thermal degradation rate. At the same time, it is well known that interactions of the sulfonate group with metal ions tend to increase with the ion's valence.<sup>[89]</sup>

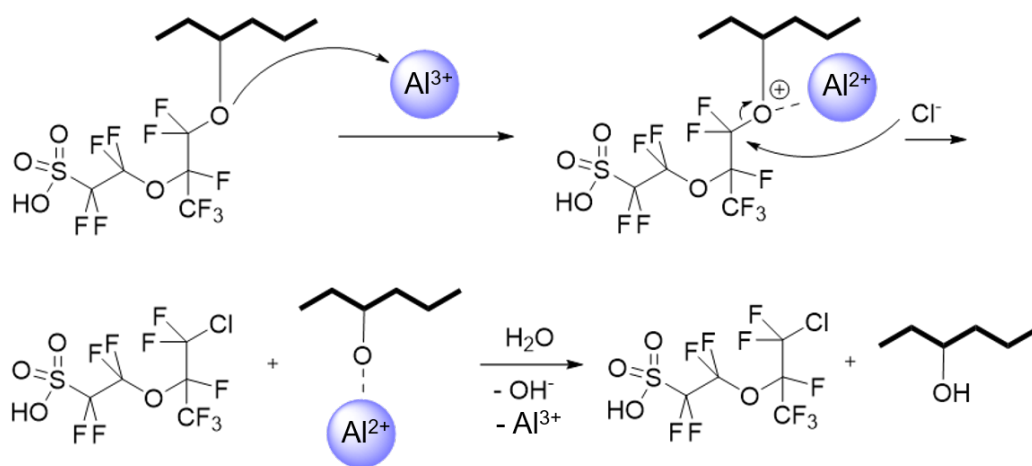


**Figure 10:** Aluminum Lewis acid-catalyzed PFSA degradation mechanism by side chain ether cleavage.<sup>[90]</sup>

Depending on a particular cation's binding strength to the sulfonate groups, every single contact of the polymer with a cation causes proton displacement while the metal cation is incorporated into the membrane. This is known to be a cumulative process as investigated with the help of  $\text{Na}^+$ ,  $\text{Ni}^{2+}$  and  $\text{Fe}^{3+}$  examples.<sup>[91]</sup> During further exposition, most ions displace protons quantitatively within 24 h in a 2 M metal chloride solution.<sup>[92]</sup> Ion exchange can be used as a powerful lever in membrane processing, because it influences its mechanical and physical properties directly as shown by Moore *et al.*<sup>[93]</sup> and Wilson *et al.*<sup>[62]</sup> This thesis builds up on their work and employs PFSA ion exchange towards industrialization of green technologies. Therefore, the influence of sulfonate-metal cation interaction was investigated in both, MEA fabrication during the so-called decal process and during operation

when employing high-molar electrolytes. The latter case demonstrates a model system, where PEM electrolysis is used as a model for further technologies, such as CO<sub>2</sub> electroreduction.

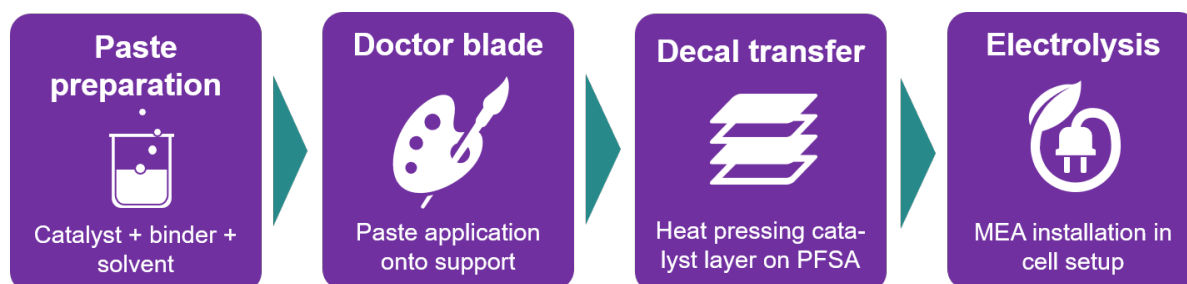


**Figure 11:** Schematic overview of the MEA fabrication process *via* decal transfer.<sup>[94]</sup>

In literature, cations with different valences (+I, +II, +III)<sup>[95]</sup> were investigated alone or in competing cation mixtures<sup>[96]</sup> and to different extents of exchange<sup>[97]</sup> towards water uptake capacity,<sup>[92]</sup> thermal behavior<sup>[63,86,87,90,98]</sup> and crystallinity.<sup>[93]</sup> Computational studies examined mixtures of bivalent and monovalent ions,<sup>[99]</sup> as well as salt partitioning.<sup>[100]</sup> Physical properties were also investigated, such as tensile and fracture resistivity,<sup>[101,102]</sup> along with different membrane types (Flemion<sup>®</sup> vs. Nafion<sup>®</sup>).<sup>[103]</sup>

It is important to differentiate between effects during processing and during operation. In the first part of the membrane-related work presented in this thesis (chapter 2.2), ionic interactions are used to modify membrane processing as it renders the polymer stable. In this context, one must be aware that cations are pre-installed in the MEA being the reason why this thesis focuses on cation back-exchange *in situ*. The second part (chapter 2.3) deals with potassium-based electrolyte usage during operation. MEAs in this study are installed in their protonated form but cations are transported over the polymeric matrix and the impact of this process on energy consumption in total is investigated. Within this scope, ion exchange can have two effects influencing the electrochemical performance of a respective MEA. First, it can be assumed that the cation mobility in the membrane is reduced as long as the foreign ion is present in the membrane. Compared to the metal ions, protons are smaller, more mobile and their movements in an aqueous environment (*via* Grotthuß mechanism) are quicker.<sup>[78]</sup> Second, the whole polymer undergoes structural changes, such as pore widening with increasing current density. This causes more ions to enter the membrane, which subsequently reduces the water content in the matrix and pores shrink again.<sup>[104]</sup> Membrane porosity, water content und

ion conductivity decrease with increasing concentration while membrane density is increased.<sup>[105]</sup> We can thus assume an additional energetic impact that must be overcome to enable  $K^+$  hopping when electrolyte salts are used.

#### 1.4.4. Li-sulfonate interactions – a pathway for morphological membrane modification

PFSA morphology is most often studied by small-angle X-ray scattering (SAXS) to learn about molecular arrangements and thermomechanical properties.<sup>[106]</sup> SAXS has shown that the ionic parts, namely the saturated sulfonate groups, form clusters among the non-polar PTFE-like matrix.<sup>[85]</sup> This leads to the formation of micellar aggregates also in aqueous solution.<sup>[107]</sup> In contrast, alkaline and earth alkaline metals can induce symmetrical and thermodynamically stable layer arrangements in sulfonate complexes.<sup>[108]</sup> Especially lithium is known in polymer electrolyte research for its ability to form stable sulfonic acid complexes connected to a polymeric backbone that are able to effectively conduct ionic species.<sup>[109]</sup> Although these highly symmetrical structures in the polymer exist, the exact unit cell and crystal system could not be identified.<sup>[110]</sup> But when subjected to thermal treatment, morphological rearrangements might be even more pronounced and lead to irreversible structural changes as opposed to protonated PFSA environments, which will be proven in the second part of this thesis.

Comparing  $Li^+$  to other alkali metal cations, it takes a special role: Except for  $Li^+$ , all alkali metal cations have a higher affinity to the sulfonate groups compared to protons.  $K^+$ ,  $Rb^+$  and  $Cs^+$  induce polymer electrolyte membrane shrinkage and density increase. Okada *et al.* found that having these cations in a solution will affect multiple PFSA membrane properties, such as water content, ionic conductivity, ionic transference number of  $H^+$  in the membrane and water permeability all decrease steeply with an increasing amount of cations present.<sup>[112]</sup> An AC impedance spectroscopy-based study by Gavach *et al.* revealed a difference between cation and proton mobility in the membrane and found the  $H^+$  mobility to increase with the amount of  $Na^+$  (and further monovalent ions) present in the polymer. Okada *et al.* refer to three important factors related to the nature of cations that determine the ionic conductivity in the membrane: affinity to the sulfonate groups, water content in the polymer matrix and water transference coefficients.<sup>[112]</sup> They suggest that these factors should be considered when designing high-performance polymer membranes

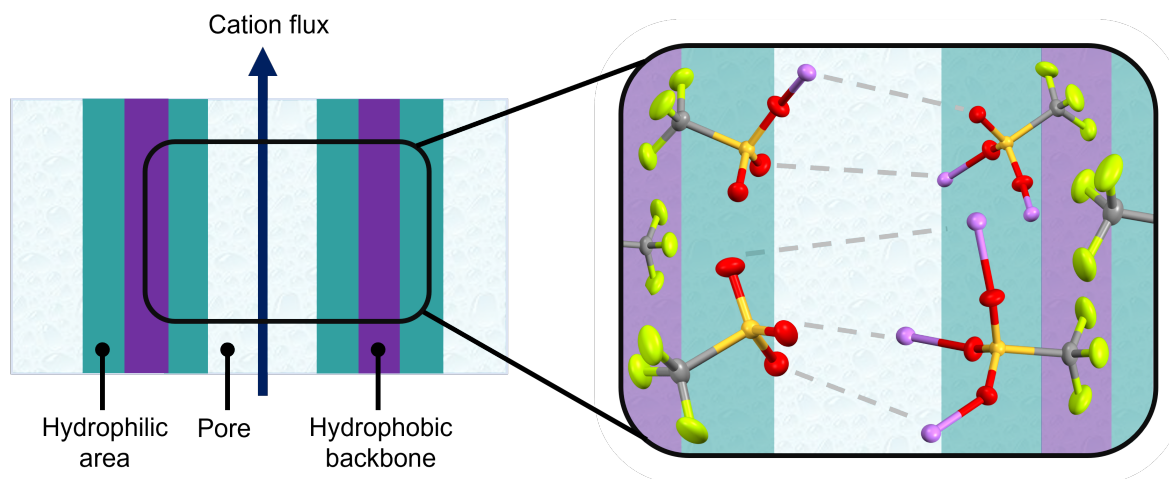


**Figure 12:** Visualization of potential PFSA layer formation in PFSA due to oxygen-lithium ionic interactions resulting in a highly ion-conductive pore structure. Lithium-triflate crystallographic structures are used as a template for analogue interactions in PFSA.<sup>[111]</sup> O – red, C – grey, S – yellow, F – green, Li – violet.

microstructurally. The present thesis builds a bridge between this suggestion and ways to implement it in practice.

#### 1.4.5. Potassium-based electrolytes and their impact on electrolysis applications

As opposed to an early introduction of metal cations in the PFSA polymer even before decal transfer, also electrolyte usage might lead to immediate cation exchange as soon as the MEA is in contact with the ion containing solution. Electrolysis applications different from PEM water electrolysis commonly use high molar electrolytes, among which the most prominent one is probably chloralkali electrolysis. Along with the well-known diaphragm (asbestos- or PTFE-based) and the mercury cell, the membrane cell provides the highest sodium hydroxide (NaOH) purity obtained from brine thanks to a PFSA membrane separating the half-cells. It is anion blocking and thus chloride impermeable but transports  $\text{Na}^+$  and therefore allowing for a 30–33% NaOH at the cathode along with chlorine gas as a product at the anode side. The cell is operated at 4.5 V enabling 400 000 A over the whole cell with typical current densities from 0.2 - 0.4 A/cm<sup>2</sup>.<sup>[113]</sup>

An additional application is CO<sub>2</sub> electroreduction for the conversion of a greenhouse gas into revalorized, feedstock chemicals such as carbon monoxide (CO). The us-

age of high molar potassium sulfate (e.g. 0.5 M  $\text{K}_2\text{SO}_4$ )<sup>[114]</sup> or electrolyte mixtures (e.g. 0.5 M  $\text{KHCO}_3$  and  $\text{K}_2\text{SO}_4$ , pH = 7)<sup>[13]</sup> is very common and comes with several advantages: The higher the electrolyte concentration, the better the electrolyte conductivity (77 mS/cm at 0.5 M vs. 211 mS/cm at 2.0 M and 60 °C), which in turn reduces ohmic losses.<sup>[115]</sup> Another advantage is that buffer-based electrolytes stabilize the pH in proximity to the cathode in a neutral to slightly basic pH-regime. Due to a continuous production of  $\text{OH}^-$  at the cathode itself, the pH in the reaction zone is always approximately 14.<sup>□</sup> This differs from the bulk pH which then depends on the electrolyte of choice. In general, acidic environments disfavor  $\text{CO}_2$  conversion and favor HER, which should be avoided in CO2RR. An increased electrolyte concentration mitigates local pH fluctuations vs. bulk pH as proven in a computational study on 0.5 M  $\text{KHCO}_3$ .<sup>[116]</sup> For the same reason, highly conductive acids (e.g.  $\text{H}_2\text{SO}_4$ ) cannot be used and integration of a thin liquid buffer layer (e.g. 0.5 mm)<sup>[114]</sup> with  $\text{K}^+$ -based electrolytes mitigates HER competition.

At the same time, it is well known that the surplus in  $\text{K}^+$  ( $\geq 10^{-1}$  M) compared to the number of protons ( $10^{-7}$  M) leads to a mostly potassium conducting membrane. This changes the local (and over time also global) pH, since the cathode side is not supplied with protons from OER as it is the case in water electrolysis. This phenomenon is well known in  $\text{CO}_2$  reduction research and requires precise ion management over the cell to facilitate continuous operation.<sup>[13]</sup> Chae *et al.* underlined that cations occupy sulfonate groups with the consequence of a reduced contact chance for protons due to this competition.<sup>[117]</sup> The scientific question which is answered in the third part of this thesis (chapter 2.3) concerns the resistance increase in PFSA membranes when in contact with a high molar electrolyte. Due to their strong ionic interactions, more energy (in form of an increased potential) is required to push cations back to the cathode side. The direction of cation migration is opposed to the electrodiffusion direction (anode to cathode) and implications are assessed in a model water electrolysis setup to imitate real applications.

#### 1.4.6. Proton-metal cation exchange – methods to assess its potential for optimizing industrial electrolysis

PEM electrolysis relies on the quality and properties of the core part in the electrolyzer system, the proton exchange membrane. Given the strong ionic interactions as opposed to hydrogen bonding in the case of protons, the second part of this thesis covers two important questions: first, could proton-metal-exchange be used



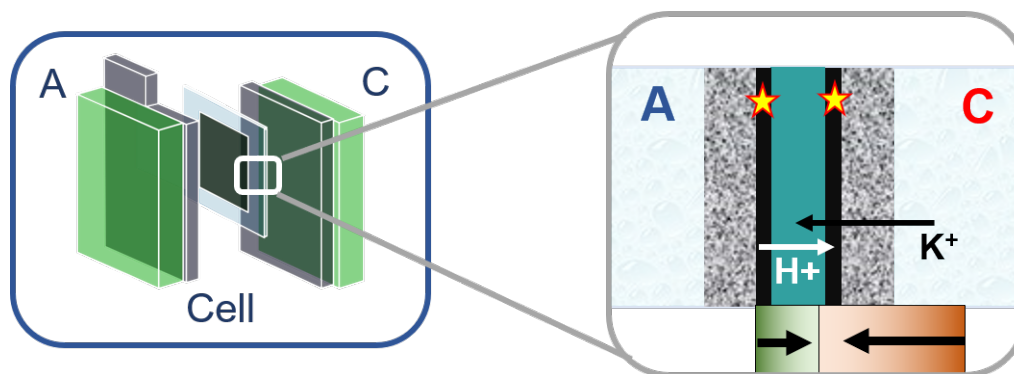


**Figure 13:** Visualization of opposed cation migration (cathode to anode side) vs. electrodiffusion direction (anode to cathode side) when high molar electrolytes are fed at the cathode side only in a model PEM water electrolysis setup.

in a constructive way during MEA fabrication and thus contribute to scaling this green technology? And second, what role do cation-sulfonate interactions play in applications that require the use of high-molar electrolytes such as CO<sub>2</sub> electrolysis? Strong ionic cation-sulfonate interactions affect a membrane's resistance in electrochemical applications. The approach for the second and third part of the thesis is thus based on the hypothesis that this resistance can be measured and leads to changes in the overall applied cell potential according to Abdol Rahim *et al.*:<sup>[118]</sup>

$$V_{\text{total}} = V_{\text{rev}} + V_{\text{act}} + V_{\text{ohm}} \quad (10)$$

This segmentation of the cell potential into different energetic contributions allows for a holistic approach of the topic of membrane-cation interactions in electrolysis applications, both, for early-stage property tuning and for *in situ*-exchange effects at the same time.

As opposed to many publications considering proton-cation exchange as membrane contamination,<sup>[89,91,97,119]</sup> the focus here is first on PFSA preparation before proceeding with MEA fabrication, electrolysis and analysis. Ion exchange is performed by immersing membrane pieces in a 2 M MeCl<sub>X</sub> (X = 1, 2, 3) solution overnight, which is enough to reach equilibrium and exchange protons for cations in a spontaneous fashion.<sup>[92,98]</sup> pH increase in the surrounding solution is found to match acid capacity.<sup>[74]</sup>

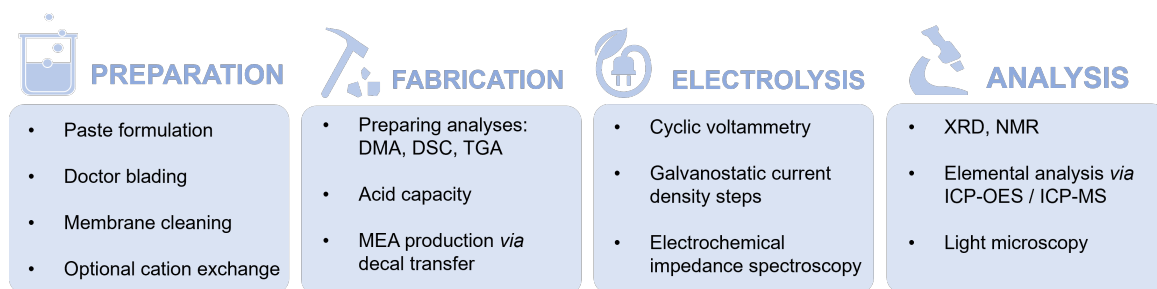


**Figure 14:** Four-step approach to assess membrane resistance information caused by cation-proton exchange in PFSA.

Analysis methods are applied both, prior to fabrication and post-electrolysis to different extents: Viscoelastic properties are assessed *via* dynamic mechanical analysis (DMA), water content can be obtained by thermogravimetric analysis (TGA) in analogy to POM materials.  $T_g$  of protonated PFSA is expected at approx.  $100\text{ }^\circ\text{C}$ <sup>[86,93]</sup> while water in a PFSA shifts it  $T_g$  towards lower temperatures.<sup>[89]</sup> DMA (to assess  $T_g$ ) bears measurement insecurities of up to  $5\text{ }^\circ\text{C}$ .<sup>[120]</sup> It turned out that differential scanning calorimetry is not a suitable method to assess the glass transition of PFSA, since only local crystallite structures are changed irreversibly.<sup>[62,121]</sup>

Decal transfer is again used for MEA fabrication with the catalysts being the state-of-the-art OER (Ir) and HER (Pt) catalysts doctor bladed onto a polyimide (Kapton<sup>®</sup>) foil. Here, a bridge is built between increased polymer stability and processability, since there are almost no existing studies regarding the latter aspect although it is highly relevant for electrolysis scale-up. Thermal parameters are crucial to enable membrane modification and facilitate processability below the decomposition temperature at approx.  $300\text{ }^\circ\text{C}$ . When coming to electrolysis, this thesis is based on the assumption that proton-metal substitution is not a permanent effect but must be reversible to a certain extent due to potential-driven back-exchange *in situ*. To date, electrochemical characteristics of ion-exchanged membranes are rarely investigated.<sup>[122]</sup>

Electrochemical characterization is composed of three investigation techniques: potentiodynamic cyclic voltammetry (CV) is used for procedure ramp-ups and to obtain information about reversibility of redox events. Electrochemical impedance spectroscopy provides information about membrane resistances and galvanostatic current density steps with potential recording allows for a monitoring of ongoing changes during electrolysis. Especially impedance spectroscopy is a demanding technique with the results provoking an ongoing debate about the true membrane

resistance.<sup>[123]</sup> Resistances are measured at 1000 Hz at low current densities to avoid bubble formation that could interfere with the sensitive setup.<sup>[124]</sup> But within this scope it is known that membrane resistances obtained from so-called *Nyquist* plots (showing both, the imaginary and real part of the measured resistances) increase with current density.<sup>[125]</sup> They depend linearly on the membrane thickness and exponentially on the applied potential.<sup>[124]</sup>

Subsequent to electrochemical characterization, MEAs and electrolyte samples are subjected to post-electrolysis analyses, e.g. *via* XRD to gain information about crystalline components arising e.g. by electrochemical metal deposition on the cathode side. Additionally, inductively coupled plasma mass spectroscopy (ICP-MS) or optical emission spectroscopy (ICP-OES) provide information about the elemental composition of a liquid sample. For this purpose, membrane cationic contents were obtained by acidic digestion of PFSA to deliberate cations and bring them in solution.

## 1.5. Scope of this thesis

Aiming at a society based on a green energy supply and a carbon neutral economy, the development of new technologies to convert electrical into chemical energy is currently being driven forward and intensified. This doctoral project arose as a part of the Siemens Energy PEM water electrolysis investigations towards scalable technologies for hydrogen production. It focused on the experimental investigation of new OER catalyst materials and developed towards catalyst-integration into membrane electrode assemblies being the core of a PEM electrolyzer. Since industrial application and scalability are among the most crucial criteria for a new technology to be applied in society, the focus of all studies is on high current densities ( $> 250 \text{ mA/cm}^2$  up to  $2.0 \text{ A/cm}^2$ ), tested at relatively small electrode areas ( $5 \text{ cm}^2$ ). Starting with scalability investigations of a Co POM OER catalyst that was found to be a promising candidate in literature as an earth-abundant and equally active Ir alternative, new projects evolved after the material was proven to be instable at OER conditions. PFSA neutralization *via* proton-metal cation exchange builds the bridge between the first and the other two parts of the thesis. The idea to create a neutral environment to stabilize the POM in a MEA assembly evolved towards a PFSA morphological tuning study and the exploration of interaction-phenomena when using an electrolyte in combination with PFSA membranes *in situ*.

**Chapter 2.1** explores POM applicability in PEM water electrolysis as an alternative OER catalyst. Its integration in a MEA system and electrochemical characterization reveal insufficient acid stability.

**Chapter 2.2** demonstrates the advantages of cation-proton metal exchange in PFSA as a lever to adapt polymer properties to the needs of MEA processing. Potential-driven substitution of  $\text{Li}^+$  by OER protons was found to be quantitative.

**Chapter 2.3** elaborates on  $\text{K}^+$ -sulfonate interactions during operation and employs a PEM water electrolysis model system to assess resistance information of PFSA and quantify its contribution to  $\text{CO}_2$  electrolysis.

These studies are placed into a broader context by the introduction (chapter 1) above and results are summarized in chapter 3. Additionally, further suggestions and follow-up approaches are provided as an outlook at the end of this thesis.

## 2. Results and discussion

Within the chapter at hand, the publications prepared in the course of this doctoral project are briefly summarized and embedded in the thesis. The respective reprint permissions aligned with detailed bibliographic data are located in chapters 7 and 8, respectively.

### 2.1. Stability evaluation of earth-abundant metal-based polyoxometalate electrocatalysts for oxygen evolution reaction towards industrial PEM electrolysis at high current densities

#### 2.1.1. Publication summary

PEM water electrolysis is of major importance in the context of the global energy transition and provides attractive advantages such as dynamic operation mode and high achievable current densities ( $2.0 \text{ A/cm}^2$ )<sup>[5]</sup> over the established alkaline water electrolysis. Forecasting future energy demand however uncovers the problem of catalyst scarcity and price. Iridium (in form of  $\text{IrO}_2$ ) as the state-of-the-art electrocatalyst for oxygen evolution reaction (OER) is amongst the rarest non-radioactive metals in the world accounting for a total share in the continental land mass of 1 ppb.<sup>[25]</sup> Within this paper, promising cobalt-based polyoxometalate materials are investigated towards their suitability as industrially relevant alternatives for  $\text{IrO}_2$ . The focus lays on processability and corrosion resistivity given the harsh acidic and oxidative conditions at the anode side of the PEM electrolyzer.

Successful catalyst synthesis and optimization of the synthetic procedure enabled a thorough catalyst characterization yielding BET surfaces ( $8.37 \text{ m}^2/\text{g}$ ), crystal water content (8.38%, 44  $\text{H}_2\text{O}$ ), elemental analyses and single crystal structures (space group  $\text{P}\bar{1}$ ,  $a = 19.901(4) \text{ \AA}$ ,  $b = 21.177(4) \text{ \AA}$ ,  $c = 24.036(5) \text{ \AA}$ ,  $\alpha = 92.689(7)^\circ$ ,  $\beta = 108.73(7)^\circ$ ,  $\gamma = 117.137(6)^\circ$ ,  $\text{Co}_9\text{Na}_{16}\text{O}_{196}\text{P}_5\text{W}_{27}$ ,  $V = 8310(3) \text{ \AA}^3$  with  $z = 2$ ;  $R^2_{\text{final}} = 0.001$ ). An integration into an industrially applicable membrane electrode assembly (MEA) was possible, paving the path for electrochemical characterization *via* cyclic voltammetry and galvanostatic current density steps. Catalyst dissolution *in situ* was proven by polarization studies with subsequent XRD analysis. This became visible as a current density peak ( $32.2 \text{ mA/cm}^2$ , 2.2 V) with subsequent collapse ( $< 5 \text{ mA/cm}^2$ ) and during galvanostatic potential increases (2.5–10 V at  $10 \text{ mA/cm}^2$ ). A subsequent

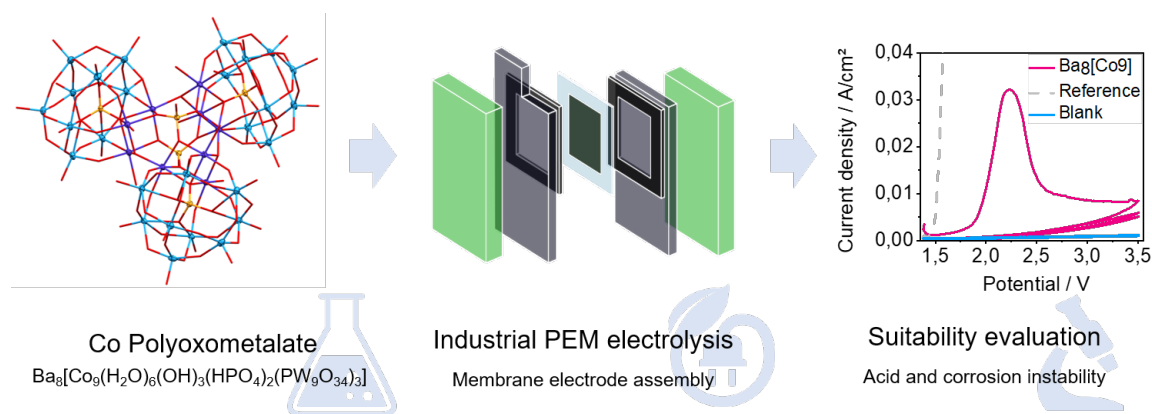


**Figure 15:** Graphical abstract of the work conducted in the first chapter including catalyst synthesis, electrochemical analysis and subsequent stability evaluation.

corrosion stability study uncovered acid-mediated decomposition for the POM anionic oxide framework, meaning insufficient thermodynamic and kinetic stability for industrial requirements in green hydrogen production.

My individual contribution to this work comprised conception, experimental work including analyses and writing the manuscript. Explicitly, I optimized the POM synthesis procedure, conducted material analysis *via* XRD, BET and UV-VIS spectroscopy. I produced the MEAs, analyzed electrochemical data and wrote the manuscript. In order to showcase the complete picture of the scientific conclusion drawn from the results, other fellow-researchers contributed to this work, namely Camila Aring da Silva Ramos Mauro, who synthesized doped POM derivatives and analyzed them *via* XRD, David Reinisch and Thomas Reichbauer, who designed experiments and helped choosing materials and methods, and Nemanja Martić, who contributed to the structure of the manuscript. Jamie Härtl conducted electrochemical measurements, Dr. Christian Jandl provided single-crystal structures, Prof. Olaf Hinrichsen helped reviewing and editing the manuscript and Dr. Günter Schmid contributed by conceptualization and supervision of the project.

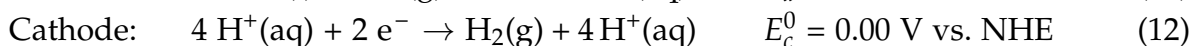
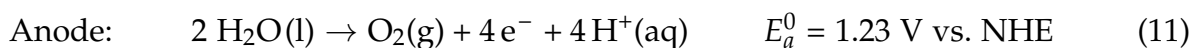
**Bibliographical data** Vetter, K.-M., Aring da Silva Ramos Mauro, C., Reinisch, D., Reichbauer, T., Martić, N., Jandl, C., Hinrichsen, O., Schmid, G., *Electrochem Sci Adv* **2021**, e202100073. <https://doi.org/10.1002/elsa.202100073>.

Reprinted with permission from Wiley-VCH Verlag GmbH & Co. KGaA, Weinheim. Copyright 2021

### 2.1.2. Introduction

The global energy transition paved the path for many research areas towards green energy conversion and storage, among which electrochemical hydrogen production is of particular importance. A promising way to achieve flexible and scalable hydrogen production is proton-exchange membrane (PEM) electrolysis combining high current densities (0.6 – 2.0 A/cm<sup>2</sup>) and high operational stability at low cell temperatures (50 – 80 °C) with a high purity of the resulting hydrogen product gas.<sup>[12]</sup>

Electrochemical water splitting into hydrogen (H<sub>2</sub>) and oxygen (O<sub>2</sub>) is composed of two half-cell reactions: the hydrogen evolution reaction (HER, reduction) and the oxygen evolution reaction (OER, oxidation).



Oxygen evolution reaction (OER) catalysts facilitating the anodic reaction must be efficient, abundant and economical while at the same time showing good stability during processing and under operating conditions at high current densities (> 1 A/cm<sup>2</sup>). Especially for OER catalyst being exposed to harsh oxidative as well as acidic conditions due to proton production at the catalyst side, suitable materials are hard to find.<sup>[24]</sup> Although metal oxides are not thermodynamically stable due to water formation as a driving force, their decomposition can be kinetically hindered. This is true for the state-of-the-art OER catalyst, iridium (Ir), which is desirably to be replaced by a suitable alternative due to its scarcity and price. A study comparing 26 existing OER catalysts under identical OER conditions (1 M H<sub>2</sub>SO<sub>4</sub>, 2 h operation time, 10 mA/cm<sup>2</sup>) could not identify a single stable candidate to replace Ir.<sup>[40]</sup>

Polyoxometalate (POM) materials are considered a promising material class for OER. The framework of many POMs, including heteropolytungstates, consists of formal d<sup>0</sup> W(VI) atoms bound to oxo (O<sup>2-</sup>) ligands which render them oxidatively resistant and hence particularly attractive as homogeneous and heterogeneous catalysts.<sup>[44]</sup> With their large anionic oxide clusters, POMs exhibit molecular as well as oxide fragment properties.<sup>[45]</sup> The fact that this material class is known for its catalytic

activity in oxidation reactions combined with the ability of several Keggin-type anionic POM clusters to conduct protons<sup>[46]</sup> further underlines their attractiveness as OER catalysts.

The POM anion  $[\text{Co}_4(\text{H}_2\text{O})_2(\text{PW}_9\text{O}_{34})_2]^{10-}$  ( $[\text{Co}_4]^{10-}$ ) was the first carbon-free OER catalyst from earth-abundant materials<sup>[43]</sup> being one of the fastest OER catalyst up to date in terms of initial turnover frequencies ( $> 5 \text{ s}^{-1}$ ), observed at pH 8 in solution.<sup>[48]</sup> Comparing this to the state-of-the-art OER catalyst iridium and its soluble complexes, (TOFs up to  $0.5 \text{ s}^{-1}$ )<sup>[49]</sup> seems promising but no long-term evaluations have been carried out so far. Investigations under realistic, industrially relevant conditions are crucial for a suitability evaluation of this catalyst material towards application. Redox tuning this so called Weakley-sandwich anion  $[\text{Co}_4]^{10-}$  by doping Mo into the tungsten framework lowered its OER overpotential by 188 mV (achieving 517 vs. 705 mV for the undoped parent compound).<sup>[53]</sup> A heterogeneous but equally active alternative to the homogeneously used  $[\text{Co}_4]^{10-}$  was presented in 2013 with the larger  $[\text{Co}_9(\text{H}_2\text{O})_6(\text{OH})_3(\text{HPO}_4)_2(\text{PW}_9\text{O}_{34})_3]^{16-}$  ( $[\text{Co}_9]^{16-}$ ) anion.  $[\text{Co}_9]^{16-}$  is obtained as a side product during the synthesis of  $[\text{Co}_4]^{10-}$  and its crystal structure is composed of similar structural moieties as  $[\text{Co}_4]^{10-}$ .<sup>[51]</sup> This catalyst was turned into a water-insoluble form by precipitation with Ba or Cs ions and subsequently used to modify amorphous carbon paste electrodes.<sup>[50]</sup> During operation, long-term stability was reported at low current densities (8 h at  $0.5 \text{ mA/cm}^2$ ). It was shown in a follow-up study that  $[\text{Co}_9]^{16-}$  was able to outperform the state-of-the-art catalyst  $\text{IrO}_2$  under acidic conditions (1 M  $\text{H}_2\text{SO}_4$ ) at low current densities (up to  $15 \text{ mA/cm}^2$ ) when embedded into a carbon paste with organic binder.<sup>[52]</sup> Constant performance was shown for approx. 24 h on an electrode surface of  $0.07 \text{ cm}^2$ .

Only few electrocatalyst materials are examined towards industrial application ( $> 1 \text{ A/cm}^2$ ) and durability after investigating and improving their catalytic performance in fundamental R&D activities.<sup>[55]</sup> In this paper, we evaluate the use of the promising  $[\text{Co}_9]^{16-}$  POM towards its industrial relevance. While  $[\text{Co}_9]^{16-}$  is the focus of this study, the insoluble form of  $[\text{Co}_4]^{10-}$  is also examined for the sake of completeness. For estimating its industrial applicability, the catalyst must undergo the following procedure: First, it must be implemented in a scalable setup, which for PEM electrolysis is a membrane electrode assembly (MEA). Second, the current density needs to be increased ( $\geq 250 \text{ mA/cm}^2$ ) to accomplish efficiency and third, long-term stability ( $> 1000 \text{ h}$ ) needs to be proven in this setting.



### 2.1.3. Experimental

#### Materials

The water used for all experiments in this study was Type 1 ultrapure water purified using the Milli-Q<sup>®</sup> Integral water purification system (18 MΩ\*cm). Chemicals for catalyst syntheses applied in this study are listed in Table 1 including suppliers and purities.

**Table 1:** Suppliers and purities of chemicals applied for catalyst syntheses in this study.

| Compound   | Supplier       | Purity<br>/ %       |
|--|----------------|---------------------|
| Na <sub>2</sub> WO <sub>4</sub> · 2 H <sub>2</sub> O | Alfa Aesar     | ≥ 99.0              |
| Na <sub>2</sub> HPO <sub>4</sub>                     | BioXtra        | ≥ 99.0              |
| Co(OAc) <sub>2</sub> · 4 H <sub>2</sub> O            | Sigma Aldrich  | ≥ 98.0              |
| CH <sub>3</sub> COOH                                 | Applichem GmbH | 100, analysis grade |
| KOAc   | BioXtra        | ≥ 99.0              |
| BaCl <sub>2</sub> · 2 H <sub>2</sub> O               | Fluka Chemika  | ≥ 99.0              |
| Mn(OAc) <sub>2</sub> · 4 H <sub>2</sub> O            | Alfa Aesar     | ≥ 98.0              |
| Fe(OAc) <sub>2</sub>                                 | Alfa Aesar     | ≥ 98.0              |
| Ni(OAc) <sub>2</sub> · 4 H <sub>2</sub> O            | Alfa Aesar     | ≥ 98.0              |

#### Catalyst synthesis

The synthesis was performed in analogy to literature procedures by Weakley *et al.*,<sup>[56]</sup> which were modified by Finke *et al.* and Galán-Mascarós *et al.*<sup>[51,57]</sup> The pH of a buffered solution containing Na<sub>2</sub>WO<sub>4</sub> (33.0 g, 100 mmol, 27.0 eq) and Na<sub>2</sub>HPO<sub>4</sub> · 2 H<sub>2</sub>O (3.30 g, 23.3 mmol, 6.27 eq) in water (95 mL) was adjusted to 7.0 with CH<sub>3</sub>COOH (100%, approx. 7.5 mL). A solution of Co(OAc)<sub>2</sub> · 4 H<sub>2</sub>O (9.00 g, 36.2 mmol, 9.75 eq) in water (30 mL) was added dropwise for 15 min through a syringe filter while the reaction mixture was heated to boiling and held at 100 °C for 2 h. A hot filtration of the mixture was performed and an aqueous solution containing KOAc (2.00 g, 20.4 mmol, 5.50 eq) was added to the filtrate. The resulting mixture was stirred at 70 °C for 5 min, cooled to room temperature overnight and cooled to -4 °C for 5 h. The mother liquor was decanted and the crude crystalline product was

quickly washed with two portions of water (5 mL). From the crude product containing sodium/potassium salts of the anions  $[\text{Co}_9(\text{H}_2\text{O})_6(\text{OH})_3(\text{HPO}_4)_2(\text{PW}_9\text{O}_{34})_3]^{16-}$  ( $[\text{Co}_9]^{16-}$ ) and  $[\text{Co}_4(\text{H}_2\text{O})_2(\text{PW}_9\text{O}_{34})_2]^{10-}$  ( $[\text{Co}_4]^{10-}$ ), the pure products were obtained by temperature-dependent extraction: Quickly soluble, pink  $\text{K}_{2.4}\text{Na}_{13.6}[\text{Co}_9(\text{H}_2\text{O})_6(\text{OH})_3(\text{HPO}_4)_2(\text{PW}_9\text{O}_{34})_3] \cdot 33 \text{H}_2\text{O}$  (9.78 g, 1.14 mmol, 31%) was extracted in two portions with water (15 mL, 20 °C) by rinsing the reaction vessel for 10 s and decanting the pink solution. The water was evaporated. More slowly soluble, violet solid  $\text{K}_{3.1}\text{Na}_{6.9}[\text{Co}_4(\text{H}_2\text{O})_2(\text{PW}_9\text{O}_{34})_2] \cdot 20 \text{H}_2\text{O}$  (12.2 g, 2.28 mmol, 48%) was recrystallized from hot water (15 mL, 70 °C).

$\text{K}_{2.4}\text{Na}_{13.6}[\text{Co}_9]$  was converted to the barium salt by metathesis: A solution of  $\text{BaCl}_2$  (179 mg, 859  $\mu\text{mol}$ , 15.0 eq) in water (3 mL) was added to a solution of  $\text{K}_{2.4}\text{Na}_{13.6}[\text{Co}_9(\text{H}_2\text{O})_6(\text{OH})_3(\text{HPO}_4)_2(\text{PW}_9\text{O}_{34})_3]$  (500 mg, 58.3  $\mu\text{mol}$ , 1.00 eq.) in water (15 mL) while stirring.  $\text{Ba}_8[\text{Co}_9]$  precipitated out of solution and the reaction mixture was stirred for 15 min. The mixture was centrifuged (4250 rpm, 4 min), the colorless mother liquor was decanted, the solid product was washed with water (2 x 20 mL) and acetone (20 mL) subsequent to drying in air overnight.  $\text{Ba}_8[\text{Co}_9(\text{H}_2\text{O})_6(\text{OH})_3(\text{HPO}_4)_2(\text{PW}_9\text{O}_{34})_3] \cdot 44 \text{H}_2\text{O}$  (452 mg, 47.8  $\mu\text{mol}$ , 82%) was obtained as a light rose solid.

The conversion of  $\text{K}_{3.1}\text{Na}_{6.9}[\text{Co}_4]$  to the barium salt was performed analogously substituting  $\text{K}_{2.4}\text{Na}_{13.6}[\text{Co}_9(\text{H}_2\text{O})_6(\text{OH})_3(\text{HPO}_4)_2(\text{PW}_9\text{O}_{34})_3] \cdot 33 \text{H}_2\text{O}$  by  $\text{K}_{3.1}\text{Na}_{6.9}[\text{Co}_4(\text{H}_2\text{O})_2(\text{PW}_9\text{O}_{34})_2] \cdot 20 \text{H}_2\text{O}$  (500 mg, 93.2  $\mu\text{mol}$ , 1.00 eq.) and heating the  $[\text{Co}_4]^{10-}$  containing solution to 70 °C to facilitate dissolution. The precipitation of the barium salt was performed at 70 °C.  $\text{Ba}_5[\text{Co}_4(\text{H}_2\text{O})_2(\text{PW}_9\text{O}_{34})_2] \cdot 20 \text{H}_2\text{O}$  (454 mg, 78.5  $\mu\text{mol}$ , 84%) was obtained as a light violet solid.

Binding  $\text{K}_{2.4}\text{Na}_{13.6}[\text{Co}_9]$  to Sustainion<sup>®</sup> was achieved by precipitation of  $\text{Ba}_8[\text{Co}_9(\text{H}_2\text{O})_6(\text{OH})_3(\text{HPO}_4)_2(\text{PW}_9\text{O}_{34})_3] \cdot 44 \text{H}_2\text{O}$  (500 mg, 58.3  $\mu\text{mol}$ , 1.00 eq.) with a Sustainion<sup>®</sup> solution (5% in ethanol) and subsequent stirring overnight.  $\text{Sust}[\text{Co}_9(\text{H}_2\text{O})_6(\text{OH})_3(\text{HPO}_4)_2(\text{PW}_9\text{O}_{34})_3] \cdot x\text{H}_2\text{O}$  was obtained as a light rose solid. Since the stoichiometry of Sustainion<sup>®</sup> is only specified as „[...] a copolymer of styrene and vinylbenzyl-Rs“ containing „10% - 90% by weight of vinylbenzyl-Rs“ (with Rs being a positively charged quaternary nitrogen bearing residue, such as imidazolium),<sup>[126]</sup> neither yields and salt stoichiometries nor crystal water content were determined. For synthesis of metal substituted POM materials,  $\text{Co}(\text{OAc})_2 \cdot 4 \text{H}_2\text{O}$  was partially replaced by the respective metal acetate. A syntheses list including replacements, yields and elemental analysis results are given in Table 4. The effective Co replace-

ment data was used to calculate the molecular weight for each compound assuming that the remaining stoichiometry and the crystal water content were not affected by the metal replacement. From this information, synthesis yields were determined.

### Catalyst decomposition studies

Temperature stability of the catalyst was examined by thermal treatment of 5 cm<sup>2</sup> squares of the supported catalyst layer before decal at 125 °C, 150 °C, 175 °C, 200 °C, 225 °C, 250 °C, 275 °C, 300 °C, 325 °C and 350 °C, respectively. Layers were analyzed by powder XRD before and after thermal treatment.

Acid stability of the catalyst was examined by treating portions of Ba<sub>8</sub>[Co<sub>9</sub>(H<sub>2</sub>O)<sub>6</sub>(OH)<sub>3</sub>(HPO<sub>4</sub>)<sub>2</sub>(PW<sub>9</sub>O<sub>34</sub>)<sub>3</sub>] · 44 H<sub>2</sub>O (100 mg, 10.6 μmol) in sulfuric acid or hydrochloric acid solutions of different pH (2.0 mL, pH = 6, 5, 4, 3, 2, 1, 0) and sonicating the resulting dispersions for 5 min. The dispersions were centrifuged and decanted. The solid precipitates were dried at ambient temperature and the mother liquors were evaporated at 70 °C overnight.

#### *Ultraviolet-visible spectroscopy (UV-VIS)*

Ultraviolet-visible spectroscopy on a Lambda 35 UV-VIS spectrometer from Perkin-Elmer was used to characterize soluble catalyst decomposition products in the liquid phase after acid treatment.

### Catalyst characterization

#### *Thermogravimetric analysis (TGA)*

To assess the crystal water content contained in the POM materials, the catalyst was analyzed with a Netzsch TG 209 F1 Libra employing a linear heating ramp of 10 °C/min from 30 °C to 300 °C in a nitrogen flow. Results are given in the Supporting Information.

#### *Elemental analysis (EA)*

Elemental analysis was performed *via* inductively coupled plasma atomic emission spectroscopy (ICP-AES) after digesting the POM materials in acid. The K/Na ratio was determined from the original data (given in wt.-%) assuming a total alkaline cation number of 16 for [Co<sub>9</sub>]<sup>16-</sup> and 10 for [Co<sub>4</sub>]<sup>10-</sup> to saturate the charge of the respective polyoxometalate anion. The found metal content was normalized to the

charge of the respective complex. From this estimation combined with the water content obtained from TGA, the molecular weight of the compound was calculated.

#### *Powder X-ray diffractometry*

Powder X-ray diffraction data was obtained using a Bruker D2 PHASER diffractometer, using Cu K radiation, at a scan rate of  $0.0\ 2^\circ\text{s}^{-1}$  for temperature stability studies and  $0.001\ ^\circ\text{s}^{-1}$  for powder and *in situ*-stability studies. Obtained diffractograms were compared to reference data from the PDF-2 2004 crystallography database if available. Correlations of the  $\text{Ba}_8[\text{Co}_9]$  characteristic reflections to h,k,l-values were calculated by insertion of the space group ( $P\bar{1}$ ) and the unit cell dimensions (a, b, c,  $\alpha$ ,  $\beta$ ,  $\gamma$ ) from the  $\text{Na}_{16}[\text{Co}_9]$  single crystal analysis into the h,k,l-generator triclinic pattern of the Bruker DIFFRAC.EVA software. Single crystal X-ray diffractometry details can be found in the Supporting Information.

#### *Brunauer-Emmett-Teller (BET) surface area determination*

Brunauer-Emmett-Teller (BET) surface areas were obtained using a micromeritics ASAP 2020 surface area and porosity analyzer using nitrogen gas ( $\text{N}_2$ ) as an analysis adsorptive. The sample weight was 180 mg and the starting pressure for the measurement was 13  $\mu\text{bar}$ .

#### *Scanning electron microscopy (SEM)*

Secondary electron imaging (SE) in the SEM (Hitachi S-4800 Scanning electron microscope) was used to characterize catalyst and layer morphology before electrochemical characterization.

#### *Membrane electrode assembly (MEA) preparation*

PFSA membranes used in this study were provided as Nafion<sup>TM</sup> N117 by Chemours. Prior to use they were immersed in a freshly prepared half-concentrated peroxy-monosulfuric acid solution overnight, washed with water, stirred in another portion of water for 60 min and finally dried at  $70\ ^\circ\text{C}$  for 15 min. The water used during membrane preparation was Type 1 ultrapure water purified using the Milli-Q<sup>®</sup> Integral water purification system (18  $\text{M}\Omega\cdot\text{cm}$ ).

For MEA fabrication, commercial Pt (for cathode) and Ir (for anode) nano powders provided by Umicore were used as reference materials. The reference Ir or Pt or freshly prepared POM catalyst powders were suspended in methanol,<sup>[63]</sup> a polymer binder was added and the suspension was intimately mixed. An overview of ink compositions is given in Table 2. The ink was doctor bladed onto polyimide foil

(Kapton<sup>®</sup>) and the resulting supported electrode was dried at 80 °C for 30 min. The catalyst loading was  $1.98 \pm 0.25$  mg/cm<sup>2</sup> for each electrode. In a decal process the Kapton<sup>®</sup>-supported electrodes (cut to 5 cm<sup>2</sup> squares), were heat transferred onto the PFSA membrane by pressing a cathode-membrane-anode sandwich with 2.5 Nm at 175 °C for 60 seconds. For catalyst evaluation versus a Pt half-MEA, the catalyst containing ink was directly coated onto the Ti grid.

**Table 2:** Overview of ink formulations used for MEA production and subsequent electrochemical characterization.

| Formulation No. | Catalyst  | Binder                       | Additives          |
|-----------------|-----------|------------------------------|--------------------|
| 1 – Reference   | Ir or Pt  | NafionTM (5%)                | none               |
| 2               | Ba8[Co9]  | NafionTM (5%)                | none               |
| 3               | Ba8[Co9]  | PTFE (5%)                    | none               |
| 4               | Ba8[Co9]  | Sustainion <sup>®</sup> (5%) | none               |
| 5               | Ba8[Co9]  | NafionTM (5%)                | Carbon black (60%) |
| 6               | Ba8[Co9]  | none                         | Carbon black (60%) |
| 7               | Sust[Co9] | none                         | Carbon black (60%) |
| 8               | Ba5[Co4]  | NafionTM (5%)                | Carbon black (60%) |
| 9 – C blind     | none      | NafionTM (5%)                | Carbon black (60%) |

#### *Resistance determination*

The transverse resistances of the catalyst layers with compositions shown in Table 2 were determined with a 4338 B Milliohm meter provided by Agilent Technologies.

#### *Electrochemical measurements*

Electrochemical measurements were conducted either in a potentiodynamic or in a galvanostatic operation mode. In potentiodynamic experiments, a potential is applied dynamically by the potentiostat and the current adapts according to the preset potential. Potentiodynamic experiments comprise cyclic voltammetry in different setups. In galvanostatic experiments a constant target current is preset by the potentiostat. Following this presetting a potential necessary to achieve this current is applied.

Cyclic voltammetry (CV) measurements were performed either in a beaker or in a PEM water electrolysis cell: CV of a  $K_{2.4}Na_{13.6}[Co_9]$  solution was performed in a

beaker using two titanium grids as electrodes and an Ag/AgCl (3M KCl) reference electrode (RE-1BP, ALS Co.). The potential was cycled three times between -1.4 and +1.4 V with a scan rate of 0.5 V/s and recorded against the Ag/AgCl reference electrode. When the insoluble Ba<sup>2+</sup> salt of a catalyst was investigated, CV was performed in a PEM water electrolysis cell provided by Scribner Associates Inc. A schematic of the PEM cell setup can be found in the Supporting Information. CV measurements were performed with a scan rate of 10 mV/s between 1.4 and 3.5 V applied cell potential. If the current compliance of 2.0 A/cm<sup>2</sup> was reached at lower potentials than the maximum applied potential of 3.5 V, the CV direction was reversed. To evaluate catalyst stability at lower potentials, further cyclovoltammetry experiments were conducted in a potential range from 1.4 to 2.0 V.

In galvanostatic experiments for monitoring *in situ* catalyst decomposition, potential data was recorded in a galvanostatic measurement mode at constant current densities of 5.00 mA/cm<sup>2</sup> or 10.0 mA/cm<sup>2</sup>, held for 20 min, respectively.

For all electrochemical measurements the respective setup is hooked up to a Methrom PGSTAT302N potentiostat equipped with a 10 A booster, both provided by Deutsche Metrohm GmbH & Co. KG. Combining the 10 A booster with a 5 cm<sup>2</sup> electrode area leads to a current compliance of 2.0 A/cm<sup>2</sup> being the maximum achievable value in this study. Ultrapure water was used for both anode and cathode side separate electrolytes pumped with a flow of 120 mL/min by a membrane pump.

#### 2.1.4. Results and discussion

To transfer [Co<sub>9</sub>]<sup>16-</sup> POM into a scalable MEA setup its material properties need to be known to guarantee smooth processability. After characterizing the catalyst by single crystal and powder X-ray diffractometry (XRD), elemental analysis (EA) and scanning electron microscopy (SEM), the catalyst was tested for BET surface and heat stability in order to make an industrially applicable MEA.

##### Catalyst characterization

Synthesis of the catalyst is performed in a two-step approach: First, the POM anionic cluster is assembled in analogy to early literature synthesis procedures yielding the soluble Na<sup>+</sup>/K<sup>+</sup> or Na<sup>+</sup> salt of both, [Co<sub>4</sub>]<sup>10-</sup> and [Co<sub>9</sub>]<sup>16-</sup>.<sup>[58]</sup> At the end of this first synthesis step, potassium acetate (KOAc) is added as crystallization facilitator. The two POM species are separated by temperature-dependent extraction.

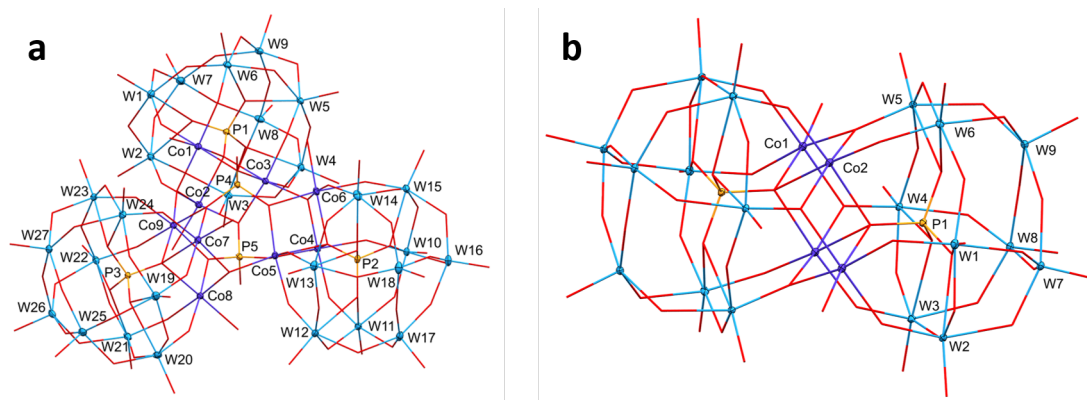


**Figure 16:** Molecular structures of the POM fragments of a)  $\text{Na}_{16}[\text{Co}_9]$  and b)  $\text{Na}_{10}[\text{Co}_4]$  as obtained by single-crystal X-ray diffraction. Ellipsoids are displayed at the 50% probability level and oxygen atoms are simplified as wireframes. Symmetry code to create equivalent positions in b): 1-x, 1-y, 1-z.

Single crystal structures were obtained from the  $\text{Na}^+$  salts of both species as depicted in Figure 16. The  $[\text{Co}_4]^{10-}$  anion, growing „beautiful violet [...] crystals” is already known with a mixture from  $\text{Na}^+$  and  $\text{K}^+$  counter cations.<sup>[58]</sup> The structure of the  $[\text{Co}_9]^{16-}$  Keggin cluster<sup>[56]</sup> as a  $\text{Na}^+$  salt is new, it was only reported as a  $\text{Rb}^+$  salt in 1984.<sup>[127]</sup> Keggin clusters consisting of  $[\text{PW}_{12}\text{O}_{40}]^{3-}$  moieties can be divided into  $\alpha$ -,  $\beta$ - ( $\gamma$ -,  $\delta$ - and  $\epsilon$ -) decreasing in symmetry in this order.<sup>[59]</sup> It was shown that due to a  $60^\circ$  torsion of the  $\text{CoO}_6$  octahedra that caps each  $\text{PW}_9\text{O}_{34}$  moiety, the  $[\text{Co}_9]^{16-}$  anion rather completes a  $\beta$ -Keggin cluster whereas the smaller  $[\text{Co}_4]^{10-}$  forms highly symmetrical  $\alpha$ -Keggin structures. Our crystallographic data confirms this finding, since  $\text{Na}_{10}[\text{Co}_4]$  was attributed formula unit  $Z = 1$ , while for  $\text{Na}_{16}[\text{Co}_9]$ ,  $Z$  equals 2. Comparing literature  $\text{Rb}_8[\text{Co}_9]$  with the  $\text{Na}^+$  salt of the same anion, the first one crystallizes in a hexagonal crystal system with the space group  $\text{P}63/\text{m}$  ( $a = 20.243(8)$ ,  $c = 20.343(6)$  Å,  $R_{\text{final}} = 0.093$ ) while the latter one crystallizes in a triclinic crystal system (space group  $\text{P}\bar{1}$ ,  $a = 19.901(4)$  Å,  $b = 21.177(4)$  Å,  $c = 24.036(5)$  Å,  $\alpha = 92.689(7)^\circ$ ,  $\beta = 108.73(7)^\circ$ ,  $\gamma = 117.137(6)^\circ$ ,  $\text{Co}_9\text{Na}_{16}\text{O}_{196.05}\text{P}_5\text{W}_{27}$ ,  $V = 8310(3)$  Å<sup>3</sup> with  $z = 2$ ;  $R^2_{\text{final}} = 0.001$ ). Bond lengths in the POM anionic cluster are comparable ( $\text{W}-\text{O}_{\text{terminal}}$ :  $1.71_{\text{Rb}}$  vs.  $1.717_{\text{Na/K}} \pm 0.004$  Å,  $\text{W}-\text{O}[\text{W}]$ :  $1.95_{\text{Rb}}$  vs.  $1.892_{\text{Na/K}} \pm 0.021$  Å,  $\text{W}-\text{O}[\text{W.P}]$ :  $2.45_{\text{Rb}}$  vs.  $2.430_{\text{Na/K}} \pm 0.009$  Å,  $\text{W}-\text{O}[\text{Co}]$ :  $1.71_{\text{Rb}}$  vs.  $1.764_{\text{Na/K}} \pm 0.006$  Å,  $\text{Co}-\text{O}$ :  $2.10_{\text{Rb}}$  vs.  $2.099_{\text{Na/K}} \pm 0.068$  Å,  $\text{P}-\text{O}$ :  $1.56_{\text{Rb}}$  vs.  $1.540_{\text{Na/K}} \pm 0.016$  Å, averaged). An exchange of the cation lowers the overall symmetry of the crystal, although the anion itself was found to be very similar. Bond length comparison did not show any significant deviation. Further crystallographic data can be found in the Supporting Information.

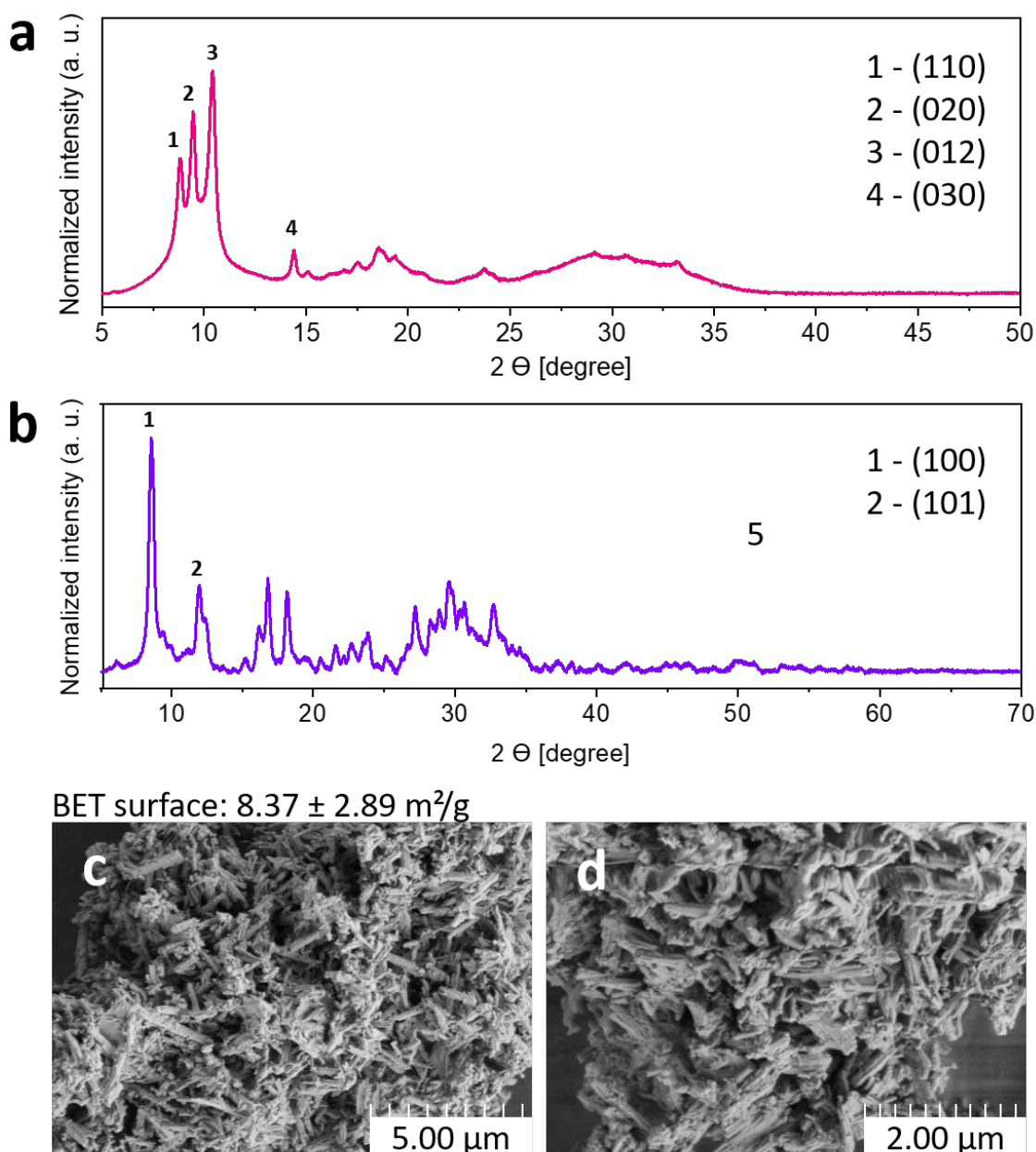


**Figure 17:** Powder XRDs for insoluble barium salts of a)  $[\text{Co}_9]^{16-}$  and b)  $[\text{Co}_4]^{10-}$  anions with (h,k,l)-indices assigned to the most prominent reflections. c) + d) Scanning electron microscopy images of  $\text{Ba}_8[\text{Co}_9]$  at different magnifications showing the needle-like structure of the POM salts.

The second synthesis step is a conversion of the water-soluble  $\text{Na}^+/\text{K}^+$  salt of the POM into its insoluble  $\text{Ba}^{2+}$  form by precipitation with  $\text{BaCl}_2$ . This step is crucial for electrolysis purposes to guarantee that the heterogeneous catalyst can be fixated onto the MEA while circulating water through the electrolysis cell. Powder X-ray



diffraction patterns reveal a rather amorphous structure of Ba<sub>8</sub>[Co<sub>9</sub>] with only few distinct reflexes (Figure 17a) while Ba<sub>5</sub>[Co<sub>4</sub>] appears more crystalline (Figure 17b). For both powder diffraction patterns (h,k,l)-indices from the respective Na<sup>+</sup> single crystal structure could be correlated with the most prominent reflexes. Reflex assignment is shown in Table 3. For [Co<sub>9</sub>]<sup>16-</sup>, SEM pictures show that Ba<sup>2+</sup> and Na<sup>+</sup> salts share the needle-like structure of their crystallites. Powder diffraction patterns of the Na<sup>+</sup>/K<sup>+</sup> POMs as well as SEM images of Ba<sub>5</sub>[Co<sub>4</sub>] can be found in the Supporting Information.

**Table 3:** Correlated (h,k,l)-indices for Ba<sup>2+</sup> POM powder diffraction patterns.

| POM type  | 2 $\Theta$ | Relative intensity / % | (h,k,l) index assigned |
|---|------------|------------------------|------------------------|
| K <sub>x</sub> Na <sub>y</sub> [Co <sub>9</sub> ] as prepared | 18.9       | 3.3                    | -                      |
| Ba <sub>8</sub> [Co <sub>9</sub> ] expected                   | -          | -                      | 8.0                    |
| Ba <sub>8</sub> [Co <sub>9</sub> ] as prepared                | -          | -                      | 8.7                    |
| K <sub>x</sub> Na <sub>y</sub> [Co <sub>4</sub> ] as prepared | 6.8        | 3.1                    | -                      |
| Ba <sub>5</sub> [Co <sub>4</sub> ] expected                   | -          | -                      | 5.0                    |
| Ba <sub>5</sub> [Co <sub>4</sub> ] as prepared                | -          | -                      | 5.5                    |
| Sust[Co <sub>9</sub> ] as prepared                            | 0.5        | 0.5                    | -                      |

In addition to XRD, elemental analyses were performed with the results normalized to the W content of the sample given in Table 4. Sust[Co<sub>9</sub>] refers to a sample that was precipitated with the anion exchange material Sustainion<sup>®</sup> instead of an alkaline or alkaline earth chloride.<sup>[128]</sup> Its exact composition is unknown,<sup>[126]</sup> but as opposed to the precipitation with Ba<sup>2+</sup> which replaces K<sup>+</sup> and Na<sup>+</sup> quantitatively, the anion exchange material (AEM) replaces only portions of the alkaline metal ions due to the large size of the polymer chains. The full (not normalized) EA results can be found in the Supporting Information along with thermogravimetric data (TGA) and BET surface area results. The crystal water content was used to calculate the exact yields and stoichiometry of the catalyst (e.g. K<sub>2.4</sub>Na<sub>13.6</sub>[Co<sub>9</sub>(H<sub>2</sub>O)<sub>6</sub>(OH)<sub>3</sub>(HPO<sub>4</sub>)<sub>2</sub>-(PW<sub>9</sub>O<sub>34</sub>)<sub>3</sub>] · 33 H<sub>2</sub>O and K<sub>3.1</sub>Na<sub>6.9</sub>[Co<sub>4</sub>(H<sub>2</sub>O)<sub>2</sub>(PW<sub>9</sub>O<sub>34</sub>)<sub>2</sub>] · 20 H<sub>2</sub>O). Bearing in mind the scaling of the catalyst, knowledge about its crystal water content is also important to precisely determine the catalyst loading and therefore the number of active centers on the MEA.

**Table 4:** Elemental analysis results (ICP-AES) for the POM materials. Except for Sust[Co9] data was normalized to the W content to facilitate comparison.

| Sample                     | Na   | K   | Ba  | P   | Co  | W  |
|----------------------------|------|-----|-----|-----|-----|----|
| $K_xNa_y[Co9]$ as prepared | 18.9 | 3.3 | -   | 4.8 | 8.6 | 27 |
| $Ba_8[Co9]$ expected       | -    | -   | 8.0 | 5.0 | 9.0 | 27 |
| $Ba_8[Co9]$ as prepared    | -    | -   | 8.7 | 5.1 | 8.9 | 27 |
| $K_xNa_y[Co4]$ as prepared | 6.8  | 3.1 | -   | 2.2 | 4.2 | 18 |
| $Ba_5[Co4]$ expected       | -    | -   | 5.0 | 2.0 | 4.0 | 18 |
| $Ba_5[Co4]$ as prepared    | -    | -   | 5.5 | 2.1 | 4.1 | 18 |
| Sust[Co9] as prepared      | 0.5  | 0.5 | -   | 1.0 | 3.3 | 32 |

MEAs are usually produced in a so called decal process, which implies pressing a supported catalyst layer onto the ion exchange membrane at elevated temperatures.<sup>[64]</sup> Since polyoxometalates as well as their protonated forms, called heteropoly acids, tend to decompose upon thermal treatment,<sup>[60]</sup> we investigated the temperature stability of  $Ba_8[Co9]$  with the results given in Figure 18.

The duration of thermal treatment during decal is usually shorter (heat pressing for 120 s) than in the shown temperature study (30 min per temperature step). However, since we want to ensure the catalyst does not suffer from the MEA production process, the temperature was held for longer. A comparison of the characteristic reflexes in the respective powder diffractograms to each other suggests that temperatures above 200 °C damage the Keggin cluster. To avoid this, MEA production was performed at 175 °C. After decal processing and before assembling the cell, we confirmed the presence of the Keggin cluster on the MEA by XRD and proved that the cluster survived the processing conditions (Figure 23). This way we can guarantee to measure the intact POM's catalyst performance. The supported catalyst layers for pressing onto the membrane were produced from slurries (formulations given in the experimental section) and the decal process was performed analogously to earlier reports.<sup>[65]</sup> Transverse resistance measurements (see Table 5) proved that POMs effectively prevent electronic flow due to their oxidic cluster (resistance overflow) and the resulting insulating character. But decal transfer onto the CEM polymer enabled conductivity since a resistance (being the inverse conductivity) was observed (10 MΩ). As resistances are still much higher than for the Ir reference (5.71 Ω for the layer and 249 Ω after decal), carbon pastes (CP) were used to overcome the

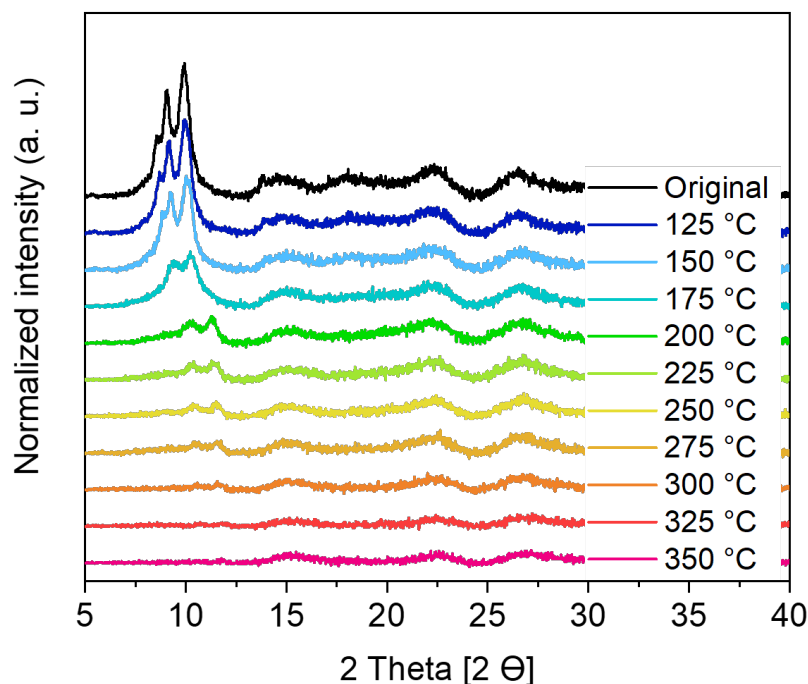


**Figure 18:** Results of temperature degradation study on  $\text{Ba}_8[\text{Co}_9]$ : Samples were heated for 30 min at each temperature step and subsequently analyzed by XRD. For decal processing, temperatures above 125 °C are necessary.

insulating properties of the oxidic POM material. The respective formulation is literature known.<sup>[52]</sup> However, since elemental carbon is prone to oxidation, another viable solution must be found to overcome the POMs insulating character. To guarantee comparison to literature we nevertheless incorporated CP-formulations in this present study.

**Table 5:** Transverse conductivities of catalyst layers and pure Nafion<sup>TM</sup>.

| Paste formulation | Specification                         | Transverse Resistance |
|-------------------|---------------------------------------|-----------------------|
| Formulation 1     | (Ir) layer                            | 5.71 $\Omega$         |
| Formulation 2     | ( $\text{Ba}_8[\text{Co}_9]$ ) layer  | -                     |
| Formulation 1     | (Ir) on MEA                           | 249 $\Omega$          |
| Formulation 2     | ( $\text{Ba}_8[\text{Co}_9]$ ) on MEA | 10.0 M $\Omega$       |
| -                 | Pure Nafion <sup>TM</sup>             | 0.30 M $\Omega$       |

### Electrochemical evaluation

As opposed to the promising results cited before,<sup>[52]</sup> recent reports state that polyoxometalate materials might not be suitable as OER catalysts. As an example, a manganese oxide layer passivating the electrode was detected in a decomposition study.<sup>[45]</sup> We performed basic cyclic voltammetric measurements with  $K_{2.4}Na_{13.6}[Co_9]$  in solution between -1.4 and +1.4 V, meaning that the potential stayed within the range below beginning water oxidation. In the case of electroreduction or oxidation taking place, it is the POM itself taking or donating electrons. This basic ability is a prerequisite for any catalyst and should appear in a cyclic voltammogram as a certain deflection. For 16-fold negatively charged  $[Co_9]^{16-}$ , up to 16 peaks could theoretically appear if single electron transfers occurred at distinct potentials. Measurement results are shown in Figure 19.

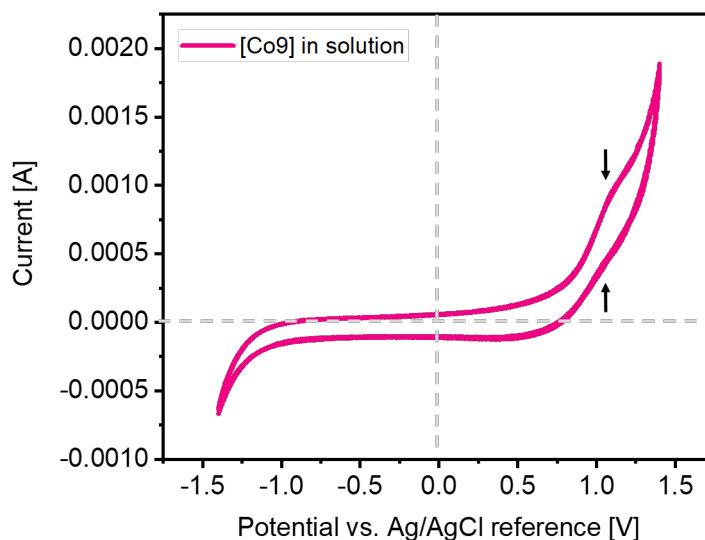


**Figure 19:** Cyclic voltammetric measurement results with  $K_{2.4}Na_{13.6}[Co_9]$  in solution between -1.4 and +1.4 V. The CV was cycled three times with the results being perfectly reproducible.

Figure 19 shows the reversible appearance of one peak at a positive potential (1.11 V in forward and 1.08 V in backward direction), which can be traced back to an oxidation reaction occurring at the POM cluster itself. The 16fold negatively charged cluster is thus able to donate at least one electron, which is a crucial ability to act as a catalyst in water oxidation. Since this oxidation is proven to be reversible (deflection in the backward direction), the cluster can accept electrons stemming from water oxidation once, the electron is donated to the electrode. The experiment proves the

POMs ability of dynamic oxidation and reduction, so the basic prerequisite for a catalyst material is fulfilled.

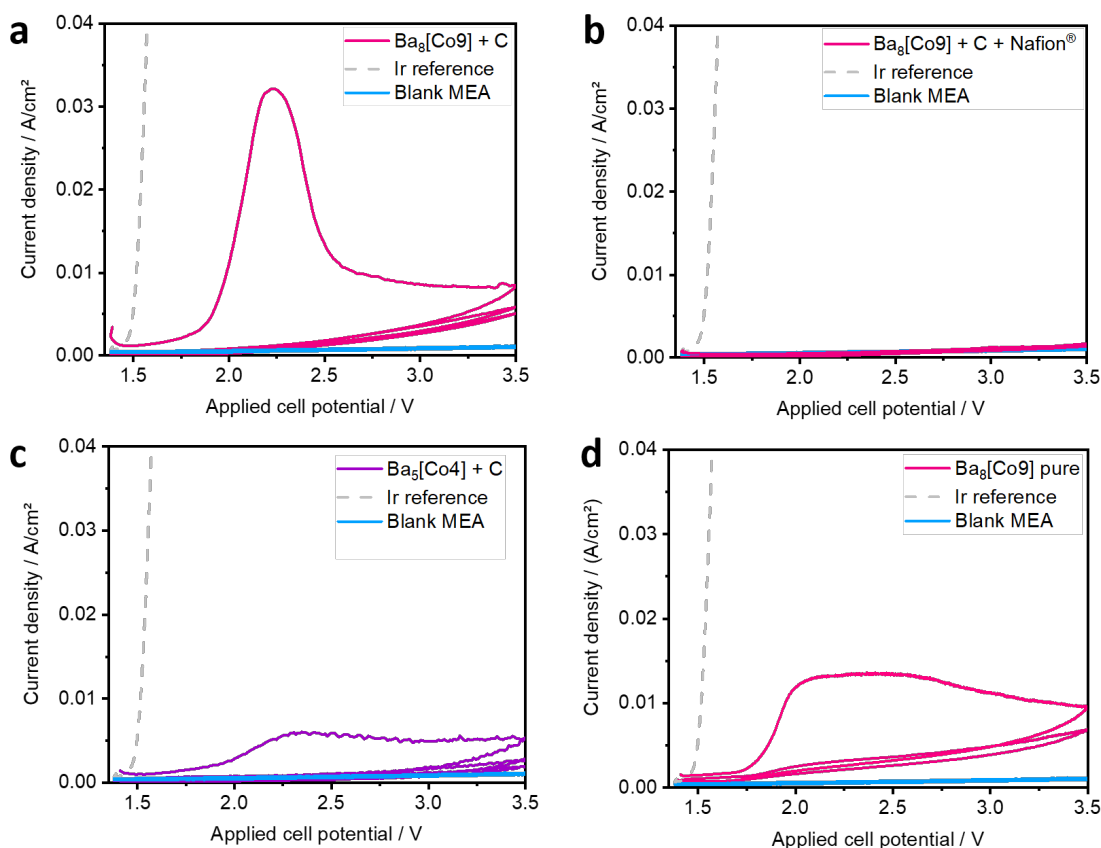


**Figure 20:** Electrochemical evaluation of POM-MEAs with different anode catalyst layer composition in a cyclic voltammetry study. a) 40%  $\text{Ba}_8[\text{Co}_9]$  plus carbon powder as described in literature,<sup>[52]</sup> b) trial to stabilize a layer identical to a) with additional Nafion<sup>TM</sup> ionomer, c) 40%  $\text{Ba}_5[\text{Co}_4]$  plus carbon powder and d) pure  $\text{Ba}_8[\text{Co}_9]$  without carbon.

PEM electrochemical measurements were performed in a modified water electrolysis cell with the setup shown in the Supporting Information. In analogy to literature, the first POM MEAs we characterized electrochemically were loaded with 40% POM incorporated in a carbon paste as shown in Figure 20.<sup>[52]</sup> Figure 20a shows the potentiodynamic polarization curve (cyclic voltammogram, CV) for a POM + CP formulation with no further modifications. A peak in current density is observed at 2.2 V but the current density reached is 32.2 mA/cm<sup>2</sup>. Although the potential is further increased after passing 2.2 V, the current density decreases during the first polarization curve yielding a parabolic curve. During a second and a third polarization cycle, the peak in performance cannot be reproduced. Here, the resulting curves

are closer to the blind value of a blank half-MEA with no catalyst at the anode side (reaching  $1.0 \text{ mA/cm}^2$  at  $3.5 \text{ V}$  applied potential). This behavior suggests that the catalytically active species (the POM catalyst) already either decompose or dissolve during the first CV. Figure 20c is the result of an analogous testing (40% POM in CP, without additional PFSA) for  $\text{Ba}_5[\text{Co}_4]$ . The same effect is visible, but it is less pronounced. Since CP electrodes are known for their instability at elevated potentials or over time,<sup>[52]</sup> we tried to fixate the catalyst onto the MEA by covering an identical, freshly pressed MEA with PFSA ionomer (Nafion<sup>TM</sup>) solution and drying it at room temperature as performed in the literature. The catalytic activity of the catalyst was quantitatively suppressed as shown in Figure 20b. Since carbon is not an option for anodic use in electrolysis due to potential carbon oxidation, we tried a different paste formulation without CP but with a PFSA binder. The result of the respective CV measurements is shown in Figure 20d. Although the current density only reached  $13.2 \text{ mA/cm}^2$ , the same behavior is visible. For this setting, identical MEAs suffer poor reproducibility with many of the resulting CVs resembling to the blind value of a blank half-MEA (with no catalyst coated on the anode side). Here, only the Ti grid acts as a catalyst at the anode side but no catalyst powder was decaled into the anode side upper polymer layer of the MEA. Additionally, the peak potential ( $2.2 \text{ V}$ ) is not to be seen as a boarder, but can be shifted towards other potentials (e.g.  $2.0 \text{ V}$  as shown in Figure 20d). We thus hypothesize that it is not the net amount of the potential applied yielding the observed curves but that further aspects cause the loss in current density over the course of the experiment. Additional attempts to stabilize the catalyst onto the MEA were undertaken by adding PTFE as a non-functional inert binder and Sustainion<sup>®</sup>, an anion exchange ionic binder, none of which yielded better results than the ones shown in Figure 20a. State-of-the-art AEM materials consist of organic, non-perfluorinated structures, which are by nature prone to oxidation under the harsh conditions at the anode side, just as the CP used in the previous experiments. As such, we did not expect an AEM material introduced at the anode side of the cell to be suitable for long-term operation but were hoping for short-term stability or performance increases. Replacing the  $\text{Ba}^{2+}$  counter cation by the AEM neither led to an increase in current density nor in a stabilized CV course. The AEM counter cations do not change the key characteristics of the POM cluster (e.g. oxidic character, acid lability and insulating properties) significantly to achieve enhanced stability. The respective polarization curves can be found in the Supporting Information.

Since decomposition or dissolution of the catalyst species is observed at increasing potential (2.0 - 2.2 V) for all experiments conducted, we monitored if a CV, cycled below the 2.2 V potential border, would be reproducible. A MEA with the same POM + C formulation was cycled twice between 1.4 and 2.0 V reaching a current density of 3.2 mA/cm<sup>2</sup> in the first and 3.0 mA/cm<sup>2</sup> in the second cycle (data given in the Supporting Information). Although the current density reached was not as high as achieved for the analogue MEA (10 mA/cm<sup>2</sup>, Figure 20a), the second CV showed higher peak performance than the pure Ti grid reference indicating that active catalyst remained on the MEA.

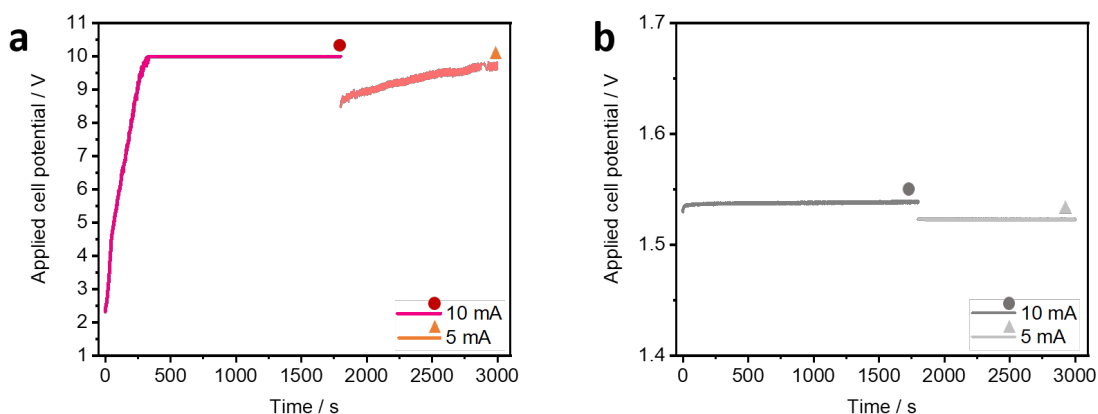


**Figure 21:** Electrochemical evaluation of a POM-MEA under galvanostatic conditions at 10 and 5 mA. Instrumental specifications lead to a maximum achievable potential limit of 10 V. Data cannot be recorded beyond this value. a) 40% Ba<sub>8</sub>[Co<sub>9</sub>] plus carbon powder as described in literature,<sup>[56]</sup> and b) reference Ir-formulation on the anode side of the MEA.

To further monitor the POM's performance degradation during cell operation *in situ*, we conducted galvanostatic experiments complementing the CVs shown above. The results in Figure 21a demonstrate how the cell potential changes over time at 10 and 5 mA/cm<sup>2</sup> static current that were applied to the cell subsequently. Figure 21b depicts the results for an Ir/Pt-standard MEA characterized under the same operating conditions. While for the latter one, the same current density can be achieved at a constant potential (10 mA/cm<sup>2</sup> at 1.54 V and 5 mA/cm<sup>2</sup> at 1.52 V), the potential increases with time for the POM MEA. This finding is well in line with our hypothesis of catalyst decomposition or dissolution. When portions of the catalyst are removed from the MEA, the potential needed to achieve the same current density increases due to fewer active centers at the electrode. The potential even raises up to 10 V to achieve 10 mA/cm<sup>2</sup> (10 V being the instrumental potential limitation

that can be tracked with the devices used). Switching to  $5 \text{ mA/cm}^2$  after this first galvanostatic step still requires very high potentials, which is a clear indication for missing active centers at the anode. In a comparison experiment, a Pt half-MEA with only the Ti grid acting as the OER catalyst at the anode side also surpasses the 10 V device limitation during the whole measurement (data shown in the Supporting Information).

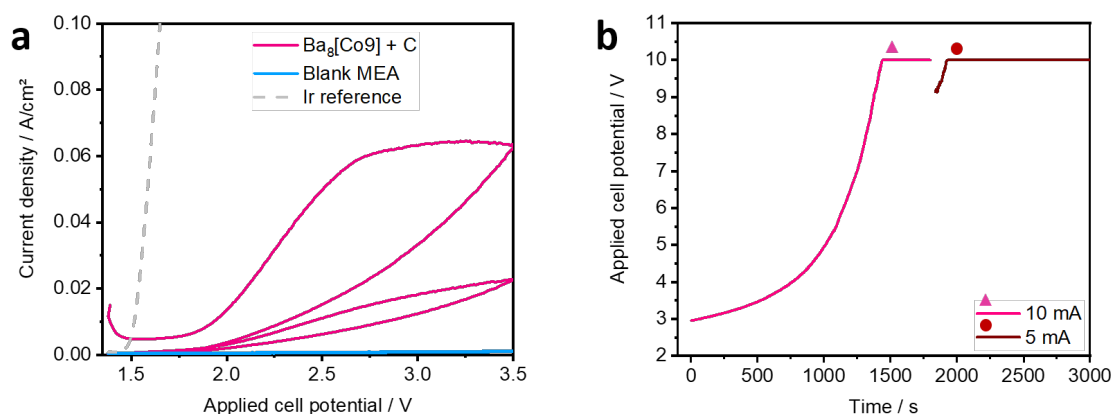


**Figure 22:** Electrochemical characterization of a Pt half-MEA with the POM catalyst containing ink coated directly onto the Ti grid.

In a last evaluation series, the POM catalyst containing ink was coated directly onto the Ti grid without subjecting the POM to the decal process. This way, not only the thermal treatment of the catalyst but also the close contact to the acidic PFSA membrane can be avoided. Cyclic voltammetry (Figure 22a) and galvanostatic (Figure 22b) characterization was performed. In cyclic voltammetry, there was no performance peak at 2.2 V but the current density increased with the applied potential until reaching  $61 \text{ mA/cm}^2$  at 3.5 V. In a second CV run, only a maximum of  $20 \text{ mA/cm}^2$  was reached, which can also be traced back to catalyst decomposition or dissolution *in situ*. Reproducing the same experiment but with 40 CV cycles, the peak performance approached the blank half-MEA (no catalyst coated onto the anode side, data shown in the Supporting Information). During galvanostatic evaluation, the potential needed to reach 10 and  $5 \text{ mA/cm}^2$ , increased and finally peaked in 10 V as for the pure Ti grid vs. a Pt half-MEA. Although the potential increase took place more slowly (10 V at 1500 s) than shown in Figure 21a (10 V at 500 s), the observed effect is the same.

To prove the disappearance of the  $\text{Ba}_8[\text{Co}_9]$  POM catalyst, powder diffractograms belonging to pre- and post-electrolysis MEA samples were recorded. The results for



a formulation of the pure POM without CP is shown in Figure 23a and a formulation of 40% POM with CP in Figure 23b. Analogous diffractograms for Ba<sub>5</sub>[Co<sub>4</sub>] as well as diffractograms of pure PFSA membrane and a pure carbon paste layer for comparison are available in the Supporting Information. They show no distinct reflexes but prove that post-electrolysis MEAs resemble the pure PFSA membrane without POM and CP.

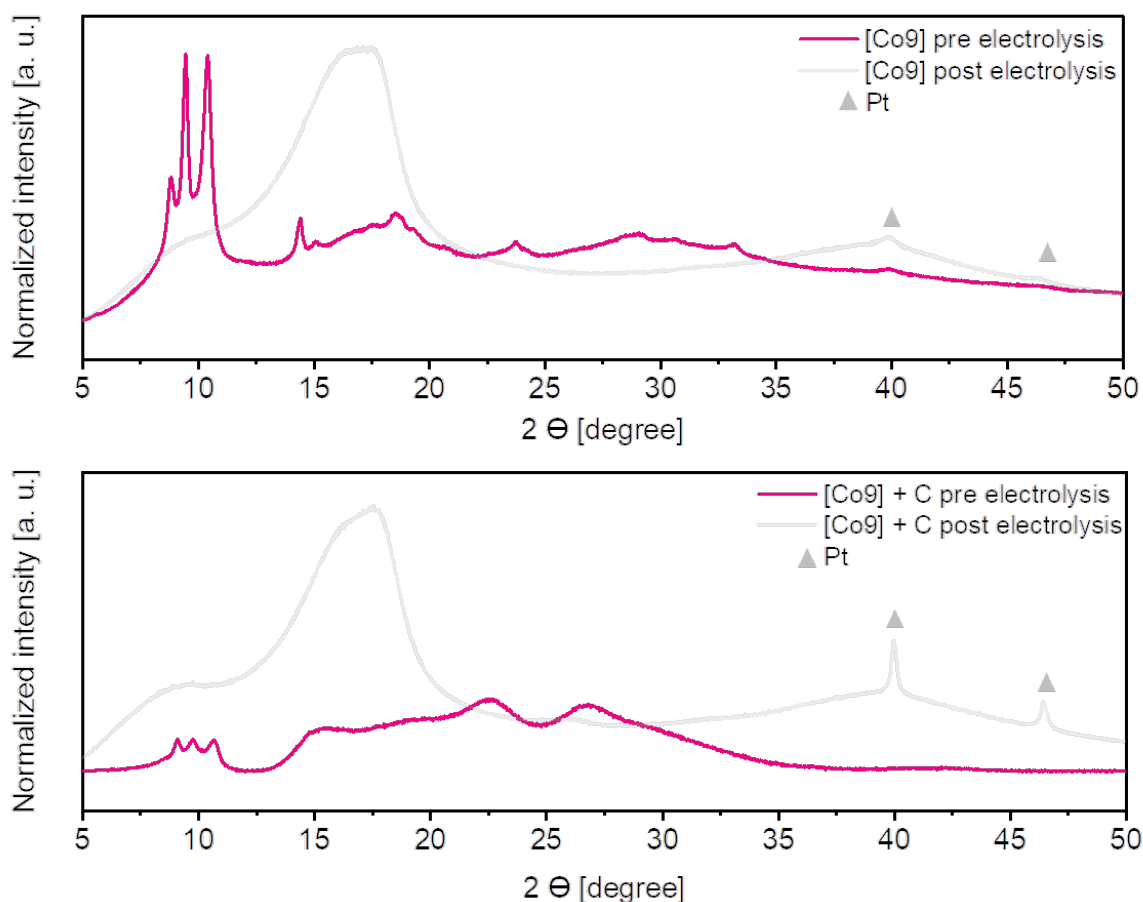


**Figure 23:** XRD study of MEAs before and after electrolysis.

Comparing pre- (magenta) and post-electrolysis (grey) diffractograms in Figure 23, the characteristic POM reflexes at 8.85, 9.64, 10.2 and 14.5° 2 $\Theta$  quantitatively disappear during electrolysis while new features appear. In the resulting post-electrolysis diffractograms new reflexes at 40.0 and 46.5 ° 2 $\Theta$  (Figure 23, grey triangles) can be attributed to platinum, which originates from the cathode side due to tight MEA contacting. This provides evidence that the POM catalyst does not stay onto the MEA during operation. The observation was identical for all MEAs examined in

water electrolysis. Although the CV shown in Figure 20 suggests the existence of catalytically active species on the MEA even post-electrolysis, the XRD (shown in the Supporting Information) proves that also in this case, no more POM is found on the MEA.

Any metal including noble metal catalysts that are said to be stable are prone to oxidation and corrosion: Ru, Au, Ir, Rh, Pt, Pd all display both transient dissolution during oxide formation at the beginning of the electrochemical process and steady-state dissolution during the OER.<sup>[41]</sup> The decisive difference is the dissolution kinetics, which ultimately decides about the industrial applicability of a material: The kinetics may vary by orders of magnitude for different metals, rendering the dissolution quick or slow. The slower the dissolution the better suitable the respective material. Thermodynamically, it is known that any oxide (except few examples, such as  $\text{IrO}_2$ ) is acid labile due to water formation as the driving force of the decomposition reaction releasing hydrated metal cations. In the presented case, we were hoping that  $\text{Ba}_8[\text{Co}_9]$  behaves like a kinetically stable oxidic tungstate cage protecting the Cobalt active centers inside. The catalyst might possess slow dissolution kinetics and thus a pronounced kinetic stability comparable to  $\text{IrO}_2$ . This phenomenon is well known for highly annealed oxides, such as  $\text{Al}_2\text{O}_3$ , being completely acid resistant. As a model for the  $\text{Co}^{2+}$  surrounding tungstate cage, the insolubility of both, tungsten dioxide and tungsten trioxide in water and in acid suggested that the outside framework could render the POM anionic cluster kinetically stable. The Pourbaix diagram of tungsten oxide and related phases confirms that both solids ( $\text{WO}_2$  and  $\text{WO}_3$ ) exist from pH 0 to pH 7.<sup>[129]</sup> But under anodic potential and acidic conditions, even the oxides aggregate and form oligotungstates (e.g.  $\text{W}_{12}\text{O}_{39}^{6-}$  and  $\text{W}_{12}\text{O}_{41}^{10-}$ ) that are partially protonated (dependent on pH) and - more importantly - highly soluble in aqueous media. Morphologically, the structural moieties in the POM cluster are closely related to these soluble structures. This way, the tungstate framework does not protect the catalytic  $\text{Co}^{2+}$  centers, but the opposite is observed. Formation of oligotungstates and tungstic acid might be an additional driving force for POM decomposition rendering the cluster both thermodynamically and kinetically unstable. The intact  $[\text{Co}_9]^{16-}$  anion is the corresponding base for  $\text{H}_{16}[\text{Co}_9]$ , a heteropolytungstatic acid derivative, which does not exist in the fully protonated form due to the acid lability of the anion. Nevertheless, there is a smooth protonation continuum between these two species depending on the of the environment pH. Decomposition takes place along this continuum potentially releasing cluster fragments and tungstate anions before full decomposition takes place. In total, this means that

due to the lack of both thermodynamic and kinetic stability, the POM is not able to withstand the industrially necessary conditions present in a water electrolyzer. This finding cannot only explain processes taking place on the MEA *in situ* but also provides insights into molecular transformations that take place post-electrolysis: Once, protonation of the POM ionic cluster has started and soluble species might have formed, the oxidic framework is labile. Even if the experiment is interrupted before surpassing the critical potential border at 2.0 - 2.2 V, the membrane is still wet and in contact with the surrounding liquid and polymer. The PFSA membrane contains protons and has a high affinity towards metal cations.<sup>[65]</sup> None of these processes is interrupted by stopping the electrochemical experiment, thus the POM cluster decomposition with all the potential driving forces still in place will go on. To differentiate between single molecular transformations, laborious techniques, such as small-angle X-ray scattering (SAXS) could be applied. Since the present work focuses on industrial applicability and providing scalable solutions, this would go beyond the scope of this work.

However, it is not clear yet whether the catalyst is only dissolved with the polyoxometalate oxidic framework still in place. This limitation could be overcome by replacing the counter cation  $Ba^{2+}$  by a more suitable alternative. A second possible reason is that the oxidic framework itself decomposes due to proton formation at the anode side *in situ*. Combined with insufficient kinetic stability of the POM cluster, this could lead to a final decomposition of the oxidic framework. If this second explanation is true, this would be an intrinsic limitation of the POM catalyst, which makes its application on industrial scale very improbable. To look closer into the origin of POM dissolution from the anode, acid stability tests were conducted.

### **POM acid stability**

Although the instability of POM catalyst renders it unsuitable for industrial operation, we examined the dissolution mechanism in more detail. We studied the difference between a pure dissolution of the POM catalyst *in situ* and its structural and molecular decomposition by conducting systematic acid treatments of both  $Ba_5[Co_4]$  and  $Ba_8[Co_9]$ . POMs were treated with sulfuric acid solutions of different pH (6, 5, 4, 3, 2, 1, 0), ultrasonicated and centrifuged. The resulting solutions were analyzed by UV-VIS spectroscopy. If the POM is completely insoluble, no ionic species go into solution and thus no absorption is expected. Results of the acid decomposition study of  $Ba_8[Co_9]$  in the form of UV-VIS spectrograms are summarized in Figure 24a.

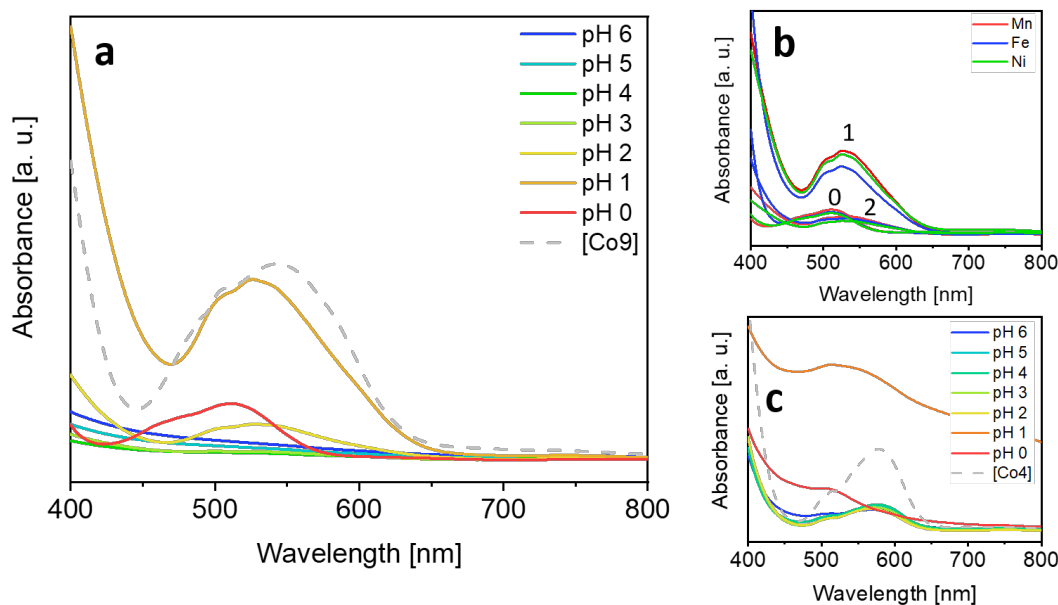


**Figure 24:** UV-VIS acid decomposition study: a)  $\text{Ba}_8[\text{Co}_9]$  after treatment with sulfuric acid of different pH (6, 5, 4, 3, 2, 1, 0); b) Mn, Fe and Ni doped  $\text{Ba}_8[\text{Co}_9]$  after treatment with sulfuric acid of different pH (2, 1, 0) and c)  $\text{Ba}_5[\text{Co}_4]$  after treatment with sulfuric acid of different pH (6, 5, 4, 3, 2, 1, 0).

For pH 6, 5, 4 and 3, there is no absorption maximum visible in the UV-VIS spectrum of acid treated  $\text{Ba}_8[\text{Co}_9]$ . This means that down to this acid concentration, the catalyst does not go into solution and is thus assumed to be stable. From pH 2 to pH 0, absorption maxima prove that the POM catalyst chemically goes into solution. A reference spectrum of  $\text{K}_{2.4}\text{Na}_{13.6}[\text{Co}_9(\text{H}_2\text{O})_6(\text{OH})_3(\text{HPO}_4)_2(\text{PW}_9\text{O}_{34})_3]$  is depicted in a dotted grey curve with the oxidic polyoxometalate framework intact showing an absorption maximum at 543 nm. The observed maxima for pH 2 at 526 nm and pH 1 at 526 nm are shifted towards smaller wavelengths and differ significantly from this reference, leading us to the conclusion that the ionic species in solution are not the same Keggin cluster as  $[\text{Co}_9]$ . We hypothesize that the POM framework known to readily undergo structural changes in solution under different conditions,<sup>[130]</sup> is starting to decompose at pH 2 and pH 1, splitting in smaller POM fragments. Ritorto *et al.* conducted a POM decomposition study in 0.5 M NaCl for a similar, C-shaped and 17-fold negatively charged Co based POM.<sup>[44]</sup> In this study, they found a similar wavelength relation where they could prove a shift towards lower wavelengths with shrinking POM fragment size.

For pH 0, the observed maximum is found at 511 nm, tracing back to free  $\text{Co}^{2+}$  ions in aqueous media,<sup>[61]</sup> meaning a complete decomposition of the heteropolytungstate framework around the cobalt atoms. Reference spectra of  $\text{Co}^{2+}$  ions both as acetate and in a phosphate buffer environment are shown in the Supporting Information. Although an analysis of the used electrolyte the same way did not yield any detectable absorption maximum, the findings of our model study are well in line with literature.<sup>[43]</sup> The stable pH range for  $[\text{Co}_9]^{16-}$  is  $5.5 < \text{pH} < 11$  and that for  $\text{pH} < 1.5$ , dissolution of the polyoxometalate framework is proven. In the same study, the catalytic activity of  $[\text{Co}_9]^{16-}$  is proven to be good at low current densities ( $0.5 \text{ mA/cm}^2$ ). In the present study, there are two components contributing to an acidic environment: First, protons are formed during anodic OER in the cell *in situ*. With increasing current density, the proton concentration in the proximity of active catalyst centers (directly at the POM anion) increases linearly meaning lower „local“ pH values. Although the measurement of such local pH is very difficult, it is commonly agreed, that it varies significantly from the bulk pH. [30] These protons may react with the oxidic POM cluster along the above-described protonation continuum of the heteropolytungstate anion. During the 16 theoretically possible protolysis reactions, the anion is protonated until, below a certain pH, water is formed under release of metal ions ( $\text{Co}^{2+}$ ) as soluble tungstate or phosphate species. Second, protons in the PFSA membrane are loosely bound to the sulfonic acid groups ( $\text{pK}_a \approx -6$ ),<sup>[69]</sup> resulting in a strong acidity of the ionomer solution and the membrane itself in an aqueous environment. Sulfonic acid groups in PFSA quantitatively dissociate in water.<sup>[75]</sup> Due to the high acidity of the sulfonic acid groups, already the membrane in its dry state is acidic: Once in contact with water molecules (e.g. at ambient conditions in air or solvents), it is known that already the first water molecules induce dissociation of the sulfonic acid groups, while the presence of undissociated  $-\text{SO}_2\text{OH}$  cannot be proven.<sup>[76]</sup> Protons (in the form of hydronium ions,  $\text{H}_3\text{O}^+$ ) become mobile and, in combination with the OER protons, contribute to acidic decomposition of the POM framework. The POM catalyst material is thus not stable in close contact to PFSA membranes or ionomers and decomposition already starts before electrolysis and continues after electrolysis on the MEA.

In literature,<sup>[52]</sup> the  $\text{Ba}_8[\text{Co}_9]$  was evaluated stable during „water electrolysis in acidic media“, meaning that sulfuric acid (1.0 M) was used as an electrolyte. „Superior performance to the state-of-the art  $\text{IrO}_2$  in sulfuric acid solution“ was shown with the POM catalyst embedded in a carbon paste electrode with an organic binder. The authors claim that indeed, this type of electrode is not applicable for long-term

experiments due to oxidation susceptibility of the carbon paste (which is also true for the organic binder). But the POM catalyst was not treated directly with acidic solution as we did in the present study. At low current densities ( $> 30 \text{ mA/cm}^2$ ), the hydrophobic CP environment and binder protect the POM catalyst from the acidic electrolyte. But at higher (industrially relevant) current densities ( $> 1000 \text{ mA/cm}^2$ ), where high proton concentrations (and low local pH) arise directly at the catalytic center, neither the CP electrode nor the catalyst itself is stable and remains intact. These conditions come close to a pure POM thrown into acidic solution, which is known to dissolve.<sup>[131]</sup>

To potentially overcome the acid solubility of the  $[\text{Co}_9]^{16-}$  anionic cluster, we tried metal doping by replacing Co with Mn, Fe and Ni. Doped POMs have not only shown an enhanced catalytic activity and selectivity e.g. in the case of isobutane oxidation yielding methacrylic acid.<sup>[54]</sup> On top of that, POM doping is known to increase grid stability.<sup>[44]</sup> As shown in Figure 24b, the same absorption pattern is found for any of the doped materials treated with acid than for the non-doped  $[\text{Co}_9]^{16-}$ . An overview of Co replacement in the respective POM anions, assessed by EA, is shown in Table 6. An exhaustive overview of elemental analysis results can be found in the Supporting Information.

We also investigated the acid stability of  $\text{Ba}_5[\text{Co}_4]$  with the results given in Figure 24c. Contrary to the larger  $[\text{Co}_9]^{16-}$  cluster, there is an absorption maximum visible at each pH. For pH 6 - 3, this maximum is found at 578 nm, matching the intact  $[\text{Co}_4]^{10-}$  reference, which is depicted as a dotted grey line. This means that the Ba salt of  $[\text{Co}_4]^{10-}$  dissolves at any pH but it is only at lower  $\text{pH} \leq 2$  that the oxidic heteropolytungstate framework starts to decompose. Its decomposition proceeds in analogy to the larger  $[\text{Co}_9]^{16-}$  anion, peaking in the release of pure  $\text{Co}^{2+}$  at pH 0.

**Table 6:** Synthesis list including Co replacements by metals, obtained yields and elemental analysis results for metal substituted POMs. Elemental analysis data was normalized to the W content to facilitate comparison.

| <b>Co replacements by M</b> | <b>Replacement / %</b> | <b>Yield / %</b>                                   | <b>Elemental analysis Co / M ratio</b>                                       | <b>Effective Co substitution / %</b> |
|-----------------------------|------------------------|--|--|--------------------------------------|
| -                           | 0                      | 31 [Co9] <sup>16-</sup><br>48 [Co4] <sup>10-</sup> | 8.6/ - [Co9] <sup>16-</sup><br>4.2/ - [Co4] <sup>10-</sup>                   | 0<br>0                               |
| Mn                          | 15                     | 18 [Co9] <sup>16-</sup><br>48 [Co4] <sup>10-</sup> | 7.2/ 0.5 [Co9] <sup>16-</sup><br>3.7/ 0.4 [Co4] <sup>10-</sup>               | 5.8<br>9.5                           |
| Fe                          | 15                     | 35 [Co9] <sup>16-</sup><br>40 [Co4] <sup>10-</sup> | 7.8/ 0.4 [Co9] <sup>16-</sup><br>3.9/ 0.3 [Co4] <sup>10-</sup>               | 4.6<br>7.1                           |
| Ni                          | 15                     | 28 [Co9] <sup>16-</sup><br>46 [Co4] <sup>10-</sup> | 7.1/ 1.5 [Co9] <sup>16-</sup><br>3.7/ 0.5 [Co4] <sup>10-</sup>               | 17<br>12                             |
| Mn, Fe, Ni                  | 30,30,30               | 25 [Co9] <sup>16-</sup><br>19 [Co4] <sup>10-</sup> | 3.2/2.0/1.1/0.9 [Co9] <sup>16-</sup><br>2.1/1.2/0.5/0.3 [Co4] <sup>10-</sup> | 47<br>48                             |

In each case, a solid precipitate remained insoluble, which was separated from the mother liquor and analyzed by XRD. The results are shown in Figure 25. For pH 0 and pH 1, the precipitate was found to be pure BaSO<sub>4</sub>, as proven by XRD, while for pH 2 the main reflections at 8.85, 9.64, 10.2 and 14.5° 2 $\Theta$  can be traced back to an intact POM framework. This supports our hypothesis of starting but incomplete decomposition at pH 2 for [Co9]<sup>16-</sup>. Additionally, the low solubility of BaSO<sub>4</sub> may further inhibit cell performance during operation. As soon as the POM negatively charged framework is protonated during electrolysis, Ba<sup>2+</sup> cations may form stable and insoluble complexes with sulfonic acid groups in the PFSA polymer membrane. This may cause irreversible transport channel blocking and lead to the formation barite-like structures in analogy to known plastering effects in the case of Ca<sub>2</sub><sup>+</sup>.<sup>[65]</sup> Since the low solubility of might well be a driving force for the dissolution of the POM salt and thus enable its decomposition in acidic media, the same acidity studies were performed with hydrochloric acid (HCl(aq)) as a control experiment yielding the same decomposition patterns at equal pH steps. The removed solvent containing

POM fragments was evaporated and the crystalline residuals were also analyzed by XRD. The diffractograms do not match any of the POM reference diffractograms. We conclude that due to the POM decomposition, mixtures of different salts are present in the solution, leading to complex diffractograms that cannot be evaluated exhaustively.

With this final experiment, we could prove the acid fragility of both, the  $[\text{Co}_4]^{10-}$  and the  $[\text{Co}_9]^{16-}$  cluster. If incorporated into a carbon paste, decomposition is slowed down but still takes place within minutes. The carbon has thus a slightly protective function but cannot fully prevent decomposition. Comparable cases can hardly be found in literature, but it was shown by Goberna-Ferrón *et al.* that a manganese analogue of the  $[\text{Co}_4]^{10-}$  catalyst, applied in its soluble form in homogenous catalysis, is not stable during OER. Reaction conditions were close to the ones in this study (10 – 50 mA, not normalized to the electrode area) and catalyst decomposition was proven after 30 min at 1.4 V applied anodic potential vs. NHE. This means 600 mV overpotential in a pH 7 buffered sodium phosphate electrolyte. The authors traced the decrease in catalytic activity back to the formation of a manganese oxide passivation layer on the electrode.<sup>[45]</sup> In the present case, we could show that the POM partially dissolves at pH around 2 with the cluster starting to fracture. Lowering the pH leads to an increasing decomposition, peaking in the release of pure  $\text{Co}^{2+}$  at pH 0.

### 2.1.5. Conclusion

Electrocatalysts need to be earth-abundant, cheap and accessible to promote scalability of electrolysis techniques as required by the global energy transition. Especially catalysts for oxygen evolution need to fulfil additional stability criteria under extremely acidic and corrosive conditions at industrially relevant current densities ( $\geq 1000 \text{ mA/cm}^2$ ) during OER. We investigated the barium-stabilized cobalt polyoxometalate  $\text{Ba}_8[\text{Co}_9(\text{H}_2\text{O})_6(\text{OH})_3(\text{HPO}_4)_2(\text{PW}_9\text{O}_{34})_3]$  ( $\text{Ba}_8[\text{Co}_9]$ ), which was proven to be very active in OER at low current densities,<sup>[52]</sup> towards its scalability and suitability to replace the state-of-the-art catalyst for OER Ir (as  $\text{IrO}_2$ ). Although thermodynamically unstable, the oxidic tungstate framework protecting the cobalt active centers made us hope for sufficient kinetic stability. After extensive material characterization (EA, TGA, BET, SEM, XRD, temperature stability investigations) we could integrate the catalyst into a MEA setup. Upon electrochemical characterization in different paste formulations, the catalyst was only able to achieve low current



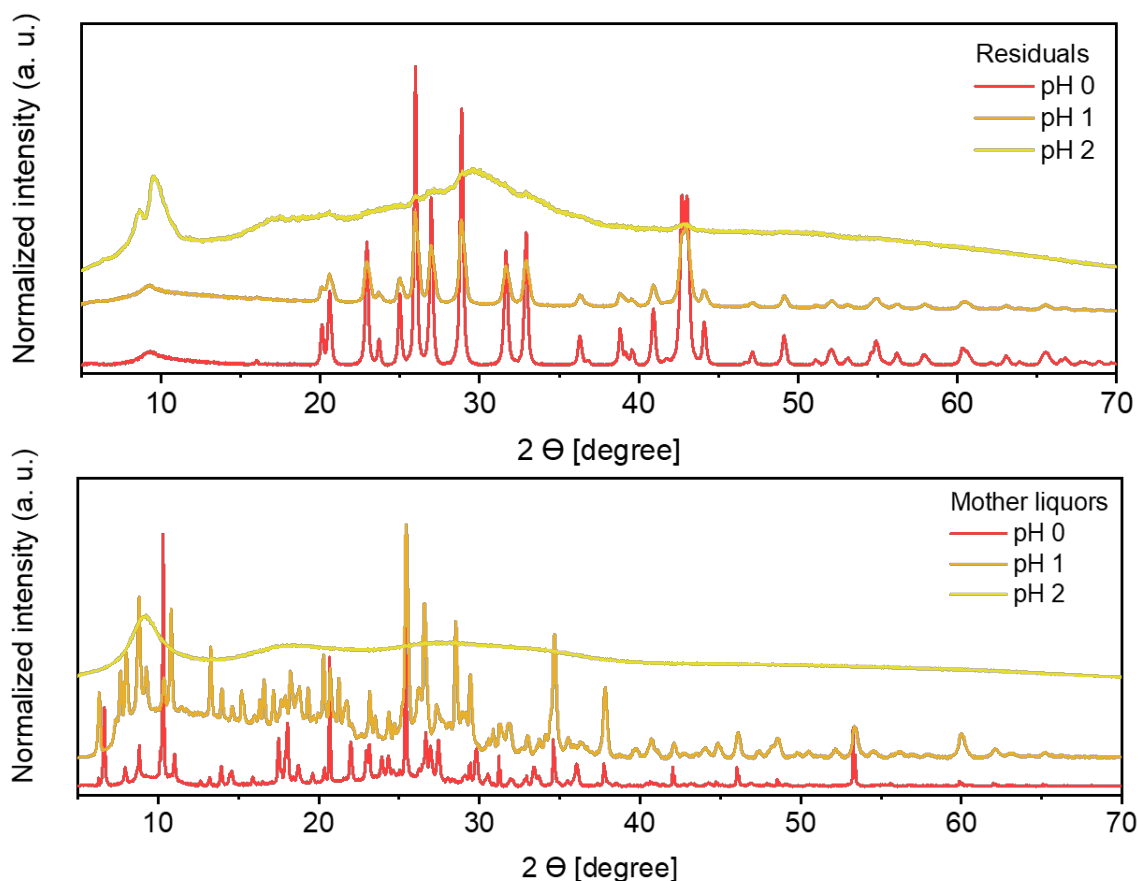


**Figure 25:** POM XRD studies after acid treatment. Above: Diffractograms from solid residuals. Below: Diffractograms from evaporated acidic mother liquors.

densities while the achieved results were poorly reproducible. We could show that the  $[\text{Co}_9]^{16-}$  cluster does not withstand the highly acidic conditions at anodic potential *in situ* during OER. Tungstic phase Pourbaix diagrams made us argue that the tungstate framework does not behave like stable  $\text{WO}_2$  or  $\text{WO}_3$  but instead form highly soluble, negatively charged oligotungstate moieties. Due to the chemical similarity of the framework to these polyanions, forming oligotungstates might even be the driving force for POM decomposition besides the formation of water.

We pointed out the relevant criteria that need to be fulfilled for industrial applicability of an OER catalysts and the most prominent challenges. Since the POM catalyst is still very promising due to its activity and speed in OER,<sup>[52]</sup> the knowledge obtained in this study could be used to integrate it into a modified setup in future studies: for example, replacing the PFSA CEM by an anion exchange membrane (AEM) would reverse the direction of electrodiffusion. Water is reduced at the cathode side re-

leasing hydroxyl anions ( $\text{OH}^-$ ), which then migrate over the AEM material to the cathode side. POM being an extraordinarily quick and effective oxidation catalyst could oxidize these  $\text{OH}^-$  while contact to acidic environment is suppressed. This way, advantages of both, POM catalysts and AEM-PEM could be combined towards green and scalable water electrolysis.

## 2.2. Morphological tuning of membrane processing by temporal proton-metal cation substitution in perfluorosulfonic acid membranes

### 2.2.1. Publication summary

In PEM water electrolysis for sustainable hydrogen production, perfluorosulfonic acid (PFSA) membranes are an important tool to ensure unidirectional ionic flow between both half-cells. When coated with catalyst material, such as platinum (Pt) or iridium (Ir), which is integrated into the upmost polymer layer of the membrane, the resulting building part is called membrane electrode assembly (MEA), building the core of an electrolyzer. The membrane polymer consists of a perfluorinated backbone and double-ether perfluorinated side chains, terminating with a sulfonic acid groups. Weak proton-sulfonate interactions (approx. 20 kJ/mol for  $\text{H}_3\text{O}^+ - \text{O}$ )<sup>[80]</sup> enable the membrane to selectively conduct protons or different cations while anionic transport is blocked. For processing and MEA preparation, the PFSA is usually provided in its protonated form. Within this paper, membrane modification in the form of proton-metal cation exchange is investigated towards changes in the resulting viscoelastic properties. Additionally, a phenomenon called potential-driven substitution is discovered, enabling a quantitative back-exchange of  $\text{Li}^+$  driven by  $\text{H}^+$  *in situ*.

Cation-exchanged membranes were prepared ( $\text{Li}^+$ ,  $\text{Na}^+$ ,  $\text{K}^+$ ,  $\text{Mg}^{2+}$ ,  $\text{Zn}^{2+}$ ,  $\text{Ca}^{2+}$ , tetramethyl ammonium [ $\text{TMA}^+$ ] tetrabutyl ammonium [ $\text{TBA}^+$ ]) and we observed that their glass transition temperatures ( $T_g$ ) correlated well with the processability in an industrial MEA fabrication *via* decal transfer. Based on the binding energies of the respective metal cation, we determined membrane resistances through impedance spectroscopy and differentiated between initial and permanent effects, the latter arising from heat-induced, stable structural arrangements of the polymer side chains. *In-situ* potential-driven substitution (PDS) of the metal ions by protons was quantified (1.5 A/cm<sup>2</sup>, rate = 0.2 mmol/cm<sup>2</sup> per minute). However, morphological changes in the membrane remained and we identified the possibility for morphological tuning of membrane fabrication by temporal proton-metal cation substitution.

As the first author of this paper I developed the idea behind the work, designed the concept and conducted the experimental work including material analysis. Additionally, I modified PFSA membranes and conducted the analysis of their viscoelastic properties *via* DMA and their electrochemical behavior *via* potentiodynamic cy-

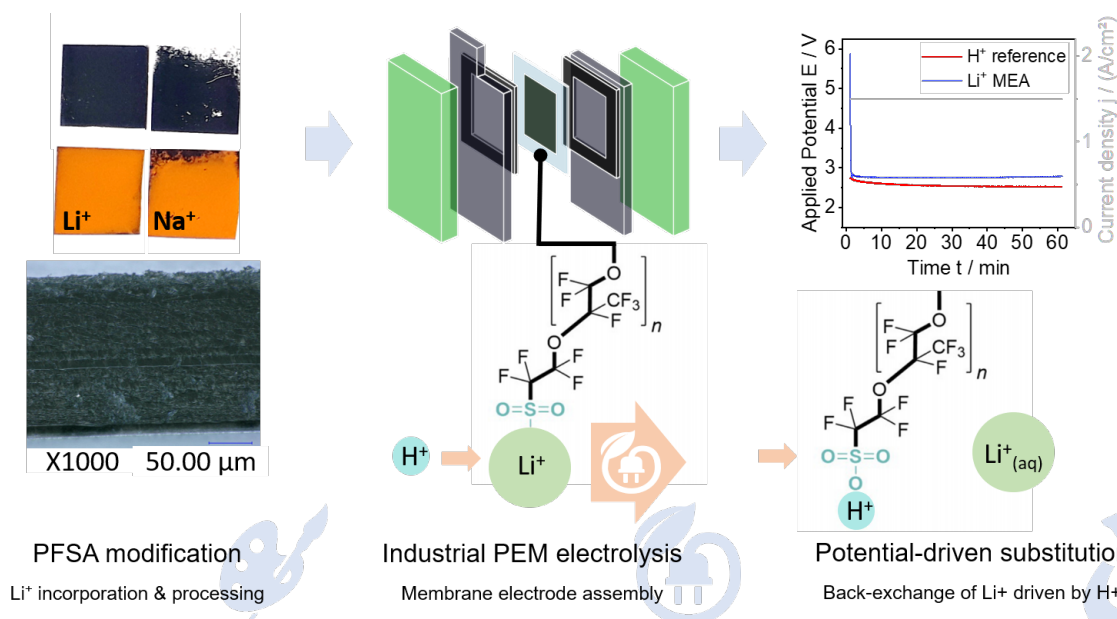


**Figure 26:** Graphical abstract of the work conducted in the second chapter including membrane modification, electrochemical analysis and potential-driven substitution *in situ*.

clovoltammetry and galvanostatic current density steps. I assessed membrane resistance information *via* impedance spectroscopy, analyzed all obtained data and wrote the manuscript. The work was rounded up by contributions of fellow researchers, namely Thomas Reichbauer, who helped with the design of experiments and choice of resources, Nemanja Martić, who helped with the paper concept and David Reinisch, who introduced me to the technique of impedance spectroscopy and helped to obtain the data. Prof. Olaf Hinrichsen provided support in writing and reviewing as well as financial sources and Dr. Günter Schmid contributed to the concept and supervised the work.

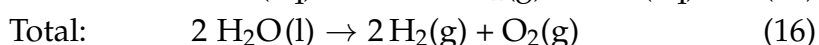
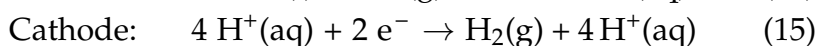
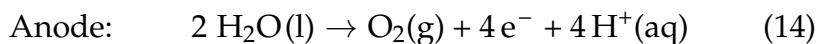
**Bibliographical data** Kim-Marie Vetter, Thomas Reichbauer, Nemanja Martić, David Reinisch, Olaf Hinrichsen, Günter Schmid, Morphological tuning of membrane processing by temporal proton-metal cation substitution in perfluorosulfonic acid membranes, *Electrochimica Acta*, Volume 362, 2020, 137182, ISSN 0013-4686, <https://doi.org/10.1016/j.electacta.2020.137182>.

Reprinted with permission from Elsevier Ltd., Amsterdam. Copyright 2020

### 2.2.2. Introduction

In the context of the global Energiewende, hydrogen is widely seen as one of the key energy carriers and a core of future sustainable technologies.<sup>[11]</sup> It can play a major role in decarbonizing sectors such as transportation, building heat and power and industrial energy use towards a so called „hydrogen economy“. A promising technology for the production of green hydrogen is the field of proton exchange membrane (PEM) electrolysis, providing advantages such as dynamic operation and high voltage efficiency.<sup>[5]</sup>

Perfluorosulfonic acid (PFSA) membranes are state of the art cation exchange devices in PEM electrolysis exhibiting advanced cation transport properties as well as physical and mechanical stability.<sup>[5]</sup> These properties are crucial for large-scale fabrication of membrane electrode assemblies (MEA), building the core of the PEM electrolyzer. In most electrolysis and fuel cell applications, PFSA membranes are used in the protonated form, where cation conductivity with an optimum at 55 – 65 °C and the transport capacity are crucial operation parameters.<sup>[82]</sup> In water electrolysis applications, water oxidation takes place at the anode side of the cell, releasing molecular oxygen as the gaseous product and solvated protons (equation 14). This process is called oxygen evolution reaction (OER). The protons migrate to the cathode, where they are reduced to molecular hydrogen as shown in equation 15.



In the case of fuel cells, this redox reaction is reversed.<sup>[5,93]</sup> Cations different from protons can enter the membrane during or before operation and displace protons due to stronger coordinating interactions with the sulfonate groups.<sup>[62]</sup> This ion exchange within the membrane is an important lever in membrane processing, because it directly influences its mechanical and physical properties as shown by Moore *et al.*<sup>[93]</sup> and Wilson *et al.*<sup>[62]</sup> We build up on this available knowledge, largely extend the scope use our insights for membrane modifications towards industrialization of green technologies. As such, membrane modifications can potentially be exploited in the MEA area scale-up, because it provides a thermal degree of freedom during

MEA production involving thermal treatment under pressure in a so-called decal process. PFSA is prone to losing the sulfonate groups first during thermal decomposition, beginning at approx. 300 °C, and it is known that saturating the polymer with K<sup>+</sup> ions prevents the C-S-cleavage thus rendering the polymer more stable.<sup>[98]</sup> The temperature required for initiating a throughout movement of the polymer is called  $\alpha$ -relaxation and has been associated with the glass transition temperature ( $T_g$ ) for a long time.<sup>[84,85]</sup> Although there was some controversy about the genuine  $T_g$  of PFSA,<sup>[62]</sup> we will stick to the traditional definition, since a holistic movement of all polymer chain parts is required for successful membrane processing. Shifting this temperature by cation exchange will alter the PFSA membrane properties. Various studies have investigated cation exchange effects on water uptake and capacity,<sup>[92]</sup> thermal behavior<sup>[63,86,87,90,98]</sup> and crystallinity<sup>[121]</sup> of the membranes. Cations with different valence (+I, +II, +III)<sup>[95]</sup> and of different nature (metal vs. alkylammonium cations)<sup>[62]</sup> were investigated in competing cation mixtures<sup>[112]</sup> and to different degrees of exchange.<sup>[97]</sup> The ionic uptake was studied both practically and theoretically with mixtures of bivalent and monovalent ions,<sup>[99]</sup> and salt partitioning has been investigated in a theoretical study.<sup>[100]</sup> A work on PFSA cation-exchanged thin films investigated to which extent are protons displaced by competing ions,<sup>[92]</sup> others focus on the effect the exchange has on the cation mobility activation energy and the thermal stability,<sup>[90]</sup> tensile and fracture resistivity,<sup>[101,103]</sup> and even the capability of cation conductivity.<sup>[97]</sup> In addition to studies of different membrane types (Flemion<sup>®</sup> vs. Nafion<sup>®</sup>),<sup>[103]</sup> theoretical simulations have also been performed, highlighting the poisoning effect of cation exchange in polymer electrolyte membrane (PEM) fuel cells.<sup>[122]</sup>

This short literature review shows the interest in cation exchanged PFSA membranes that are sometimes considered as polluted or contaminated.<sup>[89,91,97,119,122]</sup> Unlike this rather negative interpretation, other groups highlight the positive impact of an ion exchange on the membranes' properties.<sup>[63,98,112]</sup> In our work, we will build the bridge between increased polymer stability and processability because there are hardly any reports focusing on this latter aspect in a MEA production process although the importance of thermal parameters to MEA preparation is well known.<sup>[132]</sup> Additionally, the proton-metal substitution cannot be assumed to be permanent, but so far, also electrochemical characteristics of cation exchanged MEAs are rarely investigated.<sup>[122]</sup> In the context of the *Energiewende* and sustainable power sources, the scalability of MEA production is an important factor for industrial applications<sup>[64]</sup> and the potential scale up of green technologies such as water

electrolysis for hydrogen production.<sup>[11]</sup> Subsequently, a good electrochemical performance at industrially relevant current densities ( $> 1 \text{ A/cm}^2$ ) is the purpose of any commercially applied MEA.<sup>[11]</sup>

The aim of this study is to exploit the effects of countercation exchange in PFSA as a lever for membrane processability. Initial effects induced by the metal ions binding to the sulfonate groups will be differentiated from permanent morphological changes. To address these two aspects, cyclic voltammetry (CV) as well as potentiostatic and galvanostatic investigations were performed. The latter ones were used to fathom whether the different cations were re-substituted by protons from the water oxidation at the anode side during electrolysis. We call this phenomenon *in-situ* potential-driven substitution (PDS). Finally, the rate and extent of back-exchange were determined in galvanostatic operation mode at  $1.5 \text{ A/cm}^2$ . As exchange ions we employed a broad variety of commonly used cations, such as:  $\text{Li}^+$ ,  $\text{Na}^+$ ,  $\text{K}^+$ ,  $\text{Mg}^{2+}$ ,  $\text{Zn}^{2+}$ ,  $\text{Ca}^{2+}$ , tetramethyl ammonium [ $\text{TMA}^+$ ] and tetrabutyl ammonium [ $\text{TBA}^+$ ]. Assessment of the glass transition temperature ( $T_g$ ), limitations in membrane processability as well as the quantitative reversibility of cation exchange in PFSA-based MEAs upon electrochemical characterization will be shown. This transfer of scientific knowledge to scalable processes and exploitation of ion exchange effects in PFSA considering industrial needs is an important step towards green and sustainable technologies for energy conversion and storage.

### 2.2.3. Experimental

#### Membrane preparation

PFSA Membranes used in this study were provided as Nafion<sup>TM</sup> N117 by Chemours. Prior to use they were immersed in a freshly prepared half-concentrated peroxy-monosulfuric acid solution overnight, washed with water, stirred in another portion of water for 60 min and finally dried at  $70 \text{ }^\circ\text{C}$  for 15 min. The water used during membrane preparation was Type 1 ultrapure water purified using the Milli-Q<sup>®</sup> Integral water purification system ( $18 \text{ M}\Omega\cdot\text{cm}$ ).

#### Membrane countercation exchange

2 M solutions from each metal or alkylammonium chloride were prepared using ultrapure water. Salts used in this study are listed in Table 7 including suppliers and purities.

**Table 7:** Suppliers and purities of metal or alkylammonium ( $M^{n+}$ ) salts used for PFSA counter-cation exchange.  $\text{pH}_{\text{start}}$  and  $\text{pH}_{\text{end}}$  indicate pH values of a 2 M solution of the salt before and after immersing the PFSA membrane for 24 h.

| Salt                                   | Supplier          | Purity / %  | $\text{pH}_{\text{start}}$ | $\text{pH}_{\text{end}}$ |
|--|-------------------|-------------|----------------------------|--------------------------|
| LiCl                                   | Fluka Analytical  | $\geq 98.0$ | 4.0                        | 1.0                      |
| NaCl                                   | J. T. Baker       | $\geq 99.5$ | 4.0                        | 1.0                      |
| KCl                                    | Merck             | $\geq 99.5$ | 4.0                        | 1.0                      |
| MgCl <sub>2</sub>                      | Magnesia Lüneburg | $\geq 97.0$ | 8.0                        | 1.0                      |
| ZnCl <sub>2</sub>                      | Fluka Chemika     | $\geq 98.0$ | 3.5                        | 1.0                      |
| CaCl <sub>2</sub> · 2 H <sub>2</sub> O | Merck             | $\geq 99.5$ | 3.0                        | 1.0                      |
| TMACl                                  | Fluka Chemika     | $\geq 98.0$ | 6.0                        | 2.5                      |
| TBACl                                  | Fluka Chemika     | $\geq 99.0$ | 6.0                        | 3.0                      |

The saturated cation-exchanged ( $M^{n+}$ -exchanged) membranes were prepared by immersing membrane pieces of 12 cm<sup>2</sup> in 12 mL of a 2 M  $MCl_n$  solutions for 24 h, which is enough to reach equilibrium.<sup>[98]</sup> To make sure that each mobile proton in the PFSA could be replaced by the respective metal ion, an excess of metal chloride was used. Considering the equivalent weight of Nafion<sup>®</sup> (EW = 1100 g PFSA per mole of sulfonic acid residue), the amount of salt present in the immersion solution equals approx. 50-fold the amount of sulfonic acid residues in the membrane samples. The mother liquor was removed, the ion exchanged membranes were then washed with ultrapure water followed by stirring in another portion of ultrapure water for 30 min and finally dried at 70 °C for 15 min.

The pH change before and after immersing the membrane was recorded (see Table 7) reaching a lower end value of down to  $\text{pH} = 1$  for metal ion solutions due to the displaced protons being released into the solution upon substitution. This matches the expectation pH value of  $\text{pH} \approx 1.2$  calculated from the number of protons in the membrane. The same expectation value is true for all cations, irrespective of their nature, assuming a quantitative exchange.<sup>[92]</sup> In the case of the amino-based organic cations, the exchange was incomplete, since pH values remained above the  $\text{pH} = 1.2$  mark. In a control experiment, an ion exchanged membrane for each ion was immersed in a fresh 2 M solution, which in all cases maintained the original pH,



proving that equilibrium was reached for each sample already in the first immersion step.

### Membrane characterization

In order to investigate thermal and mechanical properties of the cation-exchanged membranes, we employed two different characterization techniques. Differential scanning calorimetry (DSC) measurements were performed with a Netzsch DSC 204 F1 Phoenix device using 14–16 mg squared membrane samples from different membrane spots in an inert aluminum pan with pierced lid. As a reference, an identical but empty aluminum pan with pierced lid was measured along with each sample. Measurements were performed in an N<sub>2</sub> atmosphere with 20.0 mL/min and 70.0 mL/min gas flows applying a dynamic temperature mode from 25 °C to 250 °C with a ramp of 10 °C/min. The temperature program was repeated twice for each sample.

Dynamic mechanical analysis (DMA) measurements were performed with a Netzsch DMA 242 E device and an additional DMA 242 C controller with TASC 414/4 controller. Samples with a thickness of 170 μm were cut to rectangular shape, sized 12 mm × 3.4 mm, and installed in the tension sample holder. The torque applied to the clamping screws was 1.5 cN\*m. Samples were analyzed in the tensile mode under N<sub>2</sub> flow (150 mL/min) with no preloaded force and a maximum force of 3.0 N. A sinusoidal amplitude of 40 μm was applied at 1.0 Hz during a heating of 3 °C/min from 30 °C to 250 °C. The extensional storage modulus (E'), extensional loss modulus (E'') and the loss factor  $\tan \delta = (E''/E')$  were recorded as a function of temperature or time.

### MEA production and microscopy

For MEA fabrication commercial Pt (for cathode) and Ir (for anode) nanopowders provided by Umicore were used. The catalyst powders were suspended in methanol,<sup>[98]</sup> the suspension was doctor bladed onto polyimide foil (Kapton<sup>®</sup>) and the resulting supported electrode was dried at 80 °C for 30 min. In a decal process the Kapton<sup>®</sup>-supported electrodes (cut to 5 cm<sup>2</sup> squares), were heat transferred onto the PFSA membrane by pressing a cathode-membrane-anode sandwich with 2.5 Nm at 225 °C for 60 seconds. The Kapton<sup>®</sup> squares were weighted before and after the decal process, leading to a constant catalyst loading of 2.0 mg/cm<sup>2</sup> to ensure complete catalyst transfer from the Kapton<sup>®</sup> support to the membrane.

For microscopy pictures, Pt half-MEAs were cut and their cross sections were investigated using a Keyence VHX-6000 digital microscope with a magnification of 1000 diameters.

## Electrochemical MEA characterization

### *Electrolysis setup*

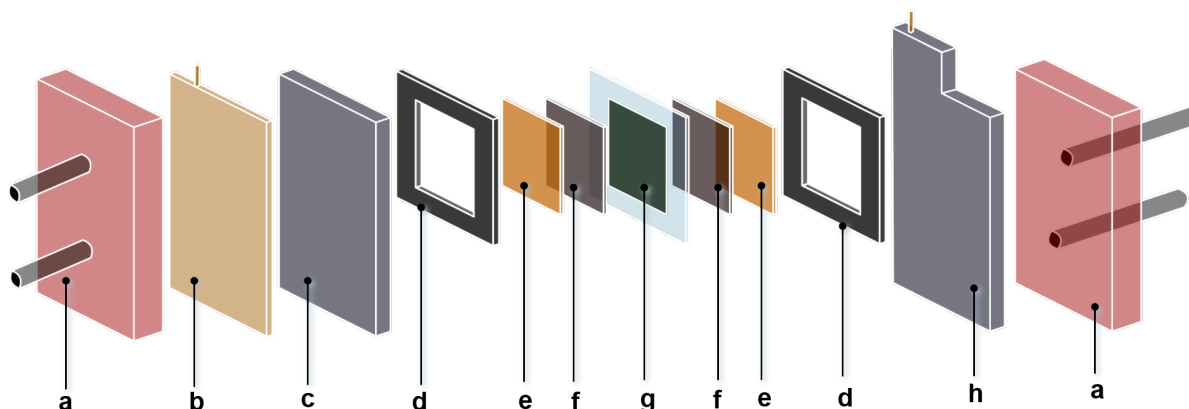


**Figure 27:** Installation for water electrolysis used in this study for electrochemical performance determination. The cathode side is shown on the left, the anode side is shown on the right. The setup is composed of two end plates (a), a current collector (b), a graphite (c) and a titanium (h) flow field, EPDM sealings (d), titanium grids with different mesh widths (e, f) and the MEA in the middle (g).

Electrochemical characterization was performed in a water electrolysis cell adapted from a fuel cell kit provided by Scribner Associates Inc. A schematic of the setup is shown in Figure 27. The original anode graphite serpentine flow field (Figure 27c), was replaced by an analogous titanium component (Figure 27h), also provided by Scribner Associates Inc. The cell is composed of an end plate with flexible tubes for water circulation (Figure 27a), a gold plated copper current collector (b), the graphene serpentine flow field (c), an ethylene propylene diene monomer rubber (EPDM) sealing (d), a wide-meshed and a subsequent fine-meshed titanium grid (thicknesses 0.40 mm and 0.35 mm, respectively, (e) and (f)) and finally the MEA in the middle of the device (g). For the anode side, this order is mirrored replacing the graphite flow field and the current collector by the titanium component.

For electrochemical measurements, this installation is hooked up to a Methrom PG-STAT302N potentiostat and a 10 A booster, both provided by Deutsche Metrohm GmbH & Co. KG. Combining the 10 A booster with a 5 cm<sup>2</sup> electrode area leads to a current compliance of 2.0 A/cm<sup>2</sup> being the maximum achievable value in this

study. For all measurements, freshly prepared cation exchanged MEAs were used. Ultrapure water was pumped separately for both anode and cathode side with a flow of 120 mL/min by a membrane pump.

#### *Peak performance determination via cyclic voltammetry (CV)*

Two types of electrochemical measurements were performed: first, potentiodynamic cyclovoltammetry (CV) for assessing the peak performance of the MEA and secondly, potentiostatic and galvanostatic experiments to evaluate the *in-situ* potential-driven substitution of metal ions by protons originating from the anodic OER. For cyclovoltammetry purposes, the ultrapure water electrolyte was cycled. The measurement method consisted of potentiodynamic CVs with different scanning rates (1 mV/s; 10 mV/s; 100 mV/s) and a minimum and maximum potential of 1.4 V and 3.5 V, respectively. After two CVs at low scanning rate (1 mV/s), a faster one was repeated five times (10 mV/s) and a superfast one (100 mV/s) was conducted once. Afterwards, the 10 mV/s CV was repeated until the obtained polarization curve was constantly reproduced, but 80 times at maximum. If the current compliance of 2.0 A/cm<sup>2</sup> was reached at lower potentials than the maximum applied potential of 3.5 V, the CV direction was reversed.

#### *Impedance spectroscopy*

Membrane resistances were measured using galvanostatic impedance spectroscopy on a Methrom PGSTAT302N potentiostat with FRA32M unit and a 10 A booster, both provided by Deutsche Metrohm GmbH & Co. KG. MEAs were prepared from freshly ion-exchanged membranes as described above. For Li<sup>+</sup> and Zn<sup>2+</sup> MEAs, a 0.25 M solution of the respective metal ion chloride was used as electrolyte. Impedance was measured at constant current densities (2 mA/cm<sup>2</sup>, 10 mA/cm<sup>2</sup>, 20 mA/cm<sup>2</sup>, 200 mA/cm<sup>arg</sup>) after reaching steady state at the respective current density.

#### *Potential-driven substitution (PDS) of metal ions in potentiostatic and galvanostatic measurements*

The *in-situ* potential-driven substitution (PDS) of metal ions by OER protons was investigated by potentiostatic experiments. Ultrapure water was used in a single pass flow mode. MEAs were subjected to a low, constant potential of 2.0 V first and the current density was recorded as a function of time. After reaching steady state, the potential was raised in 200 mV steps and held for 10 min at each step. Finally, at a potential of 3.5 V, the potential was held until no more change in current density occurred or until the maximum of 2.0 A/cm<sup>2</sup> was reached. If the latter was the

case, the potential was downregulated by 200 mV and held again. Afterwards, a CV between 1.4 and 3.5 V with a scan rate of 10 mV/s, which is identical to the ones described earlier, was performed and compared to initial CV in the potentiodynamic CV measurement series.

To quantify the PDS of metal ions by protons stemming from the anodic OER, a galvanostatic experiment was performed on a Li<sup>+</sup> exchanged MEA applying a constant current density of 1.5 A/cm<sup>2</sup> and recording the potential as a function of time. The rate of PDS was calculated from the potential drop at the beginning of the experiment. Calculations in detail can be found in the Supporting Information.

#### 2.2.4. Results and discussion

A cheap and easy way to alter physical and mechanical characteristics of the membrane is to exchange the highly acidic proton, which complements each sulfonate group at the end of the polymer side chains. Figure 28a shows the molecular structure of PFSA with both, the perfluorinated polymer backbone and the more mobile side chains bearing protonated sulfonate groups. Earlier studies have shown that ion concentration in an aqueous environment is decisive for the uptake of a competing cation into a PFSA membrane. Depending on the cation's binding strength to the sulfonate group, every single contact of the membrane with a cation may lead to a proton displacement, incorporating this ion into the membrane.<sup>[91]</sup> The strength of interaction between the sulfonate anion and the respective cation varies for different ion types and valences. Also, different ions might cause different morphologies within the membrane due to the coordinative behavior of the sulfonate groups to the metal ion. It is important to notice that already for the commonly used acid form of PFSA, there is a wide range of morphological studies. The polymers' complex morphological nature is most often studied by small-angle X-ray scattering (SAXS) to reveal molecular arrangements and gather insights about thermomechanical properties.<sup>[106]</sup> Although many aspects still remain unclear, the ionic sulfonic acid groups are known to form clusters that are distributed among the non-polar PTFE-like environment.<sup>[85]</sup> As such, PFSA forms micellar aggregates in an aqueous solution,<sup>[107]</sup> whereas alkaline and earth alkaline metals can induce symmetrical and thermodynamically stable layer arrangements in sulfonate complexes.<sup>[108]</sup> In polymer electrolyte research, especially lithium is known to form stable but highly ion conducting sulfonic acid complexes, covalently attached to a polymeric backbone.<sup>[109]</sup> This complex formation is the reason for different behaviors of protonated

vs. lithiated ion exchange polymers. In this study, a broad variety of ions was comparatively studied towards their influences on membrane processing. In Figure 28b the cations used for ion exchange in this study are depicted without hydration shell true to scale according to their respective effective (metals and proton) or crystallographic (alkylammonium salts) ionic radii.<sup>[72,73]</sup> Table 28 also shows a list of the used ions including ionic radii<sup>[72,73]</sup> and  $T_g$  literature data (where available)<sup>[62,86,121]</sup> as well as the data assessed in this present study.

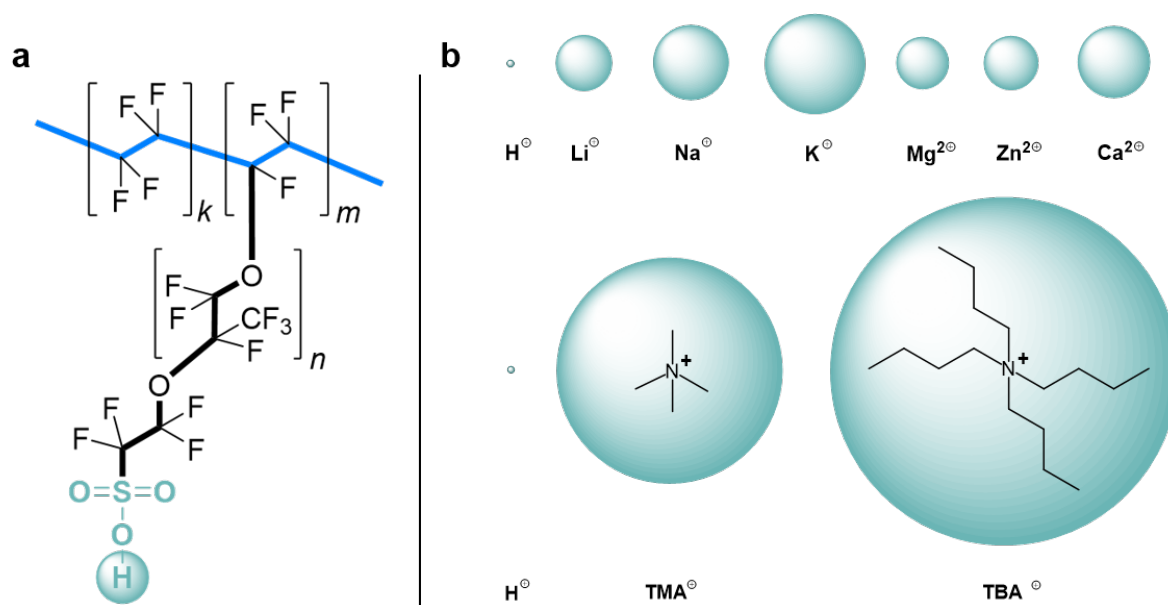


**Figure 28:** (a) Illustration of the molecular structure of perfluorinated sulfonic acid (PFSA) with the polymer backbone highlighted in bold blue and the side chain indicated in bold black. The sulfonic acid group bearing the mobile proton is depicted in light turquoise; (b) Size comparison of the cations investigated herein. The illustration is true to scale in accordance with the ionic radii listed in Table 8. Since theoretical, negative values of the effective ionic radius of a proton cannot be illustrated, it is depicted with an assumed ionic radius of 10 pm.

Provided that replacing PFSA protons by different metal ions will cause altered morphologies in the polymer structure of the membrane, ion exchange might serve as a valuable tool for adapting the physical and mechanical properties of the membrane. Therefore, stability and processability considerations during the MEA production process represent the first part of this paper. The MEAs' industrial applicability and electrochemical characterization are addressed in the second part of this study. Upon application of a potential *in situ*, metal ions present in the MEA will migrate from the anode to the cathode side and thereby be replaced by protons originating from the anodic OER. Due to the high solvation energy of the protons and the resulting high acidity of the sulfonic acid groups in the PFSA polymer, the ion exchange capacity

of a MEA in the protonated form is very high. In contrast, metal ions have a higher binding energy to the sulfonate groups and the binding is of coordinative character, resulting in reduced chain mobility due to more stable morphologies. Metal ions in the membrane could reversibly and/or irreversibly block some of the cation transport channels and therefore reduce the cation transport capacity. This would then be visible in a reduced electrochemical performance. Therefore, a quick and quantitative *in-situ* potential-driven substitution (PDS) of the metal ions is highly desirable.

**Table 8:** List of cations used for counterion exchange in PFSA membranes in this study including effective ionic radii of metal cations<sup>[72]</sup> and the proton<sup>[72]</sup> and crystallographic radii for alkylammonium salts<sup>[73]</sup> as well as literature data for  $T_g$  (where available)<sup>[62,86,121]</sup> and  $T_g$  assessed by DMA in this study.

| Ion              | Ionic radius<br>/ pm | Literature $T_g$<br>/ °C | Found $T_g$<br>°C |
|------------------|----------------------|--------------------------|-------------------|
| H <sup>+</sup>   | -18 <sup>[76]</sup>  | 100 <sup>[44,50]</sup>   | 96                |
| Li <sup>+</sup>  | 76 <sup>[76]</sup>   | -                        | 201               |
| Na <sup>+</sup>  | 102 <sup>[76]</sup>  | 240 <sup>[43]</sup>      | 226               |
| K <sup>+</sup>   | 138 <sup>[76]</sup>  | -                        | 243               |
| Mg <sup>2+</sup> | 72 <sup>[76]</sup>   | -                        | -                 |
| Zn <sup>2+</sup> | 74 <sup>[76]</sup>   | -                        | 216               |
| Ca <sup>2+</sup> | 100 <sup>[76]</sup>  | -                        | 100               |
| TMA <sup>+</sup> | 347 <sup>[131]</sup> | 240 <sup>[43]</sup>      | 231               |
| TBA <sup>+</sup> | 494 <sup>[131]</sup> | 100 <sup>[43]</sup>      | 82                |

### Influence of ion exchange on the membrane's viscoelastic properties and processability

MEAs are produced *via* heat-pressing supported catalyst layers onto a membrane, a process called decal process.<sup>[98]</sup> Keeping the focus on industrial processability of the PFSA membrane on a large scale, the parameter of interest is the glass transition temperature ( $T_g$ ), which must be lower than the decal transfer temperature in order to guarantee complete catalyst transfer onto and even into the upmost layer of the membrane polymer. The catalyst is supposed to be mixed with this upmost polymer

layer during the heat-pressing, which can only be properly performed if the polymer is ductile enough.

#### *T<sub>g</sub> determination by DSC*

DSC measurements performed in this study yielded results and thermograms that were in accordance with known literature data.<sup>[62,121]</sup> Furthermore, performing the temperature program of the DSC measurement twice on a sample confirmed, that this technique is not suitable for comprehensively describing the thermal behavior of the PFSA samples, since determination of T<sub>g</sub> is not possible. It can nevertheless be used for decomposition studies.<sup>[90]</sup> Experimental data and their interpretation can be found in the Supporting Information.

#### *T<sub>g</sub> determination by DMA*

In literature, only Na<sup>+</sup> and alkylammonium ion exchanged PFSA membranes have been analyzed by DMA.<sup>[62]</sup> For the first time, the study on hand provides a systematic comparison of T<sub>g</sub> for ions of different type (organic vs. inorganic), size (67–494 pm) and valence (+I vs. +II). DMA measurements yield information about the viscoelastic properties of a sample when subjected to an oscillating force while temperature is uniformly ramped up. At the glass transition regions of polymers, a significant change in the measured E modulus as well as a maximum in attenuation change is observed in the thermogram. Results obtained for ion exchanged membranes of all ions listed in Table 8 are shown in Figure 29.

The maximum of tan  $\delta$  is found at 96 °C, representing the glass transition temperature. This is in excellent agreement with the available literature data of 100 °C.<sup>[86,121]</sup> Water in a PFSA is known to shift T<sub>g</sub> towards lower values,<sup>[89]</sup> although this method is known to have measurement insecurities of up to 5 K.<sup>[120]</sup>

With increasing ionic radius of the cation, T<sub>g</sub> shifts towards higher temperatures. Compared to the protonated form (green), the T<sub>g</sub> of Li<sup>+</sup> exchanged PFSA is shifted to 201 °C (red) while for Na<sup>+</sup> it is found to be 226 °C (blue) and 243 °C for K<sup>+</sup> (black). This insight significantly broadens the scope of earlier literature data, that is only available for Na<sup>+</sup> PFSA.<sup>[62]</sup> The tan  $\delta$  curve maxima originate from so called  $\alpha$ -relaxation in the sample, describing the temperature at which polymer side chains begin to move. At that point, the available thermal energy is sufficient to overcome the interaction energy of the sulfonate groups and the respective counterions.<sup>[62]</sup> Since for protonated PFSA this is mainly hydrogen bonding interactions, the maximum is found at low temperatures whereas for the alkali metal exchanged samples

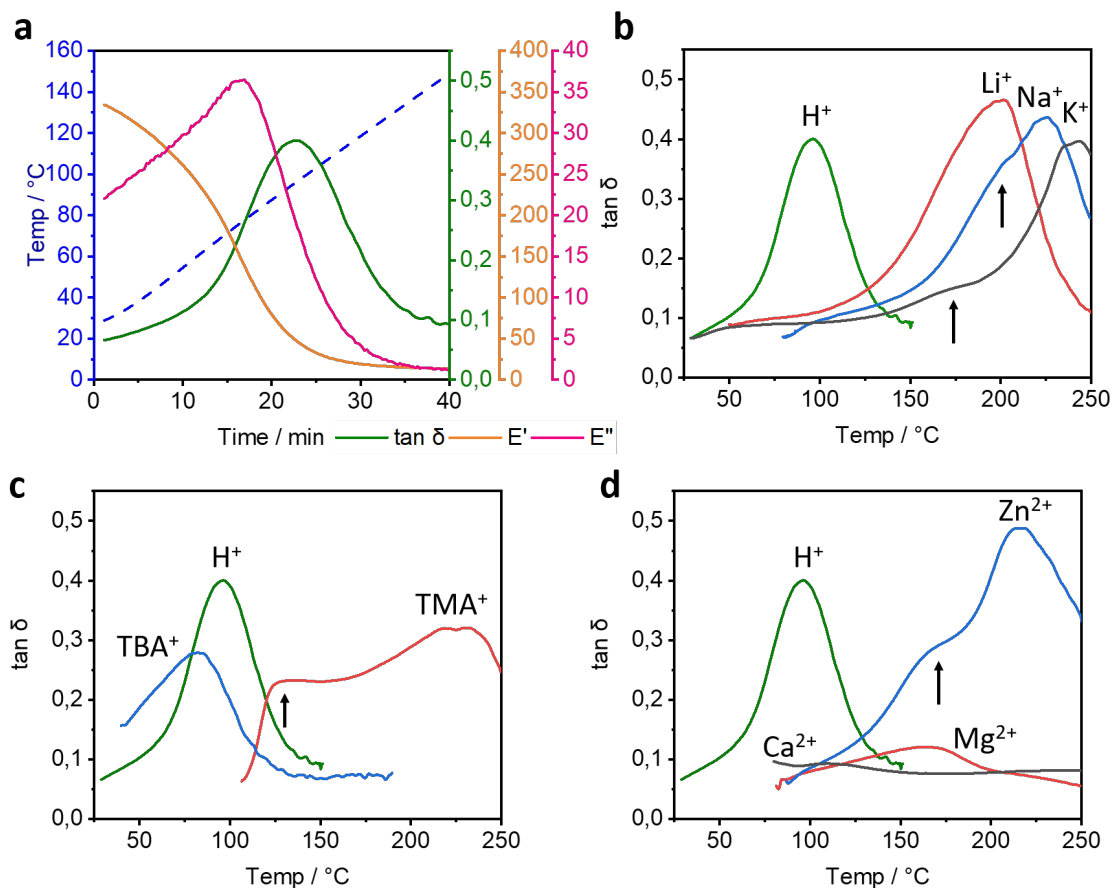


**Figure 29:** Dynamic mechanical analysis results for PFSA membranes in the protonated form as well as in different ion exchanged forms. (a) Pristine PFSA:  $E'$  curve depicted in yellow is the extensional storage modulus,  $E''$  shown in red indicates the extensional loss modulus. The loss factor  $\tan \delta = (E''/E')$  depicted in green gives the glass transition point ( $T_g$ ) and the blue dashed line represents the linear temperature ramp for the measurement; (b)  $\tan \delta$  curves for protonated PFSA as well as for alkaline metal cation exchanged PFSA; (c)  $\tan \delta$  curves for protonated PFSA as well as for alkylammonium cation exchanged PFSA; (d)  $\tan \delta$  curves for protonated PFSA as well as for bivalent metal cation exchanged PFSA. Arrows highlight shoulders resulting from  $\beta$ -relaxations in the PFSA backbone. In Figure 3 b–d  $\tan \delta$  of protonated PFSA is used to reference samples against each other.

the interactions are of coordinative and even electrostatic nature and thus higher in energy.<sup>[62]</sup> Therefore, the respective  $\tan \delta$  maxima are shifted to higher temperatures. For a glass transition, not only the electrostatic interactions have to be overcome, but a rather completely dynamic movement of both, the backbone and the side chains is necessary to enable processability of the material at  $T_g$ . Movement of the backbone chains is called  $\beta$ -relaxation (global movement) or  $\gamma$ -relaxation (local movement of  $-\text{CF}_2$ -fragments). These relaxations usually occur at temperatures below the  $\alpha$ -transitions. In the case of  $\text{H}^+$  ( $T_g = 96 \text{ }^\circ\text{C}$ ) and  $\text{Li}^+$  ( $T_g = 201 \text{ }^\circ\text{C}$ ) PFSA,



the backbone relaxations coincide with the  $\alpha$ -relaxation resulting in a single maximum with no shoulder in the DMA thermogram. In the  $\text{Na}^+$  and the  $\text{K}^+$  curves, shoulders at lower temperatures (approx. 200 °C for  $\text{Na}^+$  and approx. 170 °C for  $\text{K}^+$ ) are observed, originating from the  $\beta$ -relaxation ( $\gamma$ -relaxations occur at approx. -10 K).<sup>[86]</sup>

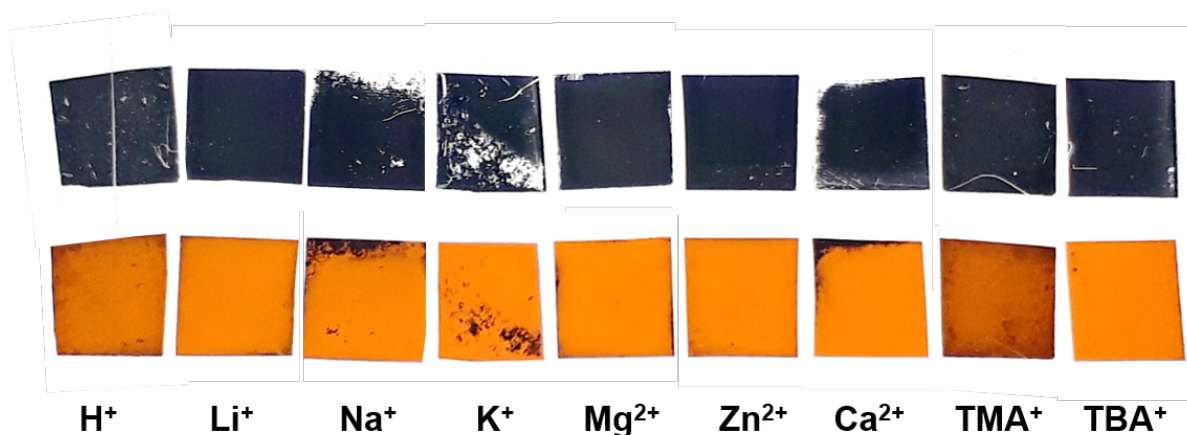
Alkylammonium ion exchanged PFSA produced thermograms are depicted in Figure 29c. Compared to the (H<sup>+</sup>) version,  $T_g$  for TMA<sup>+</sup> exchanged PFSA is shifted to 231 °C (red). A distinct  $\beta$ -relaxation is visible at much lower temperature around 130 °C. TBA<sup>+</sup> is known to have plasticizing effects in PFSA known from literature (blue).<sup>[63]</sup>  $T_g$  is found to be 82 °C for TBA<sup>+</sup> exchanged PFSA without a clearly distinguishable  $\beta$ -relaxation signal. These results underline that the size of the counter cation is not the only way to influence the membranes' processability: Although TMA<sup>+</sup> has a larger ionic radius than  $\text{K}^+$ , the respectively substituted PFSA membranes show a lower  $T_g$ . This is due to weak Van-der-Waals interactions of the methyl groups with the perfluorinated polymer backbone, which becomes more pronounced with increasing chain length as seen in the TBA<sup>+</sup> cation's plasticizing character.

Figure 29d shows thermograms of the three bivalent cation exchanged PFSA membranes (blue:  $\text{Zn}^{2+}$ , black:  $\text{Ca}^{2+}$  and red:  $\text{Mg}^{2+}$ ), for which there are no equivalents in literature. The thermograms reveal a curiosity: For the  $\text{Zn}^{2+}$  case, the course of the curve is comparable to the ones of alkaline metals discussed previously with a  $T_g$  at 216 °C and a  $\beta$ -relaxation signal around 170 °C highlighted by the arrow. The curves for  $\text{Mg}^{2+}$  and  $\text{Ca}^{2+}$  do not show any clear  $T_g$  but only low intensity maxima (approx. 115 °C for  $\text{Ca}^{2+}$  and 160 °C for  $\text{Mg}^{2+}$ ). Their origin cannot be assigned clearly to any distinct molecular movement in the polymer network. It is well known that interactions of the sulfonate group with metal ions tend to increase with the ions valence.<sup>[89]</sup> This is why  $T_g$  for  $\text{Mg}^{2+}$  and  $\text{Ca}^{2+}$  exchanged PFSA may either occur at higher temperatures than 250 °C or they do not exist at all. This finding can be correlated with the respective sulfates' solubilities in water, which is 57.7 g/100 mL for  $\text{ZnSO}_4$ , 35.7 g/100 mL for  $\text{MgSO}_4$  and 0.205 g/100 mL for  $\text{CaSO}_4$ .<sup>[25]</sup> These solubilities directly cohere with the coordinating character of the cation.  $\text{Ca}^{2+}$  coordinates most strongly to the sulfonate groups and plasters the side chains, hindering any mobility and therefore completely preventing membrane melting.  $\text{Mg}^{2+}$ , for which sulfate solubility is higher, coordinates less strongly. In this case, the temperature program was stopped at 250 °C to avoid the formation of toxic tetrafluoroethene ( $\text{C}_2\text{F}_4$ ) around 280 °C.<sup>[83]</sup> For  $\text{Zn}^{2+}$ , coordination to the sulfonate groups is least

strong, which is why the side chain mobility is not that hindered and  $T_g$  is found below 250 °C. Nevertheless, bivalent zinc ions have a higher binding strength to the sulfonate residues than monovalent ions or even protons do, although this is not visible in the zinc membrane's glass transition, which is comparable to other PFSA samples investigated herein. To further investigate the meaning of the binding strength for the electrochemical performance of a respective MEA, the next step is to translate our obtained  $T_g$  data into membrane processability in a decal transfer.

#### *MEA production via decal transfer*

Large-scale MEA fabrication can be accomplished *via* decal transfer, which comprises heat-pressing and thereby transferring a supported catalyst layer onto or even into the upmost layers of a polymer electrolyte membrane such as PFSA. DMA results listed in Table 8 suggest that when doing a decal transfer at or slightly below 250 °C, a complete transfer is expected to be feasible for the following membranes: protonated form (96 °C),  $\text{Li}^+$  (201 °C),  $\text{Na}^+$  (226 °C),  $\text{TMA}^+$  (231 °C),  $\text{TBA}^+$  (86 °C) and  $\text{Zn}^{2+}$  (216 °C) ion exchanged PFSA. A temperature of 250 °C is high but still in an acceptable range (given the thermal decomposition of the polymer at 280 °C) to guarantee maximum catalyst transfer. Industrial scale MEA production was imitated on 5 cm<sup>2</sup> by pressing a cathode-membrane-anode sandwich between pre-heated stainless-steel blocks. For this purpose, anode and cathode supported catalyst layers were prepared without using a binder. The mixing of different PFSA species (ion-exchanged form vs. non-ion-exchanged form) was avoided by not using any CEM (e.g. PFSA) binder (usually employed in the standard protonated form) at all. A separation of additional effects caused by heterogeneity of PFSA species would be hard to accomplish. The process temperature is high enough to ensure ionic contact of catalyst and membrane. Using the pure catalyst layers in the presented form facilitated comparability among the samples.



**Figure 30:** Half-MEAs (upper row) produced *via* decal transfer and their respective negatives (lower row, remaining Kapton<sup>®</sup> substrates) on protonated as well as cation exchanged PFSA membranes. In some cases ( $H^+$ ,  $Li^+$ ,  $Mg^{2+}$ ,  $Zn^{2+}$  and  $TMA^+$ ) catalyst transfer onto the membrane was complete whereas the catalyst layer is incomplete in the case of others ( $Na^+$ ,  $K^+$ ,  $Ca^{2+}$ ). Although there is residual catalyst visible on the Kapton<sup>®</sup> negative,  $TMA^+$  exchanged PFSA results in an intact half-MEA.

**Table 9:** Optical evaluation and quantitative gravimetric data for decal transfers.

| Ion       | Optical evaluation                | Gravimetric transfer<br>/ % |
|-----------|-----------------------------------|-----------------------------|
| $H^+$     | Reference                         | 97                          |
| $Li^+$    | Better than reference             | 96                          |
| $Na^+$    | Transfer incomplete (edge effect) | 82                          |
| $K^+$     | Transfer incomplete               | 81                          |
| $Mg^{2+}$ | Comparable to reference           | - 96                        |
| $Zn^{2+}$ | Better than reference             | 95                          |
| $Ca^{2+}$ | Transfer incomplete (edge effect) | 83                          |
| $TMA^+$   | Visible catalyst residues         | 94                          |
| $TBA^+$   | Good                              | 99                          |

Figure 30 compares the results of a platinum half-MEA production for each ion exchanged membrane compared to protonated PFSA. As expected, transfer onto  $Li^+$  (96%),  $Zn^{2+}$  (95%) and  $TBA^+$  (99%) was performed well, compared to a reference  $H^+$  MEA with 97% transfer. Although  $TMA^+$  exchanged PFSA has a higher  $T_g$  and

visually seems to have a larger portion of the catalyst remaining on the Kapton<sup>®</sup> negative, gravimetric analysis proved that this portion is very small (94% transfer). The opposite is true for Na<sup>+</sup> (82%), K<sup>+</sup> (81%) and Ca<sup>2+</sup> (83%) exchanged membranes, showing significant portions of the catalyst remaining on the Kapton<sup>®</sup> support. For Mg<sup>2+</sup> a transfer of 96% catalyst onto a Mg<sup>2+</sup> exchanged membrane was reproducibly performed although no clear T<sub>g</sub> could be deduced from the DMA thermograms. In order to provide additional data regarding this finding, H<sup>+</sup>, Li<sup>+</sup> and Mg<sup>2+</sup> half-MEA cross sections were analyzed with a light microscope. Pictures are shown in Figure 31. A protonated half-MEA (Figure 31a) shows a uniform Pt catalyst layer with a thickness of  $12.7 \pm 0.5 \mu\text{m}$  (6.8% of the total cross section) and a total thickness of  $187.6 \pm 0.6 \mu\text{m}$ . A Li<sup>+</sup> MEA (Figure 31b), identified as well processable during decal transfer, bears a catalyst layer of  $10.1 \pm 0.1 \mu\text{m}$  thickness representing 5.5% of the total cross section of  $184.7 \pm 0.4 \mu\text{m}$ . Although the Li<sup>+</sup> MEAs uniform catalyst layer is slightly thinner than the reference, values and errors are in a comparable range. For Mg<sup>2+</sup> half-MEAs (Figure 31c-d), the shape and thickness of the catalyst layer differ significantly. Figure 31c shows a uniform catalyst layer with  $7.9 \pm 0.2 \mu\text{m}$  thickness while the overall MEA thickness is  $167.6 \pm 1.9 \mu\text{m}$ . Although produced the same way, there is no clear catalyst layer visible for Mg<sup>2+</sup> exchanged MEAs shown in Figure 31d. Although the decal transfer seems successful at first sight, incorporation of the catalyst particles was evidently neither as deep nor as uniform as for protonated PFSA. Furthermore, Mg<sup>2+</sup> exchanged MEAs exhibit crystallites at the interface and throughout the cross section, indicating membrane salting and thus an altered arrangement of the polymer chains. Lacking a clear T<sub>g</sub> value, Mg<sup>2+</sup> exchanged membranes are not reproducibly processable and, therefore, not suitable for a large area decal process.

Overall, the decal transfer shows a good correlation between the experimental DMA results and processability of the pre-treated membrane material. T<sub>g</sub> values evidently need to be slightly lower than the processing temperature to guarantee successful MEA production. So far, ion exchange per se does not hinder MEA production but comes with the advantage of increased thermal and mechanical membrane stability.

### **Influence of ion exchange on a MEA's electrochemical performance**

Ion exchange in PFSA membranes systems can have two different effects that influence the electrochemical performance of a respective MEA. First, due to strong binding energies of the metal cations with the sulfonate groups, it can be assumed

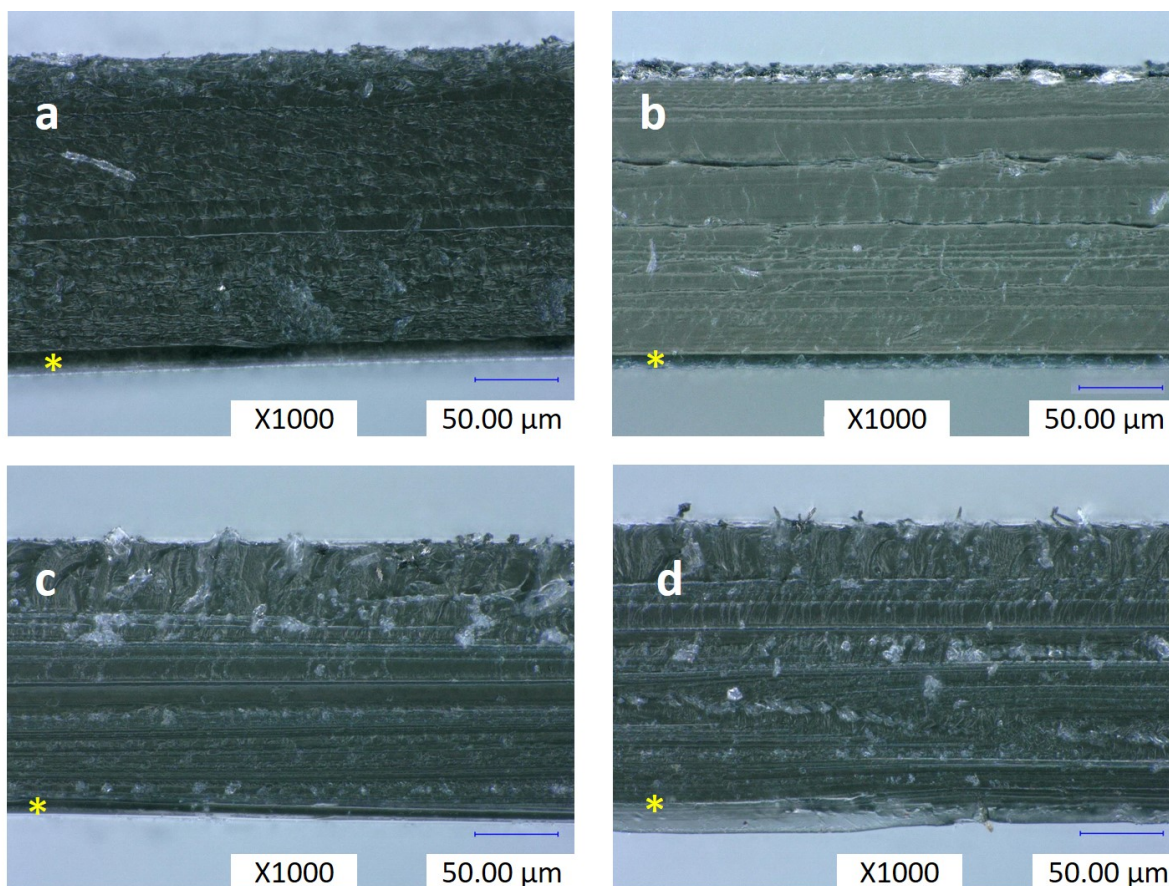


**Figure 31:** Microscopy pictures of half-MEA cross sections. (a) Protonated half-MEA showing a thick Pt-layer on the bottom. (b)  $\text{Li}^+$  half-MEA with a thinner but uniform catalyst layer and (c)-(d)  $\text{Mg}^{2+}$  half-MEAs produced by the same method but showing significant differences in shape and thickness of the catalyst layer. A yellow star indicates the Pt-side of the half-MEA and the position of the catalyst layer.

that the cation mobility in the membrane is reduced compared to the protonated form, as explained earlier, as long as the foreign ion is present in the membrane. Compared to the metal ions, protons are smaller, more mobile and their movements in an aqueous environment (*via* the *Grotthuss* mechanism) are quicker.<sup>[78]</sup> This implies a small membrane resistance and a small ohmic loss in electrolysis. A substitution of metal ions by OER protons is thus highly desirable. Metal ions may irreversibly or only reversibly block transportation channels and increase MEA resistance.

The second effect that cation exchange may induce is related to the morphology of the polymer of the membrane: During operation, cations migrate from the anode to the cathode side of the MEA and the protonated form will be at least partly restored. Still, the MEA was processed in the ion exchanged form, with the re-

spective metal ions inducing specific morphologies and arrangements of the ionic sulfonate groups. For example, they may favor the formation of layered aggregates with a stable short-range order.<sup>[108]</sup> Even if the metal ions are released at the cathode side, certain morphologies of the polymer might be permanent. Therefore, ion exchange could serve as a tool to tune the membrane's morphological properties and adapt it to industrial needs. Both aspects have been addressed in this study: initial effects were examined by potentiodynamic cyclic voltammetry (CV), whereas potentiostatic and galvanostatic measurements have been performed for long-term reversibility studies.

### *Cyclovoltammetry*

Cyclic voltammetry (CV) was performed to compare the peak performances of the  $\text{Li}^+$ ,  $\text{TBA}^+$  and  $\text{Zn}^{2+}$  exchanged MEA and reference them against a protonated MEA. This method will only address initial effects of proton-cation substitution. Potential-driven substitution (PDS) of metal ions by OER protons was investigated by potentiostatic as well as galvanostatic methods and will be addressed in the following subchapters.

CV studies resulted in polarization curves (1 mV/s scan rate) shown in Figure 32. For reference, the polarization curve of a protonated MEA is shown in red in Figure 32. The current compliance of 2.0 A/cm<sup>2</sup> is reached at  $2.36 \pm 0.03$  V applied potential in the Scribner cell configuration. Compared to the thermodynamic limit of electrochemical water splitting at  $\Delta G = 1.23$  V, the overpotential of around 300 mV is in the common range for active catalysts.<sup>[24]</sup> However, a more accurate value for comparison under real conditions is  $\Delta H = 1.48$  V, taking into account irreversible contributions such as latent heat.<sup>[26]</sup> Throughout the CV measurement procedure for one particular MEA (2 x CV 1 mV/s; 5 x CV 10 mV/s; 1 x CV 100 mV/s; CVs 10 mV/s until stable), curves for the  $\text{H}^+$  MEA were reproducible, so the scan rate was inconsequential for the polarization curves. Error values given in this section are obtained from subjecting three identical MEAs to the same measurement procedure, respectively.

A  $\text{TBA}^+$  ion exchanged MEA was subjected to the same measurement procedure with the initial CV shown in green in Figure 32. The current compliance of 2.0 A/cm<sup>2</sup> was reached at an applied potential of  $2.99 \pm 0.17$  V. This can be explained by the nature of the  $\text{TBA}^+$  ion: it is a soft, bulky and polarizable molecule. The organic butyl chains can interact with the perfluorinated PFSA backbone by van-der-Waals interactions as well as through hydrogen bonding between hydrogen and fluorine

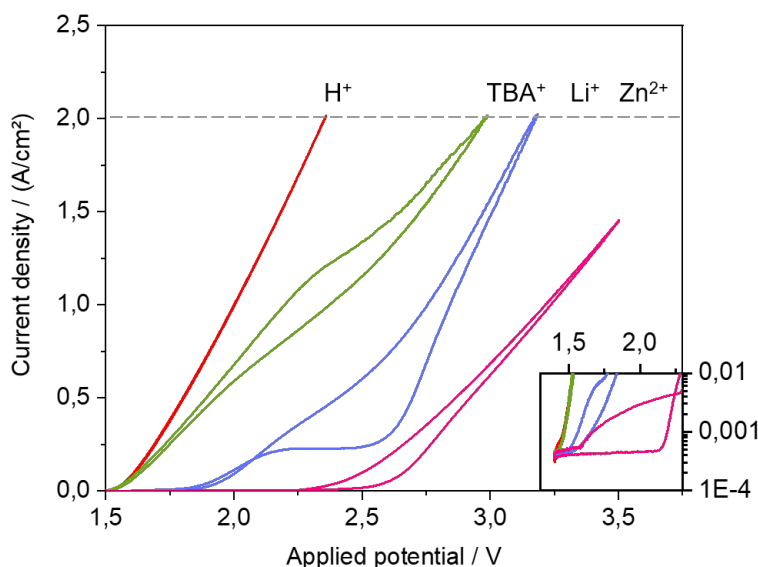


**Figure 32:** Cyclovoltammetry (CV) results for water electrolysis on an Ir/Pt-MEA system using membranes with different counteranions. Red: polarization curve of a protonated MEA serving as a reference. Green: polarization curve of a TBA<sup>+</sup> cation exchanged MEA. Blue: polarization curve of a Li<sup>+</sup> cation exchanged MEA. Magenta: polarization curve of a Zn<sup>2+</sup> cation exchanged MEA. Inset view on a logarithmic scale: Butler-Volmer consideration to assess the onset potential and thus the energy of starting ion mobility. Arrows indicate the scan direction.

atoms. Upon potential application, these additional interactions hinder the mobility of the TBA<sup>+</sup> compared to protons, which results in a lowered peak performance by approx. 600 mV.

For discussing the onset potential for ion mobility, it is helpful to first envision the consequences of ion exchange for the pH within the membrane and in close contact to the electrode. In a protonated MEA, the pH within the membrane can be assumed to be very low, around pH = 1. In contrast, ions different from H<sup>+</sup> can be expected to create a close to neutral pH ≈ 6. This pH shift can be translated into a potential difference of approx. 350 mV using the *Nernst* equation 17,

---


$$E = E^0 + \frac{RT}{z_e * F} * \ln\left(\frac{a_{ox}}{a_{red}}\right) \quad (17)$$


---

with the electrode potential  $E$ , the standard electrode potential  $E^0$ , the universal gas constant  $R$ , the absolute temperature  $T$ , the number of electrons transferred in the half-cell reaction  $z_e$ , the Faraday constant  $F$  ( $F = 96485$  C/mol) and the chemical activity  $a$  of the relevant species. This potential difference plays a major role in the shape of the obtained polarization curves. However, as cations migrate from the anode to the cathode side, they are subsequently replaced by OER protons. Therefore, a pH gradient will form from the beginning of the measurement until the point where the neutral cations have left the membrane at the cathode side. This cation transport process is not observable in the polarization curves and for determining its rate, additional measurements are needed. Constant potential and constant current experiments will be shown in the following subchapters.

In the  $\text{TBA}^+$  case, the onset potential seen in the polarization curve is comparable to the reference  $\text{H}^+$  MEA, against expectation. This can be explained by an incomplete ion exchange when the membrane is immersed in a 2 M TBACl solution. In literature, the case of ion mixtures of partial proton replacement by ions is only studied regarding competing ionic uptake into the membrane but further consequences are not studied. In the present case, with  $\text{TBA}^+$  assumed to coexist with protons as the cationic species in the PFSA, a tracking of the pH value provides insights about the completion of ion exchange. For  $\text{TBA}^+$ , a pH change from 6 to 2 was recorded. This proves an incomplete ion exchange, since the expected value for a complete exchange is  $\text{pH} = 1.2$  as calculated earlier. This fact shows that the exchange equilibrium is shifted towards protonated PFSA in the  $\text{TBA}^+$  case, compared to the metal ions. Therefore,  $\text{TBA}^+$  cation exchange is incomplete and protons possessing the highest mobility and the smallest ohmic loss in electrolysis<sup>[25]</sup> facilitate cation transport already at an onset potential of approx. 1.5 V.

Metal ions (here:  $\text{Li}^+$  and  $\text{Zn}^{2+}$ ) form sulfonate complexes within the PFSA membrane. They capture and fixate sulfonate groups in a strong ionic interaction, which equals blocking of the proton conducting moieties and results in reduced ion conductivity as well as hindered chain mobility. It is important to differentiate between initial and permanent effects, that such complex formation may have on electrochemical behavior of a metal ion exchanged membrane: Assuming a quantitative exchange for metal cations,<sup>[92]</sup> a first effect is an effective blocking of the cation transport channels by the metal ions. According to our hypothesis of PDS by OER protons, the channels will subsequently be unblocked while metal ions are released at the cathode side of the membrane. The channel blocking can be assumed to just have initial effects on the MEAs electrochemical behavior. Secondly, complex for-



mation induces specific arrangements of the polymer chains within the membrane. Once, the ions are driven out of the membrane upon potential application, these induced morphologies can yet be of permanent character and alter the electrochemical characteristics of the respective MEA. For the scope of this study, this model serves the purpose of explaining the observed electrochemical effects. Further explanations and the validation of the postulated morphological changes could be obtained by SAXS and further scattering techniques. However, this study will apply the model of complex-induced morphological changes in the membrane to new electrochemical observations on ion exchanged membranes consistently, hopefully stimulating more research in this field.

A  $\text{Li}^+$  MEA was subjected to the exact same measurement procedure with the initial polarization curve shown in blue in Figure 32. Here, the onset potential for ion mobility is shifted towards 1.8 V by approx. 300 mV compared to the reference  $\text{H}^+$  MEA. This finding is well in line with the potential shift of 350 mV calculated before, which originates from the altered pH within the membrane. As opposed to the reference and the  $\text{TBA}^+$  MEA, the  $\text{Li}^+$  ion exchange significantly decreased the performance, but it still reached the current compliance at  $3.18 \pm 0.20$  V – meaning a loss of 800 mV. From the polarization curves, it is not visible, whether this effect is due to a physical channel blocking (initial effect) or due to morphological changes of the polymer chains (permanent effect) and further investigations will be shown in the following subchapters. In addition, the metal ions present in the membrane will directly impact the membrane resistance, which is a crucial processing parameter for MEA performance. Membrane resistances by impedance spectroscopy will be addressed below.

For a  $\text{Zn}^{2+}$  exchanged MEA the polarization curve shown in magenta in Figure 32 was recorded. A current density of  $1.46 \pm 0.02$  A/cm<sup>2</sup> is reached at an applied potential of 3.5 V. Compared to the reference  $\text{H}^+$  MEA, the onset potential for ion movement is significantly shifted by 700 mV, the plot on a logarithmic scale illustrates the sharp onset at 2.2 V. An explanation can be found in the structural binding characteristics of a  $\text{Zn}^{2+}$  in the membrane. Due to its higher valence (+II), it is coordinated by two or more sulfonate groups, resulting in a stable complex with a high binding strength. This is affirmed by short Zn-O bonds in known tetrahedral zinc complexes with sulfonate ligands, resulting from strong binding energies in a geometrically favorable arrangement.<sup>[133]</sup> At the beginning of the CV measurement, these stable complexes within the membrane block the cation transport channels. Once the overpotential of +700 mV compared to the reference is spent, the binding

energy of the coordinative Zn-O bonds is overcome, and the cations become mobile. Converting the 700 mV onset potential by multiplying it with the *Faraday* constant and the number of transferred electrons ( $n = 2$ ), this overpotential equals an energy of 135 kJ/mol. Comparing this to the dissolution energy of zinc complexes involving sulfate ligands for an aqueous environment (around 120 kJ/mol),<sup>[134]</sup> calculated from the lattice energies,<sup>[81]</sup> this is in very good agreement. This supports our hypothesis of complex formation with the PFSA sulfonate groups.

Considering the entire measurement procedure of subsequent CV cycles, the Zn<sup>2+</sup> MEAs performance slightly but continuously increased in the course of the measurements. Figure 33 shows the course of the last 6 CVs of a Zn<sup>2+</sup> MEA. Each one reaches higher current densities at 3.5 V applied potential than the previous one. The green polarization curve illustrates the last cycle, representing an equilibrated state with the metal ions present in the cycled electrolyte. This behavior is well in line with our hypothesis of a PDS of the metal ions by OER protons. We hypothesize that this exchange is slower for Zn<sup>2+</sup> than for Li<sup>+</sup> because of the strong complex formation of Zn<sup>2+</sup> in the PFSA membrane. This is visible as a continuous increase in peak performance, cycle by cycle, correlating with a portion-wise unblocking of the cation transport channels. However, with these measurements, the metal ion PDS by OER protons can neither be assumed to be completed, nor can it be quantified. To gain a comprehensive understanding and to further differentiate between initial and permanent effects of ion exchange in PFSA membranes, constant potential and constant current measurements were performed with the results shown in the following subchapters.

#### *Membrane resistance determination*

Although there is an ongoing controversy about the membrane resistance of PFSA,<sup>[123]</sup> this topic is an important aspect of membrane characterization. From the obtained polarization curves shown earlier, it is possible to calculate the resistances of the Li<sup>+</sup> and the Zn<sup>2+</sup> membrane using Ohm's law. The ohmic membrane resistance  $R$  is calculated as the inverse slope  $\beta$  of a linear regression fit in the nearly linear ohmic part of the very first cyclic voltammetry run for each membrane. Linear fits as well as slopes are shown in Figure 34 and resistances are given in Table 10.

For comparison, impedance spectroscopy was used to measure membrane resistances for a protonated, a Li<sup>+</sup> and a Zn<sup>2+</sup> ion exchanged MEA. We used a 0.25 M solution of the respective metal chloride as electrolyte to provide at the anode side ions of the same type than the ones intercalated in the membrane. Given the event

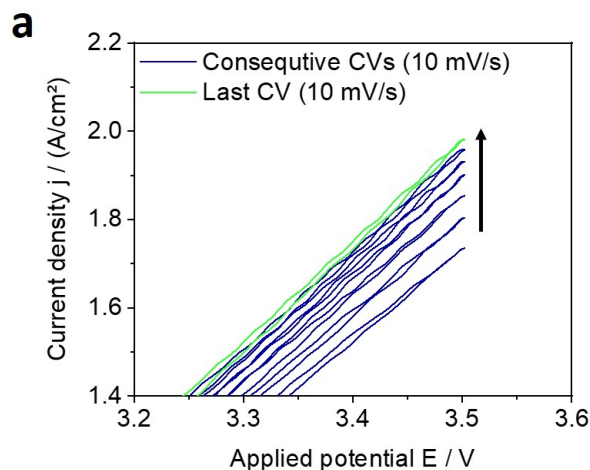


**Figure 33:** Polarization curves for water electrolysis on an Ir/Pt-MEA system using a  $\text{Zn}^{2+}$  cation exchanged MEA. CVs were run 80 times subsequently showing an increase in maximum current density reached. The polarization curves are evening out slightly below the current compliance at a potential of 3.5 V.

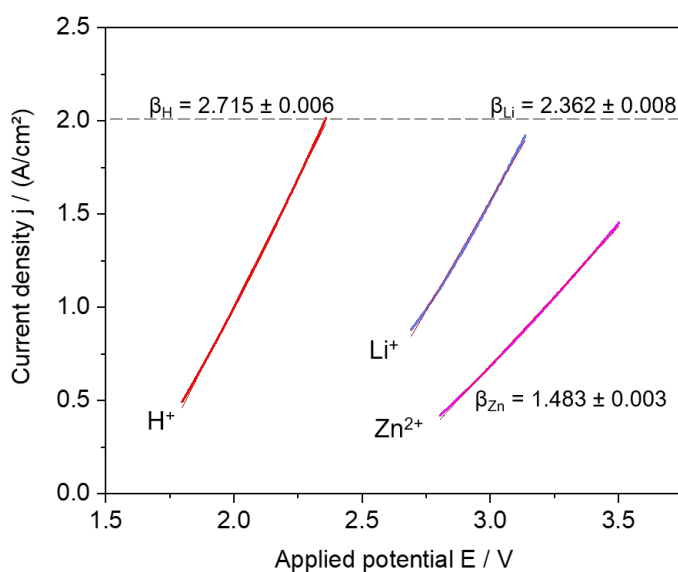


**Figure 34:** Linear regression analysis results obtained from the ohmic part of the membrane's cyclic voltammograms.

of PDS *in situ*, the ions in the membrane will migrate towards the cathode and be replaced by protons from OER. For this reason, only the very first experiment is significant for ion exchanged cases, because the saturation of the PFSA with metal ions cannot be guaranteed after different measurement cycles. Since the membrane

resistance depends on the number of ions in the membrane (due to their strong interactions with sulfonate groups), the effect of PDS was minimized by using the initial measurement at small current densities ( $2 \text{ mA/cm}^2$ ) to obtain the membrane resistance. *Nyquist* plots for the different membrane types are shown in Figure 35 and resistances measured at 1000 Hz during the first measurement are listed in Table 10.

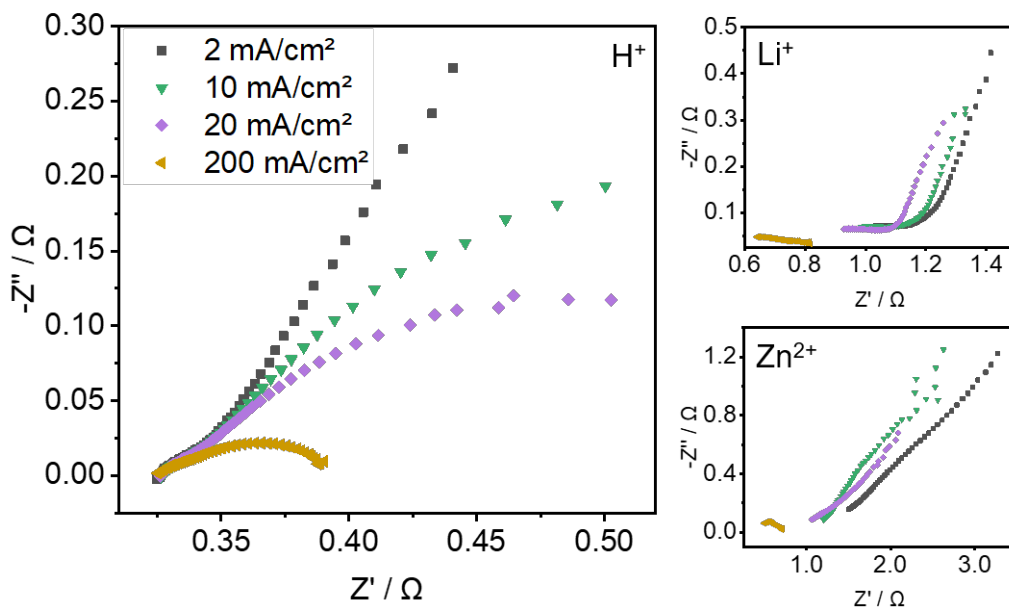


**Figure 35:** *Nyquist* plots for a protonated, a  $\text{Li}^+$  and a  $\text{Zn}^{2+}$  ion exchanged membrane at different current densities.

**Table 10:** Ohmic resistances of a protonated and the ion exchanged membranes calculated from cyclic voltammetry measurements and experimental data obtained from impedance spectroscopy. Calculated data were obtained from linear regression analysis of the linear, ohmic part of the cyclic voltammograms in Figure 32.

| Ion              | Calculated Resistance<br>/ $\Omega$ | Experimentally assessed resistance<br>/ $\Omega$ |
|------------------|-------------------------------------|--|
| $\text{H}^+$     | 0.37                                | 0.34   |
| $\text{Li}^+$    | 0.42                                | 1.13   |
| $\text{Zn}^{2+}$ | 0.67                                | 1.76   |

The resistances calculated from cyclic voltammetry increase from protonated ( $0.37 \Omega$ ) via  $\text{Li}^+$  ( $0.42 \Omega$ ) ion exchanged to  $\text{Zn}^{2+}$  ( $0.67 \Omega$ ) ion exchanged PFSA, matching the

order of increasing interaction strength between the cation and the sulfonic acid groups. Stronger binding strengths need to be overcome to facilitate ion mobility for  $\text{Li}^+$  than for  $\text{H}^+$  and for  $\text{Zn}^{2+}$ , the effect is even more pronounced. This is well in line with our hypothesis of complex formation and the dependence of the metal's binding strength with the sulfonic acid groups in the membrane. The same trend is visible in the data obtained from impedance spectroscopy: For protonated PFSA membranes, the resistance measured at 1000 Hz at a current density of  $2 \text{ mA/cm}^2$  ( $0.34 \Omega$ ) is comparable to the calculated value ( $0.37 \Omega$ ) and matches literature data.<sup>[124]</sup>  $\text{Li}^+$  ( $1.13 \Omega$ ) and  $\text{Zn}^{2+}$  ( $1.76 \Omega$ ) follow the same trend that is observed from the calculations, but it is three times as pronounced. It is commonly known, that the membrane resistance derived from *Nyquist* plots increases with current density for water electrolysis.<sup>[125]</sup> But for the metal ion exchanged MEAs, we observe the inverse effect: The measured resistance decreases with increasing current density. We hypothesize that at lower current densities, most ions in the membrane remain immobile and metal ions block the cation transportation channels resulting in higher resistances. The discrepancy between the calculated values (deduced from high current densities) and experimental values in Table 10 (measured at small current densities) is thus due to the difference in ion mobility. The values start to align when the current density is raised: The  $\text{Li}^+$  MEA approaches  $0.71 \Omega$  measured at 1000 A while the  $\text{Zn}^{2+}$  MEA approaches  $0.61 \Omega$ . But there is an overlaying effect to this explanation, which was already addressed earlier: Potential-driven substitution of the metal ions by protons from OER takes place and recovers some of the original membrane conductivity, since proton-sulfonate interactions are weaker than metal-sulfonate interactions. This reinforces the observed effect of lower resistances with increasing current density, which contrast with common expectations.<sup>[125]</sup>

#### *In-situ potential-driven substitution (PDS) of metal ions*

The applied potential is the driving force for ion movement and directly correlated to the ion mobility and the speed of *in-situ* PDS. In a comparative experiment, a constant potential of 2.0 and 3.0 V was applied to a freshly prepared  $\text{Li}^+$  MEA, respectively (results shown in the Supporting Information). During PDS, the current density is expected to increase with time as a result of metal ions being replaced by protons and therefore recovering the membranes cation exchange capacity. Depending on the applied potential, the current density increased with different rates. At an applied potential of 2.0 V, the performance increases from an initial current density of  $0.02 \text{ A/cm}^2$  to  $0.20 \text{ A/cm}^2$  over 24 hours, equaling a rate of  $0.002 \text{ mA/s}$ . At 3.0 V,

the rate equals 55 mA/s tracing back to a 660 mA increase in current density within 12 seconds.

The increase in current density in a potential-controlled mode originates from the PDS phenomenon. In the CV experiments, the effect was visible for  $\text{Zn}^{2+}$  MEAs only, cycle by cycle. To determine how much of the performance of a protonated MEA can be recovered, systematic experiments in a constant potential mode were performed on  $\text{Zn}^{2+}$  and  $\text{Li}^+$  MEAs, where the original exchange towards the metal ion by immersion is assumed to be quantitative.<sup>[92]</sup> Freshly prepared and cation exchanged MEAs were subjected to potentiostatic conditions at potential steps of 200 mV, starting at 2.0 V. The results are shown in Figure 36.

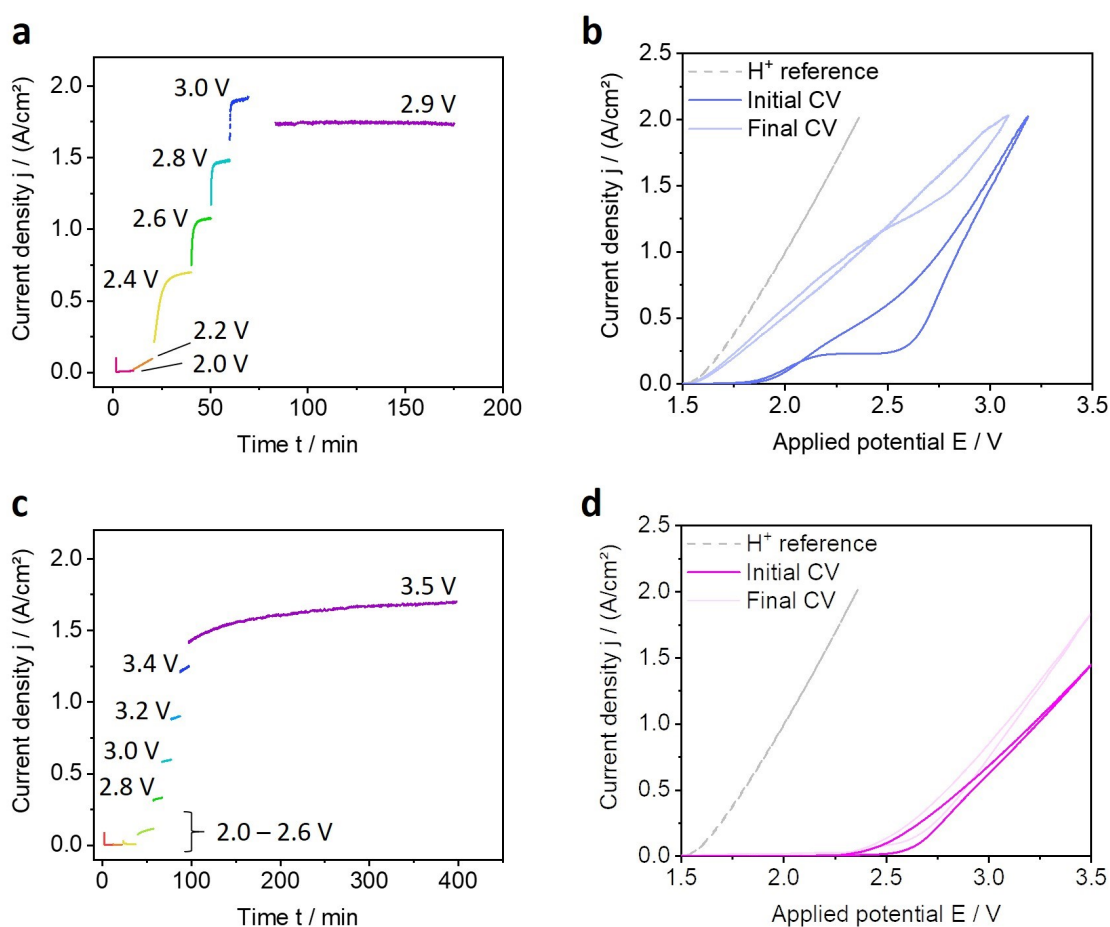


**Figure 36:** Results from potential-controlled cation back-exchange investigations of ion exchanged MEAs. a, c) Current densities obtained from potentiostatic measurements at different potential steps for  $\text{Li}^+$  (a) and  $\text{Zn}^{2+}$  (c) exchanged MEAs. (b, d) Comparison of CVs measured initially (dark color) with CVs measured after potentiostatic treatment (light color) for  $\text{Li}^+$  (b) and  $\text{Zn}^{2+}$  (d) exchanged MEAs.

In the case of  $\text{Li}^+$  MEAs (Figure 36a), a sigmoidal performance improvement is observed at each potential step until the current density asymptotically commuted in a certain value. For the highest potential applied (3.0 V), a current density of  $1.91 \text{ A/cm}^2$  is reached. A potential of 3.2 V leads to current densities above the current limitation of  $2.0 \text{ A/cm}^2$  and a reduced potential of 2.9 V showed a slightly decreasing curve for over 1.5 hours. This confirms our earlier assumption that the rate of a  $\text{Li}^+$  back-exchange is strongly potential dependent. Furthermore, the steady state at 2.9 V and a current density of approx.  $1.75 \text{ A/cm}^2$  suggests, that no more back-exchange took place by then. In contrast to the prior CV studies, the electrolyte was used single pass in this investigation to avoid equilibration with metal ions that were released from the membrane before and would therefore still be present in solution. These results can be referenced to an  $\text{H}^+$  MEA, showing constant current densities at constant potentials and reaching the current limitation of  $2.0 \text{ A/cm}^2$  already at 2.4 V (see Supporting Information). As to the extent of back-exchange, a CV was performed after the potentiostatic back-exchange procedure (Figure 36b, light blue) and compared to the initial CV from earlier measurements (Figure 36b, dark blue). A significant improvement from 3.18 V initially towards 3.07 V after the back-exchange is observed. Furthermore, the bellied shape of the initial CV starting at 2.2 V can be traced back to a substitution of the ions by OER protons. This confirms our assumption that, compared to  $\text{Zn}^{2+}$  MEAs,  $\text{Li}^+$  PDS is accomplished at a lower energy needed to unblock sulfonate groups. Since the final CV was recorded after steady state was reached, there is a permanent peak performance loss of approx. 700 mV for the  $\text{Li}^+$  MEA. Also for  $\text{Zn}^{2+}$  MEAs (Figure 36c) the speed in performance improvement depends on the applied potential. As opposed to the  $\text{Li}^+$  case, the current limitation of  $2.0 \text{ A/cm}^2$  was not reached at applied potentials of up to 3.5 V. This potential was held for a period of 5 hours, during which the improvement asymptotically approached a final value of approx.  $1.75 \text{ A/cm}^2$ . Comparing peak performances in an initial and a final CV (Figure 36d), an improvement from  $1.43 \text{ A/cm}^2$  towards  $1.81 \text{ A/cm}^2$  at 3.5 V applied potential was found.

One explanation for the observed permanent effect on electrochemical behavior might be a certain amount of  $\text{Li}^+$  or  $\text{Zn}^{2+}$  ions permanently binding to some of the sulfonate groups, which results in a reduced cation transport capacity. If this is not the case, morphological consequences of ion exchange within the membrane polymer must be considered. During processing of the membrane in the decal transfer, metal ions will induce specific arrangements of the mobile polymer side chains, since the sulfonate groups act as ligands in the so-formed complexes. After immer-

sion, the ions are present in the membrane already, but the chain structure must be assumed to still be comparable to the original protonated form of the membrane. During processing of the membrane *via* decal transfer taking place above the glass transition temperature ( $T_g$ ), the polymer main and side chains exhibit enough mobility to move and rearrange. This way, geometrically favored and stable chain arrangements will form. These morphologies are likely to be permanent, even if the ions are driven out of the membrane during electrolysis.

A first estimation of the extent of PDS can be obtained from immersing the used MEAs in an aqueous 2 M metal chloride solution again, as already performed for the initial ion exchange. During this process, an exchange of protons present in the membrane by metal ions due to different binding strengths will occur, observable by an acidification of the solution and a lowering of the pH value. Results are given in Table 11.

**Table 11:** pH changes of salt solutions before and after membranes or used MEAs were immersed. A lowering of the pH indicates an expel of protons from the membrane into solution *via* formation of HCl(aq).

| Salt for 2 M solution | Sample<br>/ $\Omega$   | Initial pH<br>/ $\Omega$ | Final pH |
|-----------------------|------------------------|--------------------------|----------|
| LiCl                  | PFSA membrane          | 4.0                      | 1.0      |
| LiCl                  | MEA after electrolysis | 4.0                      | 1.0      |
| ZnCl <sub>2</sub>     | PFSA membrane          | 3.5                      | 1.0      |
| ZnCl <sub>2</sub>     | MEA after electrolysis | 3.5                      | 2.0      |

As described above, an initial pH shift towards 1 is visible in the preparation of Li<sup>+</sup> as well as for Zn<sup>2+</sup> membranes prior to MEA production. Immersing the used MEA after the potentiostatic back-exchange procedure again resulted in a lowering of the pH, which proves that protons originating from electrolysis have been incorporated as counter cations of the sulfonate groups. Interestingly, the Li<sup>+</sup> MEA released one order of magnitude more protons into solution resulting in a lower pH, than the Zn<sup>2+</sup> MEA did, which confirms our earlier assumption, that Zn<sup>2+</sup> ions interact more strongly with the sulfonate groups. Therefore, they do not undergo PDS during electrolysis as easily as Li<sup>+</sup> ions do.



To finally quantify the rate and extent of metal ion PDS by OER protons, a  $\text{Li}^+$  MEA was subjected to galvanostatic conditions with an applied current of  $1.5 \text{ A/cm}^2$ , while the potential was recorded as a function of time. The results of this experiment are shown in Figure 37.

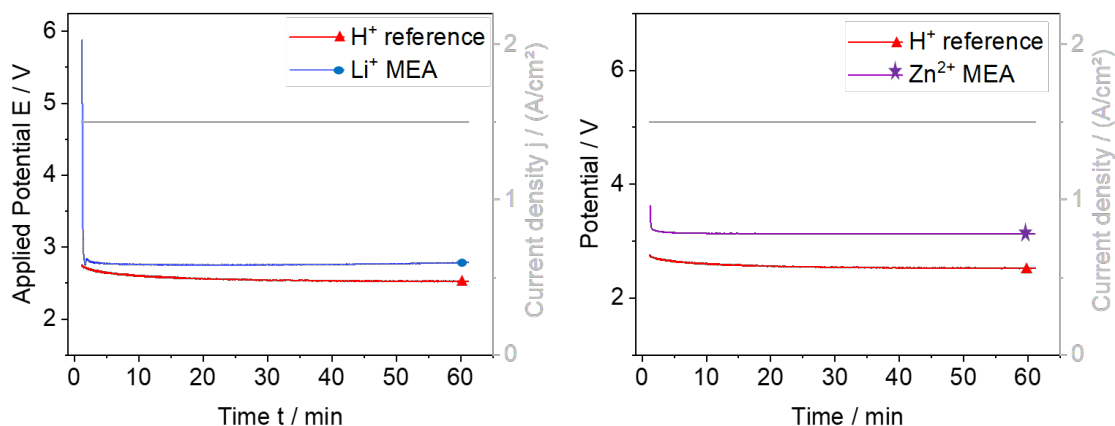


**Figure 37:** Results from galvanostatic investigations of a  $\text{Li}^+$  and a  $\text{Zn}^{2+}$  MEA (blue) with an applied constant current of  $1.5 \text{ A/cm}^2$  (grey). A standard protonated MEA (red) was used as a reference.

The  $\text{Li}^+$  MEA (Figure 37, blue curve) shows a significant potential drop from  $5.88 \text{ V}$  at  $t = 0 \text{ s}$  towards  $2.75 \text{ V}$  at  $t = 28 \text{ s}$ . Afterwards, it reached steady state and the MEAs performed constantly over a period of 1 hour with a potential of  $2.75 \text{ V}$ . The reference  $\text{H}^+$  MEA (Figure 37, red curve) does not show a comparable potential drop but a small performance increasement from  $2.73 \text{ V}$  at  $t = 0 \text{ s}$  towards  $2.70 \text{ V}$  at  $t = 50 \text{ s}$  and slowly but constantly increased in performance over 1 hour until a potential of  $2.52 \text{ V}$  was reached. After reaching steady state at  $t = 28 \text{ s}$ , all mobile  $\text{Li}^+$  ions are assumed to be driven out of the membrane and replaced by OER protons. The same experiment was carried out for a  $\text{Zn}^{2+}$  MEA with a steady state at a potential of  $3.13 \text{ V}$ . Since we expect no quantitative PDS in the  $\text{Zn}^{2+}$  case as shown in Table 11, the additional potential difference can be assigned to channel blocking by remaining  $\text{Zn}^{2+}$  ions. To quantify the PDS process, elemental analysis of the used MEAs and of a freshly exchanged  $\text{Li}^+$  membrane were performed three times by different methods, yielding the results listed in Table 12. For comparison, a  $\text{Zn}^{2+}$  MEA was analyzed in the same manner.

**Table 12:** Elemental analysis results for fresh  $\text{Li}^+$  and  $\text{Zn}^{2+}$  ion exchanged membranes and a processed,  $\text{Li}^+$  exchanged MEA after electrolysis.

|                       | Ion exchanged membrane<br>before processing |      |      | Ion exchanged MEA<br>after electrolysis |       |       |
|-----------------------|---|------|------|---|-------|-------|
| Lithium found [wt.-%] | 0.60  | 0.60 | 0.60 | < 0.5                                   | < 0.5 | < 0.5 |
| Sulfur found [wt.-%]  | 2.90  | 3.00 | 3.00 | 2.70                                    | 2.90  | 2.60  |
| Zinc found [wt.-%]    | 2.80  | -    | -    | 2.60                                    | -     | -     |
| Sulfur found [wt.-%]  | 2.80  | -    | -    | 2.60                                    | -     | -     |

Different digestion methods of the membrane were performed (acidic digestion under heat and microwave digestion) and no lithium was found within the experimental error (detection limit 0.05%). This proves that potential-driven substitution (PDS) of the  $\text{Li}^+$  ions is a quantitative and quick process with a rate of 0.2 mmol/cm<sup>2</sup> per min (calculations shown in the Supporting Information). This equals a ratio of  $4.7 \approx 5$  protons per  $\text{Li}^+$  ion, that must be produced at the anode side to achieve a quantitative exchange. In contrast,  $\text{Zn}^{2+}$  ions were proven to remain in the membrane and could not be replaced by protons from OER due to strong binding interactions with the sulfonate groups, as already argued earlier.

This finding finally explains the origin of the performance changes found in both, the potentiostatic and the galvanostatic investigations: During heat processing of the membrane in the decal transfer, metal-induced morphologies and rearrangements of the sulfonate groups have permanent effects on the membrane performance. We conclude that the binding strength of the lithium metal to the sulfonate groups in the membrane is high enough to alter the physical and mechanical properties but at the same time, it is weak enough for a fully reversible PDS of the metal ion. Alkaline and earth alkaline metals are known for their ability to induce layer arrangements in sulfonate complexes,<sup>[108]</sup> and lithium is known for its ability to form complexes with sulfonic acid-based polymers used for electrochemical applications.<sup>[109,110]</sup> In these cases, the  $\text{Li}^+$  ion induces highly symmetrical structures in the polymer although the exact unit cell and crystal system could not be identified.<sup>[110]</sup>  $\text{Li}^+$  show comparative complex formation characteristics in PFSA polymers, forming highly symmetrical structures in every ion's direct environment. We rationalize that this way, the ion serves as a template for a changed morphology throughout the whole polymeric

structure, although the event of morphological reorganization within the polymer is not fully understood yet. Hopefully, our insights stimulate further research in PFSA polymer morphology employing scattering techniques such as SAXS. Building up on an elaborated knowledge about how exactly the molecular arrangements in the membrane are influenced, ion exchange in PFSA membranes can then serve as a useful tool for industrial applications: Morphologies and therefore also cation transportation channels in the membrane can be shaped depending on the metal ion and its interaction characteristics with the sulfonate groups. This tool is very versatile, since plasticizer effects as well as stabilizing influences can be employed depending on the cation used for ion exchange. These insights can be used to broaden the spectrum of methods available for fine tuning membrane electrode assemblies in electrochemical hydrogen production.

### 2.2.5. Conclusion

The mechanical properties of PFSA membranes are crucial for scaling membrane electrode assembly (MEA) production for electrolyzers, because the catalyst in many cases is transferred and connected to the membrane *via* a decal process. We demonstrated that processing parameters, especially  $T_g$  can be tuned by temporarily incorporating metal cations of different sizes, valences and character into the membrane. Based on processability considerations, lithium ( $\text{Li}^+$ ) was chosen to investigate the full process sequence including electrochemical characterization. We differentiated between an actual blocking of the cation transportation channels by the metal ion (initial effect) and metal ion induced polymer chain arrangements (permanent effect). For the first time, the phenomenon that we call *in-situ* potential-driven ion substitution (PDS) was quantified and used to restore the proton conduction properties of the ion modified and subsequently processed MEA. Based on lattice energy correlations, we reasoned that morphological changes in the membrane emerged to be permanent on the measurement time scale. Although the incorporated metal ions were proven to increase the membrane resistance in the first place, the PDS of  $\text{Li}^+$  by OER protons was shown to be quantitative and its rate was determined ( $0.2 \text{ mmol/cm}^2$  per minute). We conclude that the incorporation of metal ions into the PFSA membrane can serve as a flexible tool for fine tuning membrane electrode assemblies. Doing so, a transfer of scientific knowledge to scalable technologies was performed considering industrial needs towards green and sustainable energy conversion and storage. Building up on this fundament, we will investigate processing

parameters in greater depth in the future and hope to stimulate further research in this field.

## 2.3. $K^+$ transport in perfluorosulfonic acid membranes and its influence on membrane resistance in $CO_2$ electrolysis

### 2.3.1. Publication summary

Besides PEM electrolysis, the global energy transition requires further measures towards a green and sustainable energy economy. Especially technologies for carbon capture and storage (CCS) enjoy increasing popularity. One prominent example is the electrochemical reduction of  $CO_2$  to value-added products (e.g. CO or hydrocarbons) bearing the potential of decarbonization both, at point sources and in a broader context.<sup>[135]</sup> Common approaches to optimize catalyst<sup>[136]</sup> or cell design<sup>[114]</sup> are complemented in the presented study: its focus is on the core of the electrolyzer setup, the membrane that separates both half-cells. As in PEM water electrolysis, it is also common in  $CO_2$  electroreduction, to employ PFSA-based cation exchange membranes. The combination with the use of high molar electrolytes requires for a deeper investigation of cation-transport properties and their impact on the cell potential during operation.

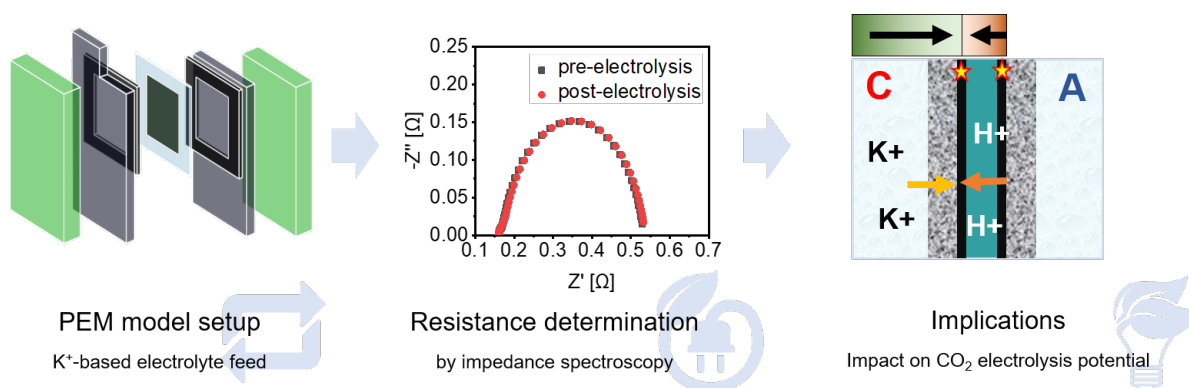


**Figure 38:** Graphical abstract of the work conducted in the third chapter including characterization in a PEM water electrolysis model system, resistance determination both, theoretically and experimentally, and implications for  $CO_2$  electrolysis.

A PEM water electrolysis model system is used to investigate  $K^+$ -sulfonate interactions and their influence on increasing the membrane resistance at different electrolyte concentrations. This way, it mimics a  $CO_2$ -electrolyzer device and is used in two operation modes: First in a mixed and second in a separate electrolyte mode. Carbonate and sulfate electrolytes ( $KHCO_3$ ,  $K_2SO_4$ ) are supplied to the half-cells of ultrapure water. The membrane resistance increased by  $1.7 \Omega \text{ cm}^2$  (cathode side only) to  $4.2 \Omega \text{ cm}^2$  (mixed electrolyte), which caused a significant voltage contribu-

tion that can be traced back to  $K^+$  transport over the membrane. The root cause (ionic interactions instead of hydrogen bonds) was quantified to 527–545 mV and a further effect was observed, revealing the limits of the applied model system: in the case of  $K^+$  overload compared of the available active centers, the membrane was not able to transport all required charge carriers due to space-charge limitation, which resulted in a steep voltage increase beyond the instrument compliance. For the industrially most relevant case (electrolyte at the cathode side only), an operation optimum was suggested at around 300 – 500 mA/cm<sup>2</sup>. At this current density,  $K^+$  is effectively driven back to the cathode side and large resistive contributions as well as overload are prevented. The membrane resistance was found to be an important building block that contributes to the total cell voltage and complements existing studies in this field.

My personal contribution as the first author of this paper comprises conceptualization and planning of the studies. I conducted most experimental work, such as membrane characterization (adic capacity determination, DMA and MEA fabrication) as well as electrochemical experiments (CVs and GSs) and post-electrolysis investigations (NMR, XRD and microscopy). I digested the membranes and analyzed all data obtained during this study. I conducted thermodynamic considerations, designed all figures and wrote the manuscript. Fellow researchers contributed to this work, namely Jamie Härtl, who performed impedance measurements and verification (repetition) studies. David Reinisch helped to develop the experimental concept, Thomas Reichbauer performed NMR and introduced me to acid capacity determinations, Nemanja Martić provided support proofreading the manuscript and Dr. Florian Kessler measured ICP-MS. Prof. Olaf Hinrichsen provided support in writing and reviewing as well as financial sources and Dr. Günter Schmid contributed to the concept and supervised the work.

**Bibliographical data** Vetter, K., Härtl, J., Reinisch, D., Reichbauer, T., Martić, N., Hinrichsen, O. and Schmid, G. (2021),  $K^+$  Transport in perfluorosulfonic acid membranes and its influence on membrane resistance in CO<sub>2</sub> electrolysis. ChemElectroChem. Accepted Author Manuscript. <https://doi.org/10.1002/celc.202101165>

Reprinted with permission from Wiley-VCH Verlag GmbH & Co. KGaA, Weinheim. Copyright 2021

### 2.3.2. Introduction

In the context of the global energy transition towards a green and sustainable economy, technologies for carbon capture and storage (CCS) enjoy increasing popularity. One example is the electrochemical reduction of  $CO_2$  to value-added products such as CO or hydrocarbons, which can contribute to decarbonizing sectors such as transportation, producing heat and power and industrial energy use.<sup>[11,135]</sup> Besides the common approach to optimize the catalyst in this electrochemical application,<sup>[136]</sup> current research also focuses on cell design optimization to make this green technology industrially applicable and thus broadly available in society.<sup>[114]</sup>

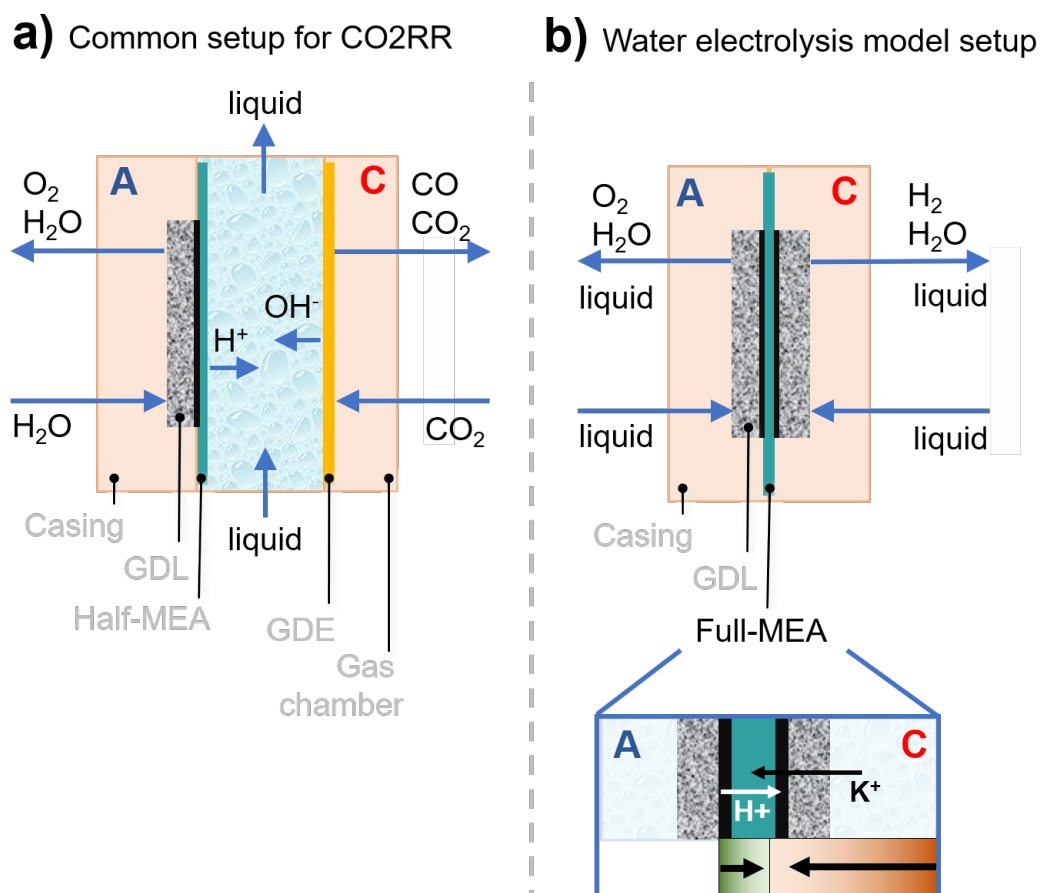


**Figure 39:** Overview of a) a half-MEA approach for  $CO_2$  electrolysis and b) the model water electrolysis mode used as a model setup in this study. The enlarged inlet in b) visualizes the interplay of proton transport from anode to cathode with the  $K^+$  uptake from an electrolyte employed at the cathode side.

### State of the art

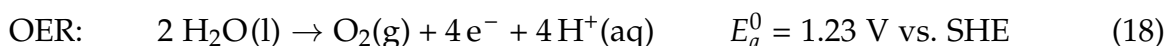
Scaling of CO<sub>2</sub> electrolysis applications has recently been started with 300 mA/cm<sup>2</sup> accomplished on a 10 cm<sup>2</sup> electrode surface in 2020 by Krause and co-workers. A commonly employed so-called half-MEA approach using a gas diffusion electrode (GDE) for CO<sub>2</sub> reduction reaction (CO<sub>2</sub>RR) at the cathode and an Ir coated perfluorosulfonic acid (PFSA) membrane at the anode side is shown in Figure 39a.<sup>[115]</sup> Catalyst coated membranes produced *via* heat-transfer of a supported catalyst powder layer onto the membrane (decal process) are called membrane electrode-assembly (MEA).<sup>[94]</sup> These MEAs (or half-MEAs when coated only at the anode side) are used in CO<sub>2</sub> electrolysis in combination with a silver-based GDE.<sup>[68,94]</sup> Highly molar electrolytes, often K<sup>+</sup>-based, are used in these cases to enhance electrolyte conductivity and guarantee charge balance across the cell. Vennekoetter et al. even employ a so-called liquid buffer layer between PFSA and GDE to control pH at the cathode.<sup>[114]</sup> In a CO<sub>2</sub> electrolysis half-MEA approach with electrolyte gap for example, they calculate 3.2 V total cell voltage required to drive the reaction. At the same time, two detrimental effects are well known: First, high-molar electrolytes might lower product selectivity<sup>[149,150]</sup> and second, K<sup>+</sup> ions (and further metal ions) interact strongly with PFSA replacing H<sup>+</sup> in the polymer structure spontaneously.<sup>[92]</sup> Existing electrolysis and fuel-cell literature points out which voltage portions might contribute to the total cell voltage as exemplified by Abdol Rahim and co-workers and elaborated later.<sup>[118]</sup> These considerations have not yet been transferred to CO<sub>2</sub> electrolysis. In this study, we aim at filling this gap by a quantification of the voltage portion accounting for K<sup>+</sup> interactions with the PFSA membrane.

### Water electrolysis model setup

The aim of the present study is to understand the influence of K<sup>+</sup> ions on the membrane resistance and thus the cell voltage in CO<sub>2</sub> electrolysis when K<sup>+</sup>-based electrolytes are used in combination with cation exchange membranes (CEMs). We model the half-MEA approach relevant for CO<sub>2</sub>RR by a well-known water electrolysis setup to reduce the system's complexity. This way, we will be able to access ohmic losses purely originating from the electrolyte's interaction with the PFSA membrane and the resulting resistance increase. The voltage portion that can be attributed to K<sup>+</sup>-PFSA interactions will be quantified and complement further known energetic contributions in CO<sub>2</sub> electrolysis.

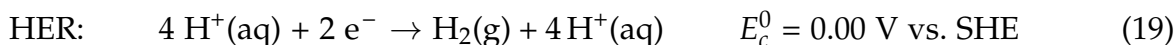


The influence of electrolyte usage on conductivity, pH, CO<sub>2</sub> uptake in the liquid phase and even product distribution in CO<sub>2</sub>RR was considered in literature before.<sup>[68,115,137]</sup> These effects directly affect the CO<sub>2</sub> electroreduction itself by changing reaction conditions or altering the reaction environment. For example, potassium bicarbonate (KHCO<sub>3</sub>, 0.1 to 2.0 M) or mixtures of the same with potassium sulphate (K<sub>2</sub>SO<sub>4</sub>) solutions at a pH around 7 are used as electrolytes with anolyte and catholyte separated by a PFSA membrane.<sup>[13,114,115,138]</sup> A study was conducted highlighting the positive impact of high concentrations on the electrolyte conductivity (0.5 M giving 77 mS\*cm vs. 2.0 M giving 211 mS\*cm). This impacts the overall operation voltage due to a reduced resistance in transporting ions over an electrolyte gap.<sup>[13]</sup> We will complement existing data by investigating membrane-electrolyte interactions in a common cell design in CO<sub>2</sub> electrolysis using a CEM to separate cathode and anode half-cells from each other. On the anode side, the membrane is coated with the catalyst for oxygen evolution reaction (OER, equation 18), iridium (Ir), resulting in a half membrane electrode assembly (half-MEA). The anode side reaction and processes in this setup are identical with water electrolysis applications.<sup>[98]</sup><sup>1</sup>




---

On the cathode side, there is an electrolyte gap with a cycled electrolyte (KHCO<sub>3</sub>, K<sub>2</sub>SO<sub>4</sub>), which answers two purposes: First, the production of hydrogen by competing hydrogen evolution reaction (HER, equation. 19) from protons is avoided, since the slightly basic electrolyte (KHCO<sub>3</sub>, pH = 8.5) acts as a buffer and reduces proton availability at the cathode catalyst. CO<sub>2</sub>RR can thus take place. Second, CO<sub>2</sub> transport across the membrane to the anode side is avoided.




---

<sup>1</sup>1.23 V refer to the Gibbs Free Energy ( $\Delta G$ ), which is commonly used in literature to describe electrochemical processes. It is given here for the sake of comprehensibility and comparability to literature but in the discussion part, we will refer to the reaction enthalpy ( $\Delta H$ ), which is more suitable when describing processes under real conditions.

In our model system, we replace the complex CO<sub>2</sub>RR with its high intrinsic overpotential at the silver catalyst<sup>[135]</sup> by HER employing platinum (Pt) as a catalyst in a full-MEA approach. This way, the complexity of cathodic processes in CO<sub>2</sub> electrolysis is reduced and a zero-gap approach is created. In this model system, the cathode gap is formally 0, which enables us to assess membrane properties and to investigate different electrolyte interactions with the PFSA membrane. This enables a quantification of the energy barrier for cation hopping from one negatively charged sulfonic acid group ( $-\text{SO}_3^-$ ) to the next. A proton's high acidity and thus low affinity to  $-\text{SO}_3^-$  is based on hydrogen bridge interactions only (approx. 20 kJ/mol for  $\text{H}_3\text{O}^+ \cdots \text{O}^{[80]}$ ) whereas metal ions interact in an ionic fashion with  $-\text{SO}_3^-$  (170–1500 kJ/mol<sup>[139]</sup>).<sup>[62]</sup> This means a proton can tunnel across the membrane in a *Grotthuss* like fashion while cations are hopping. Once in contact with a PFSA membrane, protons saturating the terminal  $-\text{SO}_3^-$  groups are exchanged spontaneously<sup>[95]</sup> and quantitatively (95 – 100%, depending on the metal).<sup>[92]</sup> Different studies have evaluated the influence of ion exchange on the water content, permeability and ionic conductivity,<sup>[95,97,112]</sup> all stating a negative impact of metal cation vs. proton transport, e.g. a 12 times higher conductivity was found for protons than for  $\text{Na}^+$ .<sup>[140]</sup> While  $\text{Na}^+$  exhibited approx. 100 mS/cm in this study, a molar conductivity of 50.1 S/cm<sup>2</sup>/mol is found for  $\text{Na}^+$  cations in distilled water at 25 °C.<sup>[25]</sup> Although not perfectly comparable, this provides a first impression of the significance of cation-sulfonate interactions. For electrolysis applications, where the use of a liquid, aqueous salt-based electrolyte is unavoidable, there is a clear preference to use monovalent cations: It is known that the thermal stability of the PFSA polymer is increased when alkaline metals are incorporated in the membrane whereas threefold positively charged cations ( $\text{Fe}^{3+}$  and  $\text{Al}^{3+}$ ) induce membrane degradation.<sup>[89]</sup> Moreover, we showed in an earlier study that  $\text{Li}^+$  ions incorporated in PFSA can be driven out of the membrane quantitatively by applying an electrochemical potential.<sup>[65]</sup>

In this study, we work with a water electrolysis setup and employ it as a model system for CO<sub>2</sub>RR applications. Our model will help to differentiate between resistance contributions, especially stemming from the membrane in different operation modes, that are not accessible in a CO<sub>2</sub> electrolysis setup. Therefore, we obtain results in water electrolysis but transfer the obtained knowledge to CO<sub>2</sub> electrolysis at high and industrially relevant current densities.

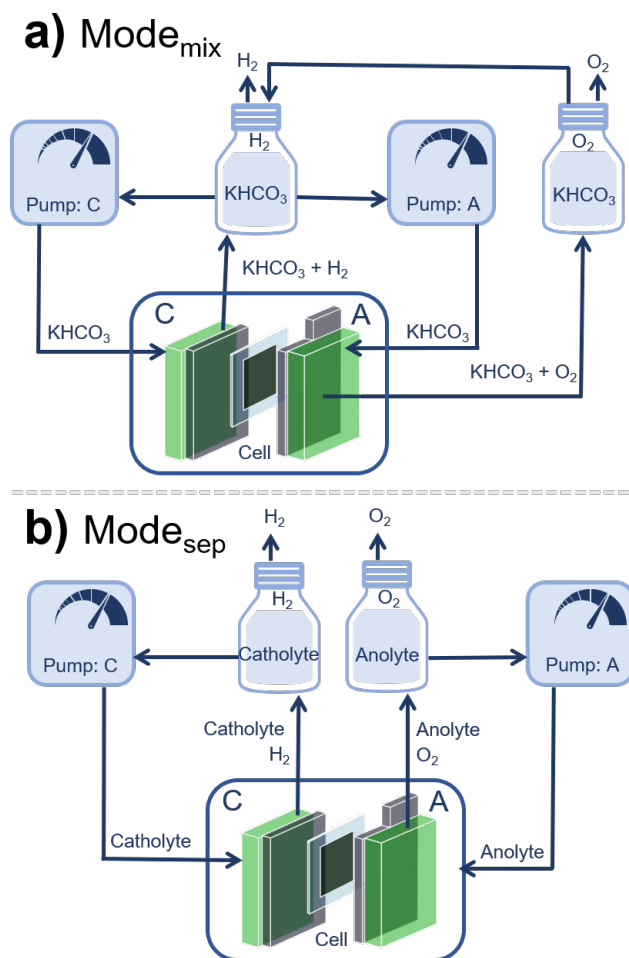


**Figure 40:** Experimental setup for electrochemical experiments in a) a mixed electrolyte configuration (mode<sub>mix</sub>) with different electrolyte reservoirs to avoid formation of explosive mixtures (oxyhydrogen) and b) in a separate electrolyte configuration (mode<sub>sep</sub>) for electrolyte variation studies. C – cathode side, A – anode side.

### 2.3.3. Experimental

A water electrolysis setup that is fed with electrolytes of different molarities is employed for all experiments. It is used to gain in-depth knowledge of resistance contributions in CO<sub>2</sub>RR that are not accessible in a real CO<sub>2</sub> electrolysis system. The full experimental procedure comprises two parts: First, the production of the membrane electrode assembly (MEA) including its pre- and post-electrolysis characterization and second, electrochemical measurements and testing. The respective methods are described in detail below:

## Membrane electrode assembly fabrication and characterization

Model MEAs were fabricated using a decal approach with Pt and Ir as HER and OER catalysts, respectively. A more detailed description of the membrane preparation and the MEA fabrication process can be found in the supporting information (SI).

### *Ion exchange capacity determination*

To monitor the cation exchange in PFSA membranes, membrane pieces (1.24 g, ambient conditions) were added to a stirred electrolyte solution (50.0 mL, 1.0 M KCl) while temperature and pH were recorded using the setup shown in Figure 41 and a combined pH electrode unitrode with integrated Pt1000 thermocouple provided by Deutsche Metrohm GmbH & Co. KG.

### *Elemental analysis (EA) by membrane digestion*

Elemental analysis was performed *via* inductively coupled plasma mass spectroscopy (ICP-MS) using a NexION<sup>®</sup> 2000 with three gas connections and hooked up to an auto sampler ENC-560DC Teledyne from Cetac Technologies. Aqueous samples (100 mL) were acidified by adding dilute nitric acid (1 mL, 1.0%). Solid samples and membranes were digested in aqua regia (6.0 mL, half-concentrated), washed (3 x 2.0 mL 2% HNO<sub>3</sub>, 3 x 2.0 mL H<sub>2</sub>O) and all liquid fractions were combined. The resulting liquid was diluted with water (100 mL total volume).

## Electrochemical measurements

### *Electrolysis setup*

The electrochemical cell that we used for the water electrolysis model is a modified Scribner cell with the schematic and details given in the SI. The cell itself is embedded into an experimental setup shown in Figure 40. Since we aim at obtaining information relevant for CO<sub>2</sub> electrolysis, we employ both mixed (mode<sub>mix</sub>, Figure 40a) and separate (mode<sub>sep</sub>, Figure 40b) operation modes.

The cell is hooked up to a Metrohm PGSTAT302N potentiostat equipped with a 10 A booster, both from Deutsche Metrohm GmbH & Co. KG. Combining the 10 A booster with a 5 cm<sup>2</sup> electrode area leads to a current compliance of 2.0 A/cm<sup>2</sup> being the maximum achievable value in this study. Liquids are pumped with a flow of 120 ml/min by a membrane pump and pH is measured in the respective anode or cathode reservoir during the experiment.

### *Electrolyte usage*

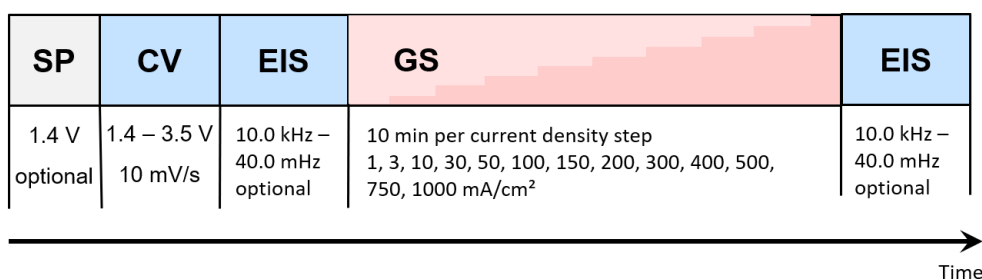


**Figure 41:** Flow chart of the electrochemical measurement procedure. SP – safety voltage, CV – cyclic voltammetry, EIS – electrochemical impedance spectroscopy, GS – galvanostatic steps.

The water used for all experiments in this study was Type 1 ultrapure water purified using the Milli-Q<sup>®</sup> Integral water purification system (18 MΩ cm). For reference experiments, ultrapure water without electrolyte salt was used at both anode and cathode side. For electrolyte variation studies, different potassium-based electrolytes (KHCO<sub>3</sub>, K<sub>2</sub>SO<sub>4</sub>, H<sub>2</sub>SO<sub>4</sub>) were used and the concentration was varied (100 μmol/L, 1.00 mmol/L, 500 mmol/L, 1.00 mol/L, 1.50 mol/L, 2.00 mol/L). The electrolytes (dissolved salts) we use are common in CO<sub>2</sub> electrolysis and their cations will interact with the PFSA anionic residues. Depending on the operation mode, electrolyte usage leads to a change in ion transport and, thus, an altered membrane resistance in the cell. Mode<sub>mix</sub> enables a constant bulk K<sup>+</sup> concentration and pH over the whole cell while in a mode<sub>sep</sub> with electrolyte at one side only causes ion transport over the cell, which affects both the membrane resistance and the cell voltage significantly.

In mode<sub>mix</sub>, both anode and cathode side of the cell are fed from the same electrolyte reservoir. Since the electrolyte is cycled multiple times (contrary to a single-pass-mode, where the electrolyte runs through the cell only once), it is pumped back into the original reservoir after passing the cell. To avoid the stoichiometric formation of oxyhydrogen,<sup>[5]</sup> the anolyte cycle passes via a second electrolyte reservoir, which serves at separating oxygen from the liquid electrolyte before cycling the liquid portion back into the shared reservoir (see Figure 40a).

#### Measurement procedure

To avoid K<sup>+</sup> ion diffusion over the membrane, a 1.4 V safety voltage was applied to the cell before performing experiments with electrolyte used at the cathode side only. Electrochemical measurement procedures consisted of two parts: first, potentiodynamic cyclic voltammetry was performed with a scan rate of 10 mV/s between 1.4 and 3.5 V applied cell voltage. If the current compliance of 2.0 A/cm<sup>2</sup> was

reached at lower voltage than the maximum applied voltage of 3.5 V, the CV direction was reversed. Second, subsequent galvanostatic measurements were conducted at different current densities (1.00, 3.00, 10.0, 30.0, 50.0, 100, 150, 200, 300, 400, 500, 750 mA/cm<sup>2</sup> and 1.00 A/cm<sup>2</sup>) and held for 10 min, respectively, while the cell voltage was recorded.

For degradation studies, the procedure was applied subsequently on a MEA and the time per galvanostatic step was extended (120 min or 300 min).

#### *Impedance spectroscopy*

Impedances were measured using galvanostatic impedance spectroscopy on a Metrohm PGSTAT302N potentiostat with FRA32M unit and a 10 A booster, both provided by Deutsche Metrohm GmbH & Co. KG. The data was recorded at constant current density (10 mA/cm<sup>arg</sup>) after reaching steady state. The frequency range comprised 10.0 kHz to 40.0 mHz with an amplitude of 5.00 mA and 66 points per decade. The equivalent circuit diagram along with an explanation of data processing can be found in the SI.

#### *Product gas analysis via gas chromatography*

CO<sub>2</sub> outgas experiments were conducted in mode<sub>mix</sub> using 1.0 M KHCO<sub>3</sub> at 1.0 A/cm<sup>2</sup> for 120 min. Gas samples were taken three times. Gas samples were taken every 15 min using gas sample bags and analyzed by a Thermo Scientific Trace 1310 gas chromatograph (GC) equipped with two thermal conductivity detector (TCD) channels.

#### *Model setup for CO<sub>2</sub> electrolysis*

All experiments are conducted in a water electrolysis model setup. We would like to underline that this is a model design, which would never be used in water electrolysis since metal ions in electrolytes have strong affinities to sulfonic acid groups and thus more energy is required to transport them over the membrane.<sup>[117]</sup> If water electrolysis was the target of this analysis, ultrapure water would be used instead of an electrolyte.<sup>[24]</sup> Also, this setup would not be employed in a realistic CO<sub>2</sub> electrolysis application case, since the competition between CO<sub>2</sub>RR and HER would lower the Faradaic efficiencies of the desired products (e.g. CO).<sup>[13]</sup> But by combining the model PEM setup with using high molar electrolyte solutions we will be able to assess membrane resistances as well as the voltage increase caused by K<sup>+</sup> transport over PFSA *via* a cation hopping mechanism from one sulfonic acid group to the next, which superimposes thermodynamic effects of pH-induced electrode potential

influences and changed ongoing reactions going along with transport-induced local pH-changes. This way we will be able to quantify an additional contribution to the cell voltage besides catalyst and gas diffusion electrode (GDE) contributions.

#### 2.3.4. Results and discussion

In CO<sub>2</sub> electrolysis, relevant electrolyte usage can be employed in two different modes: The first option is mode<sub>mix</sub> with constant electrolyte concentrations at both, anode and cathode side. The second option is a separate liquid cycle mode with electrolyte at the cathode side only (C<sub>only</sub>) and ultrapure water at the anode. (A variation of this setup can be used without liquid at the cathode side at all. In this case, water supply is performed *via* transport over the membrane and the achievable current density is thus limited by the speed of water diffusion.) As shown in Figure 39b, an interplay between K<sup>+</sup>-uptake and proton transport takes place in a C<sub>only</sub> operation mode. K<sup>+</sup> ions can be assumed to replace protons once the potassium-based electrolyte is in contact with the membrane. Due to the strong interactions with sulfonic acid groups, they are literally soaked into the PFSA polymeric matrix with attached sulfonic acid moieties. Since the ionic interaction is strong, the electrochemical resistance of the membrane will be increased by this proton-metal-ion exchange. When applying an electrochemical voltage to the cell, ionic migration takes place in the opposing direction compared to the K<sup>+</sup> soak. Protons from the anodic OER tend to push K<sup>+</sup> back to the catholyte. We investigate here, if the cation soak into the membrane can be reversed *in situ*, an effect, that we assume to be stronger with increasing current density. Current literature divides cell voltage portions and contributions in water electrolysis into distinct contributions,<sup>[118]</sup>

---

$$V_{\text{total}} = V_{\text{rev}} + V_{\text{act}} + V_{\text{ohm}} \quad (20)$$

---

where the total potential difference  $V_{\text{total}}$  is composed of the reversible voltage  $V_{\text{rev}}$  (the thermodynamic limit defining the intrinsic energy required for the process), the activation overpotential  $V_{\text{act}}$  (stemming from the reaction kinetics) and the ohmic overpotential  $V_{\text{ohm}}$  (originating from the membrane). In this study, we transfer these potential contributions to CO<sub>2</sub> electrolysis with a focus on  $V_{\text{ohm}}$ , which will be quan-

tified by our model water electrolysis setup. But we will call it  $V_{\text{ohm}}$ , since the results will show that not only ohmic parts contribute to the membrane resistance.

### PFSA ion exchange capacity determination

The basis of understanding  $\text{K}^+$ -sulfonate interactions in PFSA *in situ* is the replacement of PFSA protons by  $\text{K}^+$ . Due to strong ionic interactions of  $\text{K}^+$  with  $-\text{SO}_3^-$ , this ion exchange is a spontaneous process and occurs quantitatively for  $\text{K}^+$  ions.<sup>[92]</sup>  $\text{K}^+$  replacing  $\text{H}^+$  in the PFSA polymer matrix corresponds to membrane neutralization, while the surrounding liquid is acidified. On the basis of PFSA base titration as performed by the supplier for acid capacity determination,<sup>[141]</sup> we used the following procedure to determine the ion exchange capacity and gain knowledge about the speed and extend of exchange in our system: the pH and temperature of a 1.0 M KCl solution were monitored over time. PFSA membrane portions were added at  $t = 108$  s (see Figure 42). Within 20 s, a pH drop from 5.7 to 2.2 was observed and an equilibrium was reached at  $\text{pH} = 1.6$ . The temperature increased from  $T = 20.75$  °C at  $t = 108$  s to  $T = 20.91$  °C at  $t = 344$  s.

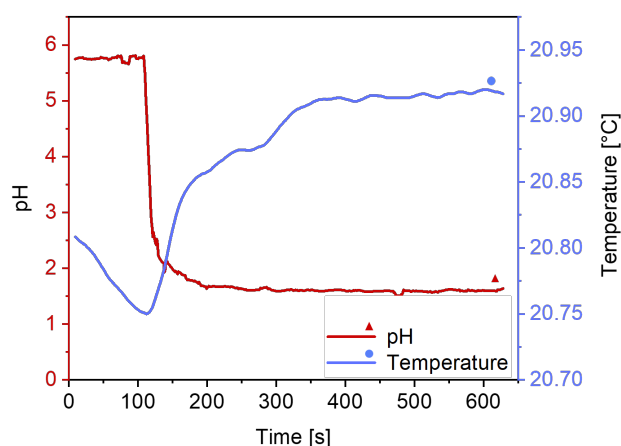
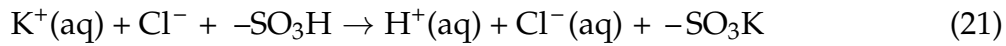


**Figure 42:** Monitoring results of pH and temperature change of a 1.0 M KCl solution containing PFSA membrane pieces added at 108 s. Note: Before adding the membrane pieces, the system is not in a thermic equilibrium (falling temperature). Therefore, the temperature change should be understood as a tendency, not an absolute value.

These observations can be explained by an ion exchange of the protons in the membrane by  $\text{K}^+$  following the equation:





The spontaneous interaction of K<sup>+</sup> with the sulfonic acid groups is highly exothermic,<sup>[65]</sup> which is expressed by the observed temperature increase.

The pH difference can be correlated with the total number of protons available in the membrane using the equivalent weight EW = 1100 g/mol,<sup>[74]</sup> which defines the mass of PFSA polymer per mole of sulfonic acid groups. With the mass of the membrane pieces m(PFSA) = 1.24 g, the total number of available sulfonic acid groups in the sample was calculated by:

---


$$n_{-\text{SO}_3\text{H}} = \frac{m}{\text{EW}} = \frac{(1.24 \text{ g})}{1100 \text{ g/mol}} = 1.13 \text{ mmol} \quad (22)$$


---

Considering the solution volume V = 50 mL, the maximum proton concentration c can be obtained assuming a quantitative exchange.<sup>[92]</sup>

---


$$c = \frac{n}{V} = \frac{1.13 \text{ mmol}}{0.05 \text{ L}} = 22.5 \text{ mmol/L} \quad (23)$$


---

This would result in the following pH

---


$$\text{pH} = -\log(c_{\text{H}^+}) = 1.65 \quad (24)$$


---

Matching the observed value of 1.6 shown in Figure 42. For a single MEA with m(PFSA, 5 cm<sup>2</sup>) = 0.325 g, the number of sulfonic acid groups is calculated:<sup>2</sup>

<sup>2</sup>In these calculations, the PFSA hydration of approx. 5% is neglected.<sup>[77]</sup> EW refers to the minimum guaranteed acid capacity of the membrane,<sup>[74]</sup> the acid capacity is obtained from base titration by the provider.<sup>[141]</sup>

$$n_{\text{-SO}_3\text{H}} = \frac{m}{EW} = \frac{0.325 \text{ g}}{1100 \text{ g/mol}} = 295 \mu\text{mol} \quad (25)$$

Given the available acid capacity ( $\geq 0.90 \text{ meq/g} = \text{mmol/g}$ ) as specified by the provider,<sup>[141]</sup> our  $5 \text{ cm}^2$  membrane piece ( $m = 325 \text{ mg}/5 \text{ cm}^2$ ) calculates for  $\geq 0.293 \text{ mmol}/5 \text{ cm}^2 = 293 \mu\text{mol}/5 \text{ cm}^2$ , perfectly matching the obtained value within the error of experiment.

Additionally, the results in Figure 42 show that the ion exchange process is slightly quicker than a standard potentiodynamic cyclovoltammetric (CV) scan from 1.4 to 3.4 V at 10 mV/s (total time 200 s) as shown in the next section. Given the strongly bound  $\text{K}^+$  in the membrane but the need for a low-energy cation transport over or at least out of the membrane, the next question arises: Can an applied voltage overcome this high interaction energy and drive the cations over the membrane and if so, how can we quantify it?

### Basic principles: variation of the electrolysis operation mode

To realistically model  $\text{CO}_2$  electrolysis applications, two electrolyte modes ( $\text{mode}_{\text{mix}}$  and  $\text{mode}_{\text{sep}}$ ) are employed during the experimental part of this study. In a model setup, we aim at evaluating high molar salt solutions as electrolytes to study their influence on PFSA membrane resistance and quantify  $V_{\text{ohm}}$  (equation 20). This way, electrochemical voltage contributions in  $\text{CO}_2$  electrolysis will be deciphered and summarized at the end of this study.

Electrochemical experiments were conducted in a galvanostatic mode at distinct current densities (between  $1.0 \text{ mA/cm}^2$  and  $1.0 \text{ A/cm}^2$ ). Different operation modes ( $\text{mode}_{\text{mix}}$  vs.  $\text{mode}_{\text{sep}}$ ) were investigated. At each galvanostatic step, the current density was held for 10 min and the necessary voltage was recorded as a function of time. An example of the raw data can be found in the SI. The data was then averaged for each step and plotted versus current density with the results shown in Figure 43. Experiments were reproduced at least two times.

Figure 43a shows the cell voltage results obtained from feeding the electrolyte at the two different half-cells, respectively. When feeding  $1.0 \text{ M KHCO}_3$  at the cathode side only (red triangles), a shift in voltage is visible, resulting in a maximum of 4.22 V at

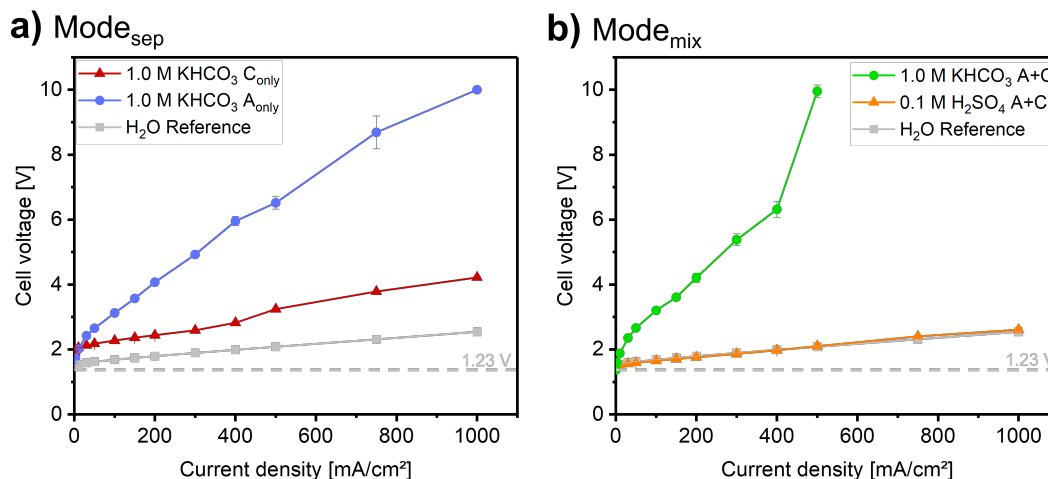


**Figure 43:** Results obtained from a variation of the electrolysis operation mode: Electrolyte studies were conducted in different experimental configurations: a) mode<sub>sep</sub> with electrolyte at one side only (and ultrapure water at the other side, respectively) and b) mode<sub>mix</sub>. Both measurements are referenced to the same control experiment with no electrolyte, but ultrapure water used at both sides (grey squares).

1.0 A/cm<sup>2</sup> vs. reference (2.54 V at 1.0 A/cm<sup>2</sup>). As hypothesized earlier, this is due to a resistance increased caused by stronger sulfonate- $K^+$  interactions. When 1.0 M KHCO<sub>3</sub> are fed at the anode (blue dots), the cell voltage exceeds 10 V at 1.0 A/cm<sup>2</sup>. Comparing the values at 750 mA/s, 8.69 V are required vs. reference (2.31 V, cathode side: 3.78 V at 750 mA/cm<sup>2</sup>). Additionally, the error is notably big, which results from an accelerated cell voltage increase during the 750 mA/cm<sup>2</sup> galvanostatic step. Such voltage increase has been described in literature at high current densities and modeled theoretically for multi-ion transport over Nafion<sup>®</sup> already. In a *Nernst-Planck* modeling, it was shown that an increased current density causes more dead-end pores to open up, increasing the number of active pores, which leads to a non-linear behavior of the voltage increase with current density.<sup>[104]</sup> Depending on the operation mode, the increase could be observed at different current densities as will be shown in the following chapter. The difference between the two operation modes is due to different resistive contributions when  $K^+$  is either soaked into the membrane (C<sub>only</sub> mode) or transported over it (mode<sub>mix</sub>). In all cases, the course of the curve is linear indicating an ohmic behavior of the membrane. In the case of a non-linear resistive behavior (e.g. exponential), there might be a space charge limitation, a phenomenon known from semiconductors and electronics.<sup>[142]</sup> Transferred to the present case, space charge limitation means an oversupply of  $K^+$  while there are not enough negative centers to enable ion hopping across the membrane

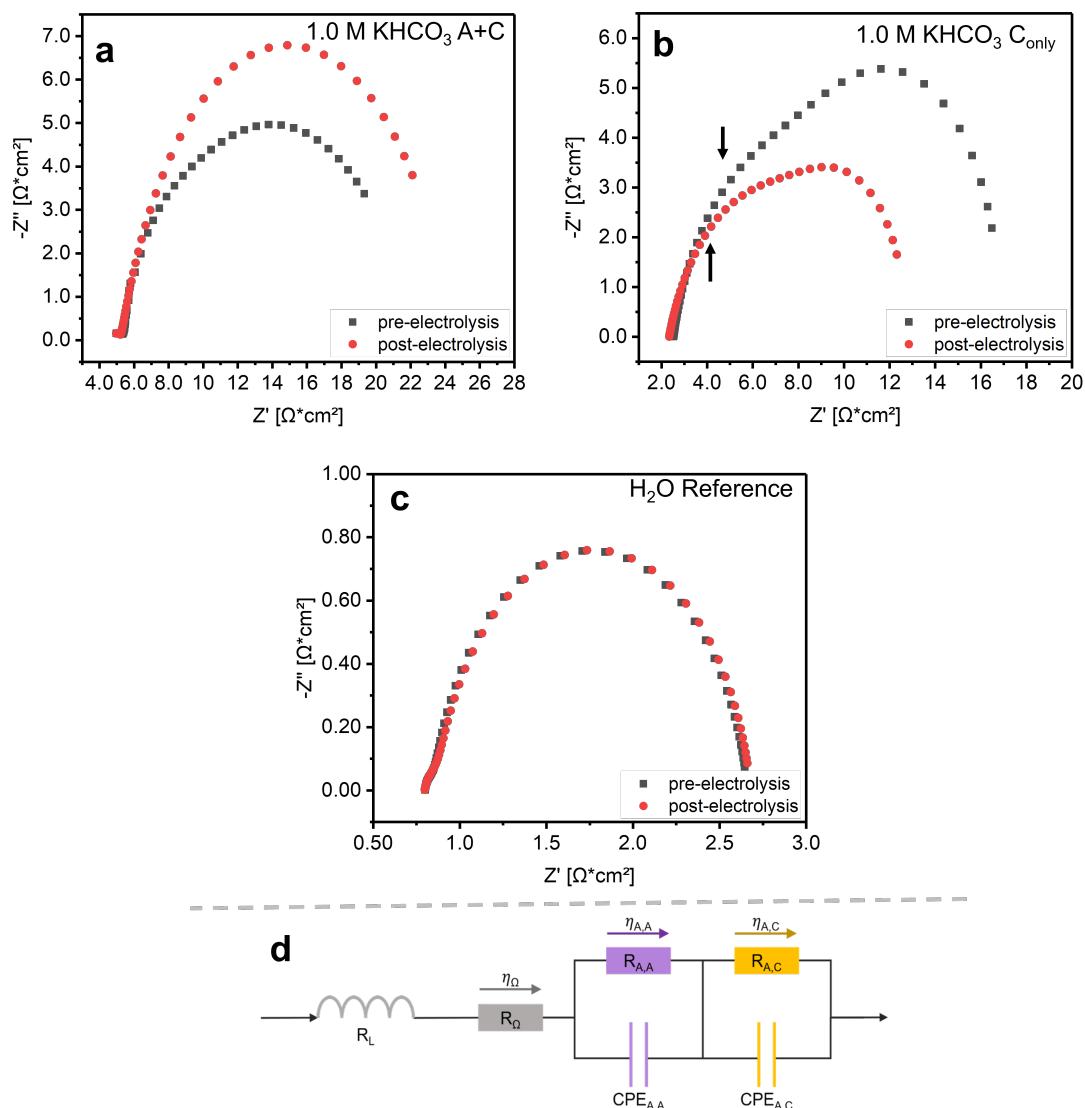
(charge carrier congestion in the membrane). The effect is caused by the strength of ionic interaction, which prevents a *Grotthuss*-like tunneling mechanism as is possible for protons *via* hydrogen bond folding and leads to an exponential increase in membrane resistance. It will be discussed in detail in the following chapters.

Figure 43b shows an even more pronounced voltage increase for mode<sub>mix</sub> with 1.0 M KHCO<sub>3</sub> with a non-linear behavior and a voltage increase at 400 mA/cm<sup>2</sup>. In this case, it can be assumed that charge transfer is exclusively performed *via* K<sup>+</sup> transportation. Since both electrolytes were constantly mixed, the K<sup>+</sup> concentration remained constant over the course of the experiment, while in the Aonly experiment shown in Figure 43a, the K<sup>+</sup> transport over the membrane caused a concentration decrease during the procedure. This leads to a decreased competition of K<sup>+</sup> with the protons from OER with increasing time. An experiment with 0.1 M H<sub>2</sub>SO<sub>4</sub> in mode<sub>mix</sub> showed little differences to the reference (H<sub>2</sub>O) case, indicating that the charge transport is exclusively accomplished by protons. This is a first indication that the increased voltage is due to the cation load at the MEA. Strong ionic interactions of the K<sup>+</sup> metal ions with the sulfonic acid groups need to be overcome while protons are only loosely bound to the negatively charged polymer end groups (formal pKa  $\approx$  -6 for -SO<sub>3</sub>H).<sup>[69]</sup> Coming back to our use case, CO<sub>2</sub> electrolysis, we observe an opposed effects regarding ionic conductivity of the membrane vs. the electrolyte itself: While the membrane resistance increases and its conductivity decreases, high molar salt solutions are commonly used to enhance electrolyte conductivity. A study was conducted highlighting the positive impact of high concentrations on the electrolyte conductivity (0.5 M giving 77 mS\*cm vs. 2.0 M giving 211 mS\*cm). The authors state that this impacts the overall operation voltage due to a reduced resistance in transporting solvated products over an electrolyte gap.<sup>[13]</sup> The general effect on membrane resistance remains however. This is true and we will complement the existing data by comparison of conductivity data in an in-depth examination of different molarities in section below. We will also take a deeper look into the ohmic part of the stationary CVs (Figure 43) and electrochemical impedance spectroscopy (EIS), which is important to quantify membrane resistances.

### **Resistance determination by electrochemical impedance spectroscopy**

The stronger ionic interactions and thus increased membrane resistances are not only reflected in a higher cell voltage required. They can also be accessed quantitatively

through impedance spectroscopy. Results from a water reference and a comparison between mode<sub>mix</sub> and  $C_{only}$  mode are shown in Figure 44.



**Figure 44:** Nyquist plots showing electrochemical impedance spectra obtained pre- and post-electrolysis: a) 1.0 M  $KHCO_3$  at anode and cathode side (A+C), b) 1.0 M  $KHCO_3$  at cathode side only ( $C_{only}$ ) and c)  $H_2O$  reference. The frequency range comprised 10.0 kHz to 40.0 mHz with an amplitude of 5.00 mA and 66 points per decade. d) Equivalent circuit diagram, on which EIS fittings are based.

EIS was performed at a current of  $10 \text{ mA/cm}^2$  (50 mA total). Standard deviations were  $\pm 10.0 \text{ m}\Omega \text{ cm}^2$  with the procedure applied three times at one MEA and  $\pm 30.0 \text{ m}\Omega \text{ cm}^2$  for three different MEAs. The obtained data was fitted with an equivalent

circuit diagram (shown in the SI), where MEA contacting is implemented as RL and assumed constant for all experiments. This allows for a comparison of the remaining resistive contributions: The ohmic contribution to the resistance can be read off the origin of the obtained *Nyquist* plots (zero crossing) in the high frequency region of the graph (HFR).<sup>[143,144]</sup> We refer to this contribution as the membrane resistance  $R_{\Omega}$ . The width of the *Nyquist* plot depicts the charge transfer resistance ( $R_{CT}$ ) and comprises kinetic as well as mass transport contributions at the electrodes, both at the anode ( $R_{A,A}$ ) and the cathode ( $R_{A,C}$ ) catalyst. It is calculated subtracting the high frequency from the low frequency resistance:  $R_{CT} = R_{LFR} - R_{HFR}$ . The essential data is summarized in Table 13.

**Table 13:** Membrane and charge transfer resistances obtained from *Nyquist* plots shown in Figure 44, normalized to the active surface area of  $5 \text{ cm}^{\text{arg}}$ . For membrane resistances, values are compared at the onset of the graph (high frequency resistance, HFR). LFR – low frequency resistance, el – electrolysis.

| Experiment                                       | Membrane              | Membrane              | LFR                   | LFR                   | HFR                   | HFR                   |
|--|-----------------------|-----------------------|-----------------------|-----------------------|-----------------------|-----------------------|
|  | resistance            | resistance            |                       |                       |                       |                       |
|  | pre-el                | post-el               | pre-el                | post-el               | pre-el                | post-el               |
|  | $\Omega \text{ cm}^2$ | $\Omega \text{ cm}^2$ | $\Omega \text{ cm}^2$ | $\Omega \text{ cm}^2$ | $\Omega \text{ cm}^2$ | $\Omega \text{ cm}^2$ |
| a) 0.5 M $\text{KHCO}_3$<br>at A+C               | 4.97                  | 4.97                  | 19.3                  | 22.1                  | 14.4                  | 17.1                  |
| b) 0.5 M $\text{KHCO}_3$<br>at $C_{\text{only}}$ | 2.53                  | 2.34                  | 16.5                  | 12.3                  | 14.0                  | 9.94                  |
| c) $\text{H}_2\text{O}$ reference                | 0.80                  | 0.80                  | 2.64                  | 2.66                  | 1.85                  | 1.86                  |

EIS results enable an evaluation of changes in the membrane resistance, which is one important part of the total cell resistance, reflected as  $V_{\text{ohm}}$  in equation 20. As we expected, the ohmic resistance for the  $\text{H}_2\text{O}$ -reference experiment is comparatively low and does not change during the experiment (Figure 44c,  $0.800 \Omega \text{ cm}^2$  pre- and post-electrolysis). Applying an electrolyte in the system at both, anode and cathode side, drastically increases the membrane resistance (Figure 44a,  $4.97 \Omega \text{ cm}^2$  pre- and post-electrolysis) by a factor of 10. Matching the results from the galvanostatic measurement procedure, the membrane resistance also increases when feeding electrolyte at the cathode side only (Figure 44b,  $2.53 \Omega \text{ cm}^2$ ). The significant difference in this case is that no  $\text{K}^+$  needs to be transported over the membrane to close the

electric circuit. Instead,  $K^+$  is only in contact with the membrane from the cathode side, soaked in but then driven back along with the electrodiffusion direction. No  $K^+$  is supplied from the anode side.<sup>[65]</sup> During the course of the experiment, the values for both these experiments do not change significantly, since the first step in the measurement procedure is a CV. The membrane is saturated with  $K^+$  due to the CV performed previously.

In addition to the membrane resistance, EIS provides insights into another resistive contribution, namely charge-transfer resistances ( $C_{TR}$ ) of the membranes, which can be accessed by subtracting HFR from LFR. The CTR is thus illustrated as the width of the *Nyquist* plot. EIS was measured at  $10 \text{ mA/cm}^2$ , marking the beginning of the ohmic region in potentiodynamic cyclovoltammetry measurements (data given in the SI). At lower current densities (*Tafel* region of the CV), conclusions cannot be drawn since the system is not in relevant operation mode, whereas gas formation (bubbles) would distort measurement results at higher current densities. In the present case, there is only minor change observable in CTR for the water reference ( $1.85$  pre- vs.  $1.86 \text{ } \Omega \text{ cm}^2$  post-electrolysis). In the  $\text{mode}_{\text{mix}}$  (Figure 44a), the CTR increases when comparing pre- ( $14.4 \text{ } \Omega \text{ cm}^2$ ) with post-electrolysis ( $17.1 \text{ } \Omega \text{ cm}^2$ ) data. This is due to an increased  $K^+$  concentration not only throughout the membrane but especially at the electrodes: At the beginning of the experiment, electrode protonation is comparatively high despite spontaneous proton-metal substitution in the PFSA polymer. In our model system, electrodes are coated into the upmost layer of the polymer membrane, which provides them with a highly acidic environment. In water electrolysis, proton supply is given by ionic transport of  $H^+$  stemming from the anodic OER. In the case of an electrolyte used in  $\text{mode}_{\text{mix}}$ ,  $K^+$  competes with  $H^+$  for being transported. At  $\text{pH} \approx 8$ , the concentration orders of magnitude differ significantly ( $c_{H^+} = 10^{-8} \text{ mol/L}$  vs.  $c_{K^+} = 10^{-1} \text{ mol/L}$ ), which implies approx. 90% transported cations are  $K^+$ .<sup>[13]</sup> Due to the strong affinity to the sulfonic acid groups, protonation at both electrodes changes during the course of the experiments and increases the CTR and thus contributes to the overall required cell voltage. In the case of a  $C_{\text{only}}$  operation mode, the effect is inversed: the CTR decreases when comparing pre- ( $14.0 \text{ } \Omega \text{ cm}^2$ ) with post-electrolysis ( $9.94 \text{ } \Omega \text{ cm}^2$ ) data. The protonation level at the beginning of the experiment is comparable to  $\text{mode}_{\text{mix}}$ . But during the course of the experiment, protonation at the electrodes is restored, since  $K^+$  is back-exchanged by protons stemming from the anodic OER until a steady state is reached. Although  $K^+$  is still soaked into the membrane (against the direction of electrodiffusion), no metal ions are transported from the anode side. These observations are well in line

with our earlier results, proving quantitative potential-driven substitution (PDS) *in situ* for  $\text{Li}^+$  ions in PFSA.<sup>[65]</sup> The different protonation levels at cathode (low protonation due to  $\text{K}^+$  drag into the membrane) and anode (high protonation due to OER) are also reflected in the *Nyquist* plot shape: In a MEA setup, differentiation between anode and cathode side resistance (expressed by two separated half-cycles) is often impossible due to a very close neighborhood and intimate interactions of the whole system.<sup>[35]</sup> Due to the differences in protonation, the electrodes become slightly differentiable and therefore, the *Nyquist* plot shows a shoulder, which can be traced back to the anode (Figure 44b, arrow). The predominant half-cycle is caused by the cathode. Here, the CTR is remarkably higher due to the high  $\text{K}^+$  concentration in close proximity to the electrode.

In our water electrolysis model we could thus demonstrate the following: when using an electrolyte, cations in the membrane cause significant increases in resistance. This translates directly into an increased required cell voltage necessary to overcome the strong ionic interactions between  $\text{K}^+$  and sulfonic acid groups. The resistance is composed of the membrane resistance and the charge transfer resistance and will be quantified in the following chapters. Combined with the insights about the space charge limits of the system shown in section 3.2, we can furthermore deduce that the ohmic portion of the voltage loss in  $\text{CO}_2$  electrolysis is itself divided into two parts: First, an interaction contribution  $V_{\text{int}}$ , which originates from the sulfonate- $\text{K}^+$  interactions and second, a space-charge contribution  $V_{\text{SC}}$ , which only appears if the  $\text{K}^+$  concentration exceeds the transport capacity determined by the present  $-\text{SO}_3^-$ . We deduce

---


$$V_{\text{ohm}} = V_{\text{int}} + V_{\text{SC}} \quad (26)$$


---

Before looking deeper into their quantification, we will first define  $V_{\text{ref}}$  for our model system. Since the use of different electrolytes comes with a change in pH (e.g. pH = 8.5 for 1.0 M  $\text{KHCO}_3$ ), which could also impact the required cell voltage, we will assess the underlying thermodynamic data in the following section.



### Thermodynamic considerations

Using different electrolytes is a popular lever to adjust pH environment in CO<sub>2</sub> electrolysis. Acidic conditions in the electrolyte as well as on the membrane cause HER competition with the desired CO<sub>2</sub> reduction and must thus be avoided. Since the cathode needs to be protected from protons, the principle of a so called liquid buffer layer consisting of e.g. a bicarbonate solution is very common.<sup>[114]</sup> Here, we need to differentiate between the bulk pH that is determined by the electrolyte used and the local pH at the electrode (GDE). As soon as protons or hydroxide ions are produced or consumed during a half-cell reaction, the local pH at the catalyst site changes. This effect is enforced with increasing current density. We have thus acidic conditions at the anodic Ir catalyst, where protons are produced from the OER. At the cathode, the environment is rather basic when K<sup>+</sup> is transported over the membrane. In CO<sub>2</sub> electrolysis, a basic environment is especially desirable since HER needs to be suppressed in favor of CO<sub>2</sub>RR. Changes in both, local and bulk pH influence the cell voltage that needs to be quantified. Together with K<sup>+</sup> transportation phenomena, this will lead us to a comprehensive contemplation of electrolyte use in CO<sub>2</sub> electrolysis. The thermodynamics relevant for the electrochemical processes considered in this study are based on the *Nernst* equation

$$E = E^0 + \frac{RT}{z_e F} * \ln\left(\frac{a_{\text{ox}}}{a_{\text{red}}}\right) \quad (27)$$

with the electrode potential  $E$ , the standard electrode potential  $E^0$ , the universal gas constant  $R = 8.31447 \text{ J mol}^{-1} \text{ K}^{-1}$ , the absolute temperature  $T$ , the number of transferred electrons  $z_e$ , the *Faraday* constant  $F = 96485.34 \text{ C mol}^{-1}$  and the activity of the respective redox partner  $a_i$ . To evaluate the impact of pH changes on the cell voltage at room temperature ( $T = 298.15 \text{ K} \equiv 25 \text{ }^\circ\text{C}$ ), the H<sup>+</sup> concentration element ( $z_e = 1$ ) is considered and the natural logarithm is converted into the decadic logarithm ( $\lg(a_{\text{H}^+}) = \ln(a_{\text{H}^+}) / \ln 10$ ). With respect to the pH definition ( $\text{pH} = -\lg a_{\text{H}^+}$ ), we obtain the following equation:

$$\Delta E = -0.059\text{V}(\text{pH}_1 - \text{pH}_2) \quad (28)$$

This causes an additional bulk pH influence on cell in addition to membrane resistances when electrolysis is performed in modesep but not for mixed electrolyte configurations. But in the latter case, there are as well changes in local pH. In a first quantification approach, we neglect local pH as a first assumption. Local pH determination is very complex,<sup>[145]</sup> since the local conditions can be fluctuating and measurement equipment must be extremely sensitive. Alternatively, we provide the following thermodynamic calculations (Table 14) visualized in Figure 45.<sup>3</sup> pH values depicted in the figure were determined experimentally and converted into an electrochemical potential using equation 28.

As an example,  $\Delta H$  (at realistic conditions) is used to correlate the reaction enthalpy with the cell voltage and the OER is considered as follows (HER as a standard is set as 0)



with  $\Delta H_{\text{H}_2\text{O}(\text{l})} = -286 \text{ kJ/mol}$  and  $\Delta H_{\text{O}_2(\text{g})} = \Delta H_{\text{H}^+(\text{aq})} = \Delta H_{\text{e}^-} = 0$ , we obtain  $\Delta H_{\text{OER}} = 572 \text{ kJ/mol}$ .

The obtained enthalpy value can be converted into the half-cell potential  $U_{\text{half-cell}}$  ( $\Delta H$ ) by

---


$$U_{\text{half-cell}}(\Delta H) = \frac{(\Delta H_{\text{OER}} * 1000 - 0.059\text{V}(\text{pH}_1 - \text{pH}_2))}{(F * e)} = 1.48\text{V} \quad (30)$$


---

The shown case gives the value for  $\Delta \text{pH} = 0$  and exemplifies the calculations underlying the following section at industrially relevant current densities. However,

---

<sup>3</sup>Thermodynamic data was assessed through the standard enthalpy of formation ( $\Delta H$ ).<sup>[25]</sup> The reason for applying  $\Delta H$  (instead of e.g. the Gibbs Free Energy  $\Delta G$  that is often used in literature<sup>[24]</sup>), is a comprehensive consideration of realistic influences, such as latent heat.<sup>[25]</sup>  $\Delta G$  is only valid in an adiabatic system at constant pressure and temperature, which is true for a turnover of 0. The system here is in equilibrium with its surroundings. Under industrially relevant conditions at high current densities, this is not the case and latent heat must be considered. The difference between  $\Delta H$  and  $\Delta G$  equals  $T^*\Delta S$ .

in an analogue calculation,  $U_{\text{half-cell}}$  ( $\Delta G$ ) based on the Gibbs Free Energy is calculated to 1.23 V,<sup>[25]</sup> which will be the basis for the following considerations due to the assumption that the current density is  $I = 0 \text{ A/cm}^2$ .

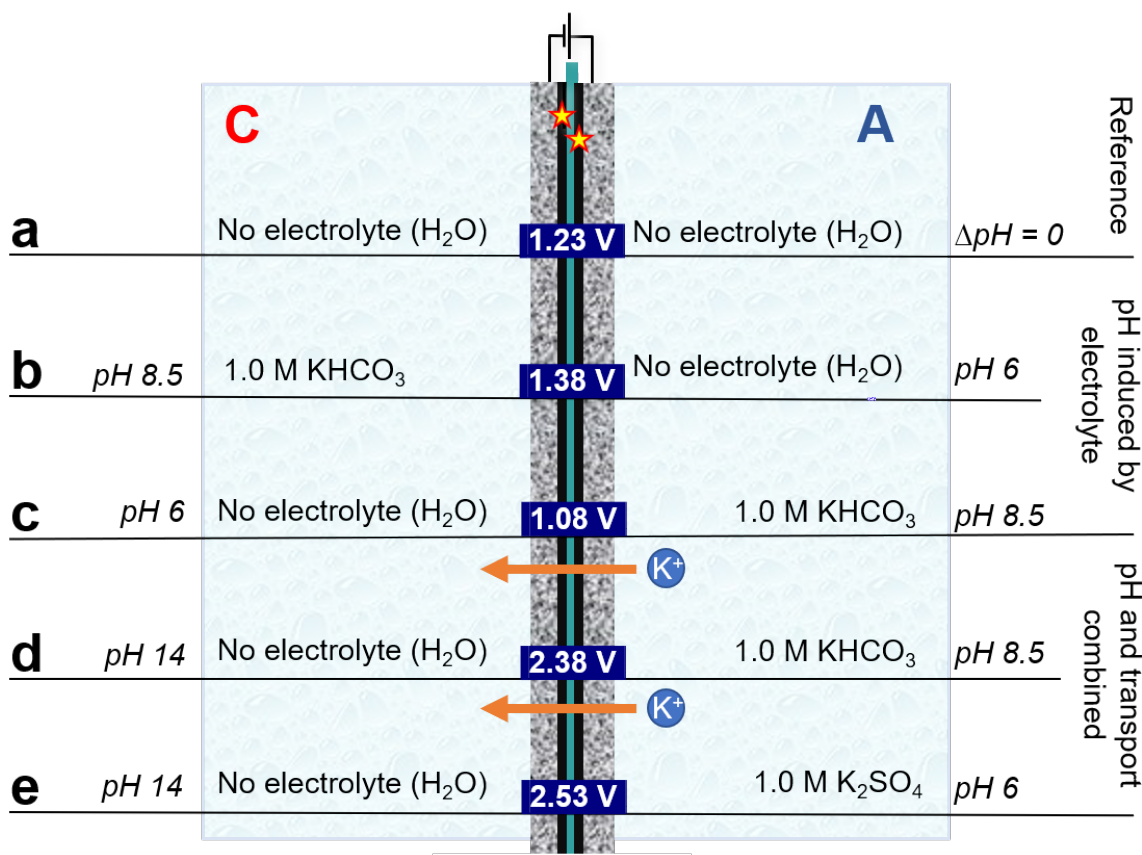


**Figure 45:** Visualization of different experimental configurations and implied pH differences. a) No electrolyte used, 1.0 M KHCO<sub>3</sub> at b) the cathode and c) the anode side. The impact of K<sup>+</sup> transport on the reaction and local pH microenvironment is considered with d) 1.0 M KHCO<sub>3</sub> and e) 1.0 M K<sub>2</sub>SO<sub>4</sub> at the anode side.

a) In the standard operation setup of a PEM electrolyzer, where only ultrapure water is cycled through the cell, there is no difference in bulk-pH and thus no pH gradient to either half-cell. Once the electrochemical reaction is initiated by an applied voltage, the pH will change locally at the catalyst sites. At the anodic iridium catalyst, protons are produced, which then migrate over the membrane, resulting in very low local pH values.<sup>[25]</sup> This effect becomes increasingly pronounced with increasing current density and since this effect cannot easily be quantified, our calculations are only valid at no (extrapolation to 0 current) or very low current densities after reaching steady state, e.g. at the 1.0 mA/cm<sup>2</sup> galvanostatic point. At this

current density, the observed cell voltage was 1.46 V. Compared to 1.23 V (the thermodynamic limit of the reaction at no current density), the approx. 200 mV voltage loss can be attributed to setup specific losses e.g. in the form of latent heat.

**b)** If an electrolyte is used at the cathode side only, the difference in pH is caused by the cathode side. In the case of  $\text{KHCO}_3$  with a pH of 8.5, protons crossing the membrane might be consumed by the electrolyte before being consumed by the electrochemical reaction for generating  $\text{H}_2$ . The pH induced difference in potential is  $\Delta E = 2.5 * 0.059 \text{ V} = 0.15 \text{ V}$ , which is required in addition to the thermodynamic limit of water splitting (1.23 V).<sup>[24]</sup>

**c)** If the electrolyte is used at the anode side, the pH gradient is mirrored compared to b). The pH difference arises through the anode, which leads to an inverted algebraic sign. The required thermodynamic potential limit is formally reduced by 0.15 V.

**d)** In addition to the mere pH difference ( $\text{KHCO}_3$  electrolyte at the anode side only), the  $\text{K}^+$  transport over the membrane is considered in this case. Stronger interactions with the membrane as well as a high  $\text{K}^+$  availability ( $10^{-1} \text{ M}$ ) at low current densities ( $\text{H}^+$  availability  $10^{-7} \text{ M}$ ) makes  $\text{K}^+$  the main charge carrier transported across the membrane.<sup>[13]</sup> This being the fundament of our interpretations, there are almost no protons available for electroreduction at the cathode side. As such, water is reduced instead of protons ( $2 \text{ H}_2\text{O} + 2 \text{ e}^- \rightarrow \text{H}_2 + 2 \text{ OH}^-$ ) leaving  $\text{OH}^-$  as a side product, which in turn increases first the local and during operation also the overall pH in the catholyte. This change in pH needs to be considered thermodynamically, leading to a pH-induced voltage difference of 330 mV. Considering the changed ongoing reaction, the galvanic series states +0.4 V.<sup>[25]</sup> Theoretically extending the reaction time to  $t \rightarrow \infty$ , this case leads to 1.0 M  $\text{KOH}(\text{aq})$  at the cathode side and water at the anode side, since protons cause bicarbonate decomposition into water and  $\text{CO}_2$ .

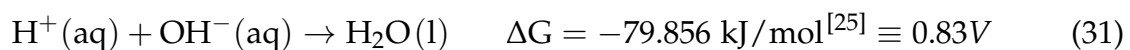
**e)** In this last and most energy consuming case, the  $\text{K}^+$  transport is also considered but the electrolyte salt was replaced by  $\text{K}_2\text{SO}_4$ . The induced pH difference is thus bigger by 2.5 compared to case d), which leads to a maximum thermodynamic volt-

age requirement of 470 mV  $\approx$  0.5 V. At  $t \rightarrow \infty$ , the same case will end up in a 1.0 M KOH(aq) at the cathode side and  $H_2SO_4$  formation at the anode side.

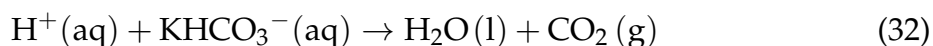
**Table 14:** Thermodynamic considerations towards different experimental configurations shown in Figure 45. pH induced potential differences were calculated using equation 28 in combination with the experimental pH data given in Figure 45.

|    | <b>Cathode reaction</b>  | <b>Anode reaction</b>  | <b>pH induced potential difference</b> | $E_{cell}^0$ |
|----|--|--|--|--------------|
| a) | $4 H^+(aq) + 4 e^- \rightarrow 2 H_2(g)$<br>$E_c^0 = 0.00 \text{ V}$               | $2 H_2O(l) \rightarrow O_2(g) + 4 e^- + 4 H^+(aq)$<br>$E_a^0 = 1.23 \text{ V}$ | 0.00 V                                 | 1.23 V       |
| b) | $4 H^+(aq) + 4 e^- \rightarrow 2 H_2(g)$<br>$E_c^0 = 0.00 \text{ V}$               | $2 H_2O(l) \rightarrow O_2(g) + 4 e^- + 4 H^+(aq)$<br>$E_a^0 = 1.23 \text{ V}$ | +0.150 V                               | 1.38 V       |
| c) | $4 H^+(aq) + 4 e^- \rightarrow 2 H_2(g)$<br>$E_c^0 = 0.00 \text{ V}$               | $2 H_2O(l) \rightarrow O_2(g) + 4 e^- + 4 H^+(aq)$<br>$E_a^0 = 1.23 \text{ V}$ | -0.150 V                               | 1.08 V       |
| d) | $4 H_2O(l) + 4 e^- \rightarrow 2 H_2(g) + 4 OH^-(aq)$<br>$E_c^0 = 0.830 \text{ V}$ | $2 H_2O(l) \rightarrow O_2(g) + 4 e^- + 4 H^+(aq)$<br>$E_a^0 = 1.23 \text{ V}$ | +0.330 V                               | 2.38 V       |
| e) | $4 H_2O(l) + 4 e^- \rightarrow 2 H_2(g) + 4 OH^-(aq)$<br>$E_c^0 = 0.830 \text{ V}$ | $2 H_2O(l) \rightarrow O_2(g) + 4 e^- + 4 H^+(aq)$<br>$E_a^0 = 1.23 \text{ V}$ | +0.470 V                               | 2.53 V       |

These calculations show that using an electrolyte on the anode side has a formal positive effect since the thermodynamic potential limit is reduced. Under real conditions however, when  $K^+$  transport is considered, the additional energy required for cases d) and e) is comparable to the neutralization energy following the equation 31, when the stoichiometry ( $n = 2$ ) is considered.



During the experiment, local pH changes affect the global pH in the respective electrolyte, since  $K^+$  and  $OH^-$  accumulate in the catholyte compartment, while  $H^+$  recombines with sulfate anions producing sulfuric acid or induces bicarbonate anion decomposition in the anolyte compartment producing KOH. This is visible in a measurable, global pH shift from pH 6 to pH 5 at the anode side (if  $K_2SO_4$  is used) and a shift from pH 6 to pH 7 at the cathode side at the end of the experimental procedure. If  $KHCO_3$  is used as the anolyte, the proton surplus is consumed as soon as in contact with the bulk, according to the following equation:



The difficulty regarding local pH values remains unsolved and current research focuses on finding a solution to this problem.<sup>[146]</sup> However, in a mathematical model study it was shown that the conditions at the electrode (during  $CO_2$  electrolysis) are increasingly fluctuating the closer it gets to the electrode and the higher current densities become, but with an increased concentration, local pH values at the electrode converge increasingly towards the bulk pH.<sup>[116]</sup> In summary, these considerations provide us with  $V_{rev} = 1.48$  V, which is the thermodynamic limit for our water electrolysis system at industrially relevant current densities. pH analyses showed that additional voltage contributions must be considered when using  $mode_{sep}$ . We will include these finding in our later transfer of the obtained knowledge to our  $CO_2$  electrolysis use case.

### **Concentration variation in separate electrolyte mode ( $mode_{sep}$ ) using catholyte only**

$CO_2$  electroreduction takes place at the cathode side of the cell. When in contact with the membrane,  $K^+$  is soaked into the PFSA polymeric structure and impacts the membrane resistance. This becomes visible in a significant voltage increase. To investigate the dependence on concentration and current density, we conducted a study employing  $KHCO_3$  in different concentrations (1.0 mM, 0.5 M, 1.0 M, 1.5 M) at the cathode side only while using ultrapure water at the anode side. Results are given in Figure 46a with the reference measurement (ultrapure water used in both half cells) represented by grey squares. As a measure of data clearing, the reference

measurement was subtracted from each concentration curve giving the pure overpotential caused by K<sup>+</sup>. These results are depicted in Figure 46b and represent purely the portion of the applied voltage that is due to the usage of an electrolyte instead of ultrapure water.

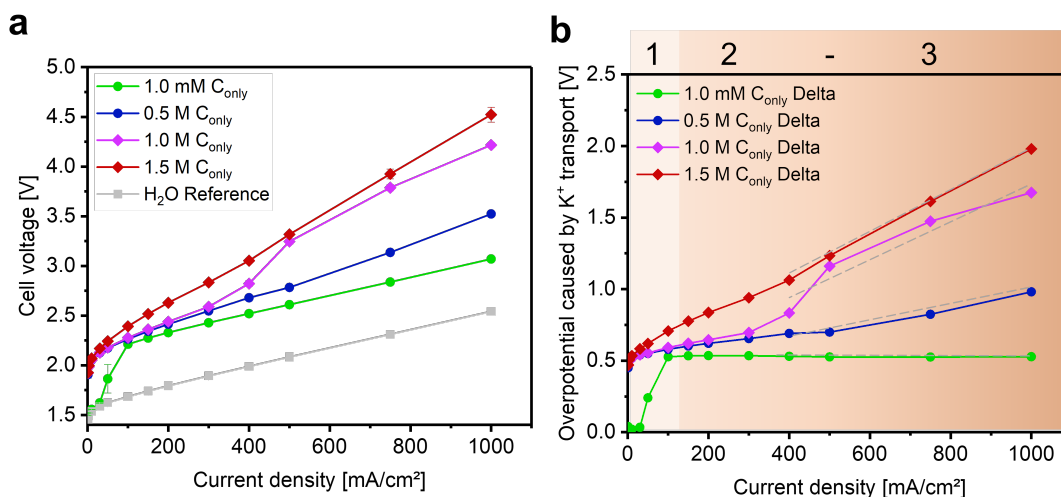


**Figure 46:** Concentration variation study in modesep with electrolyte used at the cathode side only. a) results of the original study and b) pure K<sup>+</sup>-induced overpotentials obtained from subtracting reference mean values at each current density step from the respective results with electrolyte at the cathode side only (C<sub>only</sub>) experiments at different concentrations (1.0 mM, 0.5 M, 1.0 M and 1.5 M KHCO<sub>3</sub>).

For the lowest concentration (1.0 mM) the required voltage was shifted. Above 100 mA/cm<sup>2</sup>, the linear course of the curve was identical to the reference measurement with a similar slope. The voltage required at 100 mA/cm<sup>2</sup> was 527 mV higher (2.21 V vs. 1.68 V). Even at the highest measured current density (1.0 A/cm<sup>2</sup>), the shift from the reference remains the same (3.07 V vs. 2.54 V). The remaining concentration curves show strongly increased cell voltages with increasing concentration. At a low current density of 30 mA/cm<sup>2</sup> (reference at 1.59 V) the differences between the different concentrations did not show any significant resistance increases yet (0.5 M at 2.13 V, 1.0 M at 2.13 V and 1.5 M at 2.17 V). With increasing current density (1.0 A/cm<sup>2</sup>) also the voltage increased (e.g. 4.52 V for 1.5 M vs. 2.54 for the reference) but not as sharply as observed in mode<sub>mix</sub>. In the present mode<sub>sep</sub>, no K<sup>+</sup> transport across the membrane is performed. The observed voltage shift with subsequent further increases can rather be explained by an overlay of V<sub>int</sub> and V<sub>SC</sub>: The cell voltage shift of 527 mV accounts for V<sub>int</sub>, while at higher concentrations the space charge effects contribute to the required voltage increase. At the same time,

the space-charge-limitation is not as pronounced as before in mode<sub>mix</sub>, since  $K^+$  is not transported over the membrane but only driven back to the cathode side. More insight about the  $C_{\text{only}}$  mode as shown by Haas et al.<sup>[13]</sup> and its implications for  $CO_2$  electrolysis can be obtained from the overpotentials caused by  $K^+$  shown in Figure 46b: We attributed three current density regimes to the graph as illustrated by range 1, 2 and 3 in Figure 46b. A clear differentiation can only be made between range 1 and 2. Ranges 2 and 3 smooth out resulting in a clear slope from ca.  $300 \text{ mA/cm}^2$ . The slopes in range 3 are depicted as grey dotted lines and are listed in Table 15.

**Table 15:** Slopes obtained from the linear, ohmic region of  $C_{\text{only}}$  overpotential curves depicted in Figure 46. The respective linear fits are shown as grey dotted lines in the graph.

| Concentration | Slope<br>(membrane resistance)                 |
|---------------|--|
| 1.0 mM        | $-3.68 \pm 5.16 \mu\Omega \text{ cm}^2$        |
| 0.5 M         | $0.499 \pm 0.056 \text{ m}\Omega \text{ cm}^2$ |
| 1.0 M         | $1.32 \pm 0.25 \text{ m}\Omega \text{ cm}^2$   |
| 1.5 M         | $1.50 \pm 0.02 \text{ m}\Omega \text{ cm}^2$   |

Plotting the slopes against concentration, a linear fit is obtained. The slopes equal the membrane resistance according to Ohm's law ( $R = U/I$ ) but within this, just the portion of the resistance that is caused by the metal cations' presence, since the reference measurement was subtracted. The obtained resistances are not directly comparable to those obtained by electrochemical impedance spectroscopy, since impedance is measured at very small current densities and under frequency application ( $f = 1000 \text{ Hz}$ ). However, the resistance values allow for valuable insights at industrial conditions in the cell. At the smallest concentration, the slope is slightly negative but very small. With increasing current density and concentration, the slopes increase ( $0.499 \text{ m}\Omega \text{ cm}$  for  $0.5 \text{ M}$  vs.  $1.50 \text{ m}\Omega \text{ cm}$  for  $1.5 \text{ M}$ ). Once a voltage is applied to the cell,  $K^+$  is driven back to the cathode side and out of the membrane and its reentrance is hindered, since it runs against the electrodiffusion direction of the protons generated at the anode. The underlying model is visualized in Figure 47 to look deeper into this current density dependent phenomenon and gain in-depth knowledge about the complex processes in the cell.



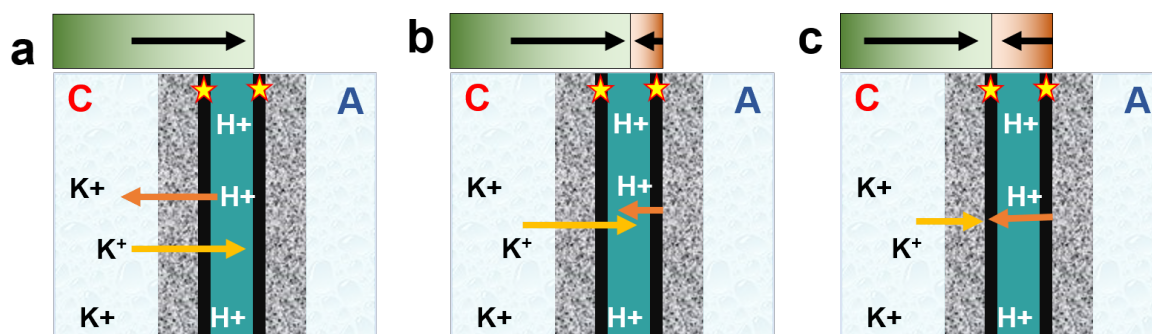


**Figure 47:** Visualization of cation migration directions at a) open circuit potential (without applied voltage and thus current), b) low current density and c) high current density. C – cathode, A – anode.

It is important to notice that before applying a voltage to the cell, a significant portion of the protons saturating the PFSA sulfonic acid groups is already replaced by  $K^+$ , to understand the processes in the membrane: given the quick ion exchange discussed earlier, it is shown in Figure 47a that the electrolyte is cycled first, when no voltage is applied, and the experiment is started second. A so-called safety voltage was applied to the cell (1.4 V), which is small enough to not cause too much damage to the dry cell and to avoid immediate water electrolysis but high enough to prevent free diffusion over the cell. ICP-MS elemental analysis provided information that no  $K^+$  diffusion into the anolyte occurs, which would be opposed to the electrodiffusion direction. Given the quick ion exchange and the strong  $K^+ - SO_3^-$  interactions, it can nevertheless be assumed that once a cation encounters the polymer, it is taken up into the membrane at the PFSA-electrolyte interphase. The driving force is even more pronounced since the pH of a  $KHCO_3$  solution is slightly alkaline (pH = 8.5), so protons exiting the membrane are neutralized immediately, water is formed and neutralization energy is released as latent heat, since the „acid“  $CO_2$  leaves the system as gas. Analyzing a  $K^+$  saturated MEA from the  $C_{only}$  operation mode via ICP-MS elemental analysis gave a number of  $250 \mu\text{mol } K^+$  content, which accounts for 83% of the available sulfonic acid groups in the membrane. As such, the assumptions where the following model is built on were confirmed.

Once a voltage is applied, the  $K^+$  that is already in the MEA leads to a significant increase in membrane resistance. We investigated the phenomenon called potential-driven substitution (PDS) in an earlier study<sup>[65]</sup> and found that high current densities are required to quantitatively drive alkaline metal ions out. At low current densities (Figure 47b), the  $K^+$  ion uptake into the membrane competes with this PDS, both processes pushing into opposite directions. With increasing current density protons

from the anode side become higher in concentration and successfully drive  $K^+$  back to the cathode half-cell. At high current densities (Figure 47c),  $K^+$  reuptake should be prohibited but still the required voltage increases with higher concentrations as visible from the slopes in Figure 46b. This could be due to remaining metal content or morphological changes in the membrane as will be discussed in the next sections.

### Concentration variation in mixed electrolyte mode ( $mode_{mix}$ )

In addition to  $mode_{sep}$ ,  $C_{only}$  studies, there are also  $mode_{mix}$  setups known in literature bearing the advantage to guarantee constant reaction conditions in a potential long-term experimental  $CO_2$ -electrolysis design.<sup>[13]</sup> In Figure 48a, the experiment was conducted with 1.0 mM concentration  $KHCO_3$ .

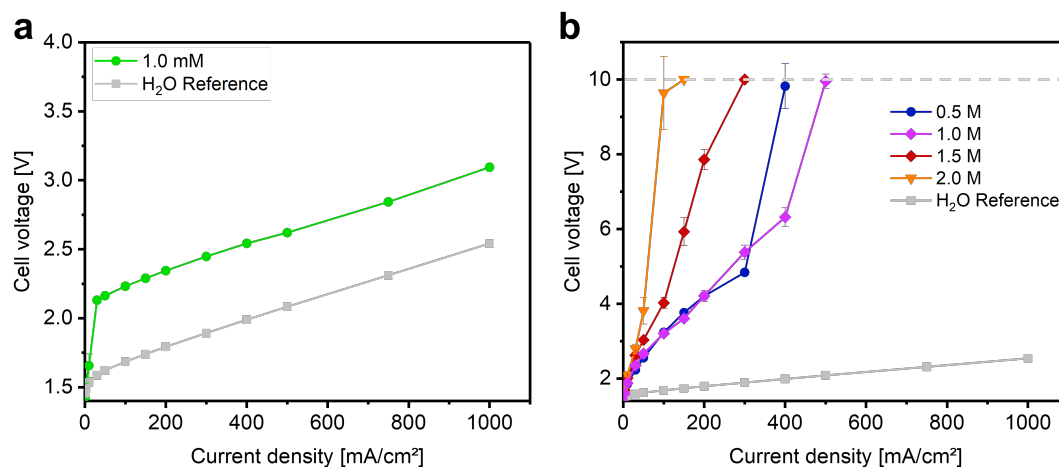


**Figure 48:** Concentration variation study in  $mode_{mix}$  showing a) the effect of a small concentration and b) increasing cell voltages with increasing concentration.

Explanations of the observations will follow the order of first looking into the small concentration regime and confirming  $V_{int}$ , then comparing low and high concentration regimes and finally put our model system in the context of existing literature and explain its shortcomings.

In the low current density regime, a voltage shift of 545 mV is observed. The value is very close to the one observed in  $C_{only}$  mode (527 mV). Both values match an earlier theoretical simulation of changed counterions in a PEM fuel cell (PEM FC), which is found to be around 300–400 mV).<sup>[147]</sup> Although it is difficult to differentiate complex ongoing processes in the cell *in situ*, the unchanged slope of the graph implies that the 522 mV offset is purely due to an increased ohmic resistance: a

higher activation energy is required to initiate cation movement over the membrane even at low metal cation concentrations. A *Tafel* like logarithmic depiction of Figure 46a and Figure 48a is given in Figure 49 and will provide further clarification:

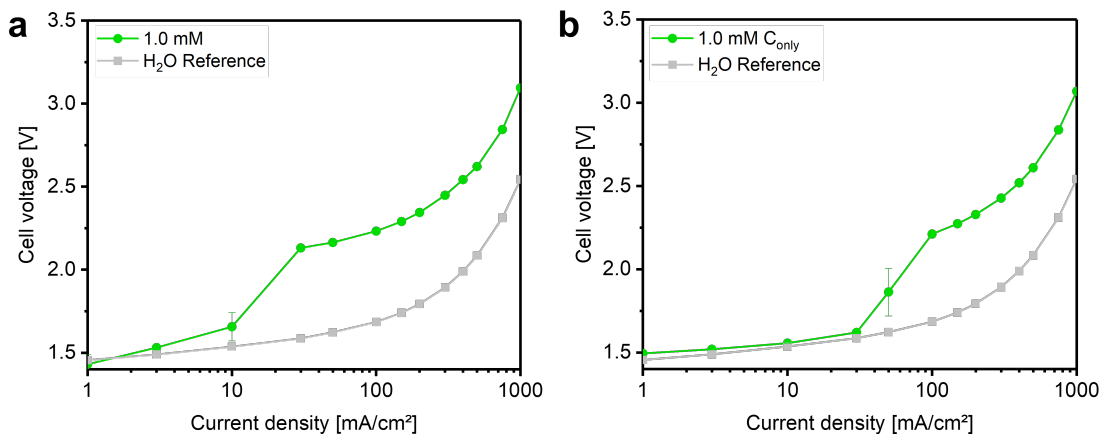


**Figure 49:** *Tafel* plots of 1.0 mM KHCO<sub>3</sub> concentrations in a) mode<sub>mix</sub> and b) mode<sub>sep</sub>.

At small concentrations, the course of the curve is independent of the operation mode until the current density reaches 30–50 mA/cm<sup>2</sup>. The voltage shift accounts for approx. 550 mV in both cases, which can be correlated with the solubility of potassium sulfate: Converting the solvation energy of potassium sulfate ( $E_s = 132.3$  kJ/mol for K<sub>2</sub>SO<sub>4</sub>)<sup>[25]</sup> according to  $E_s = -nFV$  ( $n = 2$ , K<sub>2</sub>SO<sub>4</sub>,  $F = 96485$  C/mol) into the required voltage to overcome this process, this accounts for 0.69 V, being in the same range as the observation. We conclude that this contribution ( $V_{int}$ ) originates purely from the K<sup>+</sup>-sulfonate interaction, while at higher current densities, space charge limitations contribute to the observable cell voltage. The voltage increase at 30 or 50 mA/cm<sup>2</sup>, respectively, marks the point, where K<sup>+</sup> begins to move and cationic transport starts. At smaller current densities, only protons cause ion movement and charge balance. K<sup>+</sup> is stuck in the membrane and the applied cell voltage is not high enough yet to induce ion movement.

In the high concentration regime in mode<sub>mix</sub> (depicted in Figure 48b), a significant voltage increase is observed at different current densities. Sharp increases are observed at 400 mA/cm<sup>2</sup> (0.5 and 1.0 M KHCO<sub>3</sub>), at 300 mA/cm<sup>2</sup> (1.5 M) and at 100 mA/cm<sup>2</sup> (2.0 M), respectively. To understand the observations, it is important to know that protons can tunnel through the membrane due to their ability to move in a *Grotthuss* like electron pair shift. The observed non-linear graphs and steep curves trace back to K<sup>+</sup> transport, occurring *via* physical ion hopping. When the sharp volt-

age increase occurs, the existing sulfonate groups cannot transport as many  $K^+$  as required by the set current density. This phenomenon is called space-charge limit and the resulting voltage contribution is called  $V_{SC}$ . Rare existing literature confirms non-linear behavior of the membrane voltage increase vs. current density when  $Na^+$  is transported over a Nafion N-1110.<sup>[104]</sup>

Ongoing molecular processes can be described as follows: in the original protonated form without a voltage applied, a hydrated PFSA membrane is known to bear approx. 15 water molecules per sulfonic acid group, which enable certain side chain mobility and overall polymer flexibility.<sup>[25,77]</sup> Once a voltage is applied, this flexibility causes pore formation to transport protons (or other cations) along the electrodiffusion gradient. At higher current densities, more transport channels (pores) in the membrane need to be active to cope with the high proton or cation load. Along with this, active pores will be widened, increasing their diameter. Given the strong ionic interactions of  $K^+$  with the sulfonic acid groups and the spontaneous ion exchange in the membrane, a widened pore system will cause more metal ions to enter the membrane, saturate any available negative charge and finally cause the system to require large voltage to drive these ions over the membrane. This is the point, where the space charge limit (or depletion region) is reached and the voltage increases significantly until reaching the setup voltage compliance. Now, there is a large amount of metal ions in the membrane, which causes additional effects: While membrane density is increased, its water content and swelling capacity is decreased, which causes pores to shrink again. This goes along with an overall morphological change of the flexible PFSA polymeric structure, which impacts membranes conductivity, ion mobility and thus membrane resistance.<sup>[105]</sup>

In the last part of this subsection, our model system is put into context of existing literature and a reality check with  $CO_2$  electrolysis is done: It is important to mention that there are existing  $CO_2$  electrolysis systems in literature running for several thousand hours in mode<sub>mix</sub> without space charge limits observed at al.<sup>[13]</sup> This is where the differences between our model system and real applications as shown in Figure 39 become important: Having a full-MEA system instead of a half-MEA approach with electrolyte gap and GDE implies that there is a Pt catalyst layer at the cathode side of the MEA acting as an additional barrier that prevents cation expel into the electrolyte. This is well in line with the EIS results shown in Figure 44, where the significantly increased charge transfer resistance proves this explanation right and contributes to the space charge limitation observed throughout all experiments in mode<sub>mix</sub> from 0.5 M molar upwards. An additional shortcoming of our model

system is the lack of pH balance: as shown earlier (under *Thermodynamic considerations*), the competing K<sup>+</sup> transport causes the need to take protons for the cathodic HER from water under consumption of the neutralization energy necessary to split H<sup>+</sup> from OH<sup>-</sup>. Therefore, protons that are not transported over the membrane stay at the anode and cause acidification of the Helmholtz layer near the anode. Since KHCO<sub>3</sub> acts as a buffer according to equation 32, CO<sub>2</sub> is released as protons are captured.

We performed some additional experiments to correctly embed our model system into the context of literature data and to verify how e.g. KHCO<sub>3</sub> decomposition impacts our system. A galvanostatic experiment was run for 2 h at 1.0 A/cm<sup>2</sup> where CO<sub>2</sub> was found in the product gas as a proof of concept (2.4% vs. 0.04% present in the atmosphere<sup>[148]</sup>). The anodic pH was increased from 8.5 to 9.0 and qualitative evidence for carbonate existence in the electrolyte was given by BaCO<sub>3</sub> precipitation from a BaCl<sub>2</sub> solution. The additional gas formation at the anode side however does not account for the space charge limit expressed by the strongly raised voltage. This is verified by an anion variation study, where potassium sulfate was used as an electrolyte (data given in the SI). The observed data was analogue to the KHCO<sub>3</sub> case considered in Figure 48. Comparing CO<sub>2</sub> (2.4%) and O<sub>2</sub> (14.2%) concentration at the anode side, we can calculate the K<sup>+</sup>/H<sup>+</sup> competition during the experiment: under consideration of the Faradaic stoichiometry (1 K<sup>+</sup> transported per CO<sub>2</sub> formed and 4 H<sup>+</sup> produced per O<sub>2</sub> formed) we get

---


$$\frac{4c_{\text{O}_2} - c_{\text{CO}_2}}{c_{\text{CO}_2}} = 22.8 \approx 23 \quad (33)$$


---

23 is thus the number of protons transported for one K<sup>+</sup> to be removed from the membrane in the present model system. In addition, this section made clear the limitations and shortcomings of the system, especially in mode<sub>mix</sub>. Moving towards real CO<sub>2</sub> electrolysis applications, where a half-MEA approach with electrolyte gap is common to employ (see Figure 39), final considerations concerning electrolyte conductivity and resistance will merge all voltage contributions in a final explanation for V<sub>total</sub> within the limits of the model system.

### Electrolyte conductivities

Local acidic conditions favor HER competition and disfavor CO<sub>2</sub>RR in CO<sub>2</sub> electrolysis. Since the cathode needs to be protected from protons, the principle of a so called liquid buffer layer is very common to apply.<sup>[114]</sup> The buffer layer is an additional liquid layer between the membrane (which is often a PFSA-based CEM) and the cathode. To avoid resistive voltage increases due to this layer, it must exhibit a significant conductivity, which increases with ion concentration. Supposed this buffer layer is a KHCO<sub>3</sub> solution, we have measured conductivities for all electrolytes used in this study and converted them into an additional resistance with an assumed gap thickness of 180  $\mu\text{m}$ , which equals the diameter of the Nafion<sup>®</sup> N117 membrane.

**Table 16:** Measured electrolyte conductivities and calculated ohmic resistances of an assumed 180  $\mu\text{m}$  gap liquid buffer layer.

| Electrolyte concentration | Measured conductivity           | Calculated resistance            |
|---------------------------|---------------------------------|----------------------------------|
| 1.0 mM                    | 111 $\mu\text{S}\cdot\text{cm}$ | 163 $\Omega\text{ cm}^2$         |
| 0.5 M                     | 39.0 $\text{mS}\cdot\text{cm}$  | 461 $\text{m}\Omega\text{ cm}^2$ |
| 1.0 M                     | 71.1 $\text{mS}\cdot\text{cm}$  | 253 $\text{m}\Omega\text{ cm}^2$ |
| 1.5 M                     | 86.1 $\text{mS}\cdot\text{cm}$  | 209 $\text{m}\Omega\text{ cm}^2$ |

As expected, conductivity increases and thus resistance of the buffer layer decreases with increasing concentration. This is clearly a positive impact of electrolyte usage. But one must keep in mind that for CO<sub>2</sub> reduction the product distribution is also affected by the K<sup>+</sup> concentration. Even though they are good from the conductivity point of view, highly molar electrolytes do not always favor good CO<sub>2</sub> reduction reaction selectivity.<sup>[149,150]</sup> A gap width of 0.5–2.0 mm is common in literature.<sup>[114]</sup> By dividing the measured conductivities by the gap width and calculating the inverse of the obtained values, the data from Table 4 (1.5 M) translate into a 0.3–2.8  $\Omega\text{ cm}^2$  resistance, which can be converted into  $V_{\text{gap}} = 0.28\text{--}1.12\text{ V}$  voltage contribution using Ohm's law. With this information at hand, we can now bring all parts from the water electrolysis model together and provide a wholistic approach for our model system towards scalable CO<sub>2</sub> electrolysis.

### Sum-up cell voltage contributions

With the help of a PEM water electrolysis model system, we quantified voltage contributions caused by K<sup>+</sup>-sulfonate interactions and rounded this approach with thermodynamic considerations and calculations. Merging all voltage contributions, we base our conclusions on the voltage partitioning for water electrolysis applications known from literature:<sup>[118]</sup>

$$V_{\text{total}} = V_{\text{rev}} + V_{\text{act}} + V_{\text{ohm}} \quad (34)$$

This is applicable for PEM water electrolysis in general. Our aim is to transfer the knowledge obtained from the water electrolysis model system to CO<sub>2</sub> electrolysis and suggest a breakdown as follows with the respective contributions explained below:

$$V_{\text{total}} = V_{\text{rev}} + V_{\text{pH}} + V_{\text{gap}} + V_{\text{ohm}} + V_{\text{CO}_2} \quad (35)$$

$V_{\text{rev}}$  was elaborated earlier (under *Thermodynamic considerations*) and can easily be quantified to  $V_{\text{rev}} = 1.47 \approx 1.5$  V.<sup>[26,114]</sup> (Our approach of using  $\Delta H$  instead of  $\Delta G$  is supported by stating that  $V_{\text{OC}} = 1.23$  V is only true at under p, T equilibrium conditions.<sup>[118]</sup>) Using C<sub>only</sub> operation mode and following up on the thermodynamic considerations, we take another intrinsic voltage contribution into account,  $V_{\text{pH}}$ , arising from the asymmetric electrolyte use. For KHCO<sub>3</sub> usage at the cathode side while ultrapure water is used at the anode side, we get  $V_{\text{pH}} = 0.15$  V (see Table 2). Moving on from these intrinsic contributions towards cell design related contributions, a gap between membrane and cathode side GDE needs to be considered as well, which we assessed through the electrolyte conductivity as  $V_{\text{gap}} = 280$  mV.

We saw that  $V_{\text{ohm}}$  can be split into  $V_{\text{ohm}} = V_{\text{int}} + V_{\text{SC}}$ , where only  $V_{\text{int}}$  is applicable for a transfer to CO<sub>2</sub> electrolysis, since it represents the more industrially relevant case of mode<sub>sep</sub> with electrolyte usage in a C<sub>only</sub> operation mode.  $V_{\text{SC}}$  can be traced back to a space charge limited K<sup>+</sup> overload effect, which revealed the shortcomings

and limits of our system. We saw that the Pt electrode directly on the membrane prevents  $K^+$  from being expelled into the electrolyte. In our case ( $C_{\text{only}}$ ),  $V_{\text{ohm}}$  thus equals  $V_{\text{int}}$  and can be read off Figure 46b at 1.5 M and the optimal operation current (400 mA/cm<sup>2</sup>) to be  $V_{\text{int}} = 0.75$  V. We found that the pure interaction is approx. 550 mV and during operation, the membrane resistance is increased due to strong sulfonate- $K^+$  interactions.

The last contribution  $V_{\text{CO}_2}$  accounts for a fraction that is intrinsic in  $\text{CO}_2$  electroreduction and varies from 200 to 400 mV, depending on the operation mode.<sup>[114]</sup> This fraction is not accessible in our model water electrolysis system but equals  $V_{\text{CO}_2} = 520$  mV when comparing all remaining contributions to a literature target voltage of  $V_{\text{total}} = 3.2$  V for a  $\text{CO}_2$  electrolysis half-MEA approach with electrolyte gap at the anode side.<sup>[114]</sup> Potential explanations for this voltage portion are catalyst overpotentials (e.g. at a silver electrode), different electrochemical reactions or altered reaction mechanisms for the same reaction. We will look into this question in a future publication under realistic  $\text{CO}_2$  electrolysis conditions.

### 2.3.5. Conclusion

Combining cation exchange membranes with the use of high molar electrolytes is very common in  $\text{CO}_2$  electroreduction. Within this study it was investigated, how  $K^+$ -sulfonate interactions increase membrane resistance dependent on the electrolyte concentration. Therefore, a model PEM water electrolysis setup mimicking  $\text{CO}_2$  electrolysis was used in a mixed (mode<sub>mix</sub>) and in a separate electrolyte mode (mode<sub>sep</sub>). We were able to quantify different voltage contributions according to the suggested breakdown of the total cell voltage:

---


$$V_{\text{total}} = V_{\text{rev}} + V_{\text{pH}} + V_{\text{gap}} + V_{\text{ohm}} + V_{\text{CO}_2} \quad (36)$$


---



**Table 17:** Overview of identified voltage contributions to the total cell voltage. To reach  $V_{total}$ , not all contributions need to be taken into account, since some of them are dependent on the operation mode or concentration regime. To guarantee comparison to literature, data was collected and compared at a current density of  $300 \text{ mA/cm}^2$ .

| Contribution<br>at $300 \text{ mA/cm}^2$     | Name                           | Value<br>/ V |
|--|--------------------------------|--------------|
| Thermodynamic ( $\Delta H$ )                 | $V_{rev}$                      | 1.47         |
| Membrane resistance ( $K^+$ , anode $H_2O$ ) | $V_{ohm} = V_{int} (+ V_{SC})$ | 0.550–0.750  |
| Gap resistance                               | $V_{gap}$                      | 0.280 - 1.12 |
| pH-induced resistance                        | $V_{pH}$                       | 0.150        |
| $CO_2$ electrolysis intrinsic contributions  | $V_{CO_2}$                     | $\geq 0.520$ |
| Sum of theoretical contributions (example)   | $V_{total}$                    | 3.20         |

There are highly complex processes and engineering challenges to overcome for scaling  $CO_2$  electrolysis. This study deconvoluted different voltage contributions summarized in Table 17 with some of them dependent on the operation mode ( $V_{gap}$ ) or concentration regime ( $V_{SC}$ ). The focus was on membrane resistance increases caused by  $K^+$ -sulfonate interactions. Within the scope of the employed PEM water electrolysis model, all kinetic contributions caused by the membrane could thus be explained. However, some remaining 520 mV discrepancy to literature cannot be assigned yet. In a future publication we will consider a real  $CO_2$  electrolysis setup and elaborate on this missing voltage contribution to gain in-depth mechanistic understanding of  $CO_2RR$ , which is neglected in this water electrolysis model study due to model limitations.

### 3. Summary and outlook

As an important part of the energy transition, hydrogen is often seen as a very promising green energy carrier. However, in order to be consistent, it is necessary to obtain it from renewable sources, e.g. PEM electrolysis fed by sustainable electricity. This thesis addressed three important aspects from two overall categories related to PEM water splitting: the first topic complex referred generally to OER catalyst material optimization and especially price reduction through Ir replacement. The second thematic block, comprising part two and three of the work, was located in the field of cation exchange polymers, especially focusing on PFSA and its interactions with cations different from protons. All three chapters within this thesis follow an overall way through the core of a PEM electrolyzer cell: The first part starts at the anode side and investigates a cobalt-based polyoxometalate as an Ir replacement at anodic conditions as an OER catalyst. Moving forward towards the core of the cell, this catalyst is embedded into a MEA at the anode side, which led to important insights about polymer tuning possibilities. Building up on this, the third part provided insights about PFSA-cation interactions *in situ* when employing an electrolyte during operation. This way, important information could be obtained relevant for further sustainable technologies, such as CO<sub>2</sub> electrolysis. In this technique, the cathode side is of particular importance, which finally complements anode and membrane aspects and round the thesis.

In chapter 2.1 the barium-stabilized cobalt polyoxometalate Ba<sub>8</sub>[Co<sub>9</sub>(H<sub>2</sub>O)<sub>6</sub>(OH)<sub>3</sub>-(HPO<sub>4</sub>)<sub>2</sub>(PW<sub>9</sub>O<sub>34</sub>)<sub>3</sub>] (Ba<sub>8</sub>[Co<sub>9</sub>]) was investigated towards its ability to withstand the extremely acidic and oxidative conditions at industrially relevant current densities in a scalable MEA setup. Literature suggested it could be a very active catalyst with the potential to replace IrO<sub>2</sub>, an assumption that was reinforced by the oxidic tungstate framework of the POM protecting the cobalt active sites, which might be kinetically stable to resist acidic decomposition. A thorough material characterization (EA, TGA, BET, SEM, XRD, temperature stability investigations) enabled catalyst integration into a MEA setup. Upon electrochemical characterization in different paste formulations, the catalyst achieved low current densities, which were not reproducible at one MEA. The POM oxidic cluster was shown to decompose given the harsh anodic conditions during OER. From tungstic phase Pourbaix diagrams it became clear that the tungstate framework forms highly soluble, negatively charged oligotungstate moieties instead of behaving like stable WO<sub>2</sub> or WO<sub>3</sub>. The catalytically active Co<sup>2+</sup> centers were released in solution instead of being protected by the tungstic framework. The high solubility of the formed species might even act

as a driving force that additionally accelerates POM decomposition on the MEA due to thermodynamically favored water formation through oxide dissolution and the release of solvation energy stemming from  $\text{Co}^{2+}$  as well as from further fragments.

Although the study proved that POMs are not potential candidates for Ir replacement in future PEM systems, it pointed out relevant criteria that must be fulfilled for a catalyst to be scalably integrated into an industrially relevant process, such as the PEM electrolyzer. As an outlook, the most prominent challenge is still to overcome an oxidic materials' intrinsic acid lability given the harsh oxidative conditions at the anode side. Although acid-labile, the POM catalyst still exhibits a high activity and speed in OER,<sup>[52]</sup> so the knowledge obtained here could be used in further studies: Instead of a PFSA membrane creating an acidic environment at the anode side, the cation migration direction could be reversed when using an AEM. Water would then be reduced at the cathode side and hydroxyl ions ( $\text{OH}^-$ ) be the migrating species, moving along the electrodiffusion gradient. Extraordinarily quick and effective oxidation catalysts, such as the POM, could oxidize these  $\text{OH}^-$  while contact to acidic environment is suppressed. In this context, POMs could be investigated along with further oxidic substance classes, such as perovskites, since in this scenario, acid lability would no longer be a criterion for the choice of catalyst material.

Chapter 2.2 looked deeper into proton-metal cation exchanges and revealed ways to manually enhance the polymers stability for processing by metal cation integration but at the same time drive these cations out of the membrane by applying a potential *in situ*. It is known that mechanical properties of PFSA are crucial for scaling MEA production and enable effective processing. Often, the catalyst is embedded into the upmost polymer layer *via* heat-mediated decal transfer. Processing parameters, especially  $T_g$  can be modified by temporarily incorporating metal cations (and others such as amine-based cations) into the membrane. Processability considerations revealed that lithium ( $\text{Li}^+$ ) is most likely to produce positive outcomes during decal and underwent the full MEA fabrication process: It was first integrated into the PFSA and the respective membrane was subjected to decal, producing a MEA that was electrochemically analyzed. A differentiation between pore blocking by the metal ion (initial effect) and metal ion induced polymer chain arrangements (permanent effect) could be made. For the first time, potential-driven substitution *in situ* was described in literature and found to be quantitative for lithium ions. Its rate was quantified (0.2 mmol/cm<sup>2</sup> per minute at 1.0 A/cm<sup>2</sup>) and although a resistance increase was observed in the first place (assessed through electrochemical impedance spectroscopy), the back-exchange was quantitative. Remaining differences between the  $\text{Li}^+$ -treated MEA and the reference protonated one can be traced back to permanent morphological changes within the PFSA polymeric matrix.

An important implication is that proton-cation exchange can be used as a lever for fine-tuning membrane properties. Especially when treated with heat, as is the case during decal transfer, the additional provided energy enables the dynamic polymer network to move and rearrange according to the structural particularities of sulfonate-metal complexes within the membrane. The full scope of these morphological changes could be assessed using SAXS and further scattering techniques to fully understand PFSA morphology. Additionally, a deeper understanding of the processes going on when in contact with water will be helpful to conclude about *in situ*-behavior of the polymer. As an important complement, feasibility studies need to be conducted that examine application in real setups picturing realistic and industrially relevant process conditions, such as high current densities, long-term operation and large electrode areas to be integrated into the systems.

Chapter 2.3 investigated how combining cation exchange membranes with the use of high molar electrolytes affects membrane resistance in CO<sub>2</sub> electroreduction. It was studied, how K<sup>+</sup>-sulfonate interactions increase membrane resistance dependent on the electrolyte concentration. Therefore, a model PEM water electrolysis setup mimicking CO<sub>2</sub>-electrolysis was used in a mixed (mode<sub>mix</sub>) and in a separate electrolyte mode (mode<sub>sep</sub>). Quantification of different potential contributions was possible according to a suggested breakdown of the total cell voltage:

---


$$V_{\text{total}} = V_{\text{rev}} + V_{\text{pH}} + V_{\text{gap}} + V_{\text{mem}} + V_{\text{CO}_2} \quad (37)$$


---

There are highly complex processes and engineering challenges to overcome for a successful scaling of CO<sub>2</sub> electrolysis. This part of the thesis attributed portions of the total cell potential to different contributing effects with some of them dependent on the operation mode ( $V_{\text{gap}}$ ) or concentration regime ( $V_{\text{SC}}$ ). The focus was on membrane resistance increases caused by K<sup>+</sup>-sulfonate interactions. In an operation mode with separate liquid cycles (mode<sub>sep</sub>) (electrolyte at the cathode side only, C<sub>only</sub>), an operation optimum was found at 400 mA/cm<sup>2</sup>. All identified potential contributions to the total cell voltage are briefly summarized below. It must be noticed that in order to reach  $V_{\text{total}} = 3.2$  V, not all contributions need to be taken into account, since some of them are dependent on the operation mode or concentration regime. Contributions assumed at a current density at 300 mA/cm<sup>2</sup> and comprise

$V_{\text{rev}}(\Delta H) = 1.47 \text{ V}$ ,  $V_{\text{mem}} = 0.55 - 0.75 \text{ V}$ ,  $V_{\text{gap}} = 0.28 - 1.12 \text{ V}$ ,  $V_{\text{pH}} = 0.15 \text{ V}$  and  $V_{\text{CO}_2} \geq 0.52 \text{ V}$ .

The employed PEM water electrolysis model could not explain some remaining 520 mV discrepancy to literature. This CO<sub>2</sub>-electrolysis specific contribution is analyzed by a second PhD thesis in the group. The work will consider a real CO<sub>2</sub> electrolysis setup and elaborate on this missing potential contribution to gain in-depth mechanistic understanding of CO<sub>2</sub>RR, which is neglected in this water electrolysis model study due to model limitations. Employing a realistic CO<sub>2</sub> setup, future work will use H<sub>2</sub>SO<sub>4</sub> at the anode side and K<sub>2</sub>SO<sub>4</sub>, acidified with H<sub>2</sub>SO<sub>4</sub>, at the cathode side. This corresponds to the mode<sub>sep</sub> C<sub>only</sub> in the model system employed in this work. K<sup>+</sup> is still the predominant carrier as justified in this thesis and  $V_{\text{CO}_2}$  can be assessed.

This thesis provided fundamental information towards scaling and enhancing existing approaches for green and sustainable energy conversion by PEM electrolysis. Given the enormous speed of the energy demand increase and the growing population as well as constantly increasing greenhouse gas emissions, there is still a lot of work ahead of us: in the context of a broad and comprehensive solution approach, PEM electrolysis needs to be developed further along with additional innovations, such as AEM-based technologies and renewable electricity generation. The present work in the field of OER catalyst alternatives opened an additional question: Is the present approach *via* catalyst activity usually seen in literature the correct way to go? In line with some pioneer studies, the present results suggest to rather approach the search for new catalyst materials from a systematic and stability-focused point of view. Membrane stability and modification studies provided insights about the flexibility and broad applicability of PFSA in general. However, PFSA is a perfluorinated polymer and e.g. EU policies might change towards stricter regulations for perfluorinated substances. In a prospective approach it is thus important to investigate further technologies in parallel, namely anion exchange membrane-polymer electrolyte membrane (AEM-PEM) technology. While PEM will still be important to dynamically and locally convert excess intermittent electricity from renewable sources into hydrogen, AEM-PEM has the potential of scalability due to earth-abundant catalysts that can be used as well as non-perfluorinated polymer matrix. Above all, available technologies and findings need to be compiled and translated into a sustainable supply grid, acting locally where possible and enabling global impacts at the same time.

## 4. References

- [1] Projektträger Jülich, Forschung für Nachhaltigkeit - FONA. 2021; <https://www.fona.de/de/aktuelles/>.
- [2] Fleischer, M.; Jeanty, P.; Wiesner-Fleischer, K.; Hinrichsen, O. In *Zukünftige Kraftstoffe*; Maus, W., Ed.; Springer: Berlin, Heidelberg, 2019; Vol. 11; pp 224–250.
- [3] Chi, J.; Yu, H. Water electrolysis based on renewable energy for hydrogen production. *Chinese Journal of Catalysis* **2018**, *39*, 390–394.
- [4] Ursua, A.; Gandia, L. M.; Sanchis, P. Hydrogen production from water electrolysis: Current status and future trends. *Proceedings of the IEEE* **2012**, *100*, 410–426.
- [5] Carmo, M.; Fritz, D. L.; Mergel, J.; Stolten, D. A comprehensive review on PEM water electrolysis. *International Journal of Hydrogen Energy* **2013**, *38*, 4901–4934.
- [6] Deluga, G. A.; Salge, J. R.; Schmidt, L. D.; Verykios, X. E. Renewable hydrogen from ethanol by autothermal reforming. *Science* **2004**, *303*, 993–997.
- [7] Paidar, M.; Fateev, V.; Bouzek, K. Membrane electrolysis – history, current status and perspective. *Electrochimica Acta* **2016**, *209*, 737–756.
- [8] LeRoy, R. L.; Janjua, M. B. I.; Renaud, R.; Leuenberger, U. Analysis of time-variation effects in water electrolyzers. *Journal of the Electrochemical Society* **1979**, *126*, 1674–1682.
- [9] Baharudin, L.; James Watson, M. Hydrogen applications and research activities in its production routes through catalytic hydrocarbon conversion. *Reviews in Chemical Engineering* **2018**, *34*, 43–72.
- [10] Lee, H.; Lee, B.; Byun, M.; Lim, H. Economic and environmental analysis for PEM water electrolysis based on replacement moment and renewable electricity resources. *Energy Conversion and Management* **2020**, *224*, 113477.
- [11] Hydrogen Council, Hydrogen Scaling Up: A Sustainable Pathway for the Global Energy Transition. 2017; <https://hydrogencouncil.com/en/study-hydrogen-scaling-up/>.

- [12] Smolinka, T.; Günther, M.; Garcke, J. NOW-Studie: Stand und Entwicklungspotenzial der Wasserelektrolyse zur Herstellung von Wasserstoff aus regenerativen Energien.
- [13] Haas, T.; Krause, R.; Weber, R.; Demler, M.; Schmid, G. Technical photosynthesis involving CO<sub>2</sub> electrolysis and fermentation. *Nature Catalysis* **2018**, *1*, 32–39.
- [14] Bundesministerium für Wirtschaft und Energie, Die Nationale Wasserstoffstrategie. 2020; <https://www.bmwi.de/Redaktion/DE/Publikationen/Energie/die-nationale-wasserstoffstrategie.html>.
- [15] Kleperis, J., Ed. *Electrolysis*; InTech: Rijeka, Croatia, 2012.
- [16] Mauritz, K. A.; Moore, R. B. State of understanding of Nafion. *Chemical reviews* **2004**, *104*, 4535–4585.
- [17] Bessarabov, D. G., Wang, H., Li, H., Zhao, N., Eds. *PEM electrolysis for hydrogen production: Principles and applications*; CRC Press: Boca Raton, Florida, 2016.
- [18] Rost, U.; Podleschny, P.; Schumacher, M.; Muntean, R.; Pascal, D. T.; Mutascu, C.; Koziol, J.; Marginean, G.; Brodmann, M. Long-term stable electrodes based on platinum electrocatalysts supported on titanium sintered felt for the use in PEM fuel cells. *IOP Conference Series: Materials Science and Engineering* **2018**, *416*, 012013.
- [19] Göhl, D.; Rueß, H.; Schlicht, S.; Vogel, A.; Rohwerder, M.; Mayrhofer, K. J. J.; Bachmann, J.; Román-Leshkov, Y.; Schneider, J. M.; Ledendecker, M. Stable and active oxygen reduction catalysts with reduced noble metal loadings through potential triggered support passivation. *ChemElectroChem* **2020**, *7*, 2404–2409.
- [20] Busch, M.; Halck, N. B.; Kramm, U. I.; Siahrostami, S.; Krttil, P.; Rossmeisl, J. Beyond the top of the volcano? – A unified approach to electrocatalytic oxygen reduction and oxygen evolution. *Nano Energy* **2016**, *29*, 126–135.
- [21] Yokoyama, Y.; Miyazaki, K.; Miyahara, Y.; Fukutsuka, T.; Abe, T. In situ measurement of local pH at working electrodes in neutral pH solutions by the rotating ring–disk electrode technique. *ChemElectroChem* **2019**, *6*, 4750–4756.
- [22] Stock, J. T., Ed. *Electrochemistry, past and present*; ACS symposium series; American Chemical Society: Washington, DC, 1989; Vol. 390.

- [23] Schmittinger, W.; Vahidi, A. A review of the main parameters influencing long-term performance and durability of PEM fuel cells. *Journal of Power Sources* **2008**, *180*, 1–14.
- [24] Tahir, M.; Pan, L.; Idrees, F.; Zhang, X.; Wang, L.; Zou, J.-J.; Wang, Z. L. Electrocatalytic oxygen evolution reaction for energy conversion and storage: A comprehensive review. *Nano Energy* **2017**, *37*, 136–157.
- [25] Lide, D. R., Ed. *CRC Handbook of Chemistry and Physics: A ready-reference book of chemical and physical data: 2004–2005*, 85th ed.; CRC Press: Boca Raton, 2004.
- [26] Schalenbach, M. A Perspective on low-temperature water electrolysis – challenges in alkaline and acidic technology. *International Journal of Electrochemical Science* **2018**, 1173–1226.
- [27] O'Halloran, K. P. et al. Revisiting the polyoxometalate-based late-transition-metal-oxo complexes: The "oxo wall" stands. *Inorganic Chemistry* **2012**, *51*, 7025–7031.
- [28] Reier, T.; Nong, H. N.; Teschner, D.; Schlögl, R.; Strasser, P. Electrocatalytic oxygen evolution reaction in acidic environments - reaction mechanisms and catalysts. *Advanced Energy Materials* **2017**, *7*, 1601275.
- [29] Jiao, Y.; Zheng, Y.; Jaroniec, M.; Qiao, S. Z. Design of electrocatalysts for oxygen- and hydrogen-involving energy conversion reactions. *Chemical Society reviews* **2015**, *44*, 2060–2086.
- [30] Reier, T.; Oezaslan, M.; Strasser, P. Electrocatalytic oxygen evolution reaction (OER) on Ru, Ir, and Pt catalysts: A comparative study of nanoparticles and bulk materials. *ACS Catalysis* **2012**, *2*, 1765–1772.
- [31] Danilovic, N.; Subbaraman, R.; Chang, K.-C.; Chang, S. H.; Kang, Y. J.; Snyder, J.; Paulikas, A. P.; Strmcnik, D.; Kim, Y.-T.; Myers, D.; Stamenkovic, V. R.; Markovic, N. M. Activity-stability trends for the oxygen evolution reaction on monometallic oxides in acidic environments. *The journal of physical chemistry letters* **2014**, *5*, 2474–2478.
- [32] Pi, Y.; Zhang, N.; Guo, S.; Guo, J.; Huang, X. Ultrathin laminar Ir superstructure as highly efficient oxygen evolution electrocatalyst in broad pH range. *Nano letters* **2016**, *16*, 4424–4430.
- [33] International Renewable Energy Agency, Green Hydrogen Cost Reduction: Scaling up Electrolysers to Meet the 1.5 °C Climate Goal. 2020.



- [34] Rozain, C.; Mayousse, E.; Guillet, N.; Millet, P. Influence of iridium oxide loadings on the performance of PEM water electrolysis cells: Part I – Pure IrO<sub>2</sub>-based anodes. *Applied Catalysis B: Environmental* **2016**, *182*, 153–160.
- [35] Hegge, F.; Lombeck, F.; Cruz Ortiz, E.; Bohn, L.; von Holst, M.; Kroschel, M.; Hübner, J.; Breitwieser, M.; Strasser, P.; Vierrath, S. Efficient and stable low iridium loaded anodes for PEM water electrolysis made possible by nanofiber interlayers. *ACS Applied Energy Materials* **2020**, *3*, 8276–8284.
- [36] Yang, J.; Cooper, J. K.; Toma, F. M.; Walczak, K. A.; Favaro, M.; Beeman, J. W.; Hess, L. H.; Wang, C.; Zhu, C.; Gul, S.; Yano, J.; Kisielowski, C.; Schwartzberg, A.; Sharp, I. D. A multifunctional biphasic water splitting catalyst tailored for integration with high-performance semiconductor photoanodes. *Nature materials* **2017**, *16*, 335–341.
- [37] Zhang, M.; de Respini, M.; Frei, H. Time-resolved observations of water oxidation intermediates on a cobalt oxide nanoparticle catalyst. *Nature chemistry* **2014**, *6*, 362–367.
- [38] Risch, M.; Ringleb, F.; Kohlhoff, M.; Bogdanoff, P.; Chernev, P.; Zaharieva, I.; Dau, H. Water oxidation by amorphous cobalt-based oxides: in situ tracking of redox transitions and mode of catalysis. *Energy & Environmental Science* **2015**, *8*, 661–674.
- [39] Cheng, X.; Shi, Z.; Glass, N.; Zhang, L.; Zhang, J.; Song, D.; Liu, Z.-S.; Wang, H.; Shen, J. A review of PEM hydrogen fuel cell contamination: Impacts, mechanisms, and mitigation. *Journal of Power Sources* **2007**, *165*, 739–756.
- [40] McCrory, C. C. L.; Jung, S.; Ferrer, I. M.; Chatman, S. M.; Peters, J. C.; Jaramillo, T. F. Benchmarking hydrogen evolving reaction and oxygen evolving reaction electrocatalysts for solar water splitting devices. *Journal of the American Chemical Society* **2015**, *137*, 4347–4357.
- [41] Cherevko, S.; Zeradjanin, A. R.; Topalov, A. A.; Kulyk, N.; Katsounaros, I.; Mayrhofer, K. J. J. Dissolution of noble metals during oxygen evolution in acidic media. *ChemCatChem* **2014**, *6*, 2219–2223.
- [42] Wang, Z.; Zheng, Y.-R.; Chorkendorff, I.; Nørskov, J. K. Acid-stable oxides for oxygen electrocatalysis. *ACS Energy Letters* **2020**, *5*, 2905–2908.

- [43] Soriano-López, J.; Goberna-Ferrón, S.; Carbó, J. J.; Poblet, J. M.; Galán-Mascarós, J. R. *Polyoxometalate Chemistry; Advances in Inorganic Chemistry*; Elsevier, 2017; Vol. 69; pp 155–179.
- [44] Ritorto, M. D.; Anderson, T. M.; Neiwert, W. A.; Hill, C. L. Decomposition of a-type sandwiches. Synthesis and characterization of new polyoxometalates incorporating multiple d-electron-centered units. *Inorganic Chemistry* **2004**, *43*, 44–49.
- [45] Goberna-Ferrón, S.; Soriano-López, J.; Galán-Mascarós, J. Activity and stability of the tetramanganese polyanion  $[\text{Mn}_4(\text{H}_2\text{O})_2(\text{PW}_9\text{O}_{34})_2]^{10-}$  during electrocatalytic water oxidation. *Inorganics* **2015**, *3*, 332–340.
- [46] Pope, M. T.; Müller, A. Chemie der Polyoxometallate: Aktuelle Variationen über ein altes Thema mit interdisziplinären Bezügen. *Angewandte Chemie* **1991**, *103*, 56–70.
- [47] Vetter, K.-M.; Aring da Silva Ramos Mauro, C.; Reinisch, D.; Reichbauer, T.; Martić, N.; Jandl, C.; Hinrichsen, O.; Schmid, G. Stability evaluation of earth-abundant metal-based polyoxometalate electrocatalysts for oxygen evolution reaction towards industrial PEM electrolysis at high current densities. *Electrochemical Science Advances* **2021**, *75*, 155.
- [48] Huang, Z.; Luo, Z.; Geletii, Y. V.; Vickers, J. W.; Yin, Q.; Wu, D.; Hou, Y.; Ding, Y.; Song, J.; Musaev, D. G.; Hill, C. L.; Lian, T. Efficient light-driven carbon-free cobalt-based molecular catalyst for water oxidation. *Journal of the American Chemical Society* **2011**, *133*, 2068–2071.
- [49] Blakemore, J. D.; Schley, N. D.; Kushner-Lenhoff, M. N.; Winter, A. M.; D'Souza, F.; Crabtree, R. H.; Brudvig, G. W. Comparison of amorphous iridium water-oxidation electrocatalysts prepared from soluble precursors. *Inorganic Chemistry* **2012**, *51*, 7749–7763.
- [50] Soriano-López, J.; Goberna-Ferrón, S.; Vígara, L.; Carbó, J. J.; Poblet, J. M.; Galán-Mascarós, J. R. Cobalt polyoxometalates as heterogeneous water oxidation catalysts. *Inorganic Chemistry* **2013**, *52*, 4753–4755.
- [51] Finke, R. G.; Droege, M. W.; Domaille, P. J. Trivacant heteropolytungstate derivatives: 3. Rational syntheses, characterization, two-dimensional tungsten-183 NMR, and properties of tungstometallophosphates  $\text{P}_2\text{W}_{18}\text{M}_4(\text{H}_2\text{O})_2\text{O}_{68}^{10-}$  and  $\text{P}_4\text{W}_{30}\text{M}_4(\text{H}_2\text{O})_2\text{O}_{112}^{16-}$  (M = cobalt, copper, zinc). *Inorganic Chemistry* **1987**, *26*, 3886–3896.

- [52] Blasco-Ahicart, M.; Soriano-López, J.; Carbó, J. J.; Poblet, J. M.; Galán-Mascaros, J. R. Polyoxometalate electrocatalysts based on earth-abundant metals for efficient water oxidation in acidic media. *Nature chemistry* **2018**, *10*, 24–30.
- [53] Martin-Sabi, M.; Soriano-López, J.; Winter, R. S.; Chen, J.-J.; Vilà-Nadal, L.; Long, D.-L.; Galán-Mascarós, J. R.; Cronin, L. Redox tuning the Weakley-type polyoxometalate archetype for the oxygen evolution reaction. *Nature Catalysis* **2018**, *1*, 208–213.
- [54] Cavani, F.; Mezzogori, R.; Pigamo, A.; Trifirò, F. Improved catalytic performance of Keggin-type polyoxometalates in the oxidation of isobutane to methacrylic acid under hydrocarbon-lean conditions using antimony-doped catalysts. *Chemical Engineering Journal* **2001**, *82*, 33–42.
- [55] Rabis, A.; Rodriguez, P.; Schmidt, T. J. Electrocatalysis for polymer electrolyte fuel cells: recent achievements and future challenges. *ACS Catalysis* **2012**, *2*, 864–890.
- [56] Weakley, T. J. R.; Evans, H. T.; Showell, J. S.; Tourné, G. F.; Tourné, C. M. 18-Tungstotetracobalto(II)diphosphate and related anions: A novel structural class of heteropolyanions. *Journal of the Chemical Society, Chemical Communications* **1973**, 139–140.
- [57] Galán-Mascarós, J. R.; Gómez-García, C. J.; Borrás-Almenar, J. J.; Coronado, E. High nuclearity magnetic clusters: Magnetic properties of a nine cobalt cluster encapsulated in a polyoxometalate,  $[\text{Co}_9(\text{OH})_3(\text{H}_2\text{O})_6(\text{HPO}_4)_2(\text{PW}_9\text{O}_{34})_3]^{16-}$ . *Advanced Materials* **1994**, *6*, 221–223.
- [58] Evans, H. T.; Tourné, C. M.; Tourné, G. F.; Weakley, T. J. R. X-Ray crystallographic and tungsten-183 nuclear magnetic resonance structural studies of the  $[\text{M}_4(\text{H}_2\text{O})_2(\text{XW}_9\text{O}_{34})_2]^{10-}$  heteropolyanions (M = Co(II) or Zn, X = P or As). *Journal of the Chemical Society, Dalton Transactions* **1986**, 2699–2705.
- [59] Keggin, J. F. The structure and formula of 12-phosphotungstic acid. *Proceedings of the Royal Society of London. Series A* **1934**, *144*, 75–100.
- [60] Mestl, G.; Ilkenhans, T.; Spielbauer, D.; Dieterle, M.; Timpe, O.; Kröhnert, J.; Jentoft, F.; Knözinger, H.; Schlögl, R. Thermally and chemically induced structural transformations of Keggin-type heteropoly acid catalysts. *Applied Catalysis A: General* **2001**, *210*, 13–34.

- [61] Banić, N.; Vraneš, M.; Abramović, B.; Csanádi, J.; Gadžurić, S. Thermochromism, stability and thermodynamics of cobalt(II) complexes in newly synthesized nitrate based ionic liquid and its photostability. *Dalton Trans. (Cambridge, England : 2003)* **2014**, 43, 15515–15525.
- [62] Wilson, M. S.; Valerio, J. A.; Gottesfeld, S. Low platinum loading electrodes for polymer electrolyte fuel cells fabricated using thermoplastic ionomers. *Electrochimica Acta* **1994**, 1994, 355–363.
- [63] Page, K. A.; Cable, K. M.; Moore, R. B. Molecular origins of the thermal transitions and dynamic mechanical relaxations in perfluorosulfonate ionomers. *Macromolecules* **2005**, 38, 6472–6484.
- [64] Choi, M.; Kim, J. K.; Kim, J.; Yang, S.; Park, J.-E.; Kim, O.-H.; Cho, Y.-H. PtRu/C catalyst slurry preparation for large-scale decal transfer with high performance of proton exchange membrane fuel cells. *The Royal Society of Chemistry Advances* **2018**, 8, 36313–36322.
- [65] Vetter, K.-M.; Reichbauer, T.; Martić, N.; Reinisch, D.; Hinrichsen, O.; Schmid, G. Morphological tuning of membrane processing by temporal proton-metal cation substitution in perfluorosulfonic acid membranes. *Electrochimica Acta* **2020**, 137182.
- [66] Heitner-Wirguin, C. Recent advances in perfluorinated ionomer membranes: structure, properties and applications. *Journal of Membrane Science* **1996**, 120, 1–33.
- [67] Gelbard, G. Organic synthesis by catalysis with ion-exchange resins. *Industrial & Engineering Chemistry Research* **2005**, 44, 8468–8498.
- [68] Reinisch, D.; Schmid, B.; Martić, N.; Krause, R.; Landes, H.; Hanebuth, M.; Mayrhofer, K. J.; Schmid, G. Various CO<sub>2</sub>-to-CO electrolyzer cell and operation mode designs to avoid CO<sub>2</sub>-crossover from cathode to anode. *Zeitschrift für Physikalische Chemie* **2019**, 234, 1115–1131.
- [69] Kreuer, K. D.; Ise, M.; Fuchs, A.; Maier, J. Proton and water transport in nano-separated polymer membranes. *Le Journal de Physique IV* **2000**, 10, Pr7–279–Pr7–281.
- [70] Gierke, T. D.; Munn, G. E.; Wilson, F. C. The morphology in nafion perfluorinated membrane products, as determined by wide- and small-angle X-ray studies. *Journal of Polymer Science: Polymer Physics Edition* **1981**, 19, 1687–1704.

- [71] Kusoglu, A.; Weber, A. Z. New insights into perfluorinated sulfonic-acid ionomers. *Chemical reviews* **2017**, *117*, 987–1104.
- [72] Shannon, R. D. Revised effective ionic radii and systematic studies of interatomic distances in halides and chalcogenides. *Acta Crystallographica* **1976**, 751–767.
- [73] Banait, J. S.; Sidhu, K. S.; Walia, J. S. Transference numbers and solvation studies in n-butanol. *Canadian Journal of Chemistry* **1984**, 303–305.
- [74] Chemours™, Sicherheitsdatenblatt gemäß Verordnung (EG) Nr. 1907/2006: Nafion™ N117. 2018; <https://www.quintech.de/wp-content/uploads/2020/07/SDS-NM117-2019-DE.pdf>.
- [75] Tarokh, A.; Karan, K.; Ponnurangam, S. Atomistic MD study of nafion dispersions: role of solvent and counterion in the aggregate structure, ionic clustering, and acid dissociation. *Macromolecules* **2020**, *53*, 288–301.
- [76] Laporta, M.; Pegoraro, M.; Zanderighi, L. Perfluorosulfonated membrane (Nafion): FT-IR study of the state of water with increasing humidity. *Physical Chemistry Chemical Physics* **1999**, *1*, 4619–4628.
- [77] Shi, S.; Weber, A. Z.; Kusoglu, A. Structure/property relationship of Nafion XL composite membranes. *Journal of Membrane Science* **2016**, *516*, 123–134.
- [78] Atkins, P. W. *Kurzlehrbuch Physikalische Chemie*; John Wiley & Sons: Weinheim, 2001.
- [79] Fuller, T. F.; Newman, J. Experimental determination of the transport number of water in Nafion 117 membrane. *Journal of the Electrochemical Society* **1992**, *139*, 1332–1337.
- [80] Markovitch, O.; Agmon, N. Structure and energetics of the hydronium hydration shells. *The journal of physical chemistry. A* **2007**, *111*, 2253–2256.
- [81] Yoder, C. H. Geochemical applications of the simple salt approximation to the lattice energies of complex materials. *American Mineralogist* **2005**, *90*, 488–496.
- [82] Rieke, P. C.; Vanderborgh, N. E. Temperature dependence of water content and proton conductivity in polyperfluorosulfonic acid membranes. *Journal of Membrane Science* **1987**, 313–328.
- [83] Samms, S. R.; Wasmus, S.; Savinell, R. F. Thermal stability of Nafion® in simulated fuel cell environments. *Journal of the Electrochemical Society* **1996**,

- [84] Kyu, T.; Hashiyama, M.; Eisenberg, A. Dynamic Mechanical Studies of Partially Ionized and Neutralized Nafion Polymers. *Canadian Journal of Chemistry* **1983**, 680–687.
- [85] Yeo, S. C.; Eisenberg, A. Physical properties and supermolecular structure of perfluorinated ion-containing (Nafion) polymers. *Journal of Applied Polymer Science* **1977**, 875–898.
- [86] Osborn, S. J.; Hassan, M. K.; Divoux, G. M.; Rhoades, D. W.; Mauritz, K. A.; Moore, R. B. Glass transition temperature of perfluorosulfonic acid ionomers. *Macromolecules* **2007**, 40, 3886–3890.
- [87] Steck, A.; Yeager, H. L. Water sorption and cation-exchange selectivity of a perfluorosulfonate ion-exchange polymer. *Analytical Chemistry* **1980**, 52, 1215–1218.
- [88] Li, N.; Araya, S. S.; Kær, S. K. Long-term contamination effect of iron ions on cell performance degradation of proton exchange membrane water electrolyser. *Journal of Power Sources* **2019**, 434, 226755.
- [89] Bas, C.; Reymond, L.; Danérol, A.-s.; Albérola, N. D.; Rossinot, E.; Flandin, L. Key counter ion parameters governing polluted nafion membrane properties. *Journal of Polymer Science Part B: Polymer Physics* **2009**, 47, 1381–1392.
- [90] Iwai, Y.; Yamanishi, T. Thermal stability of ion-exchange Nafion N117CS membranes. *Polymer Degradation and Stability* **2009**, 94, 679–687.
- [91] Bas, C.; Albérola, N. D.; Flandin, L. Effects of contaminant on thermal properties in perfluorinated sulfonic acid membranes. *Journal of Membrane Science* **2010**, 363, 67–71.
- [92] Determining extent of ion-exchange in various counterion Nafion membranes using prompt gamma neutron activation analysis (PGAA). 2001.
- [93] Moore, R. B.; Cable, K. M.; Croley, T. L. Barriers to flow in semicrystalline ionomers. A procedure for preparing melt-processed perfluorosulfonate ionomer films and membranes. *Journal of Membrane Science* **1992**, 7–14.
- [94] Saha, M. S.; Paul, D. K.; Peppley, B. A.; Karan, K. Fabrication of catalyst-coated membrane by modified decal transfer technique. *Electrochemistry Communications* **2010**, 12, 410–413.

- [95] Shi, M.; Anson, F. C. Dehydration of protonated Nafion<sup>®</sup> coatings induced by cation exchange and monitored by quartz crystal microgravimetry. *Journal of Electroanalytical Chemistry* **1997**, *425*, 117–123.
- [96] Okada, T.; Satou, H.; Okuno, M.; Yuasa, M. Ion and water transport characteristics of perfluorosulfonated ionomer membranes with H<sup>+</sup> and alkali metal cations. *The Journal of Physical Chemistry B* **2002**, *106*, 1267–1273.
- [97] Lopes, T.; Kim, D. S.; Kim, Y. S.; Garzon, F. H. Ionic transport and water vapor uptake of ammonium exchanged perfluorosulfonic acid membranes. *Journal of the Electrochemical Society* **2012**, B265–B269.
- [98] Lage, L. G.; Delgado, P. G.; Kawano, Y. Thermal stability and decomposition of Nafion<sup>®</sup> membranes with different cations using high-resolution thermogravimetry. *Journal of Thermal Analysis and Calorimetry* **2004**, *75*, 521–530.
- [99] Tandon, R.; Pintauro, P. N. Divalent/Monovalent cation uptake selectivity in a Nafion cation-exchange membrane: experimental and modeling studies. *Journal of Membrane Science* **1997**, *136*, 207–219.
- [100] Bontha, J. R.; Pintauro, P. N. Water orientation and ion solvation effects during multicomponent salt partitioning in a Nafion cation exchange membrane. *Chemical Engineering Science* **1994**, *49*, 3835–3851.
- [101] Jia, R.; Han, B.; Levi, K.; Hasegawa, T.; Ye, J.; Dauskardt, R. H. Effect of cation contamination and hydrated pressure loading on the mechanical properties of proton exchange membranes. *Journal of Power Sources* **2011**, *196*, 3803–3809.
- [102] Jia, R.; Dong, S.; Hasegawa, T.; Ye, J.; Dauskardt, R. H. Contamination and moisture absorption effects on the mechanical properties of catalyst coated membranes in PEM fuel cells. *International Journal of Hydrogen Energy* **2012**, *37*, 6790–6797.
- [103] Grava, M. W.; Okada, Y.; Kawano, Y. Thermal characterization of Flemion<sup>®</sup> membranes substituted by alkali metal cations. *Journal of Thermal Analysis and Calorimetry* **2007**, 163–168.
- [104] Moshtarihah, S.; Oppers, N. A. W.; de Groot, M. T.; Keurentjes, J. T. F.; Schouten, J. C.; van der Schaaf, J. Nernst–Planck modeling of multicomponent ion transport in a Nafion membrane at high current density. *Journal of Applied Electrochemistry* **2017**, *47*, 51–62.

- [105] Lehmani, A.; Turq, P.; Périé, M.; Périé, J.; Simonin, J.-P. Ion transport in Nafion<sup>®</sup> 117 membrane. *Journal of Electroanalytical Chemistry* **1997**, *428*, 81–89.
- [106] Page, K. A.; Landis, F. A.; Phillips, A. K.; Moore, R. B. SAXS analysis of the thermal relaxation of anisotropic morphologies in oriented Nafion membranes. *Macromolecules* **2006**, *39*, 3939–3946.
- [107] Szajdzinska-Pietek, E.; Wolszczak, M.; Plonka, A.; Schlick, S. Structure and dynamics of micellar aggregates in aqueous nafion solutions reported by electron spin resonance and fluorescence probes. *Macromolecules* **1999**, *32*, 7454–7460.
- [108] Shubnell, A. J.; Kosnic, E. J.; Squattrito, P. J. Structures of layered metal sulfonate salts: Trends in coordination behavior of alkali, alkaline earth and transition metals. *Inorganica Chimica Acta* **1994**, *216*, 101–112.
- [109] Harris, C. S.; Rukavina, T. G. Lithium ion conductors and proton conductors: Effects of plasticizers and hydration. *Electrochimica Acta* **1995**, 2315–2320.
- [110] Yamamoto, T.; Ushiro, A.; Yamaguchi, I.; Sasaki, S. Synthesis, structure, and chemical properties of lithium salts of poly(2-methoxyaniline-5-sulfonic acid). *Macromolecules* **2003**, *36*, 7075–7081.
- [111] Brooks, N. R.; Henderson, W. A.; Smyrl, W. H. Lithium trifluoromethanesulfonate acetonitrile adduct. *Acta Crystallographica Section E Structure Reports Online* **2002**, *58*, m176–m177.
- [112] Okada, T.; Møller-Holst, S.; Gorseth, O.; Kjelstrup, S. Transport and equilibrium properties of Nafion<sup>®</sup> membranes with H<sup>+</sup> and Na<sup>+</sup> ions. *Journal of Electroanalytical Chemistry* **1998**, *442*, 137–145.
- [113] Du, F.; Warsinger, D. M.; Urmi, T. I.; Thiel, G. P.; Kumar, A.; Lienhard V, J. H. Sodium hydroxide production from seawater desalination brine: Process design and energy efficiency. *Environmental science & technology* **2018**, *52*, 5949–5958.
- [114] Vennekoetter, J.-B.; Sengpiel, R.; Wessling, M. Beyond the catalyst: How electrode and reactor design determine the product spectrum during electrochemical CO<sub>2</sub> reduction. *Chemical Engineering Journal* **2019**, *364*, 89–101.
- [115] Krause, R.; Reinisch, D.; Reller, C.; Eckert, H.; Hartmann, D.; Taroata, D.; Wiesner-Fleischer, K.; Bulan, A.; Lueken, A.; Schmid, G. Industrial application aspects of the electrochemical reduction of CO<sub>2</sub> to CO in aqueous electrolyte. *Chemie Ingenieur Technik* **2020**, *92*, 53–61.



- [116] Gupta, N.; Gattrell, M.; MacDougall, B. Calculation for the cathode surface concentrations in the electrochemical reduction of CO<sub>2</sub> in KHCO<sub>3</sub> solutions. *Journal of Applied Electrochemistry* **2006**, *36*, 161–172.
- [117] Chae, K. J.; Choi, M.; Ajayi, F. F.; Park, W.; Chang, I. S.; Kim, I. S. Mass transport through a proton exchange membrane (Nafion) in microbial fuel cells. *Energy & Fuels* **2008**, *22*, 169–176.
- [118] Abdol Rahim, A. H.; Tijani, A. S.; Kamarudin, S. K.; Hanapi, S. An overview of polymer electrolyte membrane electrolyzer for hydrogen production: Modeling and mass transport. *Journal of Power Sources* **2016**, *309*, 56–65.
- [119] Moukheiber, E.; Bas, C.; Alberola, N. D.; Flandin, L. Infrared and thermal behaviour of proton exchange membrane (PEM) after cationic contamination. *Journal of Membrane Science* **2013**, *431*, 105–112.
- [120] Wampfler, B.; Affolter, S.; Ritter, A.; Schmid, M. *Messunsicherheit in der Kunststoffanalytik: Ermittlung mit Ringversuchsdaten*; Hanser: München, 2017.
- [121] Spry, D. B.; Fayer, M. D. Proton transfer and proton concentrations in protonated Nafion fuel cell membranes. *The Journal of Physical Chemistry. B* **2009**, *113*, 10210–10221.
- [122] Vielstich, W. *Handbook of Fuel Cells: Fundamentals, Technology and Applications*; Wiley Interscience: Hoboken, NJ, 2010.
- [123] Büchi, F. N.; Scherer, G. G. In-situ resistance measurements of Nafion<sup>®</sup> 117 membranes in polymer electrolyte fuel cells. *Journal of Electroanalytical Chemistry* **1996**, *404*, 37–43.
- [124] Tsampas, M. N.; Pikos, A.; Brosda, S.; Katsaounis, A.; Vayenas, C. G. The effect of membrane thickness on the conductivity of Nafion. *Electrochimica Acta* **2006**, *51*, 2743–2755.
- [125] Phillips, R.; Dunnill, C. W. Zero gap alkaline electrolysis cell design for renewable energy storage as hydrogen gas. *RSC Advances* **2016**, *6*, 100643–100651.
- [126] Masel, I. R.; Chen, Q.; Liu, Z.; Kutz, R. B. (Masel et al.). Ion-conducting membranes: United States Patent. 2017.
- [127] Weakley, T. J. R. The crystal structures of rubidium 20-tungstocobaltato(II)diarsenate(III) hydrate, Rb<sub>8</sub>[As<sub>2</sub>CoW<sub>20</sub>O<sub>68</sub>(OH<sub>2</sub>)<sub>2</sub>] · 10 H<sub>2</sub>O and its zinc analogue. *Inorganica Chimica Acta* **1984**, 13–18.

- [128] Kutz, R. B.; Chen, Q.; Yang, H.; Sajjad, S. D.; Liu, Z.; Masel, I. R. Sustainion imidazolium-functionalized polymers for carbon dioxide electrolysis. *Energy Technology* **2017**, *5*, 929–936.
- [129] Nave, M. I.; Kornev, K. G. Complexity of products of tungsten corrosion: comparison of the 3D pourbaix diagrams with the experimental data. *Metallurgical and Materials Transactions A* **2017**, *48*, 1414–1424.
- [130] Knoth, W. H.; Domaille, P. J.; Farlee, R. D. Anions of the type  $(\text{RMOH}_2)_3\text{W}_{18}\text{P}_2\text{O}_{68}^{9-}$  and  $[\text{H}_2\text{OCo}]_3\text{W}_{18}\text{P}_2\text{O}_{68}^{12-}$ . A reinvestigation of B,b- $\text{W}_9\text{PO}_{34}^{9-}$ . *Organometallics* **1985**, *4*, 62–68.
- [131] van Eldik, R., Cronin, L., Eds. *Polyoxometalate chemistry*, first edition ed.; Advances in Inorganic Chemistry; AP Academic Press an imprint of Elsevier: Cambridge, MA and San Diego, CA and Oxford, 2017; Vol. volume 69.
- [132] Jung, H.-Y.; Kim, J. W. Role of the glass transition temperature of Nafion 117 membrane in the preparation of the membrane electrode assembly in a direct methanol fuel cell (DMFC). *International Journal of Hydrogen Energy* **2012**, *37*, 12580–12585.
- [133] Brandsch, T.; Schell, F.-A.; Weis, K.; Ruf, M.; Müller, B.; Vahrenkamp, H. On the ligating properties of sulfonate and perchlorate anions towards zinc. *Chemische Berichte* **1997**, *130*, 283–289.
- [134] Yoder, C. H. Application of the simple salt lattice energy approximation to the solubility of minerals. *American Mineralogist* **2006**, *91*, 747–752.
- [135] Hori, Y. In *Modern Aspects of Electrochemistry*; Vayenas, C. G., White, R. E., Gamboa-Aldeco, M. E., Eds.; Modern Aspects of Electrochemistry; Springer New York: New York, NY, 2008; Vol. 42; pp 89–189.
- [136] Kuhl, K. P.; Cave, E. R.; Abram, D. N.; Jaramillo, T. F. New insights into the electrochemical reduction of carbon dioxide on metallic copper surfaces. *Energy & Environmental Science* **2012**, *5*, 7050.
- [137] Romero Cuellar, N. S.; Wiesner-Fleischer, K.; Hinrichsen, O.; Fleischer, M. Electrochemical reduction of  $\text{CO}_2$  in water-based electrolytes  $\text{KHCO}_3$  and  $\text{K}_2\text{SO}_4$  using boron doped diamond electrodes. *ChemistrySelect* **2018**, *3*, 3591–3595.
- [138] Martić, N.; Reller, C.; Macauley, C.; Löffler, M.; Schmid, B.; Reinisch, D.; Volkova, E.; Maltenberger, A.; Rucki, A.; Mayrhofer, K. J. J.; Schmid, G. Paramelaconite-enriched copper-based material as an efficient and robust cat-

- alyst for electrochemical carbon dioxide reduction. *Advanced Energy Materials* **2019**, *9*, 1901228.
- [139] Soboyejo, W. O. *Mechanical properties of engineered materials*; Mechanical engineering; Marcel Dekker: New York, 2003; Vol. 152.
- [140] Hongsirikarn, K.; Goodwin, J. G.; Greenway, S.; Creager, S. Effect of cations ( $\text{Na}^+$ ,  $\text{Ca}^{2+}$ ,  $\text{Fe}^{3+}$ ) on the conductivity of a Nafion membrane. *Journal of Power Sources* **2010**, *195*, 7213–7220.
- [141] The Chemours Company FC, LLC, Nafion<sup>®</sup> N115, N117, N1110 Ion Exchange Materials: Extrusion Cast Membranes. 2016; <https://www.fuelcellstore.com/spec-sheets/chemours-nafion-115-117-1110-spec-sheet.pdf>.
- [142] Langmuir, I. The effect of space charge and residual gases on thermionic currents in high vacuum. *Physical Reviews* **1913**, *2*, 450–486.
- [143] Zhang, J.; Zhang, H.; Wu, J.; Zhang, J. In *Pem Fuel Cell Testing and Diagnosis*; Zhang, J., Ed.; Elsevier, 2013; Vol. 149; pp 243–282.
- [144] Babic, U.; Zlobinski, M.; Schmidt, T. J.; Boillat, P.; Gubler, L.  $\text{CO}_2$ -Assisted regeneration of a polymer electrolyte water electrolyzer contaminated with metal ion impurities. *Journal of the Electrochemical Society* **2019**, *166*, F610–F619.
- [145] Etienne, M.; Dierkes, P.; Erichsen, T.; Schuhmann, W.; Fritsch, I. Constant-distance mode scanning potentiometry. High resolution pH measurements in three dimensions. *Electroanalysis* **2007**, *19*, 318–323.
- [146] Botz, A.; Clausmeyer, J.; Öhl, D.; Tarnev, T.; Franzen, D.; Turek, T.; Schuhmann, W. Local activities of hydroxide and water determine the operation of silver-based oxygen depolarized cathodes. *Angewandte Chemie (International ed. in English)* **2018**, *57*, 12285–12289.
- [147] Greszler, T. A.; Moylan, T. E.; Gasteiger, H. A. In *Handbook of Fuel Cells*; Vielstich, W., Lamm, A., Gasteiger, H. A., Yokokawa, H., Eds.; John Wiley & Sons, Ltd: Chichester, UK, 2010; Vol. 154; p B631.
- [148] Kumar, S.; Srivastava, R.; Koh, J. Utilization of zeolites as  $\text{CO}_2$  capturing agents: Advances and future perspectives. *Journal of  $\text{CO}_2$  Utilization* **2020**, *41*, 101251.
- [149] Resasco, J.; Chen, L. D.; Clark, E.; Tsai, C.; Hahn, C.; Jaramillo, T. F.; Chan, K.; Bell, A. T. Promoter effects of alkali metal cations on the electrochemical re-

- duction of carbon dioxide. *Journal of the American Chemical Society* **2017**, *139*, 11277–11287.
- [150] Singh, M. R.; Kwon, Y.; Lum, Y.; Ager, J. W.; Bell, A. T. Hydrolysis of electrolyte cations enhances the electrochemical reduction of CO<sub>2</sub> over Ag and Cu. *Journal of the American Chemical Society* **2016**, *138*, 13006–13012.

## 5. List of Figures

|     |   |    |
|-----|---|----|
| 1.  | Production of green hydrogen and its role in the energy supply chain in Germany 2021. <sup>[1]</sup> . . . . .  | 2  |
| 2.  | Worldwide total industrial hydrogen production by source, <sup>[9]</sup> pointing out the small share of electrolysis applications. . . . .   | 3  |
| 3.  | Overview of transition metals as OER catalyst materials clustering in noble (violet) vs. earth-abundant (turquoise) metals and the so-called oxo-wall depicted as a violet background. <sup>[27]</sup> . . . . .  | 7  |
| 4.  | Structural approach to gain a systematic overview of OER catalyst materials as presented by Tahir <i>et al.</i> <sup>[24]</sup> . . . . .   | 9  |
| 5.  | Single crystal structures of POM anionic clusters obtained as sodium salts (Na <sup>+</sup> omitted for clarity). The anionic clusters were investigated as OER catalysts in their insoluble form (as barium salt). <sup>[47]</sup> . . . . .   | 10 |
| 6.  | Overview of methods used in the first part of this thesis. . . . .  | 12 |
| 7.  | Scribner installation for water electrolysis. The cathode side is shown on the left, the anode side is shown on the right. The setup is composed of two end plates (a), a current collector (b), a graphite (c) and a titanium (h) flow field, EPDM sealings (d), titanium grids with different mesh widths (e, f) and the MEA in the middle (g). <sup>[65]</sup> . . . . . | 13 |
| 8.  | Overview of PFSA application fields. . . . .  | 14 |
| 9.  | PFSA molecular structure and potential bonding of a trivalent metal cation. Ionic radii are given for H <sup>+</sup> , Li <sup>+</sup> and K <sup>+</sup> . The depiction is true to scale and the proton is illustrated with an assumed radius of 10 pm, since the theoretical, effective radius is negative. <sup>[72,73]</sup> . . . . .                                 | 16 |
| 10. | Aluminum Lewis acid-catalyzed PFSA degradation mechanism by side chain ether cleavage. <sup>[90]</sup> . . . . .  | 18 |
| 11. | Schematic overview of the MEA fabrication process <i>via</i> decal transfer. <sup>[94]</sup> . . . . .  | 19 |

12. Visualization of potential PFSA layer formation in PFSA due to oxygen-lithium ionic interactions resulting in a highly ion-conductive pore structure. Lithium-triflate crystallographic structures are used as a template for analogue interactions in PFSA.<sup>[111]</sup> O – red, C – grey, S – yellow, F – green, Li – violet. . . . . 21
13. Visualization of opposed cation migration (cathode to anode side) vs. electrodiffusion direction (anode to cathode side) when high molar electrolytes are fed at the cathode side only in a model PEM water electrolysis setup. . . . . 23
14. Four-step approach to assess membrane resistance information caused by cation-proton exchange in PFSA. . . . . 24
15. Graphical abstract of the work conducted in the first chapter including catalyst synthesis, electrochemical analysis and subsequent stability evaluation. . . . . 28
16. Molecular structures of the POM fragments of a)  $\text{Na}_{16}[\text{Co}_9]$  and b)  $\text{Na}_{10}[\text{Co}_4]$  as obtained by single-crystal X-ray diffraction. Ellipsoids are displayed at the 50% probability level and oxygen atoms are simplified as wireframes. Symmetry code to create equivalent positions in b): 1-x, 1-y, 1-z. . . . . 37
17. Powder XRDs for insoluble barium salts of a)  $[\text{Co}_9]^{16-}$  and b)  $[\text{Co}_4]^{10-}$  anions with (h,k,l)-indices assigned to the most prominent reflections. c) + d) Scanning electron microscopy images of  $\text{Ba}_8[\text{Co}_9]$  at different magnifications showing the needle-like structure of the POM salts. . . . . 38
18. Results of temperature degradation study on  $\text{Ba}_8[\text{Co}_9]$ : Samples were heated for 30 min at each temperature step and subsequently analyzed by XRD. For decal processing, temperatures above 125 °C are necessary. 41
19. Cyclovoltammetric measurement results with  $\text{K}_{2.4}\text{Na}_{13.6}[\text{Co}_9]$  in solution between -1.4 and + 1.4 V. The CV was cycled three times with the results being perfectly reproducible. . . . . 42
20. Electrochemical evaluation of POM-MEAs with different anode catalyst layer composition in a cyclovoltammetry study. a) 40%  $\text{Ba}_8[\text{Co}_9]$  plus carbon powder as described in literature,<sup>[52]</sup> b) trial to stabilize a layer identical to a) with additional Nafion<sup>TM</sup> ionomer, c) 40%  $\text{Ba}_5[\text{Co}_4]$  plus carbon powder and d) pure  $\text{Ba}_8[\text{Co}_9]$  without carbon. 43

21. Electrochemical evaluation of a POM-MEA under galvanostatic conditions at 10 and 5 mA. Instrumental specifications lead to a maximum achievable potential limit of 10 V. Data cannot be recorded beyond this value. a) 40% Ba<sub>8</sub>[Co<sub>9</sub>] plus carbon powder as described in literature,<sup>[56]</sup> and b) reference Ir-formulation on the anode side of the MEA. . . . . 45
22. Electrochemical characterization of a Pt half-MEA with the POM catalyst containing ink coated directly onto the Ti grid. . . . . 46
23. XRD study of MEAs before and after electrolysis. . . . . 47
24. UV-VIS acid decomposition study: a) Ba<sub>8</sub>[Co<sub>9</sub>] after treatment with sulfuric acid of different pH (6, 5, 4, 3, 2, 1, 0); b) Mn, Fe and Ni doped Ba<sub>8</sub>[Co<sub>9</sub>] after treatment with sulfuric acid of different pH (2, 1, 0) and c) Ba<sub>5</sub>[Co<sub>4</sub>] after treatment with sulfuric acid of different pH (6, 5, 4, 3, 2, 1, 0). . . . . 50
25. POM XRD studies after acid treatment. Above: Diffractograms from solid residuals. Below: Diffractograms from evaporated acidic mother liquors. . . . . 55
26. Graphical abstract of the work conducted in the second chapter including membrane modification, electrochemical analysis and potential-driven substitution *in situ*. . . . . 58
27. Installation for water electrolysis used in this study for electrochemical performance determination. The cathode side is shown on the left, the anode side is shown on the right. The setup is composed of two end plates (a), a current collector (b), a graphite (c) and a titanium (h) flow field, EPDM sealings (d), titanium grids with different mesh widths (e, f) and the MEA in the middle (g). . . . . 64
28. (a) Illustration of the molecular structure of perfluorinated sulfonic acid (PFSA) with the polymer backbone highlighted in bold blue and the side chain indicated in bold black. The sulfonic acid group bearing the mobile proton is depicted in light turquoise; (b) Size comparison of the cations investigated herein. The illustration is true to scale in accordance with the ionic radii listed in Table 8. Since theoretical, negative values of the effective ionic radius of a proton cannot be illustrated, it is depicted with an assumed ionic radius of 10 pm. . . . 67

29. Dynamic mechanical analysis results for PFSA membranes in the protonated form as well as in different ion exchanged forms. (a) Pristine PFSA:  $E'$  curve depicted in yellow is the extensional storage modulus,  $E''$  shown in red indicates the extensional loss modulus. The loss factor  $\tan \delta = (E''/E')$  depicted in green gives the glass transition point ( $T_g$ ) and the blue dashed line represents the linear temperature ramp for the measurement; (b)  $\tan \delta$  curves for protonated PFSA as well as for alkaline metal cation exchanged PFSA; (c)  $\tan \delta$  curves for protonated PFSA as well as for alkylammonium cation exchanged PFSA; (d)  $\tan \delta$  curves for protonated PFSA as well as for bivalent metal cation exchanged PFSA. Arrows highlight shoulders resulting from  $\beta$ -relaxations in the PFSA backbone. In Figure 3 b–d  $\tan \delta$  of protonated PFSA is used to reference samples against each other. . . . . 70
30. Half-MEAs (upper row) produced *via* decal transfer and their respective negatives (lower row, remaining Kapton<sup>®</sup> substrates) on protonated as well as cation exchanged PFSA membranes. In some cases ( $H^+$ ,  $Li^+$ ,  $Mg^{2+}$ ,  $Zn^{2+}$  and  $TMA^+$ ) catalyst transfer onto the membrane was complete whereas the catalyst layer is incomplete in the case of others ( $Na^+$ ,  $K^+$ ,  $Ca^{2+}$ ). Although there is residual catalyst visible on the Kapton<sup>®</sup> negative,  $TMA^+$  exchanged PFSA results in an intact half-MEA. . . . . 73
31. Microscopy pictures of half-MEA cross sections. (a) Protonated half-MEA showing a thick Pt-layer on the bottom. (b)  $Li^+$  half-MEA with a thinner but uniform catalyst layer and (c)-(d)  $Mg^{2+}$  half-MEAs produced by the same method but showing significant differences in shape and thickness of the catalyst layer. A yellow star indicates the Pt-side of the half-MEA and the position of the catalyst layer. . . . . 75
32. Cyclovoltammetry (CV) results for water electrolysis on an Ir/Pt-MEA system using membranes with different counteranions. Red: polarization curve of a protonated MEA serving as a reference. Green: polarization curve of a  $TBA^+$  cation exchanged MEA. Blue: polarization curve of a  $Li^+$  cation exchanged MEA. Magenta: polarization curve of a  $Zn^{2+}$  cation exchanged MEA. Inset view on a logarithmic scale: Butler-Volmer consideration to assess the onset potential and thus the energy of starting ion mobility. Arrows indicate the scan direction. . . . . 77



33. Polarization curves for water electrolysis on an Ir/Pt-MEA system using a  $\text{Zn}^{2+}$  cation exchanged MEA. CVs were run 80 times subsequently showing an increase in maximum current density reached. The polarization curves are evening out slightly below the current compliance at a potential of 3.5 V. . . . . 81
34. Linear regression analysis results obtained from the ohmic part of the membrane's cyclic voltammograms. . . . . 81
35. *Nyquist* plots for a protonated, a  $\text{Li}^+$  and a  $\text{Zn}^{2+}$  ion exchanged membrane at different current densities. . . . . 82
36. Results from potential-controlled cation back-exchange investigations of ion exchanged MEAs. a, c) Current densities obtained from potentiostatic measurements at different potential steps for  $\text{Li}^+$  (a) and  $\text{Zn}^{2+}$  (c) exchanged MEAs. (b, d) Comparison of CVs measured initially (dark color) with CVs measured after potentiostatic treatment (light color) for  $\text{Li}^+$  (b) and  $\text{Zn}^{2+}$  (d) exchanged MEAs. . . . . 84
37. Results from galvanostatic investigations of a  $\text{Li}^+$  and a  $\text{Zn}^{2+}$  MEA (blue) with an applied constant current of  $1.5 \text{ A/cm}^2$  (grey). A standard protonated MEA (red) was used as a reference. . . . . 87
38. Graphical abstract of the work conducted in the third chapter including characterization in a PEM water electrolysis model system, resistance determination both, theoretically and experimentally, and implications for  $\text{CO}_2$  electrolysis. . . . . 91
39. Overview of a) a half-MEA approach for  $\text{CO}_2$  electrolysis and b) the model water electrolysis mode used as a model setup in this study. The enlarged inlet in b) visualizes the interplay of proton transport from anode to cathode with the  $\text{K}^+$  uptake from an electrolyte employed at the cathode side. . . . . 93
40. Experimental setup for electrochemical experiments in a) a mixed electrolyte configuration (mode<sub>mix</sub>) with different electrolyte reservoirs to avoid formation of explosive mixtures (oxyhydrogen) and b) in a separate electrolyte configuration (mode<sub>sep</sub>) for electrolyte variation studies. C – cathode side, A – anode side. . . . . 97

41. Flow chart of the electrochemical measurement procedure. SP – safety voltage, CV – cyclic voltammetry, EIS – electrochemical impedance spectroscopy, GS – galvanostatic steps. . . . . 99
42. Monitoring results of pH and temperature change of a 1.0 M KCl solution containing PFSA membrane pieces added at 108 s. Note: Before adding the membrane pieces, the system is not in a thermic equilibrium (falling temperature). Therefore, the temperature change should be understood as a tendency, not an absolute value. . . . . 102
43. Results obtained from a variation of the electrolysis operation mode: Electrolyte studies were conducted in different experimental configurations: a) mode<sub>sep</sub> with electrolyte at one side only (and ultrapure water at the other side, respectively) and b) mode<sub>mix</sub>. Both measurements are referenced to the same control experiment with no electrolyte, but ultrapure water used at both sides (grey squares). . . . . 105
44. Nyquist plots showing electrochemical impedance spectra obtained pre- and post-electrolysis: a) 1.0 M KHCO<sub>3</sub> at anode and cathode side (A+C), b) 1.0 M KHCO<sub>3</sub> at cathode side only (C<sub>only</sub>) and c) H<sub>2</sub>O reference. The frequency range comprised 10.0 kHz to 40.0 mHz with an amplitude of 5.00 mA and 66 points per decade. d) Equivalent circuit diagram, on which EIS fittings are based. . . . . 107
45. Visualization of different experimental configurations and implied pH differences. a) No electrolyte used, 1.0 M KHCO<sub>3</sub> at b) the cathode and c) the anode side. The impact of K<sup>+</sup> transport on the reaction and local pH microenvironment is considered with d) 1.0 M KHCO<sub>3</sub> and e) 1.0 M K<sub>2</sub>SO<sub>4</sub> at the anode side. . . . . 113
46. Concentration variation study in modesep with electrolyte used at the cathode side only. a) results of the original study and b) pure K<sup>+</sup>-induced overpotentials obtained from subtracting reference mean values at each current density step from the respective results with electrolyte at the cathode side only (C<sub>only</sub>) experiments at different concentrations (1.0 mM, 0.5 M, 1.0 M and 1.5 M KHCO<sub>3</sub>). . . . . 117
47. Visualization of cation migration directions at a) open circuit potential (without applied voltage and thus current), b) low current density and c) high current density. C – cathode, A – anode. . . . . 119

- 
48. Concentration variation study in mode<sub>mix</sub> showing a) the effect of a small concentration and b) increasing cell voltages with increasing concentration. . . . . 120
49. *Tafel* plots of 1.0 mM KHCO<sub>3</sub> concentrations in a) mode<sub>mix</sub> and b) mode<sub>sep</sub>. . . . . 121

## 6. List of Tables

|     |  |    |
|-----|--|----|
| 1.  | Suppliers and purities of chemicals applied for catalyst syntheses in this study. . . . .  | 31 |
| 2.  | Overview of ink formulations used for MEA production and subsequent electrochemical characterization. . . . .  | 35 |
| 3.  | Correlated (h,k,l)-indices for Ba <sup>2+</sup> POM powder diffractograms. . . . .   | 39 |
| 4.  | Elemental analysis results (ICP-AES) for the POM materials. Except for Sust[Co9] data was normalized to the W content to facilitate comparison. . . . .  | 40 |
| 5.  | Transverse conductivities of catalyst layers and pure Nafion <sup>TM</sup> . . . . .   | 41 |
| 6.  | Synthesis list including Co replacements by metals, obtained yields and elemental analysis results for metal substituted POMs. Elemental analysis data was normalized to the W content to facilitate comparison. . . . .   | 53 |
| 7.  | Suppliers and purities of metal or alkylammonium (M <sup>n+</sup> ) salts used for PFSA counterion exchange. pH <sub>start</sub> and pH <sub>end</sub> indicate pH values of a 2 M solution of the salt before and after immersing the PFSA membrane for 24 h. . . . .   | 62 |
| 8.  | List of cations used for counterion exchange in PFSA membranes in this study including effective ionic radii of metal cations <sup>[72]</sup> and the proton <sup>[72]</sup> and crystallographic radii for alkylammonium salts <sup>[73]</sup> as well as literature data for T <sub>g</sub> (where available) <sup>[62,86,121]</sup> and T <sub>g</sub> assessed by DMA in this study. . . . . | 68 |
| 9.  | Optical evaluation and quantitative gravimetric data for decal transfers. . . . .  | 73 |
| 10. | Ohmic resistances of a protonated and the ion exchanged membranes calculated from cyclic voltammetry measurements and experimental data obtained from impedance spectroscopy. Calculated data were obtained from linear regression analysis of the linear, ohmic part of the cyclic voltammograms in Figure 32. . . . .  | 82 |
| 11. | pH changes of salt solutions before and after membranes or used MEAs were immersed. A lowering of the pH indicates an expel of protons from the membrane into solution <i>via</i> formation of HCl(aq). . . . .  | 86 |

- 
12. Elemental analysis results for fresh  $\text{Li}^+$  and  $\text{Zn}^{2+}$  ion exchanged membranes and a processed,  $\text{Li}^+$  exchanged MEA after electrolysis. . . . . 88
  13. Membrane and charge transfer resistances obtained from *Nyquist* plots shown in Figure 44, normalized to the active surface area of  $5 \text{ cm}^{\text{arg}}$ . For membrane resistances, values are compared at the onset of the graph (high frequency resistance, HFR). LFR – low frequency resistance, el – electrolysis. . . . . 108
  14. Thermodynamic considerations towards different experimental configurations shown in Figure 45. pH induced potential differences were calculated using equation 28 in combination with the experimental pH data given in Figure 45. . . . . 115
  15. Slopes obtained from the linear, ohmic region of  $C_{\text{only}}$  overpotential curves depicted in Figure 46. The respective linear fits are shown as grey dotted lines in the graph. . . . . 118
  16. Measured electrolyte conductivities and calculated ohmic resistances of an assumed  $180 \mu\text{m}$  gap liquid buffer layer. . . . . 124
  17. Overview of identified voltage contributions to the total cell voltage. To reach  $V_{\text{total}}$ , not all contributions need to be taken into account, since some of them are dependent on the operation mode or concentration regime. To guarantee comparison to literature, data was collected and compared at a current density of  $300 \text{ mA/cm}^2$ . . . . . 127

## 7. Reprint permissions

### 7.1. Wiley articles

**CCC** | RightsLink® ? Help    ✉ Email Support

---

**Publisher:** John Wiley and Sons  
© 2021 The Authors. *Electrochemical Science Advances* published by Wiley-VCH GmbH

---

**Open Access Article**  
This is an open access article distributed under the terms of the [Creative Commons CC BY](#) license, which permits unrestricted use, distribution, and reproduction in any medium, provided the original work is properly cited.

You are not required to obtain permission to reuse this article.

For an understanding of what is meant by the terms of the Creative Commons License, please refer to [Wiley's Open Access Terms and Conditions](#).

Permission is not required for this type of reuse.

Wiley offers a professional reprint service for high quality reproduction of articles from over 1400 scientific and medical journals. Wiley's reprint service offers:

- Peer reviewed research or reviews
- Tailored collections of articles
- A professional high quality finish
- Glossy journal style color covers
- Company or brand customisation
- Language translations
- Prompt turnaround times and delivery directly to your office, warehouse or congress.

Please contact our Reprints department for a quotation. Email [corporatesaleseurope@wiley.com](mailto:corporatesaleseurope@wiley.com) or [corporatesalesusa@wiley.com](mailto:corporatesalesusa@wiley.com) or [corporatesalesDE@wiley.com](mailto:corporatesalesDE@wiley.com).

---

© 2021 Copyright - All Rights Reserved | [Copyright Clearance Center, Inc.](#) | [Privacy statement](#) | [Terms and Conditions](#)  
Comments? We would like to hear from you. E-mail us at [customer-care@copyright.com](mailto:customer-care@copyright.com)

**Electrochemical Science Advances****Published by Wiley (the "Owner")****LICENSE AGREEMENT FOR PUBLISHING CC-BY-NC-ND**

Date: June 28, 2021

Contributor name: Günter Schmid

Contributor address:

Manuscript number: ELSA.202100073.R1

Re: Manuscript entitled Stability evaluation of earth-abundant metal based polyoxometalate electrocatalysts for oxygen evolution reaction towards industrial PEM electrolysis at high current densities (the "Contribution")

for publication in Electrochemical Science Advances (the "Journal")

published by Wiley-VCH GmbH ("Wiley")

Dear Contributor(s):

Thank you for submitting your Contribution for publication. In order to expedite the editing and publishing process and enable Wiley to disseminate your Contribution to the fullest extent, we need to have this Agreement executed. If the Contribution is not accepted for publication, or if the Contribution is subsequently rejected, this Agreement will be null and void.

**Publication cannot proceed without a signed copy of this Agreement and payment of the appropriate article publication charge in full (without deduction of any taxes or fees).**

**A. TERMS OF USE**

1. The Contribution will be made Open Access under the terms of the [Creative Commons Attribution-NonCommercial-NoDerivatives License](#) which permits use, distribution and reproduction in any medium, provided that the Contribution is properly cited, the use is non-commercial and no modifications or adaptations are made.
2. For an understanding of what is meant by the terms of the Creative Commons License, please refer to [Wiley's Open Access Terms and Conditions](http://www.wileyauthors.com/OAA) (<http://www.wileyauthors.com/OAA>).
3. Notwithstanding acceptance, the Owner or Wiley may (but is not obliged to) require changes to the Contribution, including changes to the length of the Contribution, and/or elect not to publish the Contribution if for any reason, in the Owner's or Wiley's reasonable judgment, such publication would be inconsistent with the Core Practices and associated guidelines set forth by the Committee on Publication Ethics (a not-for-profit organization based in the UK: <https://publicationethics.org/core-practices>) or would result in legal liability, violation of Wiley's ethical guidelines, or violation of journal ethical practices. If the Owner (or Wiley, where Wiley is not the Owner) decides not to publish the Contribution, no Article Processing Charge or any other fee shall be charged. The Contributor is free to submit the Contribution to any other journal from any other publisher.

**B. RETAINED RIGHTS**

The Contributor or, if applicable, the Contributor's Employer, retains all proprietary rights in addition to copyright, such as patent rights in any process, procedure or article of manufacture described in the Contribution.

#### **C. LICENSE**

In addition to the non-exclusive rights to the Contribution the Owner has under the CC-BY-NC-ND license, the Contributor grants to the Owner, during the full term of the Contributor's copyright and any extensions or renewals, an exclusive license of all rights of copyright in and to the Contribution that the Contributor does not grant under the CC-BY-NC-ND license, and all rights therein, including but not limited to the right to publish, republish, transmit, sell, distribute and otherwise use the Contribution in whole or in part in electronic and print editions of the Journal and in derivative works throughout the world, in all languages and in all media of expression now known or later developed, for commercial purposes, and to license or permit others to do so. Such exclusive rights do not conflict with the rights granted to users under the terms of the [Creative Commons Attribution-Non-Commercial-NoDerivs License](#). For the avoidance of doubt, "Contribution" is defined to only include the article submitted by the Contributor for publication in the Journal (including any embedded rich media) and does not extend to any supporting information submitted with or referred to in the Contribution ("Supporting Information"). To the extent that any Supporting Information is submitted to the Journal, the Owner is granted a perpetual, non-exclusive license to publish, republish, transmit, sell, distribute and otherwise use this Supporting Information in whole or in part in electronic and print editions of the Journal and in derivative works throughout the world, in all languages and in all media of expression now known or later developed, and to license or permit others to do so. If the Contribution was shared as a preprint, the Contributor grants to the Owner exclusivity as to any rights retained by the Contributor in the preprint.

#### **D. CONTRIBUTIONS OWNED BY EMPLOYER**

If the Contribution was written by the Contributor in the course of the Contributor's employment as a "work-made-for-hire" and the employer owns the copyright in the Contribution, the employer company/institution agrees to the terms of use set forth in paragraph A above and must execute this Agreement (in addition to the Contributor) in the space provided below. In such case, the company/institution hereby grants to the Owner, during the full term of copyright, an exclusive license of all rights of copyright in and to the Contribution throughout the world for commercial purposes and/or to create derivative works as specified in paragraph C above.

#### **E. GOVERNMENT CONTRACTS**

In the case of a Contribution prepared under U.S. Government contract or grant, the U.S. Government may reproduce, without charge, all or portions of the Contribution and may authorize others to do so, for official U.S. Government purposes only, if the U.S. Government contract or grant so requires. (U.S. Government, U.K. Government, and other government employees: see notes at end.)

#### **F. COPYRIGHT NOTICE**

Owner (and Wiley, where Wiley is not the Owner), the Contributor, and the company/institution agree that any and all copies of the Contribution or any part thereof distributed or posted by them in print or electronic format as permitted will include the notice of copyright as stipulated in the Journal and a full citation to the final published version of the Contribution in the Journal as published by Wiley.

#### **G. CONTRIBUTOR'S REPRESENTATIONS**

The Contributor represents that: (i) the Contributor and all co-Contributors have the full power, authority and capability to enter into this Agreement, to grant the rights and license granted herein and to perform all obligations hereunder; (ii) neither the Contributor nor any co-Contributor has granted exclusive rights to, or transferred their copyright in, any version of the Contribution to any third party; (iii) the Contribution is the Contributor's original work, all individuals identified as Contributors actually contributed to the Contribution, and all individuals who contributed are included; (iv) if the Contribution was prepared jointly, the Contributor has informed the co-Contributors of the terms of this Agreement and has obtained their signed written permission to execute this Agreement on their behalf as their agent; (v) the Contribution is submitted only to this Journal and has not been published before, has not been included in another manuscript, and is not currently under consideration or accepted for publication elsewhere; (vi) if excerpts from copyrighted works owned by third parties are included, the Contributor shall obtain written permission from the copyright owners for all uses as set forth in the standard





*regulations and submit the appropriate authorisation to publish. If your status as a government employee legally prevents you from signing this Agreement, please contact the Journal production editor. If this selection does not apply to at least one author in the group, this author should also sign the form, indicating transfer of those rights which that author has and selecting the appropriate additional ownership selection option. If this applies to more than one author, one may sign on behalf of the others.*

**[ ] Other**

Including Other Government work or Non-Governmental Organisation work

*Note to Non-U.S., Non-U.K. Government Employees or Non-Governmental Organisation Employees*

*If you are employed by the World Health Organization or UNU-WIDER, please download a copy of the license agreement from <http://www.wileyauthors.com/licensingFAQ> and upload the form to the Wiley Author Services Dashboard. If your status as a government or non-governmental organisation employee legally prevents you from signing this Agreement, please contact the Journal production editor.*

Name of Government/Non-Governmental Organisation:

---

**[ ] Company/institution owned work (made for hire in the course of employment)**

If this selection does not apply to at least one author in the group, this author should also sign the form, indicating transfer of those rights which that author has and selecting the appropriate additional ownership selection option. If this applies to more than one author, one may sign on behalf of the others.

Name of Company/Institution:

---

Authorized Signature of Employer:

---

Date:

---

Signature of Employee:

---

Date:

---

**ChemElectroChem****Published by Wiley and Chemistry Europe (together the "Owner")****COPYRIGHT TRANSFER AGREEMENT**

Date: November 16, 2021

Contributor name: Guenter Schmid

Contributor address:

Manuscript number: celc.202101165

Re: Manuscript entitled K<sup>+</sup> Transport in perfluorosulfonic acid membranes and its influence on membrane resistance in CO<sub>2</sub> electrolysis (the "Contribution")

for publication in ChemElectroChem (the "Journal")

published by Wiley-VCH GmbH ("Wiley")

Dear Contributor(s):

Thank you for submitting your Contribution for publication. In order to expedite the editing and publishing process and enable the Owner to disseminate your Contribution to the fullest extent, we need to have this Copyright Transfer Agreement executed. If the Contribution is not accepted for publication, or if the Contribution is subsequently rejected, this Agreement shall be null and void.

**Publication cannot proceed without a signed copy of this Agreement.**

---

**A. COPYRIGHT**

1. The Contributor assigns to the Owner, during the full term of copyright and any extensions or renewals, all copyright in and to the Contribution, and all rights therein, including but not limited to the right to publish, republish, transmit, sell, distribute and otherwise use the Contribution in whole or in part in electronic and print editions of the Journal and in derivative works throughout the world, in all languages and in all media of expression now known or later developed, and to license or permit others to do so. "Contribution" means the article submitted by the Contributor for publication in the Journal (including any embedded rich media) and all subsequent versions. The definition of Contribution does not extend to any supporting information submitted with or referred to in the Contribution ("Supporting Information"). To the extent that any Supporting Information is submitted to the Journal, the Owner is granted a perpetual, non-exclusive license to publish, republish, transmit, sell, distribute and otherwise use this Supporting Information in whole or in part in electronic and print editions of the Journal and in derivative works throughout the world, in all languages and in all media of expression now known or later developed, and to license or permit others to do so. If the Contribution was shared as a preprint, the Contributor grants to the Owner exclusivity as to any rights retained by the Contributor in the preprint.

2. Reproduction, posting, transmission or other distribution or use of the final Contribution in whole or in part in any medium by the Contributor as permitted by this Agreement requires a citation to the Journal suitable in form and content as follows: (Title of Article, Contributor, Journal Title and Volume/Issue, Copyright © [year], copyright owner as specified in the Journal, Publisher). Links to the final article on the publisher website are encouraged where appropriate.

#### **B. RETAINED RIGHTS**

Notwithstanding the above, the Contributor or, if applicable, the Contributor's employer, retains all proprietary rights other than copyright, such as patent rights, in any process, procedure or article of manufacture described in the Contribution.

#### **C. PERMITTED USES BY CONTRIBUTOR**

**1. Submitted Version.** The Owner licenses back the following rights to the Contributor in the version of the Contribution as originally submitted for publication (the "Submitted Version"):

a. The right to self-archive the Submitted Version on: the Contributor's personal website; a not for profit subject-based preprint server or repository; a Scholarly Collaboration Network (SCN) which has signed up to the STM article sharing principles [<http://www.stm-assoc.org/stm-consultations/scn-consultation-2015/>] ("Compliant SCNs"); or the Contributor's company/ institutional repository or archive. This right extends to both intranets and the Internet. The Contributor may replace the Submitted Version with the Accepted Version, after any relevant embargo period as set out in paragraph C.2(a) below has elapsed. The Contributor may wish to add a note about acceptance by the Journal and upon publication it is recommended that Contributors add a Digital Object Identifier (DOI) link back to the Final Published Version.

b. The right to transmit, print and share copies of the Submitted Version with colleagues, including via Compliant SCNs, provided that there is no systematic distribution of the Submitted Version, e.g. posting on a listserve, network (including SCNs which have not signed up to the STM sharing principles) or automated delivery.

**2. Accepted Version.** The Owner licenses back the following rights to the Contributor in the version of the Contribution that has been peer-reviewed and accepted for publication, but not final (the "Accepted Version"):

a. The right to self-archive the Accepted Version on: the Contributor's personal website; the Contributor's company/institutional repository or archive; Compliant SCNs; and not for profit subject-based repositories such as PubMed Central, all subject to an embargo period of 12 months for scientific, technical and medical (STM) journals and 24 months for social science and humanities (SSH) journals following publication of the Final Published Version. There are separate arrangements with certain funding agencies governing reuse of the Accepted Version as set forth at the following website: <http://www.wileyauthors.com/funderagreements>. The Contributor may not update the Accepted Version or replace it with the Final Published Version. The Accepted Version posted must contain a legend as follows: This is the accepted version of the following article: FULL CITE, which has been published in final form at [Link to final article]. This article may be used for non-commercial purposes in accordance with the Wiley Self-Archiving Policy [<http://www.wileyauthors.com/self-archiving>].

b. The right to transmit, print and share copies of the Accepted Version with colleagues, including via Compliant SCNs (in private research groups only before the embargo and publicly after), provided that there is no systematic distribution of the Accepted Version, e.g. posting on a listserve, network (including SCNs which have not signed up to the STM sharing principles) or automated delivery.

**3. Final Published Version.** The Owner hereby licenses back to the Contributor the following rights with respect to the final published version of the Contribution (the "Final Published Version"):

**a.** Copies for colleagues. The personal right of the Contributor only to send or transmit individual copies of the Final Published Version in any format to colleagues upon their specific request, and to share copies in private sharing groups in Compliant SCNs, provided no fee is charged, and further provided that there is no systematic external or public distribution of the Final Published Version, e.g. posting on a listserve, network or automated delivery.

**b.** Re-use in other publications. The right to re-use the Final Published Version or parts thereof for any publication authored or edited by the Contributor (excluding journal articles) where such re-used material constitutes less than half of the total material in such publication. In such case, any modifications must be accurately noted.

**c.** Teaching duties. The right to include the Final Published Version in teaching or training duties at the Contributor's institution/place of employment including in course packs, e-reserves, presentation at professional conferences, in-house training, or distance learning. The Final Published Version may not be used in seminars outside of normal teaching obligations (e.g. commercial seminars). Electronic posting of the Final Published Version in connection with teaching/training at the Contributor's company/institution is permitted subject to the implementation of reasonable access control mechanisms, such as user name and password. Posting the Final Published Version on the open Internet is not permitted.

**d.** Oral presentations. The right to make oral presentations based on the Final Published Version.

#### **4. Article Abstracts, Figures, Tables, Artwork and Selected Text (up to 250 words).**

**a.** Contributors may re-use unmodified abstracts for any non-commercial purpose. For online uses of the abstracts, the Owner encourages but does not require linking back to the Final Published Version.

**b.** Contributors may re-use figures, tables, artwork, and selected text up to 250 words from their Contributions, provided the following conditions are met:

(i) Full and accurate credit must be given to the Final Published Version.

(ii) Modifications to the figures and tables must be noted. Otherwise, no changes may be made.

(iii) The re-use may not be made for direct commercial purposes, or for financial consideration to the Contributor.

(iv) Nothing herein will permit dual publication in violation of journal ethical practices.

#### **D. CONTRIBUTIONS OWNED BY EMPLOYER**

**1.** If the Contribution was written by the Contributor in the course of the Contributor's employment as a "work-made-for-hire" in the course of employment, the Contribution is owned by the company/institution which must execute this Agreement (in addition to the Contributor's signature). In such case, the company/institution hereby agrees to the terms of use set forth in paragraph A above and assigns to the Owner, during the full term of copyright, all copyright in and to the Contribution for the full term of copyright throughout the world as specified in paragraph A above.

**2.** In addition to the rights specified as retained in paragraph B above and the rights granted back to the Contributor pursuant to paragraph C above, the Owner hereby grants back, without charge, to such company/institution, its subsidiaries and divisions, the right to make copies of and distribute the Final Published Version internally in print format or electronically on the Company's internal network. Copies so used may not be resold or distributed externally. However, the company/institution may include information and text from the Final Published Version as part of an information package included with software or other products offered for sale or license or included in patent

applications. Posting of the Final Published Version by the company/institution on a public access website may only be done with written permission, and payment of any applicable fee(s). Also, upon payment of the applicable reprint fee, the company/institution may distribute print copies of the Final Published Version externally.

#### **E. GOVERNMENT CONTRACTS**

In the case of a Contribution prepared under U.S. Government contract or grant, the U.S. Government may reproduce, without charge, all or portions of the Contribution and may authorize others to do so, for official U.S. Government purposes only, if the U.S. Government contract or grant so requires. (U.S. Government, U.K. Government, and other government employees: see notes at end.)

#### **F. COPYRIGHT NOTICE**

The Contributor and the company/institution agree that any and all copies of the Final Published Version or any part thereof distributed or posted by them in print or electronic format as permitted herein will include the notice of copyright as stipulated in the Journal and a full citation to the Journal.

#### **G. CONTRIBUTOR'S REPRESENTATIONS**

The Contributor represents that: (i) the Contributor and all co-Contributors have the full power, authority and capability to enter into this Agreement, to grant the rights and license granted herein and to perform all obligations hereunder; (ii) neither the Contributor nor any co-Contributor has granted exclusive rights to, or transferred their copyright in, any version of the Contribution to any third party; (iii) the Contribution is the Contributor's original work, all individuals identified as Contributors actually contributed to the Contribution, and all individuals who contributed are included; (iv) if the Contribution was prepared jointly, the Contributor has informed the co-Contributors of the terms of this Agreement and has obtained their signed written permission to execute this Agreement on their behalf; (v) the Contribution is submitted only to this Journal and has not been published before, has not been included in another manuscript, and is not currently under consideration or accepted for publication elsewhere; (vi) if excerpts from copyrighted works owned by third parties are included, the Contributor shall obtain written permission from the copyright owners for all uses as set forth in the standard permissions form and the Journal's Author Guidelines, and show credit to the sources in the Contribution; (vii) the Contribution and any submitted Supporting Information contain no libelous or unlawful statements, do not infringe upon the rights (including without limitation the copyright, patent or trademark rights) or the privacy of others, do not breach any confidentiality obligation, do not violate a contract or any law, do not contain material or instructions that might cause harm or injury, and only utilize data that has been obtained in accordance with applicable legal requirements and Journal policies; and (viii) there are no conflicts of interest relating to the Contribution, except as disclosed. Accordingly, the Contributor represents that the following information shall be clearly identified on the title page of the Contribution: (1) all financial and material support for the research and work; (2) any financial interests the Contributor or any co-Contributors may have in companies or other entities that have an interest in the information in the Contribution or any submitted Supporting Information (e.g., grants, advisory boards, employment, consultancies, contracts, honoraria, royalties, expert testimony, partnerships, or stock ownership); and (3) indication of no such financial interests if appropriate.

Notwithstanding acceptance, the Owner or Wiley may (but is not obliged to) require changes to the Contribution, including changes to the length of the Contribution, and/or elect not to publish the Contribution if for any reason, in the Owner's or Wiley's reasonable judgment, such publication would be inconsistent with the Core Practices and associated guidelines set forth by the Committee on Publication Ethics (a not-for-profit organization based in the UK: <https://publicationethics.org/core-practices>) or would result in legal liability, violation of Wiley's ethical guidelines, or violation of journal ethical practices.

#### **H. USE OF INFORMATION**

The Contributor acknowledges that, during the term of this Agreement and thereafter, the Owner (and Wiley where Wiley is not the Owner) may process the Contributor's personal data, including storing or transferring data outside of the country of the Contributor's residence, in order to process transactions related to this Agreement and to communicate with the Contributor, and that the Publisher has a legitimate interest in processing the Contributor's personal data. By entering into this Agreement, the Contributor agrees to the processing of the Contributor's personal data (and, where applicable, confirms that the Contributor has obtained the permission from all other contributors to process their personal data). Wiley shall comply with all applicable laws, statutes and regulations relating to data protection and privacy and shall process such personal data in accordance with Wiley's Privacy Policy located at: <https://www.wiley.com/en-us/privacy>.

---

I agree to the COPYRIGHT TRANSFER AGREEMENT as shown above, consent to execution and delivery of the Copyright Transfer Agreement electronically and agree that an electronic signature shall be given the same legal force as a handwritten signature, and have obtained written permission from all other contributors to execute this Agreement on their behalf.

Contributor's signature (type name here):                      Günter Schmid

Date:    November 16, 2021

---

**SELECT FROM OPTIONS BELOW:**

**Contributor-owned work**

**U.S. Government work**

*Note to U.S. Government Employees*

*A contribution prepared by a U.S. federal government employee as part of the employee's official duties, or which is an official U.S. government publication, is called a "U.S. government work", and is in the public domain in the United States. If the Contribution was not prepared as part of the employee's duties, is not an official U.S. government publication, or if at least one author is **not** a U.S. government employee, it is not a U.S. government work. If at least one author is **not** a U.S. government employee, then the non-government author should also sign the form, selecting the appropriate ownership option. If more than one author is not a U.S. government employee, one may sign on behalf of the others.*

**U.K. Government work (Crown Copyright)**

*Note to U.K. Government Employees*

*The rights in a contribution prepared by an employee of a UK government department, agency or other Crown body as part of his/her official duties, or which is an official government publication, belong to the Crown and must be made available under the terms of the Open Government Licence. Contributors must ensure they comply with departmental regulations and submit the appropriate authorisation to publish. If your status as a government employee legally prevents you from signing this Agreement, please contact the Journal production editor. If this selection does not apply to at least one author in the group, this author should also sign the form, indicating transfer of those rights which that author has and selecting the appropriate additional ownership selection option. If this applies to more than one author, one may sign on behalf of the others.*

**Other**

Including Other Government work or Non-Governmental Organisation work

*Note to Non-U.S., Non-U.K. Government Employees or Non-Governmental Organisation Employees*

*If you are employed by the Australian Government, the World Bank, the World Health Organization, the International Monetary Fund, the European Atomic Energy Community, the Jet Propulsion Laboratory at California Institute of Technology, the Asian Development Bank, the Bank of International Settlements, USDA Agricultural Research Services, or are a Canadian Government civil servant, please download a copy of the license agreement from <http://www.wileyauthors.com/licensingFAQ> and upload the form to the Wiley Author Services Dashboard. If your status as a government or non-governmental organisation employee legally prevents you from signing this Agreement, please contact the Journal production editor.*

Name of Government/Non-Governmental Organisation:

---

**[ ] Company/institution owned work (made for hire in the course of employment)**

If you are an employee of Amgen, please download a copy of the company addendum from <http://www.wileyauthors.com/licensingFAQ> and return your signed license agreement along with the addendum. If this selection does not apply to at least one author in the group, this author should also sign the form, indicating transfer of those rights which that author has and selecting the appropriate additional ownership selection option. If this applies to more than one author, one may sign on behalf of the others.

Name of Company/Institution:

---

Authorized Signature of Employer:

---

Date:

---

Signature of Employee:

---

Date:

---



---




## 7.2. Elsevier article

**CCC** | RightsLink®

[Home](#)
[?](#)
[Help](#)
[Email Support](#)
[Sign in](#)
[Create Account](#)

---



**Morphological tuning of membrane processing by temporal proton-metal cation substitution in perfluorosulfonic acid membranes**

Author: Kim-Marie Vetter, Thomas Reichbauer, Nemanja Martić, David Reinisch, Olaf Hinrichsen, Günter Schmid

Publication: Electrochimica Acta

Publisher: Elsevier

Date: 1 December 2020

© 2020 Elsevier Ltd. All rights reserved.

#### Quick Price Estimate

This service provides permission for reuse only. If you do not have a copy of the content, you may be able to purchase a copy using RightsLink as an additional transaction. Simply select 'I would like to...' 'Purchase this content.'

Unclear about who you are?

If you will be reusing the content in English and additional languages, please select "Yes, including English rights" and select the number of additional languages you will be translating the content into. If you will be translating the content and not reusing it in English, please select "Yes, without English rights".

|  |   |  |   |
|--|---|--|---|
| <p>I would like to... <span style="font-size: 0.8em;">ⓘ</span></p> <p>I would like to use... <span style="font-size: 0.8em;">ⓘ</span></p> <p>Circulation</p> <p>My format is... <span style="font-size: 0.8em;">ⓘ</span></p> <p>I am the author of this Elsevier article... <span style="font-size: 0.8em;">ⓘ</span></p> | <p>reuse in a thesis/dissertation</p> <p>full article</p> <p>15</p> <p>both print and electronic</p> <p>Yes</p> | <p>I will be translating... <span style="font-size: 0.8em;">ⓘ</span></p> <p>The number of languages I will translate into is... <span style="font-size: 0.8em;">ⓘ</span></p> <p>My currency is...</p> <p>Quick Price</p> | <p>Yes, including English rights</p> <p>1</p> <p>EUR - €</p> <p>Click Quick Price</p> |
|--|---|--|---|

QUICK PRICE
CONTINUE


To request permission for a type of use not listed, please contact [Elsevier Global Rights Department](#).

Are you the **author** of this Elsevier journal article?

**CCC** | RightsLink®

[Home](#)
[?](#)
[Help](#)
[Email Support](#)
[Sign in](#)
[Create Account](#)

---



**Morphological tuning of membrane processing by temporal proton-metal cation substitution in perfluorosulfonic acid membranes**

Author: Kim-Marie Vetter, Thomas Reichbauer, Nemanja Martić, David Reinisch, Olaf Hinrichsen, Günter Schmid

Publication: Electrochimica Acta

Publisher: Elsevier

Date: 1 December 2020

© 2020 Elsevier Ltd. All rights reserved.

#### Journal Author Rights

Please note that, as the author of this Elsevier article, you retain the right to include it in a thesis or dissertation, provided it is not published commercially. Permission is not required, but please ensure that you reference the journal as the original source. For more information on this and on your other retained rights, please visit: <https://www.elsevier.com/about/our-business/policies/copyright#Author-rights>

BACK
CLOSE WINDOW

© 2021 Copyright - All Rights Reserved | [Copyright Clearance Center, Inc.](#) | [Privacy statement](#) | [Terms and Conditions](#)  
Comments? We would like to hear from you. E-mail us at [customer-care@copyright.com](mailto:customer-care@copyright.com)

## 8. Bibliographical data for complete publications

### 8.1. Stability evaluation of earth-abundant metal-based polyoxometalate electrocatalysts for oxygen evolution reaction towards industrial PEM electrolysis at high current densities

Kim-Marie Vetter,<sup>[a,b]</sup> Camila Aring da Silva Ramos Mauro,<sup>[b]</sup> David Reinisch,<sup>[a]</sup> Thomas Reichbauer,<sup>[a]</sup> Nemanja Martić,<sup>[a]</sup> Christian Jandl,<sup>[c]</sup> Olaf Hinrichsen,<sup>[b,c]</sup> Günter Schmid<sup>[a]</sup>

<sup>[a]</sup> Siemens Energy Global GmbH & Co. KG  
Freyeslebenstraße 1, 91058 Erlangen, Germany  
E-mail: guenter.schmid@siemens-energy.com

<sup>[b]</sup> Department of Chemistry  
Technical University of Munich  
Lichtenbergstraße 4, 85747 Garching bei München, Germany  
E-mail: hinrichsen@tum.de  
<https://www.department.ch.tum.de/tc1/>

<sup>[c]</sup> Catalysis Research Center  
Technical University of Munich  
Lichtenbergstraße 4, 85747 Garching bei München, Germany

*Electrochem Sci Adv* **2021**, e202100073.

DOI: 10.1002/elsa.202100073

Reprinted with permission from *Electrochem Sci Adv* **2021**, e202100073, DOI: 10.1002/elsa.202100073, copyright 2021 Wiley-VCH Verlag GmbH & Co. KGaA, Weinheim.

## 8.2. Morphological tuning of membrane processing by temporal proton-metal cation substitution in perfluorosulfonic acid membranes

Kim-Marie Vetter,<sup>[a,b]</sup> Thomas Reichbauer,<sup>[a]</sup> Nemanja Martić,<sup>[a]</sup> David Reinisch,<sup>[a]</sup> Olaf Hinrichsen,<sup>[b,c]</sup> Günter Schmid<sup>[a]</sup>

<sup>[a]</sup> Siemens Energy Global GmbH & Co. KG  
Freyeslebenstraße 1, 91058 Erlangen, Germany  
E-mail: guenter.schmid@siemens-energy.com

<sup>[b]</sup> Department of Chemistry  
Technical University of Munich  
Lichtenbergstraße 4, 85747 Garching bei München, Germany  
E-mail: hinrichsen@tum.de  
<https://www.department.ch.tum.de/tc1/>

<sup>[c]</sup> Catalysis Research Center  
Technical University of Munich  
Lichtenbergstraße 4, 85747 Garching bei München, Germany

*Electrochimica Acta* **2020**, Volume 362, 137182.

DOI: 10.1016/j.electacta.2020.137182

Reprinted with permission from *Electrochimica Acta* **2020**, Volume 362, 137182, DOI: 10.1016/j.electacta.2020.137182, copyright 2020 Elsevier Ltd., Amsterdam.

### 8.3. K<sup>+</sup> Transport in perfluorosulfonic acid membranes and its influence on membrane resistance in CO<sub>2</sub> electrolysis

Kim-Marie Vetter,<sup>[a,b]</sup> Jamie Härtl,<sup>[a]</sup> David Reinisch,<sup>[a]</sup> Thomas Reichbauer,<sup>[a]</sup> Ne-manja Martić,<sup>[a]</sup> Olaf Hinrichsen,<sup>[b,c]</sup> Günter Schmid<sup>[a]</sup>

<sup>[a]</sup> Siemens Energy Global GmbH & Co. KG  
Freyeslebenstraße 1, 91058 Erlangen, Germany  
E-mail: guenter.schmid@siemens-energy.com

<sup>[b]</sup> Department of Chemistry  
Technical University of Munich  
Lichtenbergstraße 4, 85747 Garching bei München, Germany  
E-mail: hinrichsen@tum.de  
<https://www.department.ch.tum.de/tc1/>

<sup>[c]</sup> Catalysis Research Center  
Technical University of Munich  
Lichtenbergstraße 4, 85747 Garching bei München, Germany

*ChemElectroChem* **2021**, Accepted Author Manuscript.

DOI: 10.1002/celc.202101165

Reprinted with permission from *ChemElectroChem* **2021**, e202100073, DOI: 10.1002/celc.202101165, copyright 2021 Wiley-VCH Verlag GmbH & Co. KGaA, Weinheim.

## 9. List of publications and conference contributions

### 9.1. Journal articles

- [1] **Kim-Marie Vetter**, Jamie Härtl, David Reinisch, Thomas Reichbauer, Nemanja Martic, Olaf Hinrichsen, Günter Schmid, „K<sup>+</sup> Transport in perfluorosulfonic acid membranes and its influence on membrane resistance in CO<sub>2</sub> electrolysis“ *ChemElectroChem* **2021**, accepted author manuscript. <https://doi.org/10.1002/celec.202101165>
- [2] **Kim-Marie Vetter**, Camila Aring da Silva Ramos Mauro, David Reinisch, Thomas Reichbauer, Nemanja Martic, Christian Jandl, Olaf Hinrichsen, Günter Schmid, *Electrochem Sci Adv* **2021**, e202100073. <https://doi.org/10.1002/elsa.202100073>
- [3] **Kim-Marie Vetter**, Thomas Reichbauer, Nemanja Martic, David Reinisch, Olaf Hinrichsen, Günter Schmid, *Electrochimica Acta* **2020**, Vol. 326, 137182. <https://doi.org/10.1016/j.electacta.2020.137182>
- [4] Carl D. Estrada, Hwee Ting Ang, **Kim-Marie Vetter**, Ashley A. Ponich, Dennis G. Hall, *J. Am. Chem. Soc.* **2021**, 143, 11, 4162–4167. <https://doi.org/10.1021/jacs.1c00759>
- [5] Nemanja Martic, Christian Reller, Chandra Macauley, Mario Löffler, Andreas M. Reichert, Thomas Reichbauer, **Kim-Marie Vetter**, Bernhard Schmid, David McLaughlin, Paul Leidinger, David Reinisch, Christoph Vogl, Karl J. J. Mayrhofer, Ioannis Katsounaros, Günter Schmid, *Energy Environ. Sci.* **2020**, 13, 2993–3006. <https://doi.org/10.1039/D0EE01100B>

## 9.2. Conference contributions

- 06/2019 Suncat Summer Institute, Stanford, United States of America,  
Poster on „Low temperature electrochemical CO<sub>2</sub> reduction for  
profitable synthesis of feedstock chemicals“
- 08/2019 International Conference on Carbon Dioxide Utilization (ICCDU),  
Aachen, Germany,  
Poster on „Low temperature electrochemical CO<sub>2</sub> reduction for  
profitable synthesis of feedstock chemicals“
- 10/2019 Die lange Nacht der Wissenschaften, Erlangen, Germany,  
Workshop and talks on „Power2X - Electrolyzer based production of  
valuable supplies, chemicals & green fuels: CO<sub>2</sub> to CO and more“
- 07/2020 Siemens Young Researcher Forum 2020, online,  
Talk on „Morphological membrane tuning for CO<sub>2</sub> and water  
electrolysis“
- 03/2021 Endeavor International Webinar on Chemistry, online,  
Talk on „Morphological membrane tuning by temporal proton-metal  
cation substitution“

## 9.3. Patents and invention disclosures

- 2021E12561 DE **Kim-Marie Vetter**, Günter Schmid, Jamie Härtl, Yashar  
Musayev, Thomas Reichbauer,  
„Puffersysteme zur Vermeidung korrosionsbedingter  
Degradation an Bipolarplatten und Gasdiffusionslagen in der  
PEM-Wasserelektrolyse“, 06/2021, being processed.

---

|                       |   |
|-----------------------|---|
| DE 10 2020 207 186 A1 | David Reinisch, Günter Schmid, <b>Kim-Marie Vetter</b> ,<br>Thomas Reichbauer, Nemanja Martic,<br>„CO <sub>2</sub> Elektrolyse mit Gasdiffusionselektrode und<br>Salzbildungsvermeidung durch Elektrolytwahl“                                   |
| Aktenzeichen          | 10 2020 207 186.1   |
| Anmeldetag            | 09.06.2020  |
| Offenlegungstag       | 29.10.2020  |
| DE 10 2019 218 173 A1 | David Reinisch, Christoph Vogl, <b>Kim-Marie Vetter</b> , Günter<br>Schmid, Nemanja Martic, Thomas Reichbauer,<br>„Elektrolysezelle und Verfahren zum Betreiben der<br>Elektrolysezelle zur elektrochemischen Nutzung von<br>Kohlenstoffdioxid“ |
| Aktenzeichen          | 10 2019 218 173.2   |
| Anmeldetag            | 25.11.2019  |
| Offenlegungstag       | 27.05.2021  |
| DE 10 2019 216 601 A1 | David Reinisch, Günter Schmid, Nemanja Martic, <b>Kim-Marie<br/>Vetter</b> , Thomas Reichbauer, Christoph Vogl,<br>„Elektrolyseur zur Kohlenstoffdioxidreduktion“   |
| Aktenzeichen          | 10 2019 216 601.6   |
| Anmeldetag            | 29.10.2019  |
| Offenlegungstag       | 29.04.2021  |
| DE 10 2019 209 759 A1 | <b>Kim-Marie Vetter</b> , Günter Schmid, Christian Reller,<br>Thomas Reichbauer<br>„Elektrolysesystem und Verfahren zur Herstellung von<br>Peroxydicarbonat“  |
| Aktenzeichen          | 10 2019 209 759.6   |
| Anmeldetag            | 03.07.2019  |
| Offenlegungstag       | 07.01.2021  |

## **Declaration**

The submitted thesis was supervised by Prof. Dr.-Ing. Kai-Olaf Hinrichsen and Dr. Günter Schmid.

## **Affirmation**

Hereby, I affirm that I am the sole author of this thesis. To the best of my knowledge, I affirm that this thesis does not infringe upon anyone's copyright nor violate any proprietary rights.

I affirm that any ideas, techniques, quotations, or any other material, are in accordance with standard referencing practices.

Moreover, I affirm that, so far, the thesis has not been forwarded to a third party nor is it published. I obeyed all study regulations of the Technische Universität München.

## **Remarks about the internet**

Throughout the work, the internet was used for research and verification. Many of the keywords provided herein, references and other information can be verified on the internet. However, no sources are given, because all statements made in this work are fully covered by the cited literature sources.

Garching, November 27, 2021

---

Kim-Marie Vetter



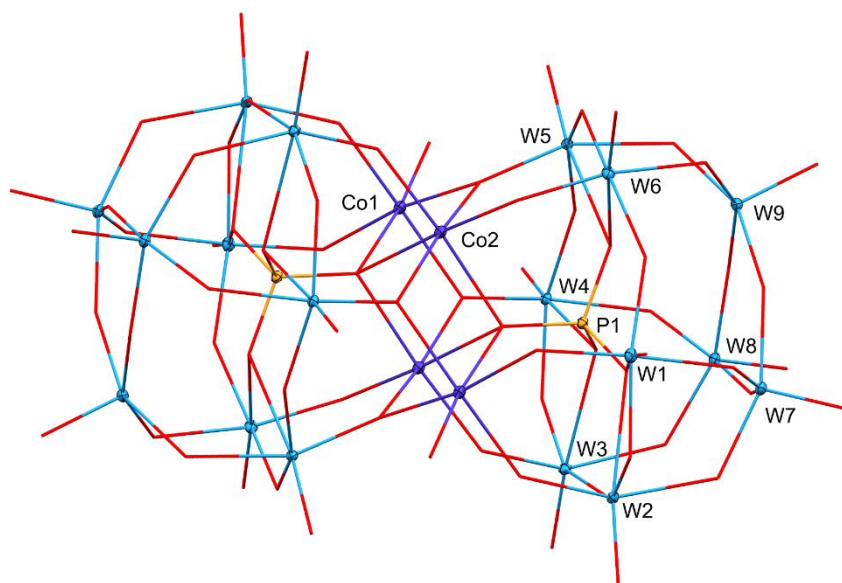
## **A. Supporting information of publications**

## Supporting Information

### X-ray crystallographic details

Data were collected on a Bruker D8 Venture single crystal x-ray diffractometer equipped with a CPAD detector (Bruker Photon II), an IMS micro source with MoK $\alpha$  radiation ( $\lambda = 0.71073 \text{ \AA}$ ) and a Helios optic using the APEX3 software package.<sup>1</sup> Measurements were performed on single crystals coated with perfluorinated ether. The crystals were fixed on top of a kapton micro sampler and frozen under a stream of cold nitrogen. A matrix scan was used to determine the initial lattice parameters. Reflections were corrected for Lorentz and polarization effects, scan speed, and background using SAINT.<sup>2</sup> Absorption correction, including odd and even ordered spherical harmonics was performed using SADABS.<sup>2</sup> Space group assignments were based upon systematic absences, E statistics, and successful refinement of the structures. The structures were solved using SHELXT with the aid of successive difference Fourier maps, and were refined against all data using SHELXL in conjunction with SHELXLE.<sup>3,4,5</sup> Hydrogen atoms in the disordered network of water and hydrated sodium ions could not be properly refined and thus were omitted. Non-hydrogen atoms were refined with anisotropic displacement parameters. Full-matrix least-squares refinements were carried out by minimizing  $\sum w(F_o^2 - F_c^2)^2$  with the SHELXL weighting scheme.<sup>3</sup> Neutral atom scattering factors for all atoms and anomalous dispersion corrections for the non-hydrogen atoms were taken from *International Tables for Crystallography*.<sup>6</sup> Images of the crystal structures were generated with Mercury.<sup>7</sup> CCDC 2045625-2045626 contains the supplementary crystallographic data for this paper. These data are provided free of charge by The Cambridge Crystallographic Data Centre.

## Compound Na<sub>10</sub>[Co<sub>4</sub>] (CCDC 2045625)



Diffraction operator C. Jandl  
scanspeed 1-5 s per frame  
dx 80 mm  
4730 frames measured in 14 data sets  
phi-scans with  $\Delta\phi = 0.5$   
omega-scans with  $\Delta\omega = 0.5$   
shutterless mode

### Crystal data

Co<sub>4</sub>O<sub>70</sub>P<sub>2</sub>W<sub>18</sub>·34.655(O)·9(Na)

$F(000) = 2406$

$M_r = 5488.16$

Triclinic, *P*

$D_x = 4.189 \text{ Mg m}^{-3}$

Hall symbol: -*P* 1

Melting point: ? K

$a = 11.4826 (17) \text{ \AA}$

Mo  $K\alpha$  radiation,  $\lambda = 0.71073 \text{ \AA}$

$b = 12.7885 (19) \text{ \AA}$

Cell parameters from 9250  
reflections

$c = 17.215 (3) \text{ \AA}$

$\theta = 2.5\text{--}26.8^\circ$

$\alpha = 97.968 (4)^\circ$

$\mu = 24.65 \text{ mm}^{-1}$

$\beta = 106.498 (3)^\circ$

$T = 100 \text{ K}$

$\gamma = 111.232 (3)^\circ$

Fragment, blue-violet

$V = 2175.3 (6) \text{ \AA}^3$

0.10 × 0.08 × 0.08 mm

$Z = 1$

*Data collection*

Bruker Photon CMOS  
diffractometer 8872 independent reflections

Radiation source: IMS microsource 8417 reflections with  $I > 2\sigma(I)$

Helios optic monochromator  $R_{\text{int}} = \underline{0.034}$

Detector resolution: 16 pixels  $\text{mm}^{-1}$   $\theta_{\text{max}} = \underline{26.4}^\circ$ ,  $\theta_{\text{min}} = \underline{2.3}^\circ$

phi- and  $\omega$ -rotation scans  $h = \underline{-14}$  14

Absorption correction: multi-scan  
SADABS 2016/2, Bruker, 2016  $k = \underline{-15}$  15

$T_{\text{min}} = \underline{0.566}$ ,  $T_{\text{max}} = \underline{0.745}$   $l = \underline{-21}$  21

93268 measured reflections

*Refinement*

Refinement on  $F^2$  Primary atom site location: iterative

Least-squares matrix: full Secondary atom site location: difference  
Fourier map

$R[F^2 > 2\sigma(F^2)] = \underline{0.015}$   $W = 1/[\Sigma^2(FO^2) + (0.0118P)^2 + 10.5441P]$   
WHERE  $P = (FO^2 + 2FC^2)/3$

$wR(F^2) = \underline{0.036}$   $(\Delta/\sigma)_{\text{max}} = \underline{0.010}$

$S = \underline{1.14}$   $\Delta\rho_{\text{max}} = \underline{1.14} \text{ e } \text{\AA}^{-3}$

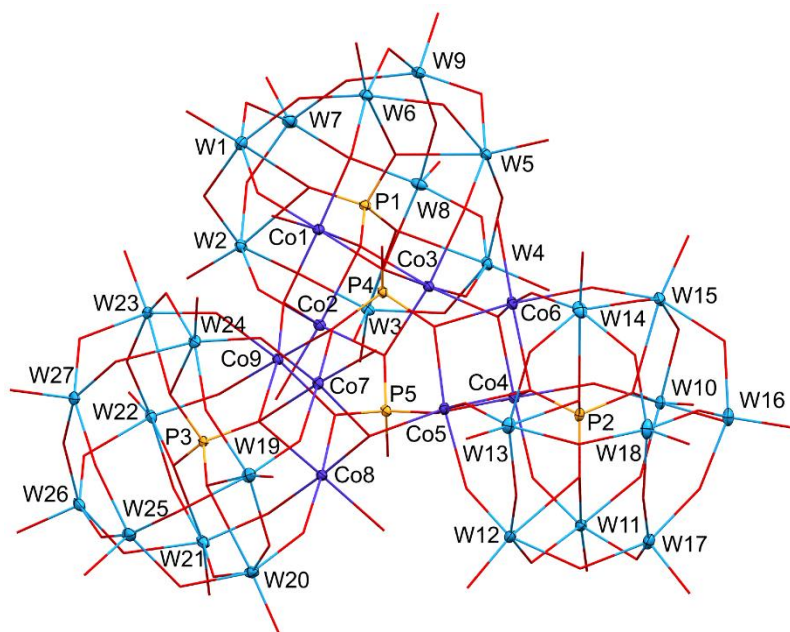
8872 reflections  $\Delta\rho_{\text{min}} = \underline{-1.00} \text{ e } \text{\AA}^{-3}$

725 parameters Extinction correction: none

245 restraints Extinction coefficient: -

- constraints

## Compound Na<sub>16</sub>[Co<sub>9</sub>] (CCDC 2045626)



Diffractometer operator C. Jandl  
scanspeed 1-10 s per frame  
dx 50 mm  
3531 frames measured in 12 data sets  
phi-scans with delta\_phi = 0.5  
omega-scans with delta\_omega = 0.5  
shutterless mode

### Crystal data

2(Co<sub>9</sub>O<sub>119</sub>P<sub>5</sub>W<sub>27</sub>)·16(Na)·77.05(O)

$F(000) = 8121$

$M_r = 9153.74$

Triclinic, *P*

$D_x = 3.658 \text{ Mg m}^{-3}$

Hall symbol: -*P* 1

Melting point: ? K

$a = 19.901(4) \text{ \AA}$

Mo  $K\alpha$  radiation,  $\lambda = 0.71073 \text{ \AA}$

$b = 21.177(4) \text{ \AA}$

Cell parameters from 8586  
reflections

$c = 24.036(5) \text{ \AA}$

$\theta = 2.2\text{--}26.7^\circ$

$\alpha = 92.689(7)^\circ$

$\mu = 19.70 \text{ mm}^{-1}$

$\beta = 108.730(7)^\circ$

$T = 100 \text{ K}$

$\gamma = 117.137(6)^\circ$

Fragment, pink

$V = 8310(3) \text{ \AA}^3$

0.40 × 0.10 × 0.02 mm

$Z = 2$

### Data collection

Bruker Photon CMOS  
diffractometer 33932 independent reflections

Radiation source: IMS microsource 31097 reflections with  $I > 2\sigma(I)$

Helios optic monochromator  $R_{\text{int}} = \underline{0.040}$

Detector resolution: 16 pixels  $\text{mm}^{-1}$   $\theta_{\text{max}} = \underline{26.4}^\circ$ ,  $\theta_{\text{min}} = \underline{1.9}^\circ$

phi- and  $\omega$ -rotation scans  $h = \underline{-24}$  24

Absorption correction: multi-scan  
SADABS 2016/2, Bruker, 2016  $k = \underline{-26}$  26

$T_{\text{min}} = \underline{0.405}$ ,  $T_{\text{max}} = \underline{0.745}$   $l = \underline{-30}$  30

308929 measured reflections

### Refinement

Refinement on  $F^2$  Primary atom site location: iterative

Least-squares matrix: full Secondary atom site location: difference  
Fourier map

$R[F^2 > 2\sigma(F^2)] = \underline{0.023}$   $W = 1/[\Sigma^2(FO^2) + (0.0192P)^2 + 118.7529P]$   
WHERE  $P = (FO^2 + 2FC^2)/3$

$wR(F^2) = \underline{0.054}$   $(\Delta/\sigma)_{\text{max}} = \underline{0.032}$

$S = \underline{0.98}$   $\Delta\rho_{\text{max}} = \underline{1.90} \text{ e } \text{\AA}^{-3}$

33932 reflections  $\Delta\rho_{\text{min}} = \underline{-2.61} \text{ e } \text{\AA}^{-3}$

2995 parameters Extinction correction: none

8190 restraints Extinction coefficient: -

20 constraints

### References

1) *APEX suite of crystallographic software*, APEX 3, Version 2016-9.0, Bruker AXS Inc., Madison, Wisconsin, USA, 2016.

2) *SAINT*, Version 8.38A and *SADABS*, Version 2016/2, Bruker AXS Inc., Madison, Wisconsin, USA, 2016/2017.

3) G. M. Sheldrick, *Acta Crystallogr. Sect. A* **2015**, *71*, 3–8.

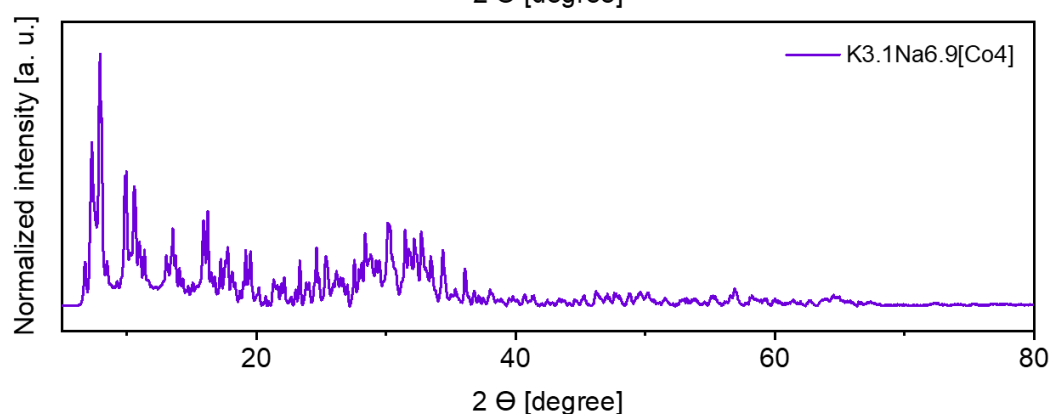
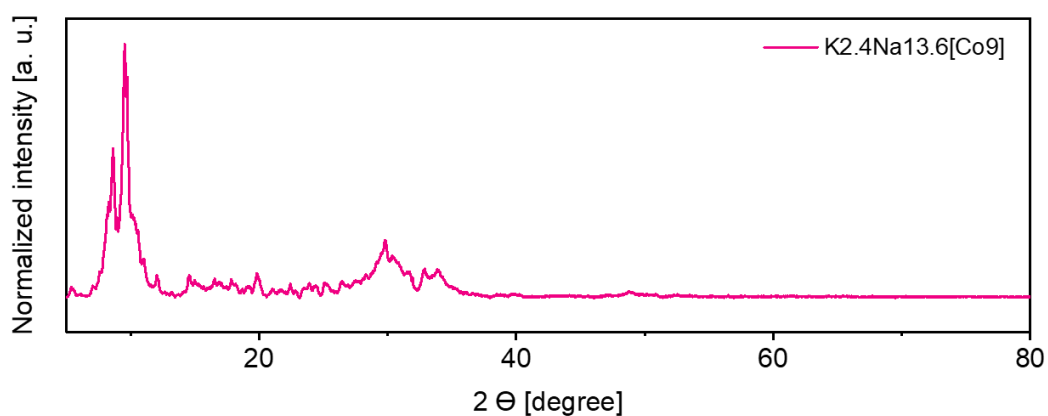
4) G. M. Sheldrick, *Acta Crystallogr. Sect. C* **2015**, *71*, 3–8.

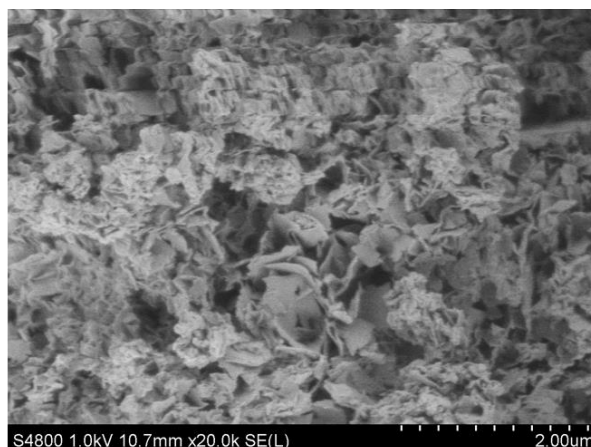
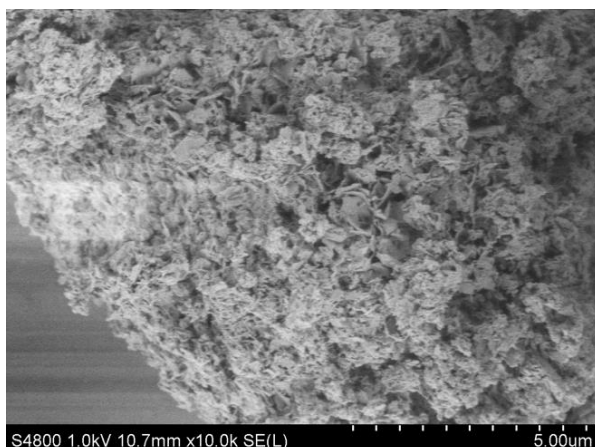
5) C. B. Hübschle, G. M. Sheldrick, B. Dittrich, *J. Appl. Cryst.* **2011**, *44*, 1281–1284

6) *International Tables for Crystallography, Vol. C* (Ed.: A. J. Wilson), Kluwer Academic Publishers, Dordrecht, The Netherlands, **1992**, Tables 6.1.1.4 (pp. 500–502), 4.2.6.8 (pp. 219–222), and 4.2.4.2 (pp. 193–199).

7) C. F. Macrae, I. J. Bruno, J. A. Chisholm, P. R. Edgington, P. McCabe, E. Pidcock, L. Rodriguez-Monge, R. Taylor, J. van de Streek, P. A. Wood, *J. Appl. Cryst.* **2008**, *41*, 466–470.

### Powder diffractograms of Na/K POM [Co<sub>9</sub>] and [Co<sub>4</sub>] and SEM images of Ba<sub>5</sub>[Co<sub>4</sub>]





## Elemental analysis results

### $K_xNa_y[Co_9]$

|                | Co     | P      | W      | Na    | K      | Ba      | Mn     | Fe     | Ni     | Total  |
|----------------|--------|--------|--------|-------|--------|---------|--------|--------|--------|--------|
| MW [g/mol]     | 58,933 | 30,974 | 183,84 | 22,99 | 39,098 | 137,327 | 54,938 | 55,845 | 58,693 | 8571,1 |
| Atoms expected | 9      | 5      | 27     | 8     | 8      | 0       | 0      | 0      | 0      |        |
| Rel. Percent   | 6,2    | 1,8    | 57,9   | 2,1   | 3,6    | 0,0     | 0,0    | 0,0    | 0,0    | 100,0  |
| Found          | 5,5    | 1,6    | 53,6   | 4,7   | 1,4    |         |        |        |        |        |

### $K_xNa_y[Co_4]$

|                | Co     | P      | W      | Na    | K      | Ba      | Mn     | Fe     | Ni     | Total  |
|----------------|--------|--------|--------|-------|--------|---------|--------|--------|--------|--------|
| MW [g/mol]     | 58,933 | 30,974 | 183,84 | 22,99 | 39,098 | 137,327 | 54,938 | 55,845 | 58,693 | 5437,5 |
| Atoms expected | 4      | 2      | 18     | 5     | 5      | 0       | 0      | 0      | 0      |        |
| Rel. Percent   | 4,3    | 1,1    | 60,9   | 2,1   | 3,6    | 0,0     | 0,0    | 0,0    | 0,0    | 100,0  |
| Found          | 4,5    | 1,2    | 60,2   | 2,9   | 2,2    |         |        |        |        |        |

### $Ba_8[Co_9]$

|                | Co     | P      | W      | Na    | K      | Ba      | Mn     | Fe     | Ni     | Total  |
|----------------|--------|--------|--------|-------|--------|---------|--------|--------|--------|--------|
| MW [g/mol]     | 58,933 | 30,974 | 183,84 | 22,99 | 39,098 | 137,327 | 54,938 | 55,845 | 58,693 | 9173,0 |
| Atoms expected | 9      | 5      | 27     | 0     | 0      | 8       | 0      | 0      | 0      |        |
| Rel. Percent   | 5,8    | 1,7    | 54,1   | 0,0   | 0,0    | 12,0    | 0,0    | 0,0    | 0,0    | 100,0  |
| Found          | 5,6    | 1,7    | 53,2   |       |        | 12,9    |        |        |        |        |

### $Ba_5[Co_4]$

|                | Co     | P      | W      | Na    | K      | Ba      | Mn     | Fe     | Ni     | Total  |
|----------------|--------|--------|--------|-------|--------|---------|--------|--------|--------|--------|
| MW [g/mol]     | 58,933 | 30,974 | 183,84 | 22,99 | 39,098 | 137,327 | 54,938 | 55,845 | 58,693 | 5813,7 |
| Atoms expected | 4      | 2      | 18     | 0     | 0      | 5       | 0      | 0      | 0      |        |
| Rel. Percent   | 4,1    | 1,1    | 56,9   | 0,0   | 0,0    | 11,8    | 0,0    | 0,0    | 0,0    | 100,0  |
| Found          | 3,9    | 1,1    | 53,5   |       |        | 12,2    |        |        |        |        |



| <b>K<sub>x</sub>Na<sub>y</sub>[Co<sub>9</sub>], 15% Mn</b> |            |            |             |            |            |            |             |            |            |        |
|--|------------|------------|-------------|------------|------------|------------|-------------|------------|------------|--------|
|  | Co         | P          | W           | Na         | K          | Ba         | Mn          | Fe         | Ni         | Total  |
| <b>MW [g/mol]</b>  | 58,933     | 30,974     | 183,84      | 22,99      | 39,098     | 137,327    | 54,938      | 55,845     | 58,693     | 8565,7 |
| <b>Atoms expected</b>                                      | 7,65       | 5          | 27          | 8          | 8          | 0          | 1,35        | 0          | 0          |        |
| <b>Rel. Percent</b>  | <b>5,3</b> | <b>1,8</b> | <b>57,9</b> | <b>2,1</b> | <b>3,7</b> | <b>0,0</b> | <b>0,9</b>  | <b>0,0</b> | <b>0,0</b> | 100,0  |
| <b>Found</b>   | <b>4,5</b> |            | <b>52,5</b> | <b>4,9</b> | <b>1,6</b> |            | <b>0,30</b> |            |            |        |

| <b>K<sub>x</sub>Na<sub>y</sub>[Co<sub>4</sub>], 15% Mn</b> |            |            |             |            |            |            |             |            |            |        |
|--|------------|------------|-------------|------------|------------|------------|-------------|------------|------------|--------|
|  | Co         | P          | W           | Na         | K          | Ba         | Mn          | Fe         | Ni         | Total  |
| <b>MW [g/mol]</b>  | 58,933     | 30,974     | 183,84      | 22,99      | 39,098     | 137,327    | 54,938      | 55,845     | 58,693     | 5435,1 |
| <b>Atoms expected</b>                                      | 3,4        | 2          | 18          | 5          | 5          | 0          | 0,6         | 0          | 0          |        |
| <b>Rel. Percent</b>  | <b>3,7</b> | <b>1,1</b> | <b>60,9</b> | <b>2,1</b> | <b>3,6</b> | <b>0,0</b> | <b>0,6</b>  | <b>0,0</b> | <b>0,0</b> | 100,0  |
| <b>Found</b>   | <b>3,9</b> |            | <b>59,5</b> | <b>2,9</b> | <b>1,8</b> |            | <b>0,44</b> |            |            |        |

| <b>K<sub>x</sub>Na<sub>y</sub>[Co<sub>9</sub>], 15% Ni</b> |            |            |             |            |            |            |            |            |            |        |
|--|------------|------------|-------------|------------|------------|------------|------------|------------|------------|--------|
|  | Co         | P          | W           | Na         | K          | Ba         | Mn         | Fe         | Ni         | Total  |
| <b>MW [g/mol]</b>  | 58,933     | 30,974     | 183,84      | 22,99      | 39,098     | 137,327    | 54,938     | 55,845     | 58,693     | 8570,8 |
| <b>Atoms expected</b>                                      | 7,65       | 5          | 27          | 8          | 8          | 0          | 0          | 0          | 1,35       |        |
| <b>Rel. Percent</b>  | <b>5,3</b> | <b>1,8</b> | <b>57,9</b> | <b>2,1</b> | <b>3,6</b> | <b>0,0</b> | <b>0,0</b> | <b>0,0</b> | <b>0,9</b> | 100,0  |
| <b>Found</b>   | <b>4,7</b> |            | <b>55,5</b> | <b>2,0</b> | <b>1,5</b> |            |            |            | <b>1,0</b> |        |

| <b>K<sub>x</sub>Na<sub>y</sub>[Co<sub>4</sub>], 15% Ni</b> |            |            |             |            |            |            |            |            |            |        |
|--|------------|------------|-------------|------------|------------|------------|------------|------------|------------|--------|
|  | Co         | P          | W           | Na         | K          | Ba         | Mn         | Fe         | Ni         | Total  |
| <b>MW [g/mol]</b>  | 58,933     | 30,974     | 183,84      | 22,99      | 39,098     | 137,327    | 54,938     | 55,845     | 58,693     | 5437,4 |
| <b>Atoms expected</b>                                      | 3,4        | 2          | 18          | 5          | 5          | 0          | 0          | 0          | 0,6        |        |
| <b>Rel. Percent</b>  | <b>3,7</b> | <b>1,1</b> | <b>60,9</b> | <b>2,1</b> | <b>3,6</b> | <b>0,0</b> | <b>0,0</b> | <b>0,0</b> | <b>0,6</b> | 100,0  |
| <b>Found</b>   | <b>4,0</b> |            | <b>60,5</b> | <b>3,1</b> | <b>1,7</b> |            |            |            | <b>0,5</b> |        |

| <b>K<sub>x</sub>Na<sub>y</sub>[Co<sub>9</sub>], 15% Fe</b> |            |            |             |            |            |            |            |            |            |        |
|--|------------|------------|-------------|------------|------------|------------|------------|------------|------------|--------|
|  | Co         | P          | W           | Na         | K          | Ba         | Mn         | Fe         | Ni         | Total  |
| <b>MW [g/mol]</b>  | 58,933     | 30,974     | 183,84      | 22,99      | 39,098     | 137,327    | 54,938     | 55,845     | 58,693     | 8566,9 |
| <b>Atoms expected</b>                                      | 7,65       | 5          | 27          | 8          | 8          | 0          | 0          | 1,35       | 0          |        |
| <b>Rel. Percent</b>  | <b>5,3</b> | <b>1,8</b> | <b>57,9</b> | <b>2,1</b> | <b>3,7</b> | <b>0,0</b> | <b>0,0</b> | <b>0,9</b> | <b>0,0</b> | 100,0  |
| <b>Found</b>   | <b>4,3</b> |            | <b>46,2</b> | <b>6,0</b> | <b>1,6</b> |            |            | <b>0,2</b> |            |        |

| <b>K<sub>x</sub>Na<sub>y</sub>[Co<sub>4</sub>], 15% Fe</b> |            |            |             |            |            |            |            |            |            |        |
|--|------------|------------|-------------|------------|------------|------------|------------|------------|------------|--------|
|  | Co         | P          | W           | Na         | K          | Ba         | Mn         | Fe         | Ni         | Total  |
| <b>MW [g/mol]</b>  | 58,933     | 30,974     | 183,84      | 22,99      | 39,098     | 137,327    | 54,938     | 55,845     | 58,693     | 5435,7 |
| <b>Atoms expected</b>                                      | 3,4        | 2          | 18          | 5          | 5          | 0          | 0          | 0,6        | 0          |        |
| <b>Rel. Percent</b>  | <b>3,7</b> | <b>1,1</b> | <b>60,9</b> | <b>2,1</b> | <b>3,6</b> | <b>0,0</b> | <b>0,0</b> | <b>0,6</b> | <b>0,0</b> | 100,0  |
| <b>Found</b>   | <b>4,1</b> |            | <b>59,4</b> | <b>3,2</b> | <b>1,8</b> |            |            | <b>0,3</b> |            |        |

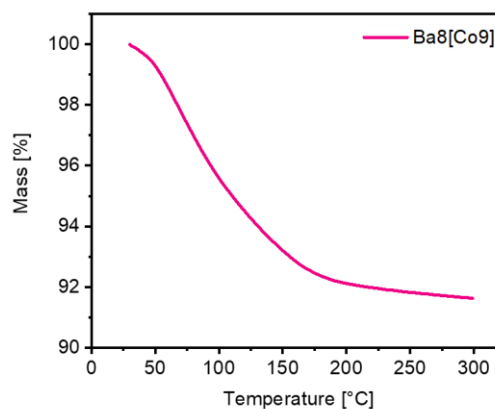
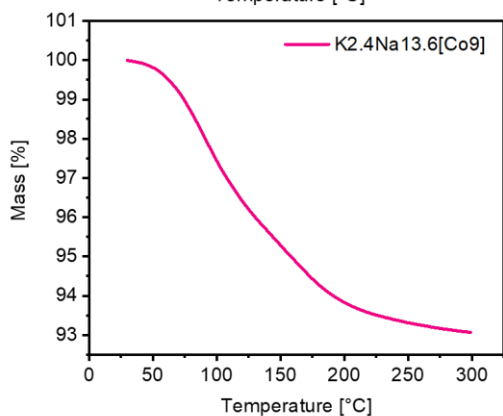
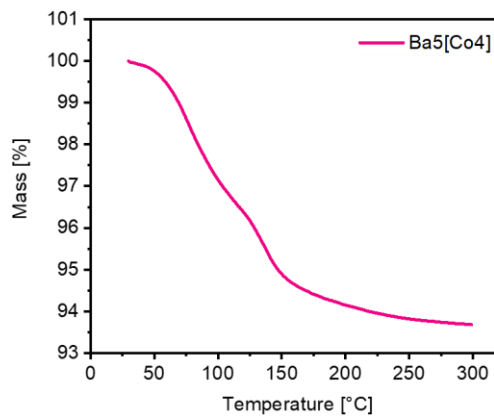
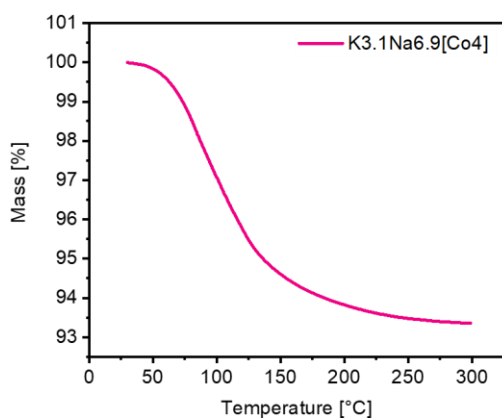
**K<sub>x</sub>Na<sub>y</sub>[Co<sub>9</sub>], 30% Mn, 30% Ni, 30% Fe**

|                       | Co         | P          | W           | Na         | K          | Ba         | Mn         | Fe         | Ni         | Total  |
|-----------------------|------------|------------|-------------|------------|------------|------------|------------|------------|------------|--------|
| <b>MW [g/mol]</b>     | 58,933     | 30,974     | 183,84      | 22,99      | 39,098     | 137,327    | 54,938     | 55,845     | 58,693     | 8710,4 |
| <b>Atoms expected</b> | 3,6        | 5          | 27          | 8          | 8          | 0          | 2,7        | 2,7        | 2,7        |        |
| <b>Rel. Percent</b>   | <b>2,4</b> | <b>1,8</b> | <b>57,0</b> | <b>2,1</b> | <b>3,6</b> | <b>0,0</b> | <b>1,7</b> | <b>1,7</b> | <b>1,8</b> | 100,0  |
| <b>Found</b>          | <b>2,1</b> |            | <b>55,0</b> |            |            |            | <b>1,2</b> | <b>0,7</b> | <b>0,6</b> |        |

**K<sub>x</sub>Na<sub>y</sub>[Co<sub>4</sub>], 30%  
Mn, 30% Ni, 30% Fe**

|                       | Co         | P          | W           | Na         | K          | Ba         | Mn         | Fe         | Ni         | Total  |
|-----------------------|------------|------------|-------------|------------|------------|------------|------------|------------|------------|--------|
| <b>MW [g/mol]</b>     | 58,933     | 30,974     | 183,84      | 22,99      | 39,098     | 137,327    | 54,938     | 55,845     | 58,693     | 5499,5 |
| <b>Atoms expected</b> | 1,6        | 2          | 18          | 5          | 5          | 0          | 1,2        | 1,2        | 1,2        |        |
| <b>Rel. Percent</b>   | <b>1,7</b> | <b>1,1</b> | <b>60,2</b> | <b>2,1</b> | <b>3,6</b> | <b>0,0</b> | <b>1,2</b> | <b>1,2</b> | <b>1,3</b> | 100,0  |
| <b>Found</b>          | <b>2,2</b> |            | <b>58,5</b> |            |            |            | <b>1,2</b> | <b>0,5</b> | <b>0,3</b> |        |

### Thermogravimetric analysis results



## BET surface results

Table S1: BET surface areas of the catalysts examined.

| Sample                             | BET surface area / m <sup>2</sup> /g |
|------------------------------------|--------------------------------------|
| Ba <sub>8</sub> [Co <sub>9</sub> ] | 8.37 ± 2.89                          |
| Ba <sub>5</sub> [Co <sub>4</sub> ] | 3.56 ± 1.53                          |

## Electrochemical cell for catalyst characterization

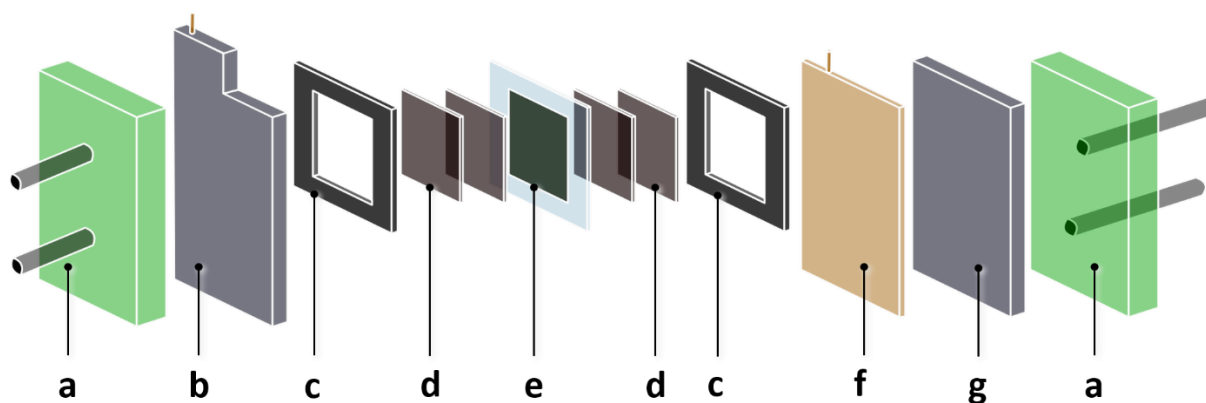
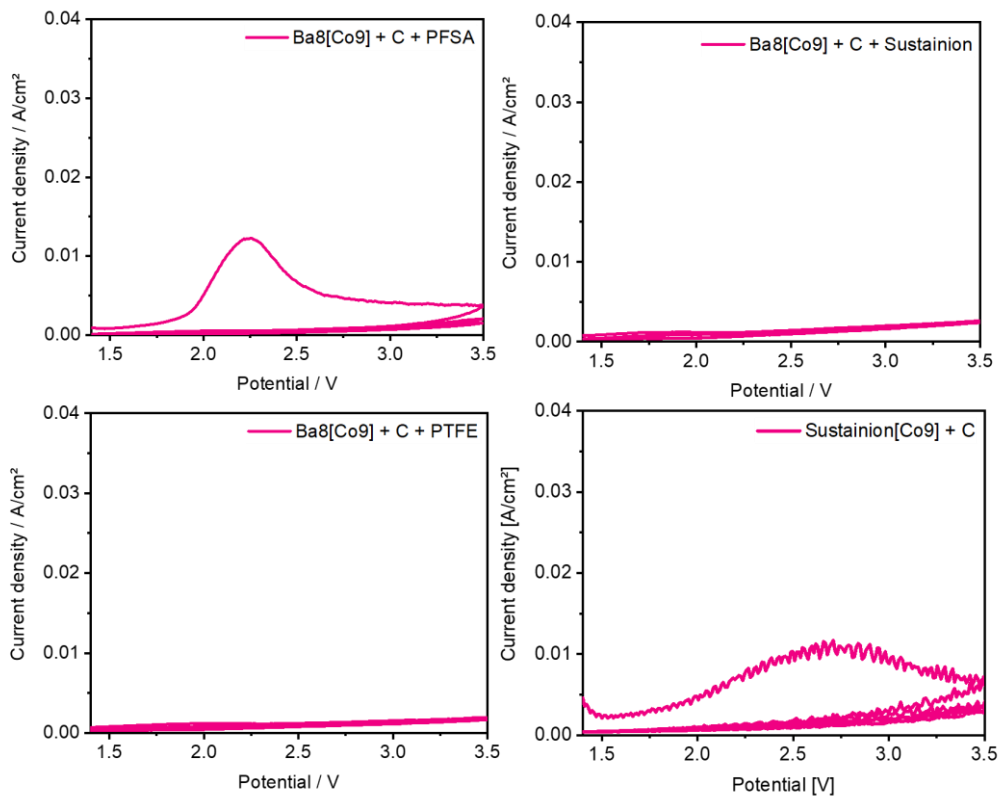


Figure S1: The installation for water electrolysis used in this study was slightly modified compared to earlier reports [21] and used for electrochemical performance determination. The cathode side is shown on the right, the anode side is shown on the left. The setup is composed of two end plates (a), a titanium (b) and a graphite (g) flow field, a gold-plated current collector (f), EPDM sealings (c), titanium grids (d) and the MEA in the middle (g).

Electrochemical characterization was performed in a water electrolysis cell adapted from a fuel cell kit provided by Scribner Associates Inc. A schematic of the setup is shown in Figure S1. The original anode graphite serpentine flow field (Figure S1c), was replaced by an analogous titanium component (Figure S1h), also provided by Scribner Associates Inc. The cell is composed of an end plate with flexible tubes for water circulation (Figure S1a), a gold plated copper current collector (b), the graphene serpentine flow field (c), an ethylene propylene diene monomer rubber (EPDM) sealing (d), a wide-meshed and a subsequent fine-meshed titanium grid (thicknesses 0.40 mm and 0.35 mm, respectively, (e) and (f)) and finally the MEA in the middle of the device (g). For the anode side, this order is mirrored replacing the graphite flow field and the current collector by the titanium component.

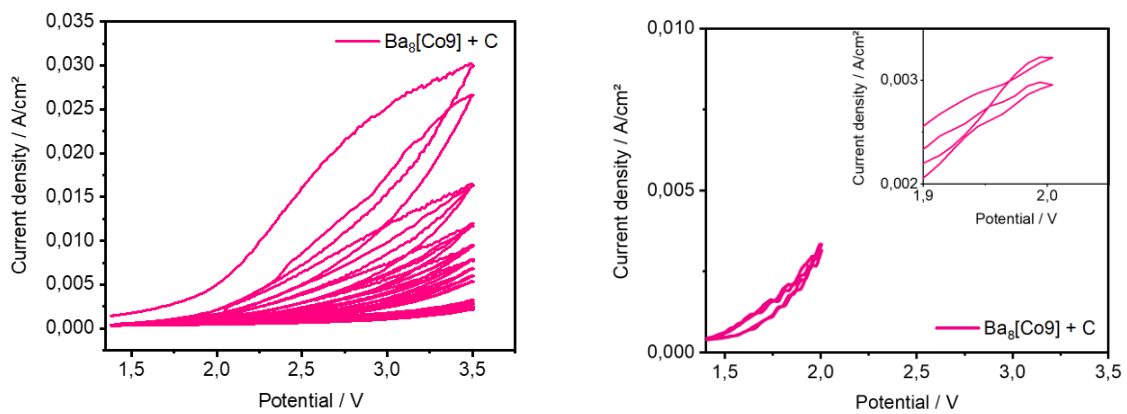
## Further CV results on MEAs with different paste formulations

Potentials given refer to the applied cell potential.



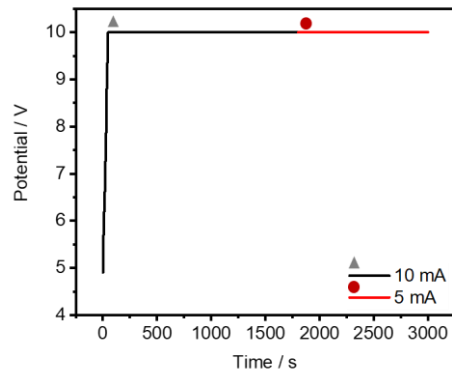
## Further CV results on Pt half-MEAs with POM containing ink coated onto the anodic Ti grid

Potentials given refer to the applied cell potential.

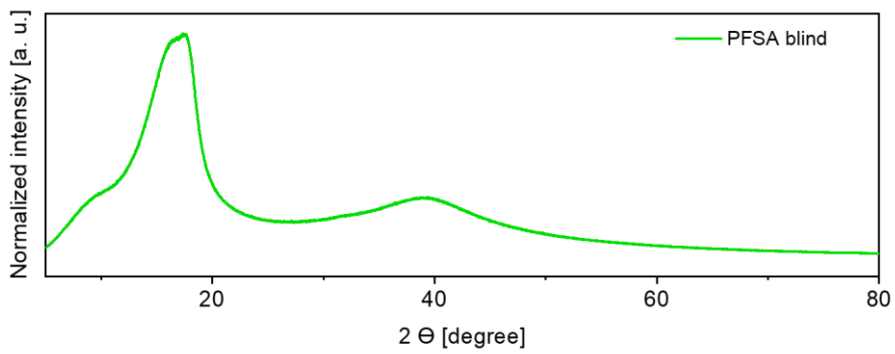
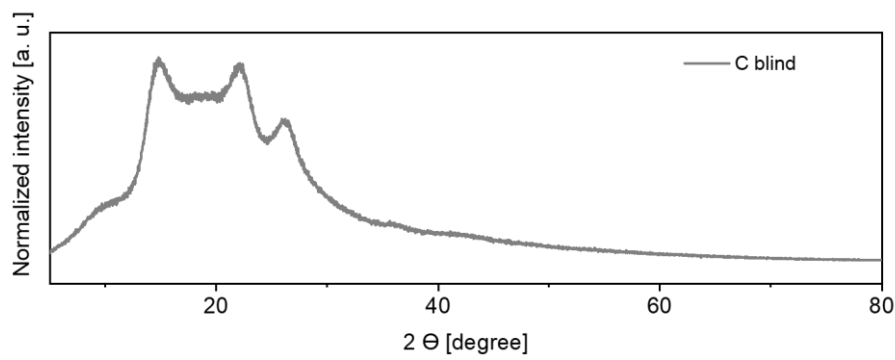
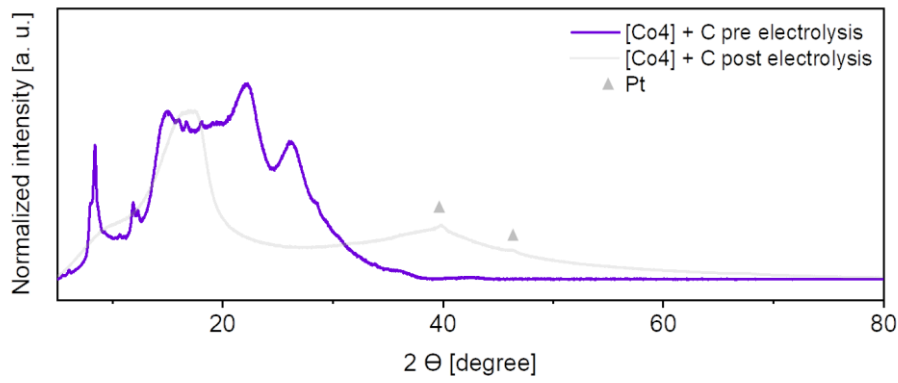


## Galvanostatic reference results for Pt half-MEA and pure Ti grid on the anode side

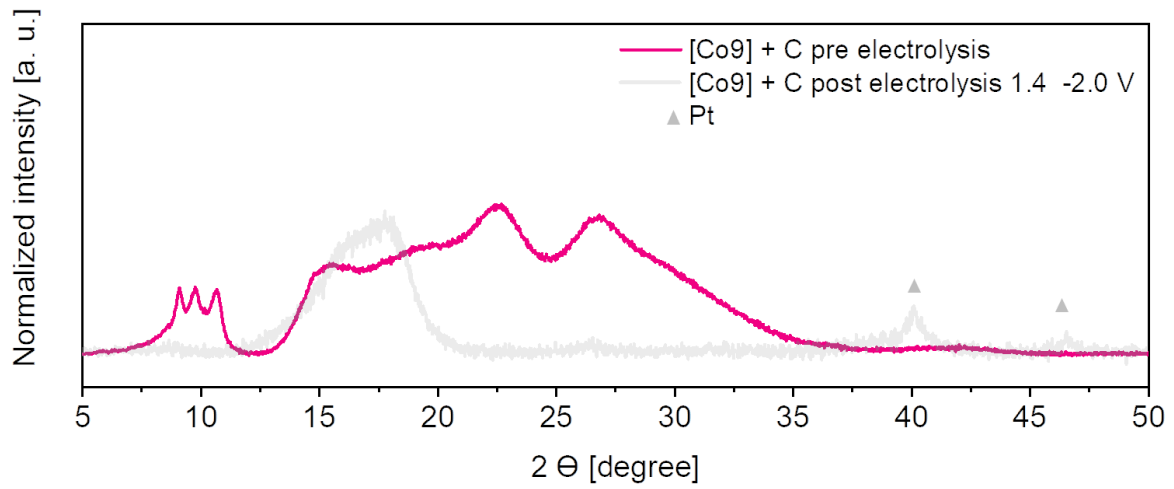
Potentials given refer to the applied cell potential.



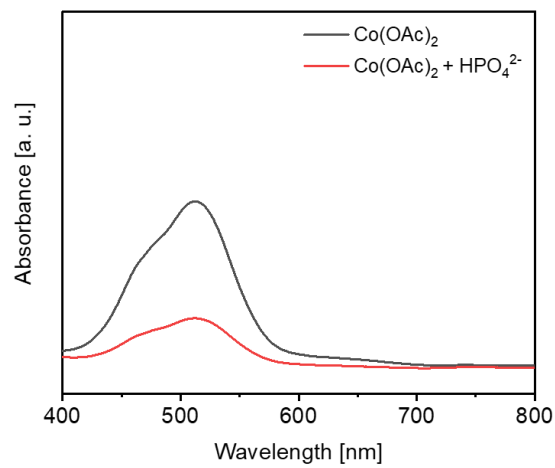
## XRD for Ba<sub>5</sub>[Co<sub>4</sub>] pre- and post-electrolysis and PFSA and CP diffractograms



### XRD for Ba<sub>8</sub>[Co<sub>9</sub>] on a MEA pre- and post-electrolysis (1.4 – 2.0 V)



### UV-Vis reference spectra of Co<sup>2+</sup> as acetate and in a phosphate environment



# Supporting Information

## Morphological Tuning of Membrane Processing by Temporal Proton-Metal Cation Substitution in Perfluorosulfonic Acid Membranes

Kim-Marie Vetter, Thomas Reichbauer, Nemanja Martić, David Reinisch, Olaf Hinrichsen, and Günter Schmid\*

### T<sub>g</sub> determination: Differential scanning calorimetry (DSC)

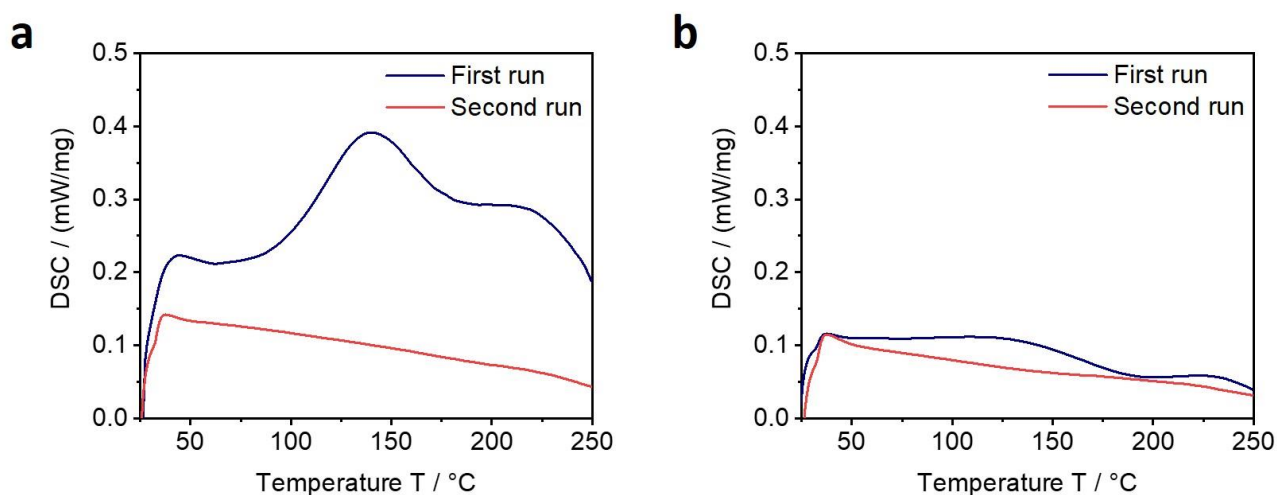


Figure A 1: Differential scanning calorimetry results for PFSA membrane in the protonated form (left) and in the K<sup>+</sup> exchanged form (right). The diagrams show two measurement runs, the first one being depicted in blue, the second one in red. Thermograms are displayed endo up.

**Note:** DSC measurements are run by referencing a sample loaded aluminum pan against an empty pan, measuring the heat flow it takes to ramp the pans temperatures up constantly. This heat flow can then be attributed to changes in the sample, such as melting or crystallization. Analysis of PFSA in the protonated form as well as the K<sup>+</sup> ion exchanged form gave the results displayed in Figure 1.

The obtained results clearly show that DSC is not a suitable method for assessing T<sub>g</sub> of a PFSA membrane. Each sample was subjected to the temperature program twice resulting in significantly different behavior for each run.

The glass transition of a polymer is an endothermic process expected to produce a positive signal in the thermogram. Since it is a reversible process, so if DSC was able to yield information about T<sub>g</sub> it is expected to be reproducible in the second run. Although the signals seen in the two thermograms are clearly positive representing endothermic processes, the latter criterion is not fulfilled. The heat flow is not reproducible in a second run and therefore not representing a glass transition T<sub>g</sub>. The signals can rather be attributed to melting of polytetrafluoroethylene (PTFE)-like crystallites within

the polymer, which is in accordance with the thermal behavior of semicrystalline polymers with slow crystallization kinetics.[4,7] This fact also explains, why the most pronounced endothermic processes appear in the same temperature range for the protonated and the  $K^+$  exchanged sample (100 -150 °C), although they are different in intensity. So evidently, the melting of PTFE-like crystallites is not strongly influenced by an ion exchange.

### Additional electrochemical data

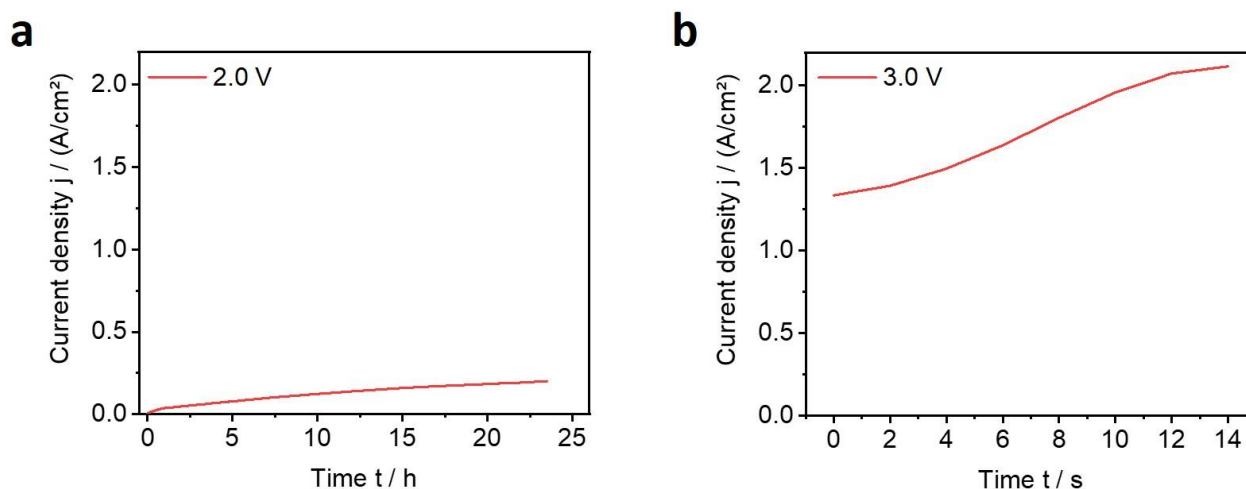


Figure B 1: Current densities for  $Li^+$  cation exchanged MEAs achieved in a constant potential mode. a) Slow performance improvement at an applied potential of 2.0 V. b) Quick performance improvement at an applied potential of 3.0 V.

**Note:** Freshly prepared MEAs were subjected to a constant potential of 2.0 V and 3.0 V, to validate the hypothesis of potential-driven substitution (PDS), and the current density was recorded as a function of time. Results of these measurements are shown in Figure B 1. In both cases, the current density improved over time, which can be traced back to a back-exchange of the  $Li^+$  ions. Their place is taken by protons originating from the anode side half-cell reaction. Supposed that cations different from protons will block the sulfonate groups and therefore hinder cation transport to a certain extent, an increase in current density at constant potential can directly be correlated to substituting the blocking ions by protons from the anodic OER and driving them out of the membrane.

There is a significant difference in the speed of current density change with respect to applied potential. Figure B 2a shows a slow improvement in current density at an applied potential of 2.0 V, where the performance increases from an initial current density of 0.02 A/cm<sup>2</sup> to 0.20 A/cm<sup>2</sup> over 24 hours. Starting at 1.34 A/cm<sup>2</sup>, the current density passes the current limitation of 2 A/cm<sup>2</sup> already within 12 seconds if a potential of 3.0 V is applied, as shown in Figure B 2b.



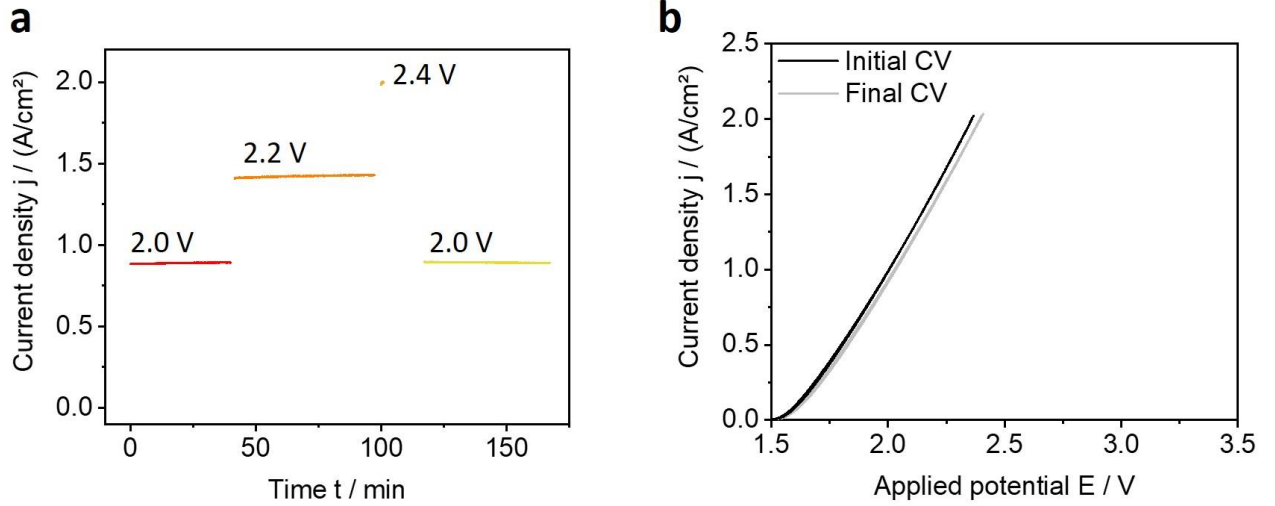


Figure B 2: Potentiostatic H<sup>+</sup> reference measurements showing a linear course for each applied potential.

### Calculation of the rate of potential-driven substitution (PDS) of metal ions by OER protons

|        |                      |                                     |
|--------|----------------------|-------------------------------------|
| Given: | Elementary charge    | $e = 1.602 * 10^{-19} C$            |
|        | Avogadro constant    | $N_A = 6.022 * 10^{23} mol^{-1}$    |
|        | Faraday constant     | $F = e * N_A = 96485 \frac{C}{mol}$ |
|        | Molar weight of PFSA | $M_{PFSA} = 388.5 \frac{g}{mol}$    |
|        | Areal weight of PFSA | $m_{PFSA} = 36.0 \frac{mg}{cm^2}$   |

For a determination of the PDS rate in the examined Li<sup>+</sup> MEA case, it is important to know that the number of sulfonic acid groups present in the membrane  $n_s$  equals the number of sulfonic acid groups and thus the number of Li<sup>+</sup> ions, a quantitative exchange assumed.  $n_s$  can be calculated from the molar weight  $M_{PFSA}$  and the mass  $m_{PFSA}$ :

$$n_s = \frac{m_{PFSA}}{M_{PFSA}} = 92.6 \frac{\mu mol}{cm^2} \quad \text{Eq. (C.1)}$$

Considering the time  $t = 28$  s until steady state was reached, the exchange rate  $r$  can now be calculated:

$$r = \frac{n_s}{t} = 0.2 \frac{mmol}{min * cm^2} \quad \text{Eq. (C.2)}$$

Furthermore, the applied current density  $I = 1.5$  A/cm<sup>2</sup> can be converted into the charge  $Q$  transported within the time  $t = 28$  s until steady state was reached:

$$Q = I * t = 42 \frac{C}{cm^2} \quad \text{Eq. (C.3)}$$

The charge  $Q$  can be further used to calculate the number of protons  $n_H$  transported during this time  $t$  with the Faraday constant  $F$ :

$$n_H = \frac{Q}{F} = 0.44 \frac{\text{mmol}}{\text{cm}^2} \quad \text{Eq. (C.4)}$$

With  $n_s$ , we can finally calculate the ration  $R$  of protons needed to replace one  $\text{Li}^+$  ion:

$$R = \frac{n_H}{n_s} = 4.7 \approx 5 \quad \text{Eq. (C.5)}$$

## References

- [1] Hydrogen Council, Hydrogen Scaling Up: A Sustainable Pathway for the Global Energy Transition, 2017, <https://hydrogencouncil.com/en/study-hydrogen-scaling-up/>, accessed 31 December 2019.
- [2] M. Carmo, D.L. Fritz, J. Mergel, D. Stolten, A Comprehensive Review on PEM Water Electrolysis, *International Journal of Hydrogen Energy* 38 (2013) 4901–4934.
- [3] P.C. Rieke, N.E. Vanderborgh, Temperature Dependence of Water Content and Proton Conductivity in Polyperfluorosulfonic Acid Membranes, *Journal of Membrane Science* (1987) 313–328.
- [4] D.B. Spry, M.D. Fayer, Proton Transfer and Proton Concentrations in Protonated Nafion Fuel Cell Membranes, *The Journal of Physical Chemistry. B* 113 (2009) 10210–10221.
- [5] K.A. Page, K.M. Cable, R.B. Moore, Molecular Origins of the Thermal Transitions and Dynamic Mechanical Relaxations in Perfluorosulfonate Ionomers, *Macromolecules* 38 (2005) 6472–6484.
- [6] R.B. Moore, K.M. Cable, T.L. Croley, Barriers to Flow in Semicrystalline Ionomers. A Procedure for Preparing Melt-Processed Perfluorosulfonate Ionomer Films and Membranes, *Journal of Membrane Science* (1992) 7–14.
- [7] M.S. Wilson, J.A. Valerio, S. Gottesfeld, Low Platinum Loading Electrodes for Polymer Electrolyte Fuel Cells Fabricated Using Thermoplastic Ionomers, *Electrochimica Acta* 1994 (1994) 355–363.
- [8] L.G. Lage, P.G. Delgado, Y. Kawano, Thermal Stability and Decomposition of Nafion® Membranes with Different Cations using High-Resolution Thermogravimetry, *Journal of Thermal Analysis and Calorimetry* (2004) 521–530.
- [9] T. Kyu, M. Hashiyama, A. Eisenberg, Dynamic Mechanical Studies of Partially Ionized and Neutralized Nafion Polymers, *Can. J. Chem.* (1983) 680–687.
- [10] S.C. Yeo, A. Eisenberg, Physical Properties and Supermolecular Structure of Perfluorinated Ion-Containing (Nafion) Polymers, *Journal of Applied Polymer Science* (1977) 875–898.

- [11] S.K. Young, S.F. Trevino, N.C. Beck Tan, R.L. Paul, Determining Extent of Ion-Exchange in Various Counterion Nafion Membranes Using Prompt Gamma Neutron Activation Analysis (PGAA). Technical Report, 2001.
- [12] S.J. Osborn, M.K. Hassan, G.M. Divoux, D.W. Rhoades, K.A. Mauritz, R.B. Moore, Glass Transition Temperature of Perfluorosulfonic Acid Ionomers, *Macromolecules* 40 (2007) 3886–3890.
- [13] Y. Iwai, T. Yamanishi, Thermal Stability of Ion-Exchange Nafion N117CS Membranes, *Polymer Degradation and Stability* 94 (2009) 679–687.
- [14] A. Steck, H.L. Yeager, Water Sorption and Cation-Exchange Selectivity of a Perfluorosulfonate Ion-Exchange Polymer, *Anal. Chem.* (1980) 1215–1218.
- [15] M. Shi, F.C. Anson, Dehydration of Protonated Nafion® Coatings Induced by Cation Exchange and Monitored by Quartz Crystal Microgravimetry, *Journal of Electroanalytical Chemistry* (1997) 117–123.
- [16] T. Okada, H. Satou, M. Okuno, M. Yuasa, Ion and Water Transport Characteristics of Perfluorosulfonated Ionomer Membranes with H<sup>+</sup> and Alkali Metal Cations, *J. Phys. Chem. B* 106 (2002) 1267–1273.
- [17] T. Lopes, D.S. Kim, Y.S. Kim, F.H. Garzon, Ionic Transport and Water Vapor Uptake of Ammonium Exchanged Perfluorosulfonic Acid Membranes, *Journal of the Electrochemical Society* (2012) B265-B269.
- [18] R. Tandon, P.N. Pintauro, Divalent/Monovalent Cation Uptake Selectivity in a Nafion Cation-Exchange Membrane: Experimental and Modeling Studies, *Journal of Membrane Science* 136 (1997) 207–219.
- [19] J.R. Bontha, P.N. Pintauro, Water Orientation and Ion Solvation Effects During Multicomponent Salt Partitioning in a Nafion Cation Exchange Membrane, *Chemical Engineering Science* 49 (1994) 3835–3851.
- [20] R. Jia, B. Han, K. Levi, T. Hasegawa, J. Ye, R.H. Dauskardt, Effect of Cation Contamination and Hydrated Pressure Loading on the Mechanical Properties of Proton Exchange Membranes, *Journal of Power Sources* 196 (2011) 3803–3809.
- [21] R. Jia, S. Dong, T. Hasegawa, J. Ye, R.H. Dauskardt, Contamination and Moisture Absorption Effects on the Mechanical Properties of Catalyst Coated Membranes in PEM Fuel Cells, *International Journal of Hydrogen Energy* 37 (2012) 6790–6797.
- [22] M.W. Grava, Y. Okada, Y. Kawano, Thermal Characterization of Flemion® Membranes Substituted by Alkali Metal Cations, *Journal of Thermal Analysis and Calorimetry* (2007) 163–168.
- [23] W. Vielstich, *Handbook of Fuel Cells: Fundamentals, Technology and Applications*, Wiley Interscience, Hoboken, NJ, 2010.

- [24] C. Bas, L. Reymond, A.-S. Danérol, N.D. Albérola, E. Rossinot, L. Flandin, Key Counter Ion Parameters Governing Polluted Nafion Membrane Properties, *Journal of Polymer Science Part B: Polymer Physics* 47 (2009) 1381–1392.
- [25] C. Bas, N.D. Albérola, L. Flandin, Effects of Contaminant on Thermal Properties in Perfluorinated Sulfonic Acid Membranes, *Journal of Membrane Science* 363 (2010) 67–71.
- [26] E. Moukheiber, C. Bas, N.D. Alberola, L. Flandin, Infrared and Thermal Behaviour of Proton Exchange Membrane (PEM) after Cationic Contamination, *Journal of Membrane Science* 431 (2013) 105–112.
- [27] H.-Y. Jung, J.W. Kim, Role of the Glass Transition Temperature of Nafion 117 Membrane in the Preparation of the Membrane Electrode Assembly in a Direct Methanol Fuel Cell (DMFC), *International Journal of Hydrogen Energy* 37 (2012) 12580–12585.
- [28] M. Choi, J.K. Kim, J. Kim, S. Yang, J.-E. Park, O.-H. Kim, Y.-H. Cho, PtRu/C Catalyst Slurry Preparation for Large-scale Decal Transfer with High Performance of Proton Exchange Membrane Fuel Cells, *The Royal Society of Chemistry Advances* 8 (2018) 36313–36322.
- [29] K.A. Page, F.A. Landis, A.K. Phillips, R.B. Moore, SAXS Analysis of the Thermal Relaxation of Anisotropic Morphologies in Oriented Nafion Membranes, *Macromolecules* 39 (2006) 3939–3946.
- [30] E. Szajdzinska-Pietek, M. Wolszczak, A. Plonka, S. Schlick, Structure and Dynamics of Micellar Aggregates in Aqueous Nafion Solutions Reported by Electron Spin Resonance and Fluorescence Probes, *Macromolecules* 32 (1999) 7454–7460.
- [31] A.J. Shubnell, E.J. Kosnic, P.J. Squattrito, Structures of Layered Metal Sulfonate Salts: Trends in Coordination Behavior of Alkali, Alkaline Earth and Transition Metals, *Inorganica Chimica Acta* 216 (1994) 101–112.
- [32] C.S. Harris, T.G. Rukavina, Lithium Ion Conductors and Proton Conductors: Effects of Plasticizers and Hydration, *Electrochimica Acta* 1995 2315–2320.
- [33] R.D. Shannon, Revised Effective Ionic Radii and Systematic Studies of Interatomic Distances in Halides and Chalcogenides, *Acta Crystallographica* (1976) 751–767.
- [34] J.S. Banait, K.S. Sidhu, J.S. Walia, Transference Numbers and Solvation Studies in n-Butanol, *Canadian Journal of Chemistry* (1984) 303–305.
- [35] B. Wampfler, S. Affolter, A. Ritter, M. Schmid, *Messunsicherheit in der Kunststoffanalytik: Ermittlung mit Ringversuchsdaten*, Hanser, München, 2017.
- [36] D.R. Lide (Ed.), *CRC Handbook of Chemistry and Physics: A ready-reference book of chemical and physical data: 2004-2005*, 85th ed., CRC Press, Boca Raton, 2004.

- [37] S.R. Samms, S. Wasmus, R.F. Savinell, Thermal Stability of Nafion® in Simulated Fuel Cell Environments, *J. Electrochem. Soc.*, <https://doi.org/10.1149/1.1836669>.
- [38] P.W. Atkins, *Kurzlehrbuch Physikalische Chemie*, John Wiley & Sons, 2001.
- [39] M. Tahir, L. Pan, F. Idrees, X. Zhang, L. Wang, J.-J. Zou, Z.L. Wang, Electrocatalytic Oxygen Evolution Reaction for Energy Conversion and Storage: A Comprehensive Review, *Nano Energy* 37 (2017) 136–157.
- [40] M. Schalenbach, A Perspective on Low-Temperature Water Electrolysis – Challenges in Alkaline and Acidic Technology, *International Journal of Electrochemical Science* (2018) 1173–1226.
- [41] T. Brandsch, F.-A. Schell, K. Weis, M. Ruf, B. Müller, H. Vahrenkamp, *Chemische Berichte* 130 (1997) 283–289.
- [42] C.H. Yoder, Application of the Simple Salt Lattice Energy Approximation to the Solubility of Minerals, *American Mineralogist* 91 (2006) 747–752.
- [43] C.H. Yoder, Geochemical Applications of the Simple Salt Approximation to the Lattice Energies of Complex Materials, *American Mineralogist* 90 (2005) 488–496.
- [44] F.N. Büchi, G.G. Scherer, In-situ Resistance Measurements of Nafion® 117 Membranes in Polymer Electrolyte Fuel Cells, *Journal of Electroanalytical Chemistry* 404 (1996) 37–43.
- [45] M.N. Tsampas, A. Pikos, S. Brosda, A. Katsaounis, C.G. Vayenas, The Effect of Membrane Thickness on the Conductivity of Nafion, *Electrochimica Acta* 51 (2006) 2743–2755.
- [46] R. Phillips, C.W. Dunnill, Zero gap alkaline electrolysis cell design for renewable energy storage as hydrogen gas, *RSC Adv.* 6 (2016) 100643–100651.
- [47] T. Yamamoto, A. Ushiro, I. Yamaguchi, S. Sasaki, Synthesis, Structure, and Chemical Properties of Lithium Salts of Poly(2-methoxyaniline-5-sulfonic acid), *Macromolecules* 36 (2003) 7075–7081.

# Supporting Information

## K<sup>+</sup> Transport in Perfluorosulfonic Acid Membranes its energetic and thermodynamic implications for CO<sub>2</sub> electrolysis

Kim-Marie Vetter, Jamie Härtl, David Reinisch, Thomas Reichbauer, Nemanja Martić, Olaf Hinrichsen and Günter Schmid\*

### Electrochemical cell for electrolyte studies

Electrochemical experiments were performed in a water electrolysis cell adapted from a fuel cell kit provided by Scribner Associates Inc. A schematic of the setup is shown in Figure S1. The original anode graphite serpentine flow field (Figure S1g), was replaced by an analogous titanium component (Figure S1b), also provided by Scribner Associates Inc. The cell is composed of an end plate with flexible tubes for water circulation (Figure S1a), a gold plated copper current collector (f), the graphene serpentine flow field (g), an ethylene propylene diene monomer rubber (EPDM) sealing (c), a titanium grid (thickness 0.40 mm, respectively, (d)) and finally the MEA in the middle of the device (e).

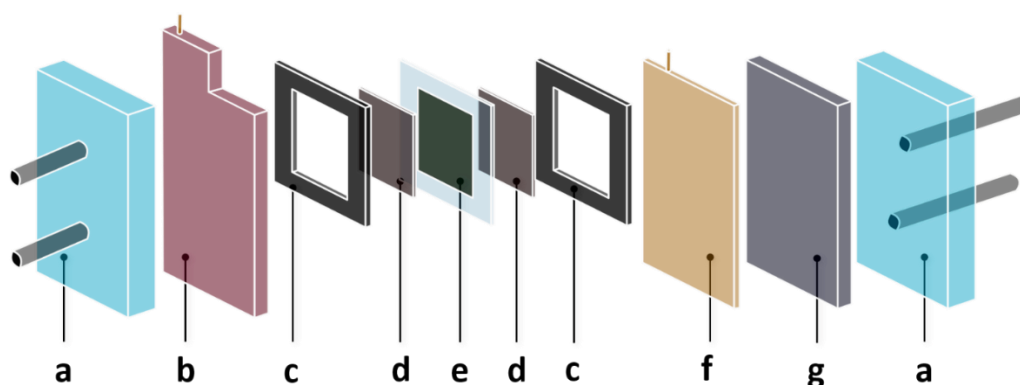


**Figure S1:** The installation for water electrolysis used in this study was slightly modified compared to earlier reports<sup>[1]</sup> and used for electrochemical performance determination. The cathode side is shown on the right, the anode side is shown on the left. The setup is composed of two end plates (a), a titanium (b) and a graphite (g) flow field, a gold-plated current collector (f), EPDM sealings (c), titanium grids (d) and the MEA in the middle (e).

### Materials

The water used for all experiments in this study was Type 1 ultrapure water purified using the Milli-Q® Integral water purification system (18 MΩ·cm). Chemicals for catalyst syntheses applied in this study are listed in Table S1 including suppliers and purities.

*Table S1: Suppliers and purities of chemicals applied in this study.*

| <b>Compound</b>                | <b>Supplier</b> | <b>Purity / %</b> |
|--------------------------------|-----------------|-------------------|
| KHCO <sub>3</sub>              | Alfa Aesar      | 99.0              |
| H <sub>2</sub> SO <sub>4</sub> | ROTIPURAN       | 96.0              |
| K <sub>2</sub> SO <sub>4</sub> | Alfa Aesar      | 99.0              |
| KOH                            | Alfa Aesar      | 99.0              |

### **Membrane preparation**

PFSA membranes used in this study were provided as Nafion<sup>®</sup> N117 by Chemours. Prior to use they were immersed in a freshly prepared half-concentrated peroxymonosulfuric acid solution overnight, washed with water, stirred in another portion of water for 60 min and finally dried at 70 °C for 15 min.

### **MEA fabrication**

For MEA fabrication, commercial Pt (for cathode) and Ir (for anode) nanopowders provided by Umicore were used as reference materials. The catalyst powders were suspended in methanol,<sup>[2]</sup> a polymer binder (Nafion<sup>®</sup>, 5%) was added and the suspension was intimately mixed. The ink was doctor bladed onto polyimide foil (Kapton<sup>®</sup>) and the resulting supported electrode was dried at 80 °C for 30 min. The catalyst loading was  $1.98 \pm 0.25$  mg/cm<sup>2</sup> for each electrode. In a decal process, the Kapton<sup>®</sup>-supported electrodes (cut to 5 cm<sup>2</sup> squares), were heat transferred onto the PFSA membrane by pressing a cathode-membrane-anode sandwich with 2.5 Nm at 175 °C for 60 seconds.

### **Membrane stability studies**

For assessing membrane stability information in contact with different electrolytes, PFSA membrane pieces (2 x 1.25 g) were immersed in electrolyte solutions (1.0 M KOH, KHCO<sub>3</sub>, and K<sub>2</sub>SO<sub>4</sub>) and liquid samples (2.0 mL) were taken weekly.

### **Nuclear magnetic resonance (NMR)**

<sup>1</sup>H and <sup>19</sup>F NMR spectra were recorded on a 300 MHz Bruker Avance 300 spectrometer equipped with an auto tune BBO, 5 mm, Ag-31P probe head, a pulsed field gradient unit and gradient shimming unit. NMR samples were prepared by taking aliquots from the membrane stability study mother liquors (600 μL) for <sup>19</sup>F NMR spectra and by diluting aliquots (300 μL) with D<sub>2</sub>O (300 μL) to mitigate the predominant H<sub>2</sub>O peak.

### **Reference electrodes**

The cathode potential was measured by an Ag/AgCl (3M KCl) reference electrode (RE-1BP, ALS Co.). The obtained Ag/AgCl potentials were converted to RHE scale using the following equation:  $E_{RHE} = E_{Ag/AgCl} + 0.196 V + 0.059 V \cdot pH$ .

## Electrochemical impedance spectroscopy

The obtained data was fitted with the equivalent circuit diagram shown in Figure S2. MEA contacting is implemented as a coil ( $R_L$ ) and held constant for all experiments. This allows for a comparison of the remaining resistive contributions: The ohmic contribution to the resistance can be read off the origin of the obtained Nyquist plots (zero crossing) in the high frequency region of the graph. We refer to this contribution as the membrane resistance  $R_\Omega$ . The width of the Nyquist plot depicts the charge transfer resistance ( $R_{CT}$ ) and comprises kinetic as well as mass transport contributions at the electrodes, both at the anode ( $R_{A,A}$ ) and the cathode ( $R_{A,C}$ ) catalyst.  $R_{CT}$  is calculated subtracting the high frequency from the low frequency resistance:  $R_{CT} = R_{LFR} - R_{HFR}$ .

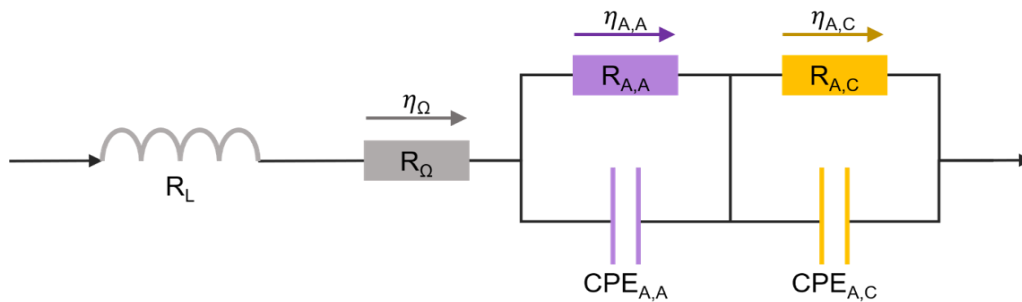


Figure S2: Equivalent circuit diagram used for data analysis obtained in impedance spectroscopy measurements.

## Raw data of the galvanostatic step procedure

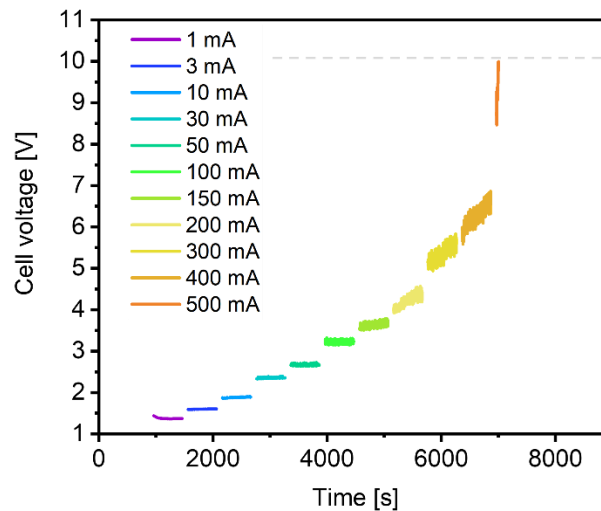
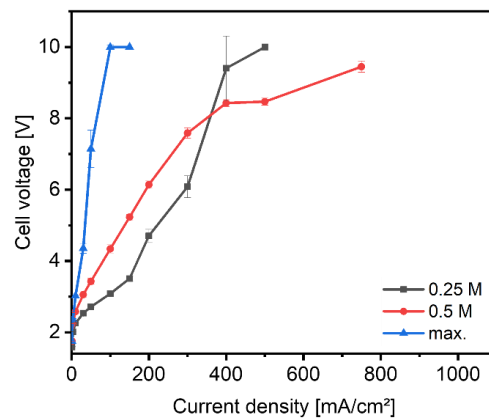


Figure S3: Example raw data of galvanostatic step procedure including a voltage drop at 500 mA/cm<sup>2</sup>. The data were obtained from a 1.0 M KHCO<sub>3</sub> mixed electrolyte experiment. After acquisition, the data obtained for each step was averaged and errors were calculated.



## Anion variation study: Potassium sulfate ( $K_2SO_4$ ) used as electrolyte



**Figure S4:** In an anion variation study, the bicarbonate electrolyte ( $KHCO_3$ ) was exchanged by  $K_2SO_4$  and concentrations were normalized to the  $K^+$  content in solution.

## Study towards membrane degradation and morphological changes in PFSA structure

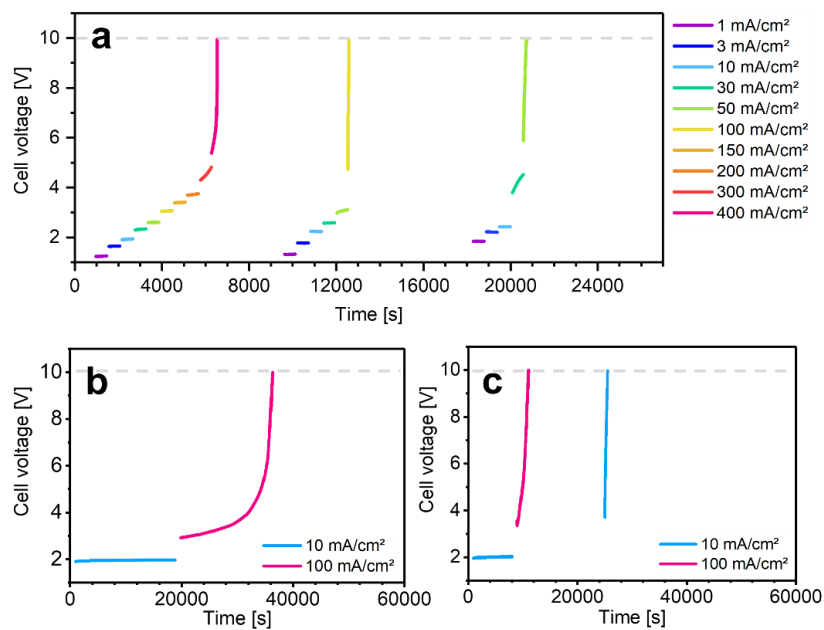


**Figure S5:** Results of MEA study towards morphological changes in the PFSA structure in a mixed electrolyte configuration with a) the same electrochemical procedure repeated three times on the same MEA, b) an extended procedure with longer galvanostatic steps (18 000 s = 5 h) and c) a combination of both (7 200 s = 2 h). A reference measurement can be found in the supporting information.

This study complements our main paper and addresses performance repeatability vs. degradation of the cell performance when feeding electrolyte at the anode side of the cell. Three types of experiments were conducted: First, the electrochemical procedure (see experimental section of the main paper) was repeated three times on the same MEA. Second, a single procedure including longer galvanostatic steps (18 000 s = 5 h) was applied and third, two repetitions of medium length (7 200 s = 2 h) were tested on a new MEA each.

While in a reference measurement, a procedure repetition produced three times the exact same data (see below), staying below 3.5 V, we observed a voltage drop when employing an electrolyte. Shown in Figure S5a, the drop occurred at 400 mA/cm<sup>2</sup> during the first experiment run and at 100 mA/cm<sup>2</sup> or 50 mA/cm<sup>2</sup> at the second run, respectively. After the drop, the voltage required increased towards the setup potential compliance (10 V) and the set current density could not be reached anymore. The cation exchange increases the membrane resistance and induces morphological changes, which leads to the following effect: When repeating the procedure and starting with small current densities first, the voltage required was higher each time, e.g. at 10 mA/cm<sup>2</sup> it was first 1.92 V, then 2.23 V and finally resulted in 2.42 V required.

Applying longer galvanostatic steps, the voltage drop occurred already at 100 mA/cm<sup>2</sup> as shown in both, **Figure S5b** and c. Comparing the time when the drop occurred with e.g. the charge flow and thus the amount of charge carriers transported over the membrane did not yield any correlation. But as discussed earlier, the literature known correlations are not linear and trace back to morphological changes in the polymer structure itself caused by the change in cationic environment around the sulfonic acid groups.<sup>[3]</sup> The fact that after the voltage dropped, it was possible to restart the procedure at reasonable but slightly increased potentials, contradicts the hypothesis of total membrane degradation. It is known that alkaline metals cause potential drops due to membrane resistances that are not due to decreased mobility in the membrane.<sup>[4]</sup> We further investigated this by employing NMR techniques to both, the electrolyte and the mother liquor obtained from a membrane degradation study (membrane exposure to 1.0 M electrolyte for 4 weeks). No membrane degradation products were found to go into solution, since neither the <sup>1</sup>H spectrum nor the <sup>19</sup>F spectrum exhibited any signals. It is known that fluoride might go into solution forming HF during PEM operation,<sup>[5]</sup> and would appear at -129 ppm in the <sup>19</sup>F spectrum.<sup>[6]</sup> Of course, possible degradation products could stay within the membrane or degradation could occur in the form of catalyst poisoning, we rather hypothesize that the change in membrane resistance is due to morphological changes in the membrane's polymeric structure. Since alkaline and alkaline earth metals can induce symmetrical and thermodynamically stable layer arrangements in sulfonate complexes<sup>[7]</sup> and it is known from polymer electrolyte research that e.g. lithium is known to form stable but highly ion conducting sulfonic acid complexes, covalently attached to a polymeric backbone,<sup>[8]</sup> complex formation during operation is most likely. During operation, K<sup>+</sup> ions hop from one sulfonate group to the next, which is a process requiring overcoming of an energy barrier. This energy is translated into an increased membrane resistance. Latent heat will increase the chain mobility and enable the polymer side chains to move and arrange around captured K<sup>+</sup> ions in a favorable way. Although many structural aspects in PFSA research still remain unclear, the ionic sulfonic acid groups have an intrinsic tendency to form clusters that are distributed among the non-polar PTFE-like environment.<sup>[9]</sup> This tendency is enforced when K<sup>+</sup> is delivered, since it will act as the central atom in sulfonate complex formation and therefore induce polymer morphological changes. This process is slow and starts at small current densities, when the charge flow is comparatively low, and chains are mobile enough to rearrange around K<sup>+</sup>. As a template for sulfonate complexes in the MEA, the respective sulfates solubility in water can be considered to obtain energetic insights.<sup>[10]</sup> Dividing the solution energy of potassium sulfate (132.3 kJ/mol for ½ K<sub>2</sub>SO<sub>4</sub>)<sup>[11]</sup> by the Faraday constant (F = 96485 C/mol) and the number of transferred electrons (z<sub>e</sub> = 1), a voltage of 1.37 V is obtained. Divided by two K<sup>+</sup> per sulfate, this is in the same order of magnitude than the activation barrier derived from the small concentration (V<sub>int</sub> = 527 mV).

## Reference experimental data for degradation study

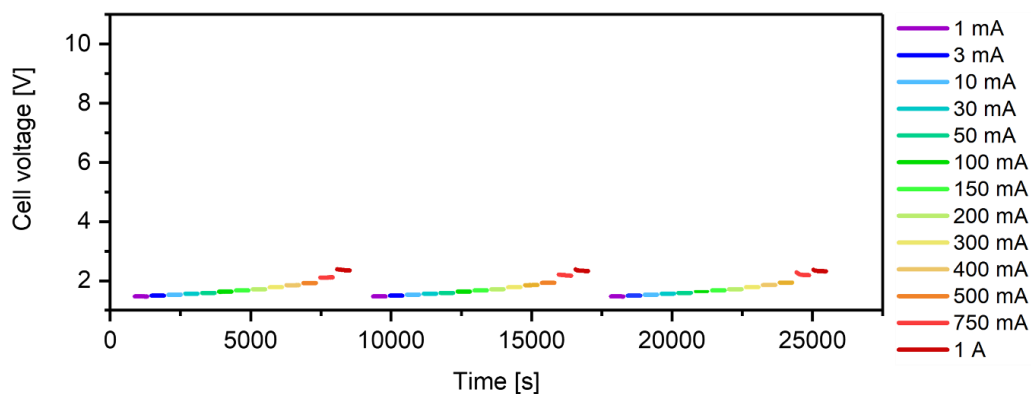


**Figure S6:** In a reference experiment for the degradation study, a standard protonated MEA was subjected three times to the same galvanostatic step procedure without using any electrolyte but ultrapure water only. Obtained values were averaged and error bars were calculated.

**Table S2:** Standard deviation calculation for repeatability experiments based on a reference water electrolysis experiment.

| Current density<br>/ mA/cm <sup>2</sup> | Potential<br>1 <sup>st</sup> run<br>/ V | Potential<br>2 <sup>nd</sup> run<br>/ V | Potential<br>3 <sup>rd</sup> run<br>/ V | Average<br>/ V | Variance<br>/ V <sup>2</sup> | Standard deviation<br>/ V |
|---|---|---|---|----------------|------------------------------|---------------------------|
| 1                                       | 1,468                                   | 1,471                                   | 1,468                                   | 1,469          | 2,00E-06                     | 0,0014                    |
| 3                                       | 1,496                                   | 1,498                                   | 1,498                                   | 1,497          | 8,89E-07                     | 0,0009                    |
| 10                                      | 1,526                                   | 1,527                                   | 1,529                                   | 1,527          | 1,56E-06                     | 0,0012                    |
| 30                                      | 1,562                                   | 1,563                                   | 1,565                                   | 1,563          | 1,56E-06                     | 0,0012                    |
| 50                                      | 1,586                                   | 1,589                                   | 1,588                                   | 1,588          | 1,56E-06                     | 0,0012                    |
| 100                                     | 1,633                                   | 1,634                                   | 1,635                                   | 1,634          | 6,67E-07                     | 0,0008                    |
| 150                                     | 1,673                                   | 1,675                                   | 1,676                                   | 1,675          | 1,56E-06                     | 0,0012                    |
| 200                                     | 1,712                                   | 1,712                                   | 1,717                                   | 1,714          | 5,56E-06                     | 0,0024                    |
| 300                                     | 1,782                                   | 1,782                                   | 1,783                                   | 1,782          | 2,22E-07                     | 0,0005                    |
| 400                                     | 1,851                                   | 1,852                                   | 1,855                                   | 1,853          | 2,89E-06                     | 0,0017                    |
| 500                                     | 1,92                                    | 1,927                                   | 1,938                                   | 1,928          | 5,49E-05                     | 0,0074                    |
| 750                                     | 2,11                                    | 2,192                                   | 2,208                                   | 2,170          | 1,84E-03                     | 0,0429                    |
| 1000                                    | 2,369                                   | 2,343                                   | 2,332                                   | 2,348          | 2,41E-04                     | 0,0155                    |

**Experimental data for the experiments with electrolyte used at the cathode side only including a 2.0 M KHCO<sub>3</sub> experiment**

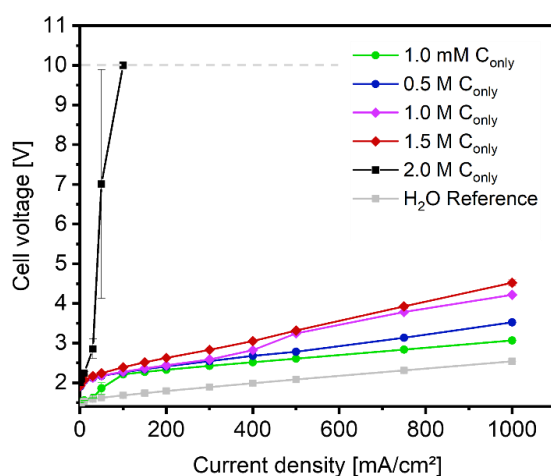


**Figure S7:** Complete electrochemical data (including a 2.0 M KHCO<sub>3</sub> experiment) for galvanostatic experiments with electrolyte used at the cathode side only and a voltage drop occurring only in the case of the highest concentration (2.0 M KHCO<sub>3</sub>).

- [1] K.-M. Vetter, T. Reichbauer, N. Martić, D. Reinisch, O. Hinrichsen, G. Schmid, *Electrochimica Acta* **2020**, 362, 137182.
- [2] L. G. Lage., P. G. Delgado, Y. Kawano, *Journal of Thermal Analysis and Calorimetry* **2004**, 75, 521.
- [3] S. Moshtarihah, N. A. W. Oppers, M. T. de Groot, J. T. F. Keurentjes, J. C. Schouten, J. van der Schaaf, *Journal of Applied Electrochemistry* **2017**, 47, 51.
- [4] Y. Iwai, T. Yamanishi, *Polymer Degradation and Stability* **2009**, 94, 679.
- [5] A. Pozio, R. F. Silva, M. de Francesco, L. Giorgi, *Electrochimica Acta* **2003**, 48, 1543.
- [6] M. Gerken, J.A. Boatz, A. Kornath, R. Haiges, S. Schneider, T. Schroer, K.O. Christe, *Journal of Fluorine Chemistry* **2002**, 116, 49.
- [7] A. J. Shubnell, E. J. Kosnic, P. J. Squattrito, *Inorganica Chimica Acta* **1994**, 216, 101.
- [8] C. S. Harris, T. G. Rukavina, *Electrochimica Acta*, 1995, 2315.
- [9] S. C. Yeo, A. Eisenberg, *Journal of Applied Polymer Science* **1977**, 875.
- [10] D. R. Lide (Ed.) *CRC Handbook of Chemistry and Physics. A ready-reference book of chemical and physical data: 2004-2005*, CRC Press, Boca Raton, **2004**.
- [11] J. M. Blanchard, R. D. Joly, J. M. Lettoffe, G. Perachon, J. Thourey, *Journal de Chimie Physique et Physico-Chimie Biologique* **1974**, 472.